SAFETY IN MINES RESEARCH ADVISORY COMMITTEE

SIMRAC

Final Project Report

Title: DEVELOP A QUANTITATIVE UNDERSTANDING OF ROCKMASS BEHAVIOUR NEAR EXCAVATIONS IN DEEP MINES

Part 1: Chapters 1 - 2

Author/s: JAL Napier, MW Hildyard, JS Kuijpers, A Daehnke, EF Sellers, F Malan, E Siebrits, MU Özbay, T Dede and PA Turner

Research Agency: CSIR: Division of Mining Technology

Project No: GAP 029

Date: Dececember 1995

EXECUTIVE SUMMARY

Control of the rock mass deformation near deep level stopes and the avoidance of damaging incidents of violent rock failure requires a fundamental understanding of rock failure mechanisms. Research work to gain this understanding has been undertaken within the ambit of the Rockmass Behaviour project GAP029. Specific outcomes of this research are as follows.

1.) The computer code WAVE has been developed to a useable degree to allow elastodynamic interactions between faults and stopes to be analysed in both two and three dimensions. Special features of WAVE allow the simulation of dynamic fault slip and simple tabular mining outlines.

2.) Numerical studies using WAVE have shown that particle velocities generated by slip on a simulated fault are in broad agreement with established distance-velocity correlations in three dimensions.

3.) Application of WAVE to simplified mining problems has shown that backfill can be effective in reducing relative closure velocities between the hangingwall and the footwall of stopes and that parting planes can trap seismic waves in the hangingwall region. Conditions for the triggering of a large fault slip event by a small precursory event have been investigated.

4.) Photoelastic studies of wave propagation in plates have confirmed the validity of numerical results computed with the WAVE code.

5.) The causes of numerical instability in the elastodynamic boundary element code TWO4D have been analysed and methods to reduce or eliminate the instabilities have been implemented.

6.) The computer code DIGS has been developed further to allow the efficient analysis of large scale interacting crack assemblies and initial work has started to allow the analysis of multiple material problems and three dimensional interacting crack problems.

7.) Studies of fundamental rock failure mechanisms have shown that the grain shape can affect the nature of rock failure strongly in terms of rapid load shedding or plastic yielding. This

provides a basis for relating the fabric of different rock types to their overall strength and brittleness.

8.) Pre-existing rock discontinuities, such as parting planes or weak joints, have been shown to play an important role in the formation of extension fracture patterns near openings.

9.) A survey has been carried out on the effect of geological structures on the pre-existing stress state in different mining districts and the potential effect of this stress state on rock failure analysis.

10.) The role of blasting in promoting fracturing around tunnels has been analysed. It is found that the blast gases can enhance the formation of additional fractures.

11.) Physical observations of slow creep-like stope closure rates have been analysed using a viscoelastic model of a simple tabular excavation with good correspondence being achieved. This forms an important basis for studies of the effect of face advance rate on seismic intensity and cyclicity.

12.) Studies to determine the creep potential of rock joints have been initiated.

ABSTRACT

Progress on the Rockmass Behaviour project GAP029 is summarised in this report for the period 1993 to 1995. The work has been carried out in three main areas of activity covering respectively, elastodynamic modelling, development of techniques for the analysis of the stope fracture zone and application of models to explore innovative design procedures.

The work on elastodynamics has centred on the analysis and application of the experimental boundary element code TWO4D and on the further development of the finite difference code WAVE. It has been found that the application of boundary element methods (such as TWO4D) to the solution of dynamic problems can be hampered by two factors. The first of these is the appearance of instabilities in the numerical solution which are exhibited as unbounded oscillations in particle motions, which can make the analysis method unusable. The cause of these instabilities appears to be associated with the shape functions that are used to represent the variation of the displacement discontinuity strength within each element used to cover the problem boundaries. The use of low order functions, such as constant or linear variation discontinuities, results in strongly singular variations in transmitted stress waves away from the elements. These stress "spikes" can, in unfavourable cases, lead to a response at a receiving position that is larger than the so-called self-effect of the sending element. In these cases, an uncontrolled resonance is set up between the elements leading to the observed instability behaviour. It has been found that the occurrence of such instabilities can be curtailed by adjusting the self-effect of all elements by a small perturbation or by adopting a more refined time-stepping scheme to update the elastodynamic solutions (the so-called half-step scheme). It has also been possible to apply a special stability analysis technique, based on control theory concepts, from which it can be inferred whether a given problem will exhibit instability behaviour before the solution is computed.

The second difficulty encountered in using elastodynamic boundary element methods is associated with the need to retain a back-history of solution values for all previous time steps preceding the current time step. This can result in long computer run times and large storage requirements for moderate sized problems.

Development of the finite difference computer code WAVE has concentrated on implementing fault slip logic for two-dimensional and three-dimensional problems, opening and closing

behaviour in cracks, cavity modelling capabilities and on the inclusion of special constructs to allow tabular mine layouts to be modelled. Considerable attention has been given to improving the graphics capabilities of WAVE for the representation of wave transmission patterns and for extracting quantitative information such as time plots of key variables and frequency analysis capabilities. Higher order differencing schemes have also been introduced to reduce dispersion in the transmission of waveforms through the numerical grid.

Initial applications of the elastodynamic codes WAVE and TWO4D have been made to simplified mining problems. One of these applications was to analyse the effect of backfill in a horizontal stope with a single parallel parting plane above the stope. A seismic source was introduced in the form of a vertical fault plane ahead of the advancing stope face. The fault plane was allowed to slip and it was observed that the parting plane could trap seismic waves in the immediate hangingwall region above the stope provided it was free to slip or to open. It also showed that backfill could reduce relative movements between the stope hangingwall and footwall.

A number of studies have been carried out to compare the seismic response monitored at varying distances away from a modelled fault ahead of a horizontal stope with empirical and theoretical seismic correlations of particle velocity with source distance. When the fault rupture was modelled in three-dimensions, the results agreed qualitatively with the empirical and theoretical particle velocities whereas a two-dimensional model tended to over-estimate the predicted particle velocities at a given distance from the fault. Also the fault rupture logic of either allowing a sudden loss of cohesion or a controlled degradation of cohesion as a function of the degree of slip, could affect both the rupture velocity on the fault and the observed peak particle velocities. Sudden loss of cohesion was associated with higher velocities. A further study of the initiation of slip on a fault between two stopes revealed that an event initially triggered in the fault region between the stopes could result in a much larger event being triggered on the fault in the hangingwall region. A three-dimensional back analysis of an actual rockburst event was carried out which showed that broad correspondence between modelled and measured particle velocities could be obtained although it was clear that the model was too simplistic to reproduce the exact details of observed waveforms.

Some effort was also made to check the validity of the elastodynamic models against the results of physical models of photodynamic experiments in which an explosive charge was initiated on the edge of a composite plate made from photoelastic materials and having a slot-shaped

opening in the centre of the plate. Very good agreement was obtained between the observed patterns of wave propagation and the numerically simulated results, adding confidence to the validity of the numerical solutions. A review has also been carried out on the attenuation of waves in fractured ground to set the basis for future investigations of the interaction of seismic waves with the stope fracture zone.

The second major area of work addressed the development of techniques to study the mechanics of the stope fracture zone. Much of this work has been based on the application of the DIGS computer code (Discontinuity Interaction and Growth Simulation) developed specifically to model the growth of fractures in brittle rock. Crack sliding and opening logic is based on assigned cohesion and friction properties and on specified dilation angles for forward and reverse sliding. A simple cohesion-weakening model, in which cohesion is specified as a linear function of the slip movement, has been implemented. Crack growth is controlled by 'tension' and 'shear' modes to control the choice of growth direction ahead of an active discontinuity. An energy based growth criterion has been formulated that allows shear banding phenomena, such as pillar foundation failure and slip lines in slope stability problems, to be simulated. Good progress has also been made in the development of a numerical solution method that can allow the analysis of large scale assemblies of interacting cracks. In addition, work has been initiated on the implementation of a multiple material model and on the formulation of influence functions for polygonal shaped elements that can be used in three-dimensional fracture growth studies.

Considerable effort has been devoted to studies of the fundamental nature of failure processes in brittle granular rock assemblies. This showed that grain shape can play a strong role in determining the load shedding capabilities of the simulated material structure. Irregular or angular shaped grains allow rapid load shedding once failure is initiated whereas rounded grains reflect hardening or reduced load shedding. By contrast fracturing through grains allows rapid strength degradation. This work also demonstrated how fracturing parallel to the major principal stress can arise in uniaxial compression as a result of grain angularity and how this is curtailed if confining stresses are applied to the sample assembly. Additional effects that control micro-fracture patterns are the presence of pores which can promote tensile fractures between the pores as opposed to the common concept of fractures initiating from the pore surfaces.

Laboratory scale physical modelling experiments have been carried out to identify the nature of fracture initiation from discontinuity interfaces and to calibrate and verify the DIGS code. Good qualitative agreement has been obtained in the case of fracture initiation from a single inclined diametral interface introduced into a Brazilian test specimen, giving some confidence to the applicability of the tensile fracture growth rule used in DIGS. Further agreement was obtained in experiments where fractures were initiated from the interfaces of a layered sample of synthetic sandstone-cement material into which one or two rectangular openings were introduced. These experiments also provided supporting evidence for a mechanism proposed for the initiation of extension fractures from parting planes in underground stopes. Some inconclusive physical modelling tests were also carried out on stacks of glass layers in which it proved to be difficult to model the observed fracture patterns. The extreme brittleness of glass and the absence of granularity make these experiments difficult to reproduce. A special test rig has also been constructed to allow triaxial tests to be carried out on rectangular shaped specimens. Initial tests in which a rectangular strip punch was used to load a biaxially confined specimen have shown the formation of wedge-shaped shear failure zones initiating near the edges of the punch. These shear fractures can be approximately modelled using the shear growth model implemented in DIGS.

A review of experiments carried out by previous investigators has shown that in many instances so-called *secondary* fractures may develop adjacent to the initial fracture configurations around openings or pre-arranged notches or sliding cracks. One such example is the development of tensile zones adjacent to wing cracks formed from the ends of a sliding crack. Numerical simulations have shown that these secondary fractures may play a strong role in the formation of splitting fractures sub-parallel to the major loading direction and may also account for slabbing and spalling. Confining stresses curtail secondary fracturing and shear mechanisms become prominent. Conversely extension type fractures must form either in direct tension or from pre-existing flaws such as joints or mobilized parting planes.

The third and final area of work covers the application of modelling concepts to innovative mining strategies and the identification of underlying mechanisms that must be understood to allow any planned intervention in controlling or engineering the mechanics of the stope fracture zone. One of the necessary factors in this respect is to understand the overall geological environment and stress field in different mining districts. A survey has been carried out to summarize known information concerning stress trends as well as to assess proposed tectonic models for these trends. It has also been demonstrated that the specification of the initial stress

state can be strongly affected by the manner in which pre-existing stresses associated with geological features such as fault structures and dykes are accounted for in any proposed numerical analysis.

A review of interaction mechanisms between excavation processes and induced fractures has been completed. This indicated that blasting can enhance the formation of fractures near tunnels ("bow-wave" fracturing) depending on the blast strategy (conventional development or smooth wall blasting). This is important in inferring the influence of blasting on the formation of keyblock structures in stopes. The propagation of blast-induced fractures from a shot hole has been modelled using a simple pressure loading model in DIGS. Observed blast patterns are reproduced as well as some fracture interactions generated in successive blasts in adjacent holes.

In devising any strategy to control the formation of fracturing, it is necessary to determine whether the rate of face advance affects the recurrence time of seismic activity. This in turn requires an understanding of the basic mechanisms controlling time-dependent "creep" behaviour in stopes. Initial work has shown that a simple visco-elastic model can be used to reproduce observed closure rates with good accuracy and that the origin of slow creep-like closure is almost certainly associated with movements on joints and discontinuities close to the excavation. The nature of these movements must be identified. To do this a number of joint surfaces in borehole cores have been mapped and will be correlated with the roughness of the surfaces subjected to creep loading experiments. This information will be used to construct representative numerical models of discontinuity relaxation associated with simulated mining step increments.

Several stope scale failure processes have been identified. These include mechanisms for the formation of wedge structures ahead of a stope face as well as the effect of inherent weaknesses, such as parting plane slip on the initiation of extension fracturing. If extension fractures initiate from mobilized parting planes and intersect the stope, the horizontal confining stress can be reduced leading to an effective widening of the stope width and subsequent formation of an unstable, unconfined failure near the stope face (rockburst). It is also suggested that where footwall failure mechanisms differ from those of the hangingwall, anomalously oriented extension fracture patterns may be initiated.

Several innovative numerical analyses have been carried out to demonstrate mechanisms of sidewall spalling and borehole slabbing (breakout) phenomena. In addition, the effect of rotating the stress field on the stimulation of fracture growth from initial microcracks by the activation of wingcracks at both ends is demonstrated. This mechanism can be used to determine the effective in-situ strength properties near openings that are advanced incrementally and which consequently cause stress rotations as the face position is changed. Other studies include estimation of the bounding limit for the size of the fracture zone, the effect of modulus sensitivity to confinement based on microfracture structure and the effect of mining depth on the expected severity of seismic activity. It is also suggested that if the stope hangingwall is strongly fragmented, support could be designed to cover a continuous strip parallel to the stope face and to provide an "umbrella" in rockburst conditions rather than be designed to maintain the integrity of the hangingwall beam.

CONTENTS

1. INTRODUCTION

The primary purpose of the rockmass behaviour research project GAP029 is to provide a quantitative understanding of the formation of fractures and behaviour of fractured rock around excavations and the mechanisms of rockbursting. This research work represents a continuation of investigations supported by the Gold Mining Industry under the auspices of the former Chamber of Mines Research Organization. This report summarizes technical details of the work carried out during the three year period from 1993 to 1995, with funding by the Safety in Mines Research Advisory Committee (SIMRAC) of the South African Department of Mineral and Energy Affairs. The report is structured in three main sections corresponding to the three enabling outputs that were included in the original project proposal document submitted and adopted in 1992.

The three enabling outputs are as follows.

Output 1: *Methods to analyse elastodynamic rock movements and rockburst mechanisms.*

Output 2: *Methods to analyse the mechanics of the fracture zone surrounding deep level excavations.*

Output 3: *Innovative mining strategies and layout designs using numerical methods.*

The enabling outputs 1, 2 and 3 are covered respectively in sections 2, 3 and 4 of this report. In the original project plan, a number of detailed working steps were identified explicitly within each enabling output. These steps are inter-related and thus the work is not reported directly under each topic but is grouped according to appropriate functional themes including the actual project plan steps.

The structure of the three main outputs reflects the philosophy of developing basic tools for the analysis of rock deformation mechanisms (outputs 2 and 3) and then applying these tools to innovative mining strategies (output 3). The motivation for this approach is that a fundamental understanding of deformation and failure mechanisms will enable mining strategies to be designed in a rational manner and should also provide some ability to predict expected failure mechanisms in specified geotechnical environments. The project structure recognizes the basic

importance of characterizing dynamic rock movements for the understanding of rockburst initiation and the effects of rockbursting on stope hangingwall stability. Dynamic computer codes have been developed to investigate the interaction between seismic waves and stope movements. Calibration of the performance of elastodynamic numerical models against physical modelling experiments has also been undertaken.

However, it is apparent that any analysis of the formation of the stope fracture zone relies completely on a fundamental understanding of the nature of rock failure. In particular, it is necessary to describe the formation of tensile or extension fractures and to distinguish between this form of fracturing and the formation of shear band or burst fracture structures. Considerable attention has therefore been directed to the investigation of micro-mechanical models of rock failure and to the study of failure mechanisms associated with different rock fabrics. The exploration of these phenomena has required efficient numerical treatment of large scale interacting crack assemblies and good progress has been made in achieving this goal. An accompanying programme of physical modelling has been carried out to calibrate and verify some of the predicted fracture mechanisms.

It must also be acknowledged that only limited progress has been made in reaching the primary goal of output 3, which represents the investigation of innovative mining strategies and possible means to engineer the stope fracture zone. In addition, the planned step 3.1, which was directed towards determining the interaction of local support units and the hangingwall structure, has been omitted entirely as this topic is covered directly by SIMRAC project GAP032, Stope and Gully Support. Nevertheless, encouraging progress has been made in applying simplified modelling strategies to simulate the propagation of blast-assisted fracturing and in identifying the nature of creep-like movements in deep level stopes. The topic of time-dependant movements that are not directly seismic in origin is important for quantifying any link between the rate of face advance and the recurrence of damaging rockbursts. Good progress has been made in characterizing the nature of discontinuity roughness with a view to determining effective joint properties and joint creep behaviour. Work summarizing the current knowledge of the tectonic environment in different gold fields and the effect of mining depth on the nature of the stope fracture zone has also begun.

2. ELASTODYNAMICS

Work reported in this section corresponds to enabling output 1 of the Rockmass Behaviour research project - *'Methods to analyse elastodynamic rock movements and rockburst mechanisms'*. Studies have concentrated on improving the numerical stability properties of the boundary element elastodynamic code TWO4D, and on developing the finite difference code WAVE, to address the problem of analysing elastodynamic movements in the rock-mass.

The first approach is to use the boundary element method to represent the effect of dynamic slip and opening motions on dislocations in an isotropic medium. In this case influence functions based on Stoke's fundamental solution for a time varying point force in an infinite medium, are computed for displacement discontinuity elements which are used to define cracks, faults or stopes at arbitrary orientations. This method for the solution of two-dimensional plane strain problems is embodied in the computer code TWO4D. However, difficulties in applying the technique have arisen due to numerical instabilities that can occur in the computed solution. The analysis of the stability characteristics of the elastodynamic displacement discontinuity method is given in section 2.1, together with strategies for pre-determining potential instabilities and avoiding instabilities.

The second approach has been to employ finite difference methods to solve explicitly the differential equations describing the propagation of elastodynamic waves. This method is encoded in the computer program WAVE. The program allows discontinuities to be specified in orientations aligned to a cartesian grid in both two and three dimensions. A number of features of WAVE are described in section 2.2.

Section 2.3 shows how these techniques have been applied in analysing mine problems. Section 2.4 shows the results of physical modelling which has been used to gain fundamental understanding, and to validate the accuracy of the codes.

The project plan objectives for elastodynamics (enabling output 1) are as follows:

Objective 1.1: *Implement numerical techniques to represent the mechanics of fault slip including the possibility of slip-weakening, velocity dependent friction and representations of fault asperities.*

Objective 1.2: *Implement numerical techniques to represent the mechanics of fault slip including the possibility of slip-weakening, velocity dependent friction and representations of fault asperities.*

Objective 1.3: *Investigate using boundary element and finite difference codes, fault slip mechanisms, interaction of seismic waves with tabular stopes and with geological structures such as dykes, and the geometric factors that determine the magnitude of dynamic movements.*

Objective 1.4: *Characterize the dynamic representation of support elements and regional support such as backfill in numerical algorithms by interpreting underground and laboratory observations.*

Objective 1.5: *Review the physics of wave attenuation in a homogenous medium and the effects of multiple fractures in the medium, and propose numerical representations for this behaviour for dynamic modelling of the stope fracture zone.*

Objective 1.6: *Characterize the causes of numerical instability in boundary element methods for two and three dimensional elastodynamic problems.*

Objective 1.7: *Characterize the error limits imposed by finite difference meshes and the treatment of absorbing boundary conditions in finite difference analyses of elastodynamic problems.*

Objective 1.8: *Extend graphics representations of dynamic movements, predicted by numerical methods, and explore applications of dynamic analyses to improving the resistance of stope layouts to rockbursts and the impact of local and regional support strategies.*

2.1 DEVELOPMENT OF BOUNDARY ELEMENT CODES

The major contribution of boundary element elastodynamics has been to characterize and improve the numerical stability of the method (Objective 1.6). The presence of intermittent instabilities in time domain indirect boundary element methods has been identified, the causes analysed, and a new time-stepping algorithm developed with improved stability and accuracy characteristics. The results of this work are reproduced here from a study on the stability properties of time domain elastodynamic boundary element methods (Siebrits and Pierce, 1995).

Numerous time domain direct and indirect boundary element methods have been published in the boundary element literature over the past 30 years, but there have been relatively few papers published which mention or examine the stability properties of these methods, contrary to the finite difference and finite element literature, where the stability theory of these methods is well established (Smith 1985, p.47, Bathe 1982, p.537). There are examples in the literature (Koller et al 1992, Andrews 1994, Mack and Crouch 1991, Siebrits and Crouch 1994, Cole et al 1978) that demonstrate that boundary element methods go unstable after a sufficient number of time steps. In fact, the authors have yet to find a boundary element method code that does not go unstable, despite unsubstantiated claims in the literature of unconditionally stable boundary element methods (Banerjee et al, 1986). In this report, the reasons why indirect boundary element methods go unstable are examined, and a new time-stepping algorithm with significantly improved stability and accuracy properties, that can be generalized and applied to any time stepping direct or indirect boundary element method, is proposed.

Evidence of instabilities

This report deals with numerical instabilities in the two-dimensional displacement discontinuity method, with brief reference to the direct method. One of the more recently published direct boundary element codes, QUADPLET (Dominguez 1993), which uses numerical quadratic spatial and analytical linear temporal integrations, can be shown to go unstable, even for a simple problem, such as an axisymmetrically loaded cylinder (the Selberg problem, Graff 1975). Figure 2.1.1 shows an instability that develops by 2000 time steps for the case where 16 elements have been used to model the boundary, and $Q1 = 0.3$,

where $Q1 = (c_1 \Delta t)/\Delta x$, and c_1 = compressional wave velocity, Δt = time step, and Δx = element size. Since the instability only develops after such a large number of time steps, one may argue that the code is "practically" stable. However, the rate at which an instability develops depends upon the problem being solved. If elements are located at acute angles with respect to each other, or are in close proximity to each other, then an instability can develop much faster, and swamp most of the transient behavior that is being monitored. This will be demonstrated in the next example.

Numerical instabilities do not necessarily disappear if the time step is reduced. They are intermittent in nature, and problem dependent. A very simple problem that illustrates this is an antiplane strain version of the displacement discontinuity code, TWO4D (Siebrits and Crouch, 1994), with constant spatial and linear temporal functional variations (viz.

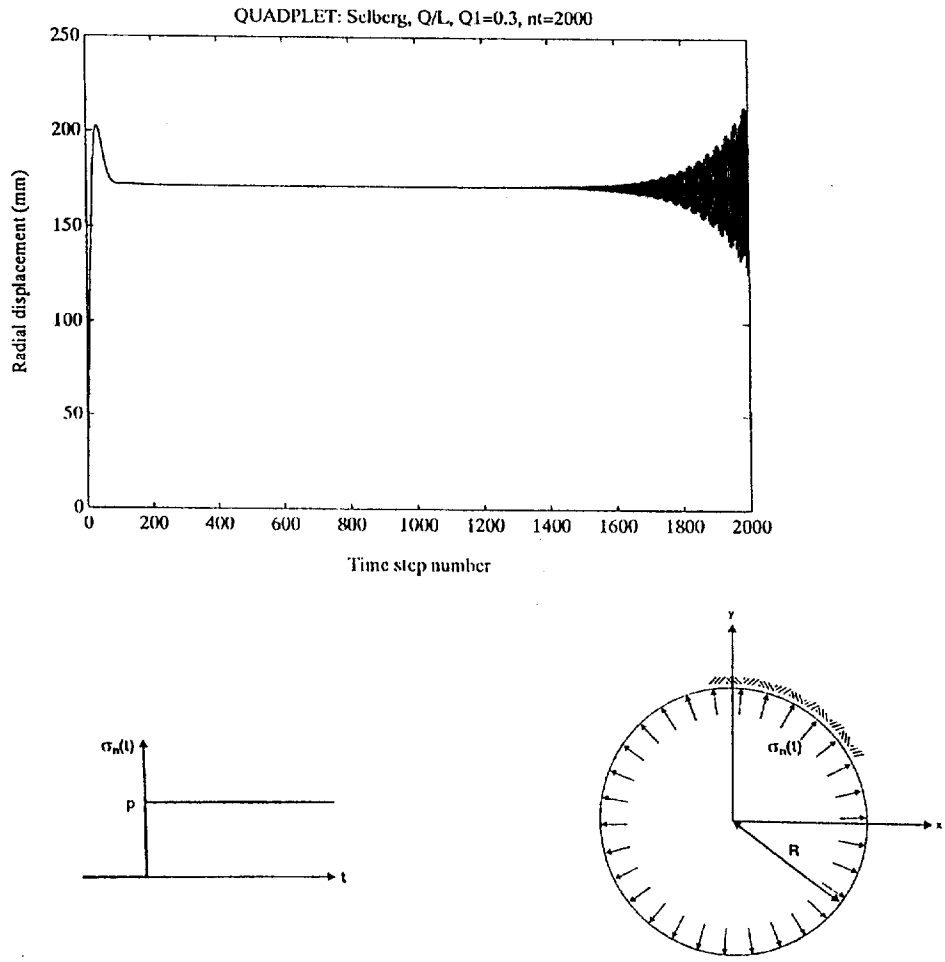

Figure 2.1.1: Evidence of instability in QUADPLET for Selberg problem

constant/linear scheme) and analytical integrations, where two elements are located opposite each other, $2\Delta x$ apart, as shown in figure 2.1.2. Table 2.1.1 highlights the intermittent nature of the instability development. In Table 2.1.1, $Q2 = (c_2 \Delta t)/\Delta x$, where c_2 is shear wave velocity. The loading pattern is immaterial. Depending on the particular combination of time step, spatial step, and problem geometry, numerical oscillations can either grow exponentially as a classical numerical instability, grow non-exponentially as a resonant instability, pulse in a resonant way with successive pulses increasing, decreasing or remaining constant in amplitude, or merely oscillate with a decreasing or unchanging amplitude. In other words, it is possible to generate almost any type of spurious oscillation.

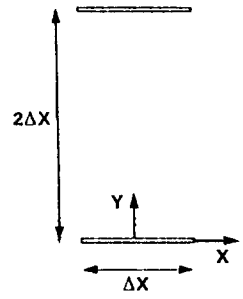

Figure 2.1.2: Two element problem geometry

Q2	0.10	0.20	0.30	0.40	0.50	0.60	0.70	0.80	0.90
stable?	no	no	yes	no	yes	yes	no	yes	yes
Q2	1.00	1.10	1.20	1.30	1.34	1.40	1.50		
stable?	yes	yes	yes	yes	no	yes	yes		

Table 2.1.1: Evidence of intermittent instabilities

In the displacement discontinuity method, even a single row of elements can go unstable. For example, in the plane strain constant/linear version of TWO4D, a single straight line of elements, with $Q1 = (c_1 \Delta t)/\Delta x = 0.5$, can be shown to be unstable by 500 time steps. In two dimensions, a Rayleigh wave propagating along a free surface (such as along a mathematical crack) does not decay with distance from the source (Graff 1975, p. 353). Thus, element to element influences along a mathematical crack construction, such as provided by the displacement discontinuity method, contain a component that does not decay with distance. It has been found that influences that decay with distance provide better stability properties in boundary element methods.

A test problem that has been used to investigate elastodynamic stability comprises two intersecting cracks, as depicted in figure 2.1.3 ("Hook" problem). Depending on the choice of $Q1$ in plane strain (or $Q2$ in antiplane strain), this problem may or may not go unstable. This applies to both the constant/linear and linear/linear versions of TWO4D. Figure 2.1.4 shows a typical unstable result obtained from the constant/linear antiplane strain version of TWO4D with $Q2$ = 0.7, where the displacement discontinuity history of element 21 is plotted (see

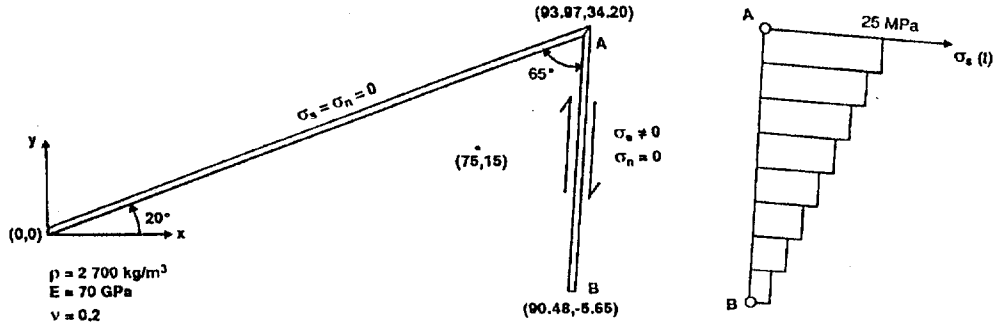

Figure 2.1.3: Geometry and loading of antiplane strain Hook problem

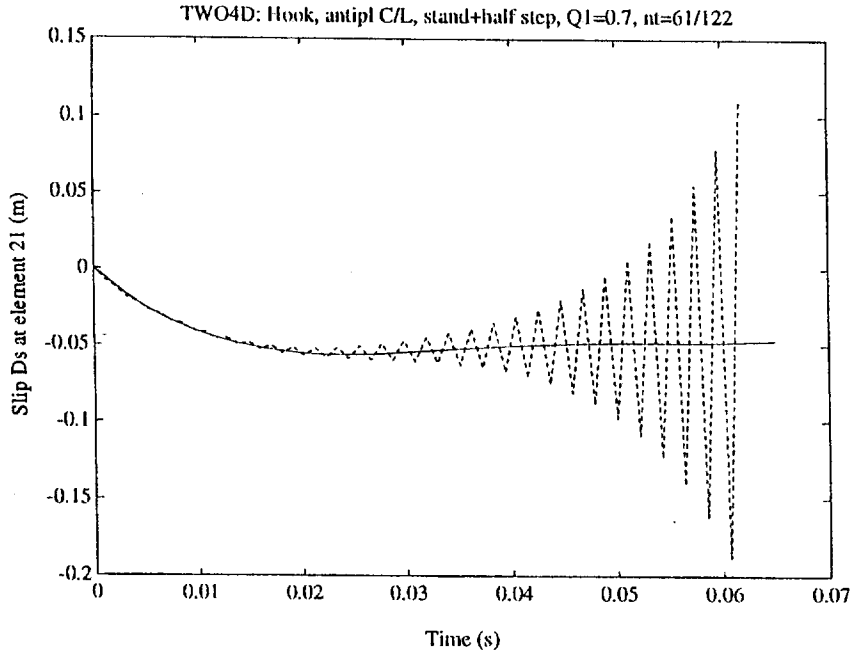

Figure 2.1.4: Slip at element 21 for antiplane strain Hook problem

figure 2.1.5). The smooth line through the unstable result is the equivalent result obtained with a new time stepping scheme, to be covered later. Figure 2.1.5 is a plot of the light cones at the first few time steps, for elements 19 and 20. It is clear that the shear wave front from element 19 chops element 21 at the second time step (shown as a dashed line). Figure 2.1.6 shows the same diagram, but for $Q1 = 0.67$, and the wave front just misses element 21 in this case. This run turns out to be stable.

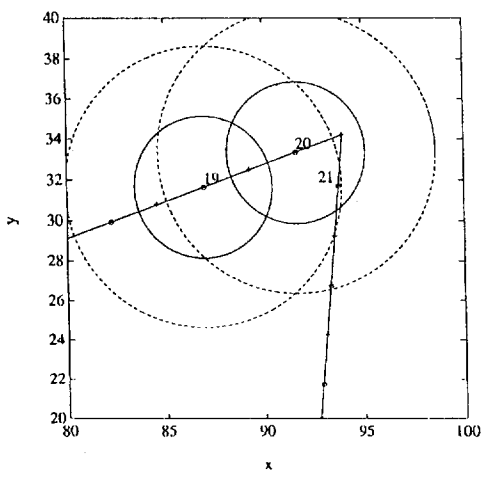

Figure 2.1.5: Light cones for Hook problem (Q2 = 0.7)

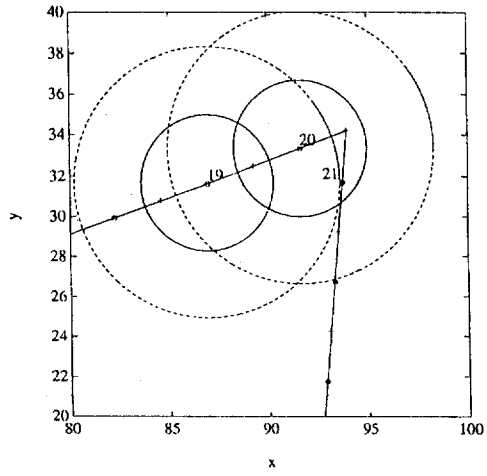

Figure 2.1.6: Light cones for Hook problem (Q2 = 0.67)

Stability analysis

The standard time stepping algorithm for the indirect methods is given by

$$\underline{\underline{C}}_0 \underline{F}_m + \sum_{k=1}^{m-1} \underline{\underline{C}}_{m-k} \underline{F}_k = \underline{b}_m \tag{2.1.1}$$

where $\underline{F}$ = vector of unknown boundary tractions and/or displacements, $\underline{\underline{C}}$ = influence coefficient matrix, $\underline{b}$ = known boundary displacement and/or traction vector, and m = current time step number. Equation 2.1.1 is a matrix convolution sum whose stability can be investigated using the z-transform and complex variable analysis. Taking the z-transform of equation 2.1.1 gives

$$\underline{b}(z) = \underline{\underline{C}}(z)\underline{F}(z) \tag{2.1.2}$$

where the z-transforms of the vector and matrix sequences $\{\underline{b}_m\}$, $\{\underline{F}_k\}$, and $\{\underline{\underline{C}}_{m-k}\}$ are defined in terms of the z-transforms of their components. For example,

$$\underline{\underline{C}}(z) = \left[c_{ij}(z)\right] = \left[\sum_{k=0}^{\infty} c_{ij,k} z^{-k}\right] \tag{2.1.3}$$

In a typical boundary element problem, $\{\underline{b}_m\}$ is specified, and $\{\underline{F}_k\}$ can be expressed as

$$\underline{F}(z) = \underline{\underline{C}}^{-1}(z)\underline{b}(z) \tag{2.1.4}$$

The sequence $\{\underline{F}_k\}$ can now be represented using the inversion formula and the adjoint formula for the inverse of a matrix as

$$\underline{F}_k = \frac{1}{2\pi i}\int_C \left\{\frac{adj\left(\underline{\underline{C}}(z)\right)}{\det\left(\underline{\underline{C}}(z)\right)}\underline{b}(z)\right\} z^{k-1} dz \tag{2.1.5}$$

where C is a contour that encloses all the poles of the expression enclosed in parentheses in equation 2.1.5. The poles that are due to the numerical scheme are determined by the zeros of

$$\det\left(\underline{\underline{C}}(z)\right) = 0 \tag{2.1.6}$$

The time-stepping scheme is numerically stable if all the zeros of equation 2.1.6 lie within the unit disc. It is necessary to locate the zeros of equation 2.1.6 in order to be able to determine if a given discretization is stable. However, each of the elements of $\underline{\underline{C}}(z)$ is an infinite series, so that potentially equation 2.1.6 has an infinite number of roots.

If the boundary elements are located within a finite region, the coefficient matrices $\{\underline{\underline{C}}_k\}$ decay as $k \to \infty$. The infinite series $c_{ij}(z)$ can be approximated by polynomials of degree at most *M*, which is sufficiently large for the dominant element to element influences to be included. Provided the truncated matrices are sufficiently small the roots that are discarded will be close to zero and will not affect the stability analysis. For an *N* degree of freedom boundary element model, the $\underline{\underline{C}}_k$ are each *N* by *N* matrices so that $\det\left(\underline{\underline{C}}(z)\right)$ is approximated by a polynomial of degree *MN*, which is denoted by

$$P_{MN}(z) = \det\left(\underline{\underline{C}}_M(z)\right) \approx \det\left(\underline{\underline{C}}(z)\right) \tag{2.1.7}$$

For large boundary element models (e.g. $N = 100$) with truncations involving even a modest number of time steps (e.g. $M = 50$), it is required to locate the roots of a 5000 degree polynomial, which is impracticable.

However, by means of the transformation $\omega = 1/z$ the unstable roots $|z| > 1$ can be mapped inside the unit disc. Therefore, we define define the complementary stability polynomial

$$Q_{MN}(z) = z^{MN} P_{MN}(1/z) \tag{2.1.8}$$

which has roots z_k inside the unit disc that correspond to the unstable roots of $P_{MN}(z)$ that fall outside the unit disc. Since $Q_{MN}(z)$ is an analytic function in the finite complex plane, the Argument principle implies that the number of roots of $Q_{MN}(z)$ contained within a closed curve C is given by $\Delta \arg(Q_{MN}(z))\big|_{z \in C} / (2\pi)$ which is an integer representing the number of times the point $\omega = Q_{MN}(z)$ winds around the origin as z traverses the curve C once in a positive direction. In particular, if the curve is a circle C_r of radius $r = 1$ then the number of roots of $Q_{MN}(z)$ within the circle is given by $\left[\arg(Q_{MN}(e^{2\pi i})) - \arg(Q_{MN}(e^{0i}))\right]/(2\pi)$, which is the number of unstable zeros for the discretization. The application of the Argument principle thus enables the stability of a particular discretization to be determined by focusing on the number of unstable roots rather than having to find all the roots.

Figure 2.1.7 shows stability information for one of the unstable two-element antiplane strain constant/linear TWO4D runs. The first plot shows the image curve $Q(z)$ as the point z traverses the unit circle C_1; the second plot shows the cumulative argument

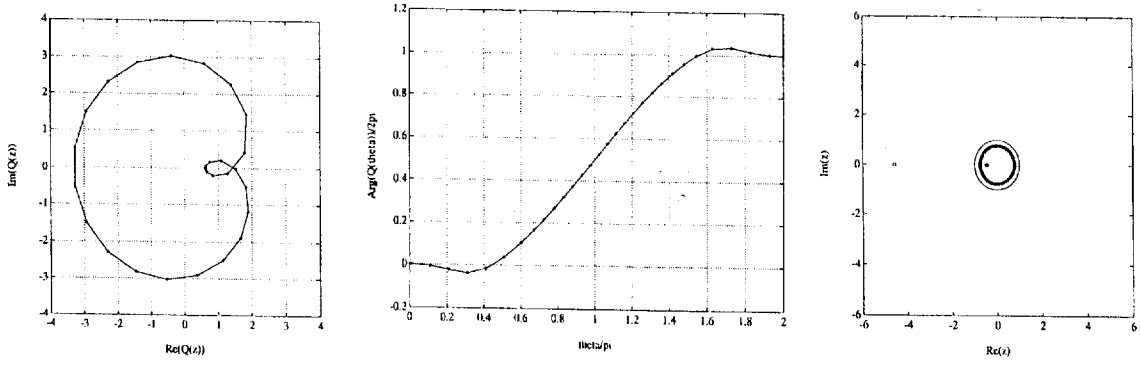

(a): Stability polynomial Q(z) as z traverses the unit disk

(b): Cumulative argument for two element problem

(c): Roots of P(z) for two element problem

Figure 2.1.7 Stability for unstable two element problem

$\arg\left(Q\left(z=e^{i\theta}\right)\right)$, $0 \le \theta \le 2\pi$, and the third plot shows the actual distribution of roots of $P(z)$ for the problem. The cumulative plot (b) predicts one unstable root.

Figure 2.1.8 shows the spatial plots (see the solid lines), observed at times $t = \Delta t$, $t = 2\Delta t$, $t = 3\Delta t$ and $t = 4\Delta t$ along the element center-line, of the wave fronts emanating from a single displacement discontinuity element. The displacement discontinuity element has been excited by triangular hat functions that act over two time intervals. In the first snap-shot at time $t = \Delta t$ the response to the triangular excitation of the displacement discontinuity element is a square-wave stress pulse $H(t-\Delta t) - H(t)$ that does not decay with distance. In the second snap-shot observed at time $t = 2\Delta t$ the response is no longer a square-wave stress pulse but a perturbation of the pulse $-H(t) + 2H(t-\Delta t) - H(t-2\Delta t)$. The perturbation of this pulse results from the diffraction pulses that arrive at y_d from the edges of the element. To the left of y_d the pulse $-H(t) + 2H(t-\Delta t) - H(t-2\Delta t)$ is subjected to interference while to the right of y_d the pulse is undisturbed. In the third snap-shot observed at time

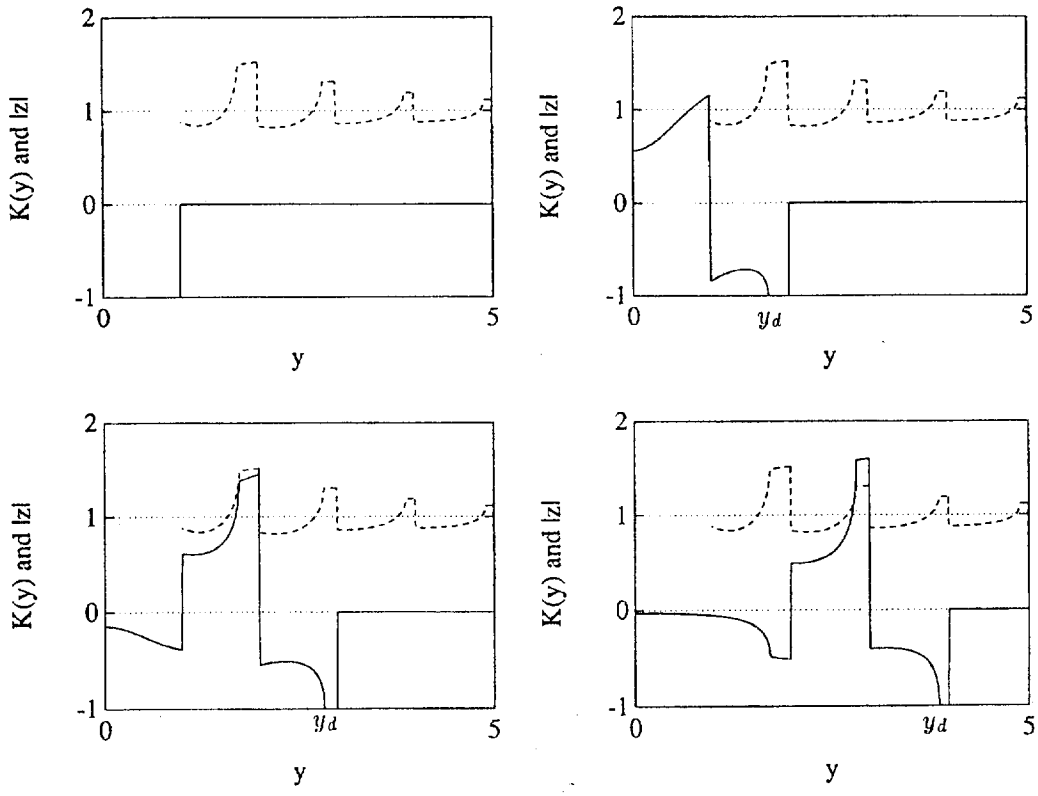

Figure 2.1.8: Stress Influences σ_{yy} along y axis for single element located at y = 0

$t = 3\Delta t$ a similar diffraction-interference pattern is observed. In this case the response is a perturbation of the pulse $-H(t-\Delta t)+2H(t-2\Delta t)\ -H(t-3\Delta t)$. It is observed that the jumps in each of these perturbed step pulses are the result of and are directly proportional to the changes in gradient in the original exciting triangular pulses.

An interesting phenomenon that can be observed after the first time step is that the stress pulse reaches a level which is larger than the unit magnitude of the self-effect (see time step $t = \Delta t$ at $y = 0$ in figure 2.1.8). Physically this implies that the displacement discontinuity element can achieve a larger stress influence on an element located at $y > 0$ than the stress influence that the element has on itself. This situation arises from the interference of the diffracted pulses that emanate from the singular points at the edges of the element. These large stress regions are referred to as persistent diffracted pulses.

From the above discussion on the persistent diffracted pulses, it can be expected that regions where the remote influences are larger than the self-effect, will be associated with poor stability. Thus if the second element is placed in one of these regions the resulting two-element problem would be expected to be unstable. In each plot of Figure 2.1.8 the magnitude of the largest root of the stability condition is represented as a function of the location y along the center-line of the displacement discontinuity element at which the second displacement discontinuity element is placed (see the dashed line). A close correlation can be observed between the regions in which the diffracted stresses are larger than the self effect and the regions within which the two element problem will be unstable because the stability root is larger than unity.

If the time step is altered (either increased or decreased) then it is possible that, due to the relative locations of the elements, no persistent diffracted pulse passes through the second element. In this case the algorithm will most likely be stable because the self-effect will dominate all the influences over the time history of the model. This is the source of the intermittent instability phenomenon demonstrated in Table 2.1.1 and is also observed in more complex displacement discontinuity models such as the Hook problem. Because the instability regions and the places where the persistent diffracted pulses occur are not identical, it is not possible to derive a simple criterion for instability based on the location of the persistent diffracted pulses. In addition, in problems with more complicated geometries the nett effect of the persistent diffracted pulses may be difficult to assess - for example when

there are two lines of elements that are not parallel. It is for this reason that the more global stability checking procedures were developed.

Improved time-stepping algorithms

Numerical instabilities can be delayed by switching from single to double precision, and by making use of averaging techniques from time step to time step (Manolis et al, 1986). Averaging methods are not desirable because they effectively damp the transient behaviour to some degree. Repetitive averaging is even less desirable because the solution is more heavily damped and can follow an incorrect path. Normalization of the influence coefficients could also be beneficial. However, none of these methods is very satisfactory, and it is desirable to develop alternative time stepping schemes in order to obtain a robust stable algorithm.

From the above discussion of stability, it can be seen that stability can be improved by increasing the size of the self-effect. A logical way of doing this is to adjust the size of the very first time step slightly by an amount ε (the ε scheme). Note that in the direct boundary element method, this would only increase the size of the displacement self-effects - the stress self-effects are constants. The ε scheme has the drawback, however, of introducing a small error into the algorithm, the result being a slight time shift in the solution. The larger the choice of ε, the larger the shift but the better the stability properties of the algorithm.

The design of a time stepping scheme that is consistent and has a larger self-effect is more complicated. The so-called half-step scheme satisfies these two requirements. This scheme is characterized by a two-stage system, involving half and full steps. The sequence of half and full steps is depicted in figure 2.1.9, and the algorithm, in the case of the indirect methods, is given by

$$\underline{\underline{C}}_0^h \underline{F}_{2m-1} + \sum_{k=0}^{m-1} \underline{\underline{C}}_{2m-1-2k}^h \underline{F}_{2k} = \underline{b}_{2m-1} \tag{2.1.9}$$

$$\underline{\underline{C}}_0^f \underline{F}_{2m} + \underline{\underline{C}}_1^f \underline{F}_{2m-1} + \sum_{k=0}^{m-1} \underline{\underline{C}}_{2m-2k}^f \underline{F}_{2k} = \underline{b}_{2m} \tag{2.1.10}$$

where h and f imply half and full steps, respectively. Figure 2.1.4 compares the results when the standard and half-step schemes are applied to the Hook problem.

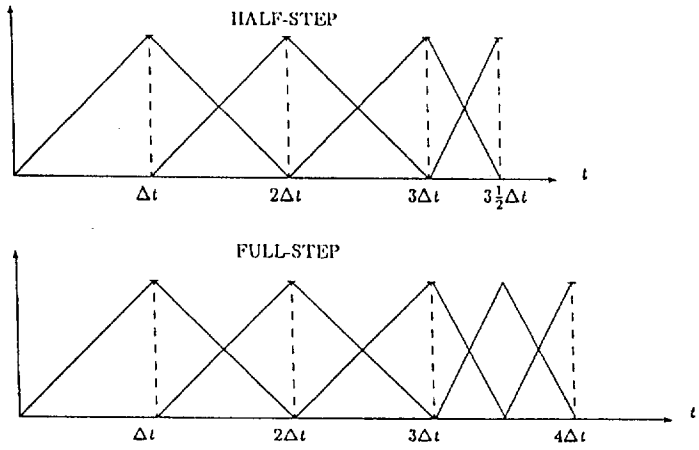

Figure 2.1.9: Half and full step sequence of time basis function for half-step scheme

In the half-step scheme, twice the number of time steps are needed to advance the solution by the same amount of time as in the standard scheme. However, larger time steps can be used because the system is more accurate. In addition, convolutions are effectively performed on time steps that are twice as large as in the case of the half-step scheme, which compensates for the fact that twice the number of time steps need to be advanced. This is demonstrated in Table 2.1.2 (compare the run times of the two 150 time step runs) for a 28 element plane strain constant/linear Hook problem, run on a Pentium 66 MHz machine.

SCHEME	NO. STEPS	RUN TIME	Q1	STABLE?
standard	75	2.05 min	1.2	no
	150	6.23 min	0.6	yes
	300	20.93 min	0.6	no
half-step	150	3.30 min	1.2	yes
	300	9.88 min	0.6	yes

Table 2.1.2: Run times for standard versus half-step schemes

Conclusions

The foregoing analysis has demonstrated the causes of numerical instabilities in time domain elastodynamic boundary element methods, with particular reference to the two-dimensional displacement discontinuity method. Numerical tools have been developed that can be used to determine whether a particular problem will go unstable or not and a new time-stepping algorithm with superior stability and accuracy properties to the standard scheme, has been proposed.

References

Andrews D.J. (1994) 'Dynamic growth of mixed-mode shear cracks'. *Bull. Seism Soc. Am.* Vol **84**, pp 1184-1198.

Banerjee P.K., Ahmad S. and Manolis G.D. (1986) 'Transient elastodynamic analysis of three-dimensional problems by boundary element method'. *Earthquake Eng. & Struct. Dyn.* Vol **14**, pp 933-949.

Bathe K-J. (1982) *Finite element procedures in engineering analysis.* Prentice-Hall, New Jersey.

Cole D.M., Kosloff D.D. and Minster J.B. (1978) 'A numerical boundary integral equation method for elastodynamics'. *Bull. Seism. Soc. Am.* Vol **68**, pp 1331-1357.

Dominguez J. (1993) *Boundary elements in dynamics.* Computational Mechanics Publications, Southampton.

Graff K.F. (1975) *Wave motion in elastic solids.* Clarendon Press, Oxford.

Koller M.G., Bonnet M. and Madariaga R. (1992) 'Modeling of dynamical crack propagation using time-domain boundary integrals'. *Wave Motion*, Vol **16**, pp 339-366.

Mack M.G. and Crouch S.L. (1991) 'The three-dimensional dynamic displacement discontinuity method'. *Boundary Elements XIII* (ed C.A. Brebbia & G.S. Gipson), pp 483-495, Computational Mechanics Publications, Southampton.

Manolis G.D., Ahmad S. and Banerjee P.K. (1986) 'Boundary element method, implementation for three-dimensional transient elastodynamics'. Chapter 2, *Developments in Boundary Element Methods-4*, ed P.K. Banerjee and J.O. Watson, pp 29-65, Elsevier, London and New York.

Siebrits E. and Crouch S.L. (1994) 'Two-dimensional elastodynamic displacement discontinuity method'. *Int. J. Num. Meth. Eng.* , Vol **37**, pp 3229-3250.

Siebrits E. and Pierce A.P. (1995) 'The stability properties of time domain elastodynamic boundary element methods'. *17th Boundary Element international conference,* Maddison, 17-19 July, 1995.

Smith G.D. (1985) *Numerical solution of partial differential equations: finite difference methods.* Clarendon Press, Oxford.

2.2 WAVE DEVELOPMENTS

WAVE has proved to be a useful tool for analysing elastodynamic problems in mining. This is firstly because it is exclusively orientated toward mining applications (and hence it is easy to apply stope and crack elements in the model), and secondly due to its efficiency it has both a fast turn-around time on simple problems (which is good for experimentation), and it allows orders of magnitude larger meshes than other available mesh-based dynamic codes, which is very important for large-scale three-dimensional models.

The memory and speed efficiency are due to the staggered grid scheme and the assumption of a regular orthogonal mesh. The major limitation in WAVE is the lack of generality due to the assumed orthogonal mesh. The staggered grid also makes the implementation of some features more complex. It would be highly desirable in the long term to have a mining-oriented code with the above advantages in terms of a similar order of efficiency in speed and in the size of problems it can address, while being more general with respect to the mining geometries which can be represented (e.g. angled faults), in the representation of varyingly oriented discrete fractures for wave propagation in the fracture zone, and in more varied materials.

One of the most attractive features of WAVE is its efficiency, and hence very large model sizes are possible, and these can be analysed with acceptable run-times. Table 2.2.1 lists

	2D MODELS			3D MODELS		
Memory	N^*	N_1^{**}	t^{***}	N^*	N_1^{**}	t^{***}
1 Mb	10,333	100	7 sec	6,200	17	2 sec
4 Mb	140,333	373	7 min	84,200	42	1 min
8 Mb	313,666	559	22 min	188,200	56	4 min
16 Mb	660,333	811	1.1 hrs	396,200	72	9 min
64 Mb	2.7 mil	1654	10 hrs	1.6 mil	117	1 hrs
128 Mb	5.5 mil	2347	26 hrs	3.3 mil	148	3 hrs
256 Mb	11 mil	3330	76 hrs	6.6 mil	187	7 hrs

* N = Total Elements
** N_1 = Elements in one dimension
*** t = Run-time on a 120 MHz Pentium PC

Table 2.2.1: Maximum 2D and 3D model sizes in WAVE, based on available memory, and the projected run-times on a 120MHz Pentium PC

some example grid sizes, projected run-times and memory requirements for a simple purely dynamic model. Run-times are based on a 120MHz Pentium PC.

The original WAVE concepts have been extended in a number of areas, mostly relating to stope or crack element behaviour. The current capabilities are:

- two- and three- dimensional models
- narrow stopes, either open or with linear stiffness representing seams or backfill
- faults with a Mohr-Coulomb slip law, slip-weakening, inhomogeneities
- opening-closure behaviour in cracks (important for wave propagation around fractures)
- absorbing boundaries to reduce reflections
- combined static-dynamic models (applied stress boundaries)
- stope layouts for three-dimensional models
- limited stope intersections (in two-dimensions only) - also allows cavity models
- higher order differencing for improved efficiency/ accuracy
- various graphical representations

Some developments represent specific objectives. In general however, their purpose is to enhance the scope of modelling, and hence to facilitate objectives such as objective 1.3 which are oriented toward applications. Important developments are discussed in more detail.

2.2.1 Overview of WAVE's basic formulation and grid scheme

WAVE uses a leap-frog time-stepping method where new stresses are calculated from velocities, and the new velocities are calculated from stresses. The stresses and velocities are solved for at different positions distributed in a staggered mesh - figure 2.2.1.1 shows these positions. It is important to note that some behaviour can be difficult to implement on a staggered mesh (for example, complications due to shear and normal stresses not being known at the same position in space). Appendix I summarizes how the basic mesh equations are developed, and may need to be referred to in understanding the details of subsequent issues - full detail can be found in Cundall (1992).

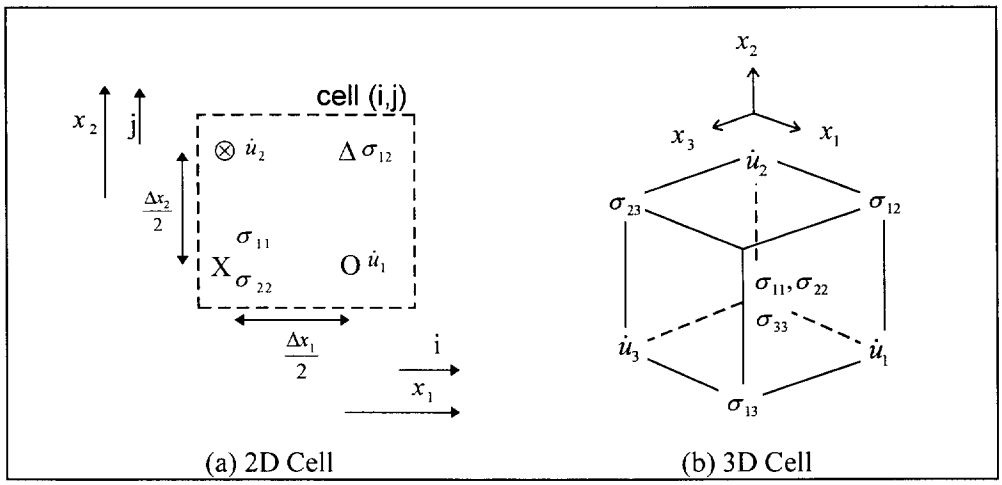

Figure 2.2.1.1: Unit Cell in the WAVE Mesh

The efficiency of the method is partially due to the staggered mesh which requires fewer grid-points and less memory for the same order of accuracy as a grid whose variables are co-incident. The assumption of a regular orthogonal grid also allows it to be memory and run-time efficient, since calculations are independent of position, and a small number of constants can be calculated and used throughout the grid.

REFERENCES

Cundall P.A. (1992) 'Theoretical basis of the program WAVE'. *Unpublished internal report, COMRO-CSIR Mining Technology*, pp 1-12.

2.2.2 Stopes/ Discontinuities

The "*stope*" element in WAVE is the generic name for all discontinuities - representing open stopes, seams, faults and cracks. A discontinuity is implemented in the mesh, as two infinitesimally thin planes on which certain grid variables are controlled, and others allowed to be dual-valued. The approach taken in deriving the equations is to write the standard mesh equation for each of the surfaces using fictitious grid-points which are not in the mesh. Stress conditions on the surface, provide the third equation allowing these fictitious values to be eliminated. The approach is illustrated for a 2D horizontal crack in Appendix I, as an aid in understanding subsequent details. Again, full detail can be found in Cundall (1992).

Faults

This work is important to objectives 1.2 and 1.3. Due to the positioning of the discontinuity in the mesh, it can be seen in the derivation in Appendix I that grid shear stresses do not fall directly on the surfaces, but an equation for the shear stress at the surface is used to rewrite the velocity calculations on the surface. With faults the surface shear stresses at these velocity points are calculated and stored and the two-step approach becomes a three-step approach: calculate new stresses, limit the shear stress according to the slip law, and then calculate the new velocities. The slip law used applies the Mohr-Coulomb limit $|\tau_{\max}| \leq c + \tan(\phi)|\sigma_n|$, where c is cohesion, ϕ is the friction angle and σ_n is the normal stress. When σ_n is tensile, the limit used is $|\tau_{\max}| \leq c$. If necessary the shear stress is reduced, and $\Delta\tau/k_s$ then indicates the increment in slip displacement where k_s is the shear stiffness and $\Delta\tau$ is the reduction in shear stress.

Due to the staggered grid scheme, three-dimensional faults have two velocity components located at different positions on the surface, such that the calculated surface shear stress components are separated in space. Figure 2.2.2.1 shows the grid positions for a surface in the x_1-x_2 plane. In this case the surface shear stress component σ_{13}^{sf} can be calculated at the position of $\dot{u}_1$ and σ_{23}^{sf} at the position of $\dot{u}_2$. The slip law must however be applied to total shear stress. To do this we need to interpolate a total shear stress, apply the slip law, and redistribute slip (stress drop) to the individual components.

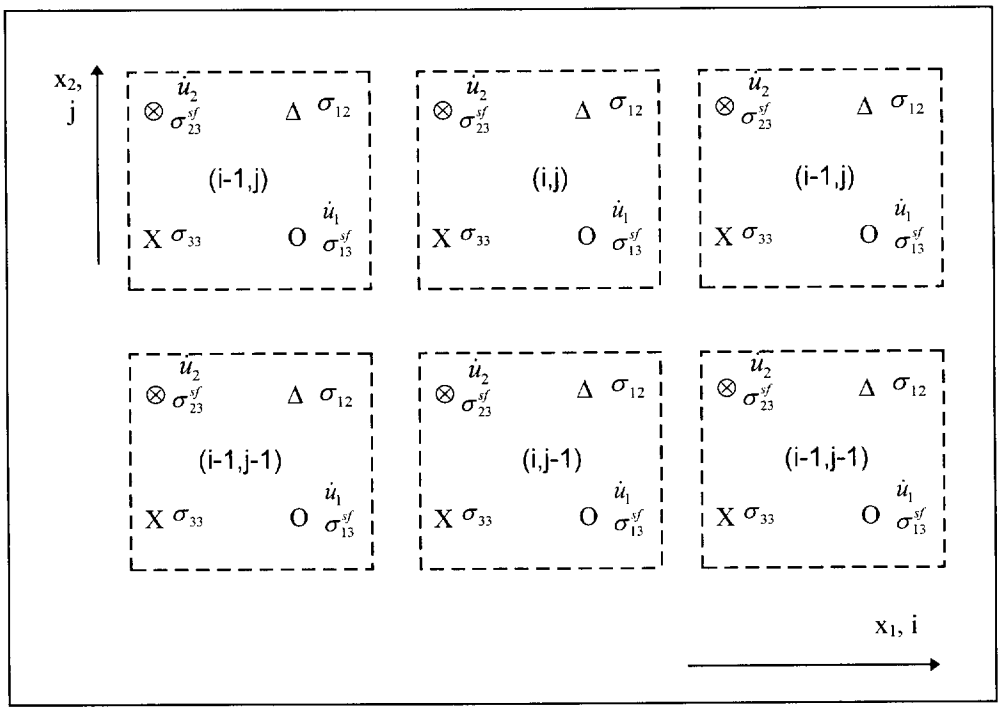

Figure 2.2.2.1 Grid values on the surface of a fault in the x_1-x_2 plane, highlighting velocities, surface stress and normal stress positions

The approach used is to calculate all the surface values of σ_{13}^{sf} and σ_{23}^{sf} at the $\dot{u}_1$ and $\dot{u}_2$ positions respectively, and then to interpolate throughout the grid storing the total shear stresses at both positions. The slip condition is applied at both positions - the limiting shear stress being calculated by interpolating the normal stress, which is located at a different position.

The method has two phases as follows:

(a) Firstly, calculate total surface shear stresses at $\dot{u}_1$ and $\dot{u}_2$ throughout the surface:

Interpolate for σ_{23}^{sf} at position $\dot{u}_1$ and hence calculate the total shear stress τ^{sf} at $\dot{u}_1$:

$$\sigma_{23}^{sf}\Big|_{\dot{u}_1}^{(i,j)} = \tfrac{1}{4}\left(\sigma_{23}^{sf(i,j)} + \sigma_{23}^{sf(i+1,j)} + \sigma_{23}^{sf(i,j-1)} + \sigma_{23}^{sf(i+1,j-1)}\right) \qquad (2.2.2.1)$$

$$\tau^{sf}\Big|_{\dot{u}_1} = \sqrt{\sigma_{13}^{sf\ 2} + \sigma_{23}^{sf}\Big|_{\dot{u}_1}^{\ 2}} \qquad (2.2.2.2)$$

Similarly, interpolate for σ_{13}^{sf} at position $\dot{u}_2$ and calculate the total shear stress at $\dot{u}_2$:

$$\sigma_{13}^{sf}\Big|_{\dot{u}_2}^{(i,j)} = \tfrac{1}{4}\left(\sigma_{13}^{sf(i,j)} + \sigma_{13}^{sf(i-1,j)} + \sigma_{13}^{sf(i,j+1)} + \sigma_{13}^{sf(i-1,j+1)}\right) \tag{2.2.2.3}$$

$$\tau^{sf}\Big|_{\dot{u}_2} = \sqrt{\sigma_{13}^{sf}\Big|_{\dot{u}_2}^{2} + \sigma_{23}^{sf\,2}} \tag{2.2.2.4}$$

(b) Now apply the slip law $|\tau_{\max}| \le c + \tan(\phi)|\sigma_n|$ throughout the surface.

For position $\dot{u}_1$, $$\sigma_n = \frac{1}{2}\left(\sigma_{33}^{(i+1,j)} + \sigma_{33}^{(i,j)}\right), \tag{2.2.2.5}$$

and if σ_n is tensile, $\sigma_n = 0$ is used in the slip law.

If $\tau^{sf}\Big|_{\dot{u}_1} > |\tau_{\max}|$ then σ_{13}^{sf} is reduced to $\sigma_{13}^{sf} = \sigma_{13}^{sf}\left[\dfrac{|\tau_{\max}|}{|\tau^{sf}|_{\dot{u}_1}|}\right]$ (2.2.2.6)

in which case $$\Delta u_{1(slip)} = \frac{\Delta\sigma_{13}^{sf}}{k_s} \tag{2.2.2.7}$$

indicates the increment in the u_1 component of slip displacement, where k_s is the shear stiffness and $\Delta\sigma_{13}^{sf}$ is the reduction in shear stress.

For position $\dot{u}_2$, $$\sigma_n = \frac{1}{2}\left(\sigma_{33}^{(i,j+1)} + \sigma_{33}^{(i,j)}\right) \tag{2.2.2.8}$$

If $\tau^{sf}\Big|_{\dot{u}_2} > |\tau_{\max}|$, then σ_{23}^{sf} is reduced to $\sigma_{23}^{sf} = \sigma_{23}^{sf}\left[\dfrac{|\tau_{\max}|}{|\tau^{sf}|_{\dot{u}_2}|}\right]$ (2.2.2.9)

in which case $$\Delta u_{2(slip)} = \frac{\Delta\sigma_{23}^{sf}}{k_s} \tag{2.2.2.10}$$

This approach has a slight memory penalty, since the interpolated values thoughout the fault need to be stored temporarily. More importantly, the interpolation will complicate future attempts to adapt the method for parallel computation, since stress calculations are directly dependent on stresses in other cells, whereas in general they are only dependent on velocity

components in other cells. Thus interpolation calculations must be completed before contributing components are changed. For this reason an alternative approach which interpolates the total surface shear stress at the normal stress position was not used. While this would simplify the application of the slip law in that it is applied at a single point, a second set of interpolations would be needed to re-distribute the slip back to the separate components, which is undesirable.

A slip-weakening rule is applied to the shear bond. The strength of the bond at each element is reduced linearly with slip, from the initial value of cohesion to a residual value (figure 2.2.2.2), where the initial cohesion (C_0), residual cohesion (C_{res}) and the slip-weakening displacement (swd) are input parameters. The slip-weakening displacement is the value of slip at which the residual cohesion is reached. The slip referred to here is the accumulated total of all slip increments, regardless of direction - or the total absolute slip (T_{aslip}). In two dimensions $T_{aslip} = \sum_{1}^{N} \left| u_{1(slip)} \right|$ and in three dimensions $T_{aslip} = \sum_{1}^{N} \sqrt{u_{1(slip)}^{\ 2} + u_{2(slip)}^{\ 2}}$, representing a summation over all time steps. The equation for the shear bond as a function of total absolute slip is

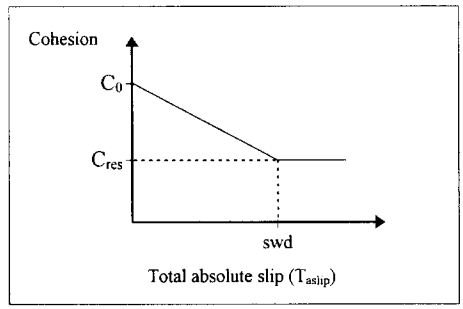

Figure 2.2.2.2 Slip-weakening Law

$$C = C_0 + (C_{res} - C_0)\frac{T_{aslip}}{swd} \qquad (\text{for } T_{aslip} \le swd)$$

$$\text{or } C = C_{res} \qquad (\text{for } T_{aslip} > swd). \qquad (2.2.2.11)$$

In general fault parameters are applied uniformly throughout the fault for better efficiency. An extended "stope" type is provided whereby any of a number of parameters (amongst them, friction, cohesion, normal and shear stiffnesses and stoping width, as well as switches enabling or disabling slip or crack-opening behaviour) may vary element by element in the "stope". This allows for inhomgeneities to be specified on a fault.

Contact logic - crack opening and closing behaviour

Contact logic in 'stopes' deals with the transition between an open and closed crack, and is important behaviour in considering wave propagation in fractured rock (objective 1.5). For example in section 2.4, the photo-elastic experiments and model comparisons show significant differences when a parting plane is allowed to open compared to when it is perfectly bonded. The contact logic also allows stope closure to be modelled, which is important in setting starting conditions for dynamic analyses, where closure will affect both the initial stress distribution and hence the source, and also the wave propagation in the vicinity of the stope.

A contact status is maintained for each element in the "stope". Parameters for stoping width and tensile strength are used to specify the conditions at which transitions from open to closed and closed to open take place. The stoping width is defined as the assumed thickness of a crack and limits the amount of interpenetration of the surfaces, while the tensile strength is the tensile stress required to open a closed crack. Switches can disable the contact logic - if set open, a crack always behaves as if open allowing infinite interpenetration, while if set closed it effectively has an infinite tensile strength.

The approach used is to calculate increments in stope variables based on both an open and a closed crack, and then to check for a transition. If none occurred during the time-step then the appropriate open or closed increment is used. Otherwise the point in time at which transition occurred is estimated, and the increments in stope variables are based on combinations of the open and closed increments for this step.

The calculations for open and closed stopes differ fundamentally in just four quantities: normal stress, normal displacement, and two components of surface shear stress (assuming three dimensions). For a stope in the x_1-x_3 plane (horizontal) these are σ_{22}, u_2^{rel}, σ_{12}^{sf} and σ_{23}^{sf}, where "*sf*" indicates a surface stress since these stresses are not at their usual locations in the grid. Here u_2^{rel} is the relative normal displacement or convergence and is not known directly, because $\dot{u}_2$ velocities are not located on the stope surface. σ_{11} and σ_{33} are dependent on $\Delta\sigma_{22}$ and σ_{13}, u_1^{rel} and u_3^{rel} are only dependent on velocities whose surface values are known. Increments in the four quantities must be calculated for both the open and

closed conditions, when one of the following rules is applied according to the current state of the contact.

(a) Stope initially open

If $$\left(u_2^{rel} + \Delta u_2^{rel\ op}\right) > st_{wid}, \tag{2.2.2.12}$$

where st_{wid} is the stoping width and $\Delta u_2^{rel\ op}$ is the convergence calculation for an open stope, then the stope has closed during this time-step. The fraction of the time-step taken to close is

$$t_{rat} = \frac{st_{wid} - u_2^{rel}}{\Delta u_2^{rel\ op}}. \tag{2.2.2.13}$$

The increments for u_2^{rel} and σ_{22} are

$$\Delta u_2^{rel} = t_{rat} * \Delta u_2^{rel\ op} + (1 - t_{rat}) * \Delta u_2^{rel\ cl} \tag{2.2.2.14}$$

$$\Delta\sigma_{22} = t_{rat} * \Delta\sigma_{22}^{op} + (1 - t_{rat}) * \Delta\sigma_{22}^{cl} \tag{2.2.2.15}$$

and in this case the same ratios are applied to σ_{12}^{sf} and σ_{23}^{sf}.

(b) Stope initially closed

If $$\left(\sigma_{22} + \Delta\sigma_{22}^{cl}\right) > T_{str}, \tag{2.2.2.16}$$

where T_{str} is the tensile strength, and $\Delta\sigma_{22}^{cl}$ is the normal stress increment for a closed stope, then the stope has opened during this time-step. The fraction of the time-step taken to open is

$$t_{rat} = \frac{T_{str} - \sigma_{22}}{\Delta\sigma_{22}^{cl}} \tag{2.2.2.17}$$

The increments for u_2^{rel} and σ_{22} are now

$$\Delta u_2^{rel} = t_{rat} * \Delta u_2^{rel\ cl} + (1 - t_{rat}) * \Delta u_2^{rel\ op} \tag{2.2.2.18}$$

$$\Delta\sigma_{22} = -\sigma_{22} \tag{2.2.2.19}$$

σ_{12}^{sf} and σ_{23}^{sf} are forced to zero.

If there is no transition in the open/closed state, then the appropriate values for the increments based on the pre-existing state are used.

It is important to note that the possiblity of transition is only determined during the stress calculation cycle. If a transition would have occurred before the velocity calculation (e.g. a stope closes), it will not manifest itself in the velocity calculations, and the velocities would (in this case) be inappropriately high (this applies only to the $\dot{u}_1$ and $\dot{u}_3$ velocities, as the $\dot{u}_2$ velocity is not calculated on the stope surface). It is unclear whether the subsequent stress calculations will correct this anomaly. Currently though, this is assumed to cause negligible error.

3D stope layouts

Stope layouts were implemented for three-dimensional models. This augments WAVE's application to more general mining problems. It has opened up the possibility of doing three-dimensional back-analyses of real events, and also comparisons on the differences in dynamic behaviour of different layouts, and is important to objective 1.3.

The approach used is to map a mine layout onto an existing rectangular stope, with solid conditions (sealed surfaces) enforced at appropriate points. A first approach used finite stiffnesses between the surfaces to approximate the solid areas. However, it was found to be necessary to implement true solid conditions, and in particular the edge conditions between the solid and open areas were critical.

For solid behaviour, all quantities on the stope surfaces must be continuous (single-valued). Solid conditions are simply obtained by performing the equivalent of grid calculations, and in storing these values both in the grid positions and for each surface of the stope (for use in calculations by adjacent elements in the stope). Edge conditions are required when there is a transition from an open to a solid area of the stope, where the calculations at the solid position involve terms from adjacent cells which are dual-valued. These edge conditions are a generalization of those needed in the three-dimensional rectangular stopes, where the dual-values are averaged to give a single quantity for equations requiring a single quantity.

An example using the layout logic is shown in figure 2.2.2.3, where wave patterns in the form of closure velocities due to a fault source ahead of the stope, are shown for a lead-lag stope, indicating how the multiple reflections lead to complicated wave patterns and pockets of high velocity.

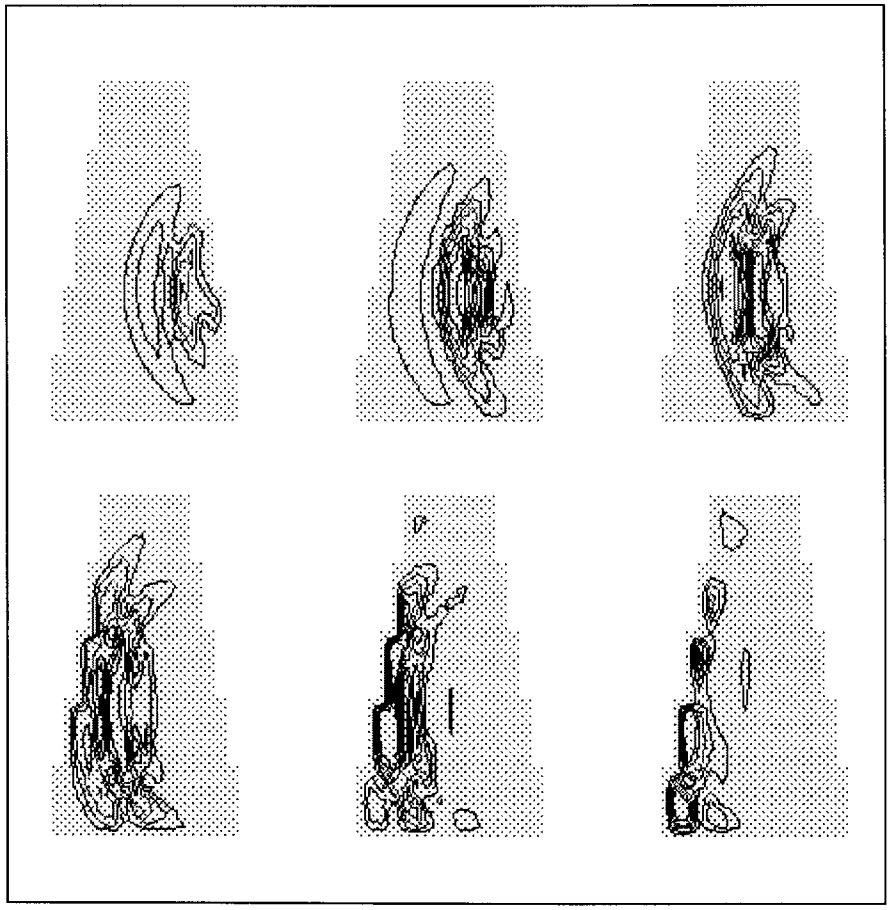

Figure 2.2.2.3: Convergence velocities in a three-dimensional stope, due to a shear event

Intersecting stopes, and cavities

An important generalization is to allow "stope" intersections. A limited form of this intersection logic was implemented - for two-dimensions, and for the assumption of open cracks at the point of intersection. This allows fractures to intersect stopes in two dimensional models, while the linking of stope elements allows two dimensional cavity problems to be modelled.

There are a number of possible types of intersection: a full intersection (where both 'stopes' extend on both sides of the intersection), partial intersections from the left, right, top or bottom (where a "stope" terminates at the intersection), corner intersections and co-linear intersections.

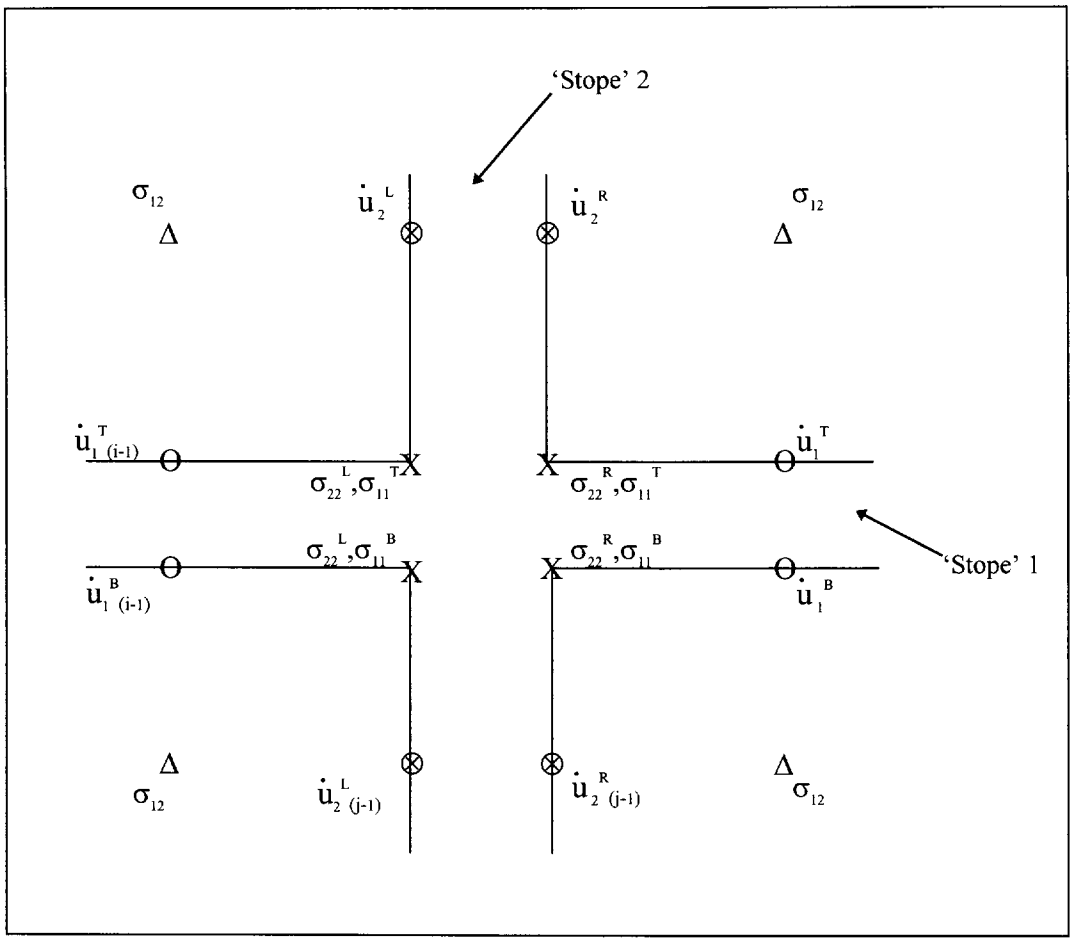

Figure 2.2.2.4: Intersection point for two intersecting 'stopes'

The first requirement is to solve for the stresses at the intersection points. The case of a full intersection is considered in figure 2.2.2.4, which shows the point of intersection between two 'stopes'. The surfaces are shown as separated, although the four corner points are coincident in terms of their position in the WAVE mesh. In general at this point of intersection there are four different surfaces, and hence four positions at which σ_{11} and σ_{22} can be calculated giving two relations between stress and known and ficticious velocities per position. Assuming a linear normal stiffness gives a third relation per position. From continuity σ_{22} is continuous across "stope" 1, and σ_{11} is continuous across "stope" 2, and

hence there are only four unknown stresses (σ_{11}^{T}, σ_{11}^{B}, σ_{22}^{L} and σ_{22}^{R} as in figure 2.2.2.4, where T and B refer to the top and bottom surface of "stope" 1, and L and R refer to the left and right surface of "stope" 2). In the single "stope" case (in Appendix I), the normal stress is solved for from three relations between normal stress, known velocities and two ficticious velocities. The intersection case, is similar in that there are four sets of three equations - however these are coupled. This leads to a sparse system of twelve equations and twelve unknowns (due to eight ficticious velocities), from which the unknown stresses can be solved. The nearest σ_{12} grid calculations are also complicated by the intersection. The structure of this calculation is unchanged, but the appropriate surface velocities must be used instead of grid velocities (figure 2.2.2.4).

The second requirement is to implement the actual intersection logic which maintains a list of intersection points, the type of intersection (full, partial etc.), and links to the 'stopes' which intersect. This logic overrides the stope stress calculations at the intersection points, and the nearest σ_{12} grid calculations. The appropriate forms of these stress calculations is dependent on the type of intersection.

The fully general case for the solution of the stope stresses has not been solved for. However if it is assumed that both "stopes" are open at the point of intersection, then the solution of the above equations is trivial ($\sigma_{11}^{T} = \sigma_{11}^{B} = \sigma_{22}^{L} = \sigma_{22}^{R} = 0$). This simplification is not made in co-linear intersections, where the general solution is less complex. The intersection logic is fully general so that if the above system of equations is solved for, these stress calculations can be readily implemented in the existing framework.

Intersecting open stope elements have been employed successfully in representing cavities. Figure 2.2.2.5 shows as an example a model of wave interaction with a 'T-shaped' tunnel, illustrated by a series of snapshots of particle velocity. Intersections of fractures with a stope can be modelled by allowing the first element of the fracture to be open (i.e. $\sigma_n = 0$ at the point of intersection). This method was employed in section 2.4.2, where the model accurately reproduces the experiment in spite of this assumption.

Extending these intersections to three dimensions is necessary before three dimensional cavities and intersecting fractures can be studied.

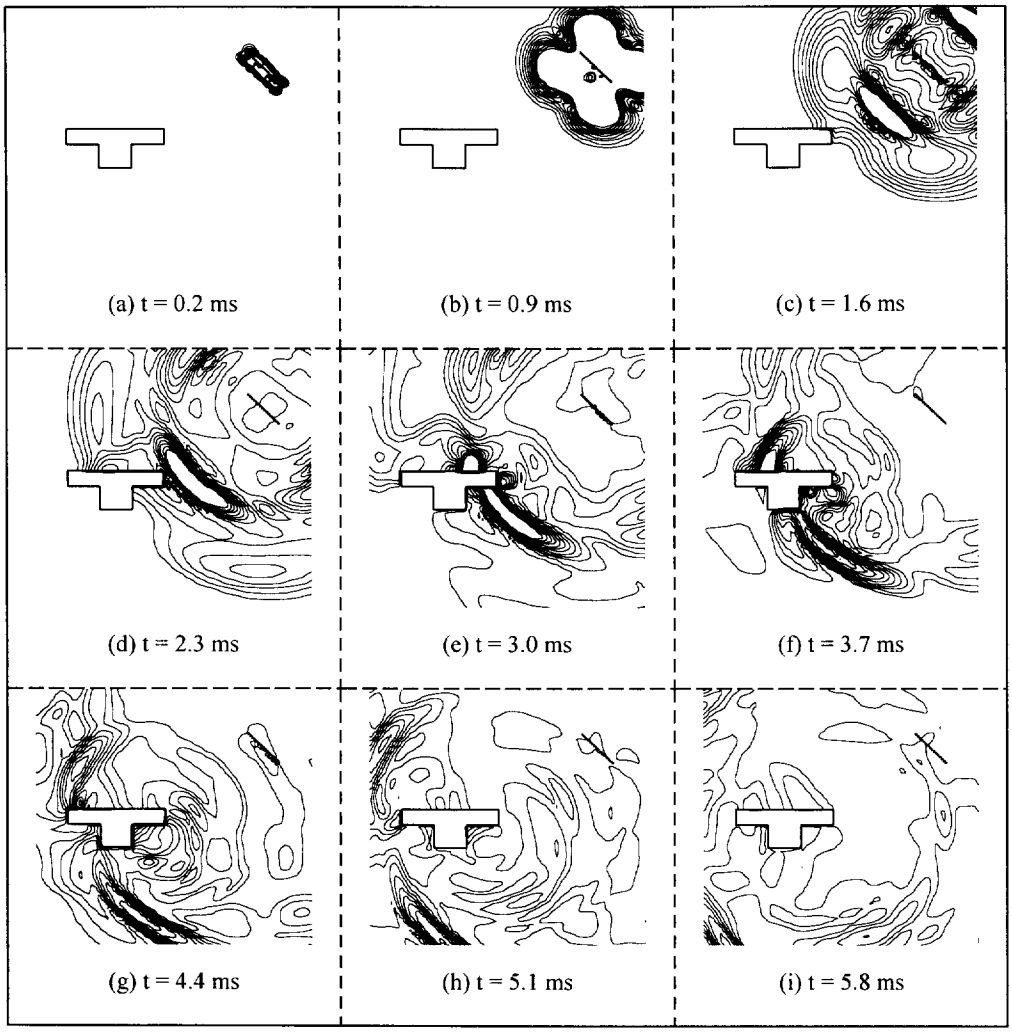

Figure 2.2.2.5: Example cavity problem, showing wave interaction with a 'T-shaped' tunnel

REFERENCES

Cundall P.A. (1992) 'Theoretical basis of the program WAVE'. *Unpublished internal report, COMRO-CSIR Mining Technology*, pp 1-12.

2.2.3 Boundaries

Two conditions are enforced at the boundaries - absorbing and applied stress conditions. The absorbing boundaries minimize reflections to approximate wave propagation in an infinite medium. The assumption used is accurate for plane waves striking the boundary with an angle of incidence of 90°. The applied stress boundaries implement an external steady-state stress field, allowing the solution of an in-situ stress state.

Combined absorbing and stress boundary conditions

The implementation of the absorbing boundary conditions is summarized in Appendix I, and detailed in Cundall (1992). To combine the absorbing boundaries with an applied stress, we note that the absorbing conditions of Appendix I must apply to the transient stress not the total stress, and that the total stress will include the stress applied at the boundary. The absorbing condition for normal motions then becomes

$$\sigma_n^{\ trans} = \sigma_n - \sigma_n^{\ bd} = C_p \rho \, \dot{u}_n \tag{1}$$

referring to the transient, total, and applied normal stresses, where $\dot{u}_n$ is the particle velocity in the direction of propagation, and C_p is the P-wave speed. Using this relation and following the approach of Appendix I but arranging terms differently, the equation for updating the normal stress at the lower boundary in two dimesions becomes

$$\sigma_{22}^{t} = \frac{1}{\left(1 + E_1 \frac{\Delta t}{\Delta x_2} \frac{1}{C_p \rho}\right)} \left[\left(1 - E_1 \frac{\Delta t}{\Delta x_2} \frac{1}{C_p \rho}\right) \sigma_{22}^{t-1} + E_1 \frac{\Delta t}{\Delta x_2} \left(2\dot{u}_2^{j} + \frac{2}{C_p \rho} \sigma_{22}^{bd}\right) + E_2 \frac{\Delta t}{\Delta x_1} \left(\dot{u}_1^{i} - \dot{u}_1^{i-1}\right) \right] \tag{2}$$

Absorbing conditions for shear motions are similarly based on the transient shear stress

$$\tau^{\ trans} = \tau - \tau^{\ bd} = C_s \rho \, \dot{u}_s \tag{3}$$

where τ and $\dot{u}_s$ are the shear stress and particle velocity perpendicular to the direction of propagation, and C_s is the S-wave speed. Using this condition and figure 2.2.3.1, we develop the equations for the velocity $\dot{u}_1$ which is also located on the lower boundary. The general equation for calculating new $\dot{u}_1$ velocities is

$$\dot{u}_1^{t+\frac{1}{2}} = \dot{u}_1^{t-\frac{1}{2}} + \frac{\Delta t}{\rho \, \Delta x_1} \Delta \sigma_{11}^{\ t} + \frac{\Delta t}{\rho \, \Delta x_2} \Delta \sigma_{12}^{\ t} \tag{4}$$

Applying this at the lower boundary, and using fictitious stresses to represent stresses falling outside the mesh, gives

$$\dot{u}_1^{t+½} = \dot{u}_1^{t-½} + \frac{\Delta t}{\rho\,\Delta x_1}\left(\sigma_{11}{}^{i} - \sigma_{11}{}^{i-1}\right) + \frac{\Delta t}{\rho\,\Delta x_2}\left(\sigma_{12}{}^{j} - \sigma_{12}{}^{j-1(f)}\right) \tag{5}$$

Condition (3) is applied at the position of $\dot{u}_1$ and at time t, by averaging σ_{12} in space and averaging $\dot{u}_1$ in time, giving

$$\sigma_{12}{}^{trans}\Big|_{\dot{u}_1} = \frac{1}{2}\left(\sigma_{12}{}^{j} + \sigma_{12}{}^{j-1(f)} - 2\sigma_{12}{}^{bd}\right) = C_s\rho\left(\dot{u}_1{}^{t+½} + \dot{u}_1{}^{t-½}\right) \tag{6}$$

Combining (5) and (6) to eliminate the fictitious stress $\sigma_{12}{}^{j-1(f)}$, gives

$$\dot{u}_1^{t+½} = \frac{1}{\left(1+\frac{\Delta t}{\Delta x_2}C_s\right)}\left[\left(1-\frac{\Delta t}{\Delta x_2}C_s\right)\dot{u}_1^{t-½} + \frac{\Delta t}{\rho\,\Delta x_1}\left(\sigma_{11}{}^{i} - \sigma_{11}{}^{i-1}\right) + \frac{\Delta t}{\rho\,\Delta x_2}2\left(\sigma_{12}{}^{j} - \sigma_{12}{}^{bd}\right)\right] \tag{7}$$

Similar equations can be derived for other boundaries, and for three dimensions.

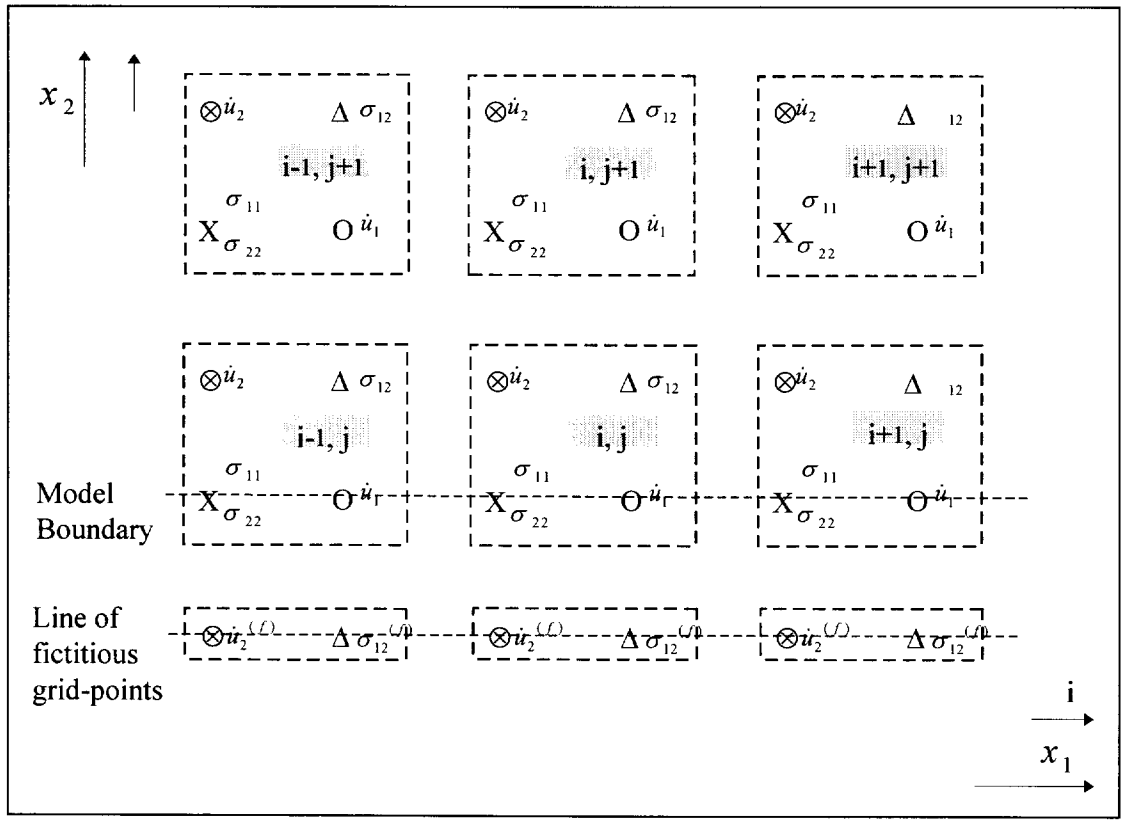

Figure 2.2.3.1: Lower grid boundary in 2D Mesh, showing line of fictitious grid-points

Corner and edge conditions

At the boundary corners in two-dimensions, and at the boundary corners and edges in three-dimensions, two or more boundary conditions are necessary. It was initially assumed that these positions could be ignored as they would contribute negligibly to reflections. It was eventually found that not calculating velocities along the edges for three dimensions, leads to serious errors. (The solution to simple hydro-static loading led to significant values of shear stress in the mesh - purely due to the velocity conditions at the edges).

Consider once again the $\dot{u}_1$ velocity at the bottom boundary. For three dimensions we have,

$$\dot{u}_1^{t+½} = \dot{u}_1^{t-½} + \frac{\Delta t}{\rho \Delta x_1}\left(\sigma_{11}{}^{i} - \sigma_{11}{}^{i-1}\right) + \frac{\Delta t}{\rho \Delta x_2}\left(\sigma_{12}{}^{j} - \sigma_{12}{}^{j-1(f)}\right) + \frac{\Delta t}{\rho \Delta x_3}\left(\sigma_{13}{}^{k} - \sigma_{12}{}^{k-1}\right) \qquad (8)$$

Taking the back edge of the lower boundary (k=1), we note that we now need a value of σ_{13} which falls outside the mesh, leading to a second fictitious stress in the equation.

$$\dot{u}_1^{t+½} = \dot{u}_1^{t-½} + \frac{\Delta t}{\rho \Delta x_1}\left(\sigma_{11}{}^{i} - \sigma_{11}{}^{i-1}\right) + \frac{\Delta t}{\rho \Delta x_2}\left(\sigma_{12}{}^{j} - \sigma_{12}{}^{j-1(f)}\right) + \frac{\Delta t}{\rho \Delta x_3}\left(\sigma_{13}{}^{k} - \sigma_{13}{}^{k-1(f)}\right) \qquad (9)$$

The condition (3) is now required to hold for both σ_{12} and σ_{13} at the $\dot{u}_1$ position. Equation (6) for σ_{12} was derived from this condition, and we can derive a similar equation for σ_{13}.

$$\sigma_{13}{}^{trans}\Big|_{\dot{u}_1} = \sigma_{13}{}^{k} + \sigma_{13}{}^{k-1(f)} - 2\sigma_{13}{}^{bd} = C_s \rho \left(\dot{u}_1{}^{t+½} + \dot{u}_1{}^{t-½}\right) \qquad (10)$$

Combining (9), (6) and (10) to eliminate the fictitious stresses $\sigma_{12}{}^{j-1(f)}$ and $\sigma_{13}{}^{k-1(f)}$, gives

$$\dot{u}_1^{t+½} = \frac{1}{\left(1 + \frac{\Delta x_1 + \Delta x_2}{\Delta x_1 \Delta x_2}\Delta t C_s\right)}\left[\left(1 + \frac{\Delta x_1 + \Delta x_2}{\Delta x_1 \Delta x_2}\Delta t C_s\right)\dot{u}_1^{t-½} + \frac{\Delta t}{\rho \Delta x_1}\left(\sigma_{11}{}^{i} - \sigma_{11}{}^{i-1}\right) + \frac{\Delta t}{\rho \Delta x_2} 2\left(\sigma_{12}{}^{j} - \sigma_{12}{}^{bd}\right) + \frac{\Delta t}{\rho \Delta x_3} 2\left(\sigma_{13}{}^{k} - \sigma_{13}{}^{bd}\right)\right] \qquad (11)$$

Similar equations can be derived for the other edges.

The solutions of stresses at the corners and edges are somewhat more complex, and expressions have not been implemented, since their omission appears to have no significant influence.

Experimental "far" boundaries

Using the applied stress boundaries to model the far-field stress field in a mining problem requires the boundaries to be very far for an accurate stress distribution to be obtained. In statics the mesh can be graded to have large elements near the boundaries. In dynamics it is undesirable to grade the mesh as these introduce reflections, so that the requirement of distant boundaries can lead to undesirably large mesh sizes, when dynamic problems involving in-situ stresses are investigated.

One solution is to approximate the effect of far field stresses at the boundaries. As an experiment, a boundary was implemented which assumes a hyperbolic fall-off between the boundary stresses and the far-field stress state. For the simplest test case of a single stope, this approach was encouraging. Figure 2.2.3.2 compares results for a two-dimensional single stope model for the cases of distant boundaries (70 x 70 elements), close boundaries (30 x 30 elements), and close boundaries with 'far' conditions applied. The results shown are for the vertical stress distribution along a line 70 metres above the stope (near the top boundary of the close model), and for stope convergence. The small model with close boundaries and 'far' conditions approximates that of the large model with distant boundaries - but with far fewer elements. It is emphasized that the above was experimental and is not necessarily the best approach. However, development of such a technique would be extremely important for three-dimensional analyses.

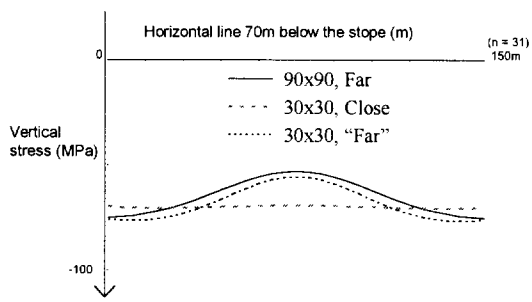

(a) Vertical stress along a line 70 metres above a 70 metre stope (near the boundary for the small models)

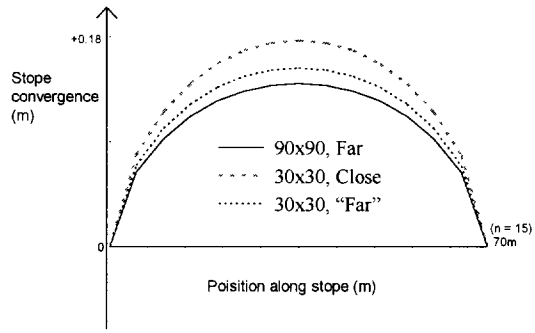

(b) Stope convergence for a 70 metre stope

Fig 2.2.3.2 : Comparisons of models with far boundaries, close boundaries and close boundaries with "far" conditions

REFERENCES

Cundall P.A. (1992) 'Theoretical basis of the program WAVE'. *Unpublished internal report, COMRO-CSIR Mining Technology*, pp 1-12.

2.2.4 Accuracy

Comparisons were made between dynamic codes WAVE, TWO4D and FLAC (Siebrits and Hildyard, 1993), which identify some of the strengths and weaknesses of the different methods. One of the problems highlighted in the finite difference codes (WAVE and FLAC) was in the propagation of high frequencies. Worst case examples were considered with sudden step-loading of a crack and the immediate de-stressing of a pre-stressed fault. The finite difference codes capture the gross behaviour, but this is swamped by significant "ringing". The cause of this ringing is numerical dispersion, where the modelled wave speed differs from the physical wave speed for high frequencies. As a result, it was important to characterize the accuracy of finite difference methods, particularly with respect to numerical dispersion (objective 1.7). Higher order differencing has been implemented in WAVE to reduce the effects of dispersion.

Dispersion

Dispersion is the variation of wave speed with frequency, and numerical dispersion indicates the departure of the modelled wave speed from the elastic wave speed, which is large for high frequencies. The effects of dispersion error become more manifest with time or distance of propagation. The causes of numerical dispersion in finite difference approximations to the wave equation, were analyzed in detail by Pierce (1995). This included a mathematical analysis of the accuracy, stability and dispersion of various differencing approximations, with specific reference to 2nd order central differencing and leap-frog time-marching as used in WAVE. Expressions are presented for the order of accuracy based on Taylor expansions, and the 2nd order scheme is shown to be a more accurate approximation to a dispersive wave equation. Expressions for the numerical group and phase velocities show that the 2nd order finite difference approximation is dispersive. In comparisons with analytic wave-forms, it is shown that where there is little high frequency content, the numerical solution is in fact very accurate. It is noted that in practical elastodynamic models, high frequency signals are common due to faults and joints and impulsive loading. Dispersive effects can be alleviated to some extent by using a sufficiently fine mesh or higher order difference schemes. Although spectral methods eliminate dispersion, they are computationally costly and are not suitable for non-linear problems and the modelling of discontinuities such as faults and

joints. The analysis of this dispersion is fairly mathematical, and it is therefore included in Appendix II.

Higher order accuracy

In order to improve dispersion error, difference schemes of 4th and higher order accuracy were added to WAVE (the general scheme uses 2nd order differencing). The purpose here can be seen as either to give greater accuracy or to give greater efficiency for the same accuracy, hence increasing the size and scope of problems that can be modelled.

The effects of dispersion error become more manifest with time or distance of propagation, but for a typical period of interest in geophysical applications it has been suggested that the maximum 'significant' frequency should be 10% of the maximum frequency in the grid, based on a 2nd order scheme (Aki and Richards, 1980) - although this is conservative for short time frames. For a given source this requires a sufficiently fine mesh, or alternatively the source frequencies must be controlled. In many problems of interest however, it is undersirable to control the source - e.g. fault slip, where high frequencies can be introduced. On the other hand a fine mesh has high memory and run-time costs. A number of papers in the literature have established the benefits of higher order difference schemes in both space and time, where numerical dispersion is improved but not eliminated (Dablain, 1986).

In WAVE, higher order spatial schemes have primarily been considered. The advantage here is that there is no increase in the memory usage over the second order scheme, although run-times are increased. In general the same accuracy as the second order scheme can be achieved with a reduction in both memory and run-time requirements. Higher order accuracy in time was experimented with, but this had the major disadvantage of increasing the memory requirements.

Consider a line in the WAVE mesh as shown in figure 2.2.4.1. For the calculation of σ_{11} at x_0, we need to evaluate the derivative $\frac{\partial \dot{u}_1}{\partial x}$ at x_0, and to approximate this we have known values of $\dot{u}_1$ at $x_0 \pm h$, $x_0 \pm 3h$, $x_0 \pm 5h$... This is true in general for each grid variable f in the WAVE mesh, where we are dealing with a function $f(x)$, with known values at $x_0 \pm h$, $x_0 \pm 3h$ etc, and $f'(x_0)$ is required (here x is either the x, y or z dimension and $h = \frac{\Delta x}{2}$).

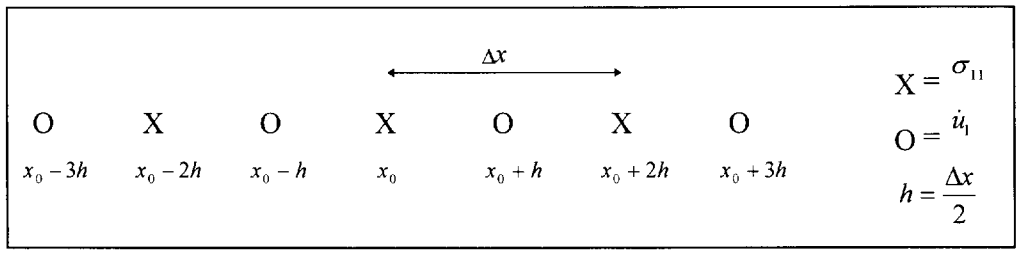

Figure 2.2.4.1: Line in the WAVE mesh showing alternating positions of σ_{11} and $\dot{u}_1$

Expanding the Taylor series for $f(x_0 + h)$ and $f(x_0 - h)$ gives

$$f(x_0 + h) = f(x_0) + f'(x_0)h + f''(x_0)\frac{h^2}{2!} + f'''(x_0)\frac{h^3}{3!} + f^{iv}(x_0)\frac{h^4}{4!} + \ldots \quad (2.2.4.1)$$

$$f(x_0 - h) = f(x_0) - f'(x_0)h + f''(x_0)\frac{h^2}{2!} - f'''(x_0)\frac{h^3}{3!} + f^{iv}(x_0)\frac{h^4}{4!} - \ldots \quad (2.2.4.2)$$

Subtracting (2.2.4.2) from (2.2.4.1) eliminates all even order terms,

$$f(x_0 + h) - f(x_0 - h) = 2\left[f'(x_0)h + f'''(x_0)\frac{h^3}{3!} + f^{v}(x_0)\frac{h^5}{5!} + \ldots \right] \quad (2.2.4.3)$$

giving

$$f'(x_0) = \frac{f(x_0 + h) - f(x_0 - h)}{2h} + O(h^2) \quad (2.2.4.4)$$

which is the second order diffference scheme.

Similarly, expanding the Taylor series for $f(x_0 + 3h)$ and $f(x_0 - 3h)$

$$f(x_0 + 3h) = f(x_0) + 3f'(x_0)h + 3^2 f''(x_0)\frac{h^2}{2!} + 3^3 f'''(x_0)\frac{h^3}{3!} + 3^4 f^{iv}(x_0)\frac{h^4}{4!} + \ldots \quad (2.2.4.5)$$

$$f(x_0 - 3h) = f(x_0) - 3f'(x_0)h + 3^2 f''(x_0)\frac{h^2}{2!} - 3^3 f'''(x_0)\frac{h^3}{3!} + 3^4 f^{iv}(x_0)\frac{h^4}{4!} - \ldots \quad (2.2.4.6)$$

$$f(x_0 + 3h) - f(x_0 - 3h) = 2\left[3f'(x_0)h + 3^3 f'''(x_0)\frac{h^3}{3!} + 3^5 f^{v}(x_0)\frac{h^5}{5!} + \ldots \right] \quad (2.2.4.7)$$

and eliminating the term in h^3 between equations 2.2.4.3 and 2.2.4.7, gives

$$f'(x_0)=\frac{-\frac{1}{24}f(x_0+3h)+\frac{27}{24}f(x_0+h)-\frac{27}{24}f(x_0-h)+\frac{1}{24}f(x_0-3h)}{2h}+O(h^4) \qquad (2.2.4.8)$$

which is the 4th order difference scheme. Continuing in the same manner, higher order schemes can be derived. The coefficients for 2nd up to 10th order accuracy developed for WAVE are listed in Table 2.2.4.1.

$f(x_0-9h)$	$f(x_0-7h)$	$f(x_0-5h)$	$f(x_0-3h)$	$f(x_0-h)$	$f(x_0+h)$	$f(x_0+3h)$	$f(x_0+5h)$	$f(x_0+7h)$	$f(x_0+9h)$
-	-	-	-	-1	1	-	-	-	-
-	-	-	$\frac{1}{24}$	$-\frac{27}{24}$	$\frac{27}{24}$	$-\frac{1}{24}$	-	-	-
-	-	$-\frac{9}{1920}$	$\frac{125}{1920}$	$-\frac{2250}{1920}$	$\frac{2250}{1920}$	$-\frac{125}{1920}$	$\frac{9}{1920}$	-	-
-	$\frac{75}{107520}$	$-\frac{1029}{107520}$	$\frac{8575}{107520}$	$-\frac{128625}{107520}$	$\frac{128625}{107520}$	$-\frac{8575}{107520}$	$\frac{1029}{107520}$	$-\frac{75}{107520}$	-
$-\frac{1225}{10321920}$	$\frac{18225}{10321920}$	$-\frac{142884}{10321920}$	$\frac{926100}{10321920}$	$-\frac{12502350}{10321920}$	$\frac{12502350}{10321920}$	$-\frac{926100}{10321920}$	$\frac{142884}{10321920}$	$-\frac{18225}{10321920}$	$\frac{1225}{10321920}$

Table 2.2.4.1: Coefficients for 2nd, 4th, 6th, 8th and 10th order differencing

The 4th order differencing was implemented in both two and three dimensions, while the 6th, 8th and 10th order differencing was limited to two dimensions. Higher order differencing is only applied to the mesh equations, and equations near stopes and boundaries are 2nd order. Development of full 4th order stope logic would be beneficial, but is relatively complex. As such only the accuracy of wave propagation through the solid is improved, while the accuracy of propagation on stope boundaries and the accuracy of aspects of the geometry are not affected. Switching down to 2nd order in the vicinity of stopes introduces an error, which limits the final steady-state accuracy of a model. This is most noticable in combined static-dynamic analyses, where if the residual velocities (steady-state error) are not much less than the values of interest in the transient/ dynamic model, then the higher order formulation cannot be used. Nevertheless, it will be shown that significant benefit is obtained by using the higher order formulation.

In Siebrits and Hildyard (1993), a series of tests were done comparing wave propagation from a two-dimensional pressurized and shearing crack for which known analytic solutions exist.

The case of step loading poses the worst possible conditions for dispersive solution methods such as finite differences and finite elements, due to the high proportion of high frequency content. The velocity at a point (at a distance of 3.5 times the source size) normal to a shear source with step loading is reproduced here to show the benefits of the higher order formulations. Figure 2.2.4.2 shows the results for a 10 element source for 2nd up to 10th order differencing, and as a control the result provided by TWO4D (which has been shown to have an accurate solution). The shape and amplitude of the response clearly improves with successively higher order formulations, and the ringing is reduced. The very high order schemes however, seem to produce larger boundary reflections due to the boundary being 2nd order, and for this reason the 4th order scheme has primarily been used in WAVE.

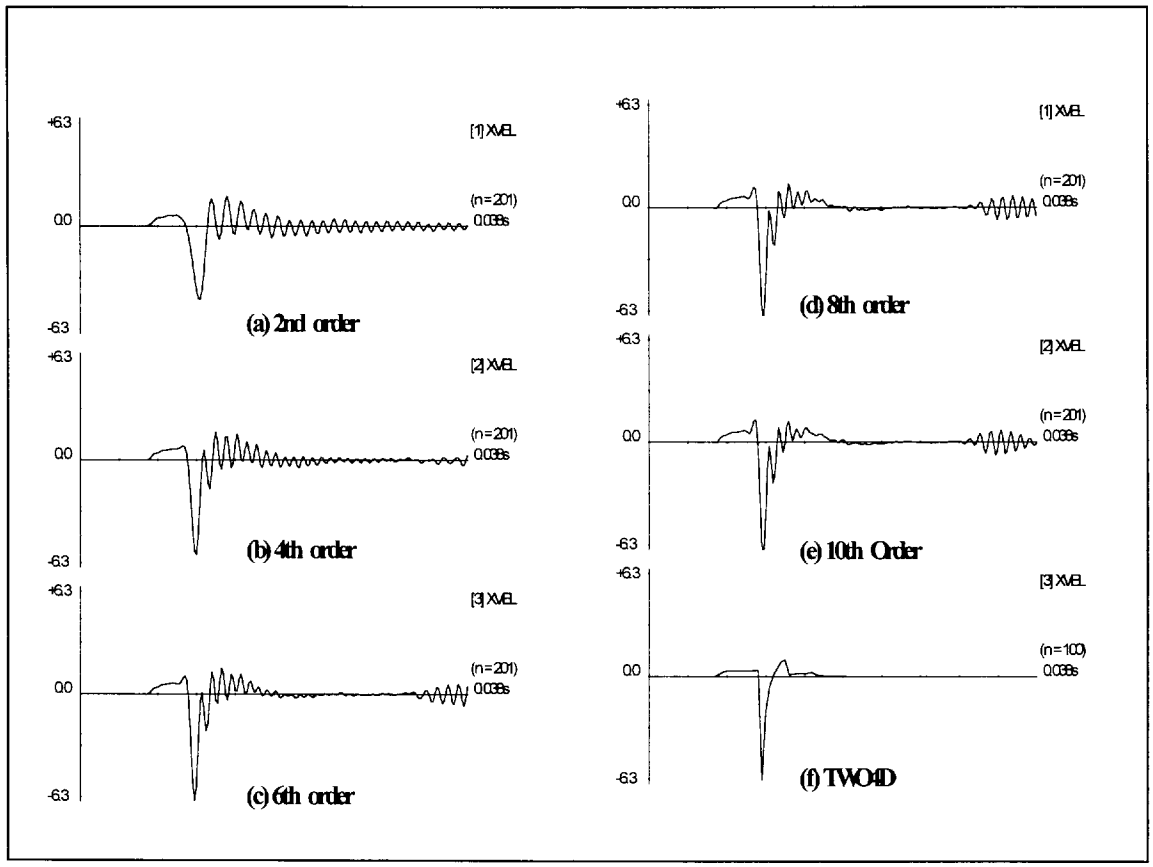

Figure 2.2.4.2: Response to a Step Shear source for Orders 2 to 10

Another approach to evaluation is to compare the size of model required to produce the same accuracy for the different schemes. This is done by choosing a finite rise-time for the source (so that it is band-limited), and then selecting the coarsest grid which produces no ringing. In figure 2.2.4.3 the TWO4D step result is compared with a 10 element source model with a 2nd

and 4th order solution, and a 20 element source model with a 2nd order solution. A rise-time of 1.2×10^{-3}s was chosen, corresponding to 12 and 24 time-steps in the 10 and 20 element source models respectively. It can be seen that to give comparable results, the 2nd order model needs to be about twice as fine as the 4th order model. In this case, the 2nd order model would require four times the memory and more than four times the run-time of the fourth order model.

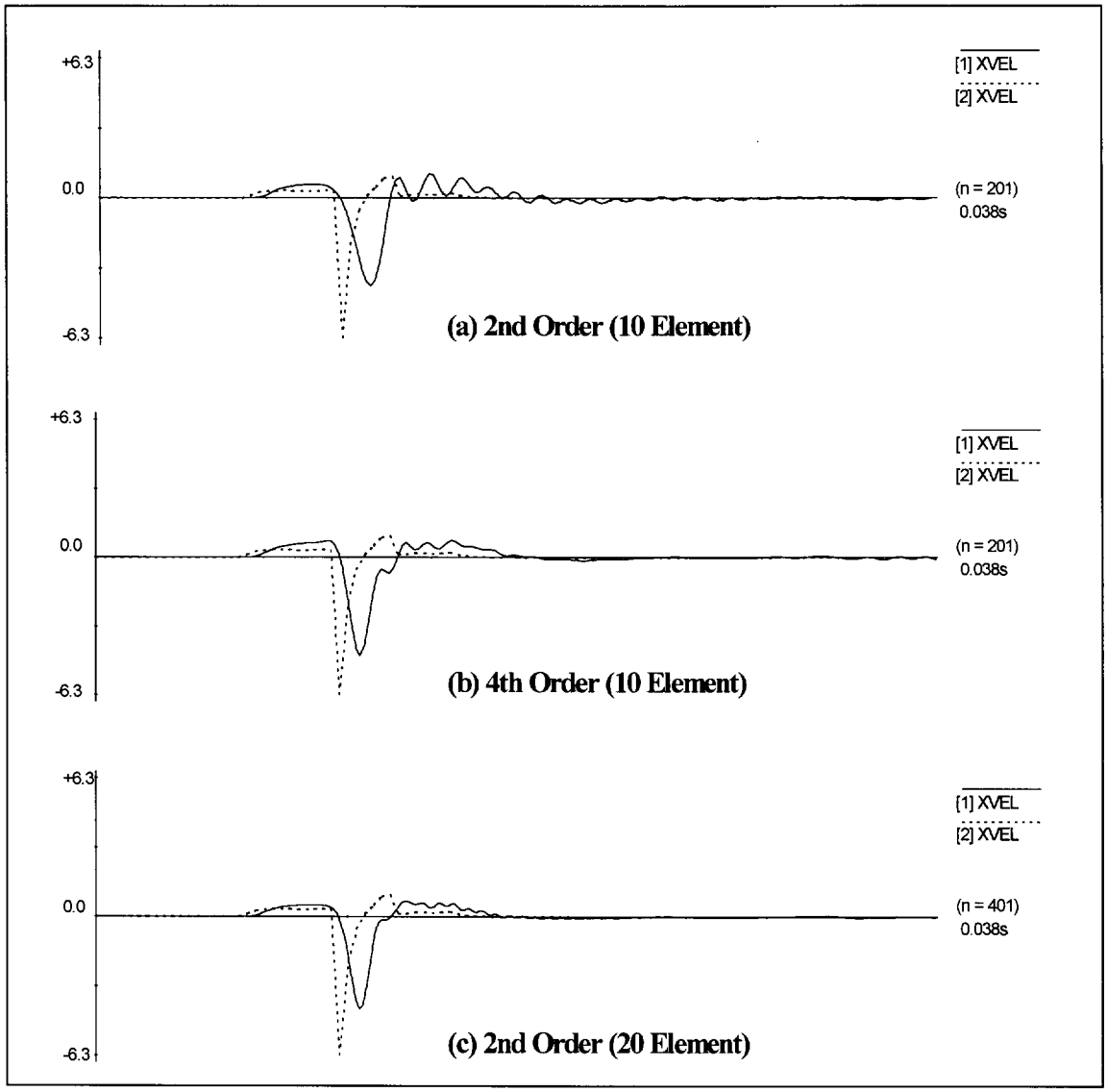

Figure 2.2.4.3: Responses to a shear source of finite rise-time (1.2 msec), comparing 2nd and 4th order solutions with the same mesh resolution and a more refined 2nd order solution. (In each case, the dashed solution shows the step response for TWO4D)

The above examples should show the optimal improvement for the higher order schemes, firstly due to the high frequency content, and also because wave propagation in a continuum is considered. A typical model may not have the same degree of high frequency content, and may have stopes, faults, parting planes etc, which are always solved at 2nd order accuracy. A comparison of convergence velocities in a simple three-dimensional stope model is shown in figure 2.2.4.4. The model consisted of a (48m) square stope and a (16m) square shear source (32m) ahead of the stope face. The convergence velocities considered are at 8m from the stope face. The three cases shown are for a 2nd and 4th order accuracy with 4m elements, and for 2nd order accuracy with 2.67m elements (a reduction of two thirds). In each case the dotted line shows a more accurate solution (4th order, 1m elements) for comparison. The accuracy of the 4th order model and more refined 2nd order model are similar - however this 2nd order result requires nearly four times the memory and run-time. The 4th order result here can be seen to become less accurate at later stages, since propagation along the stope is 2nd order.

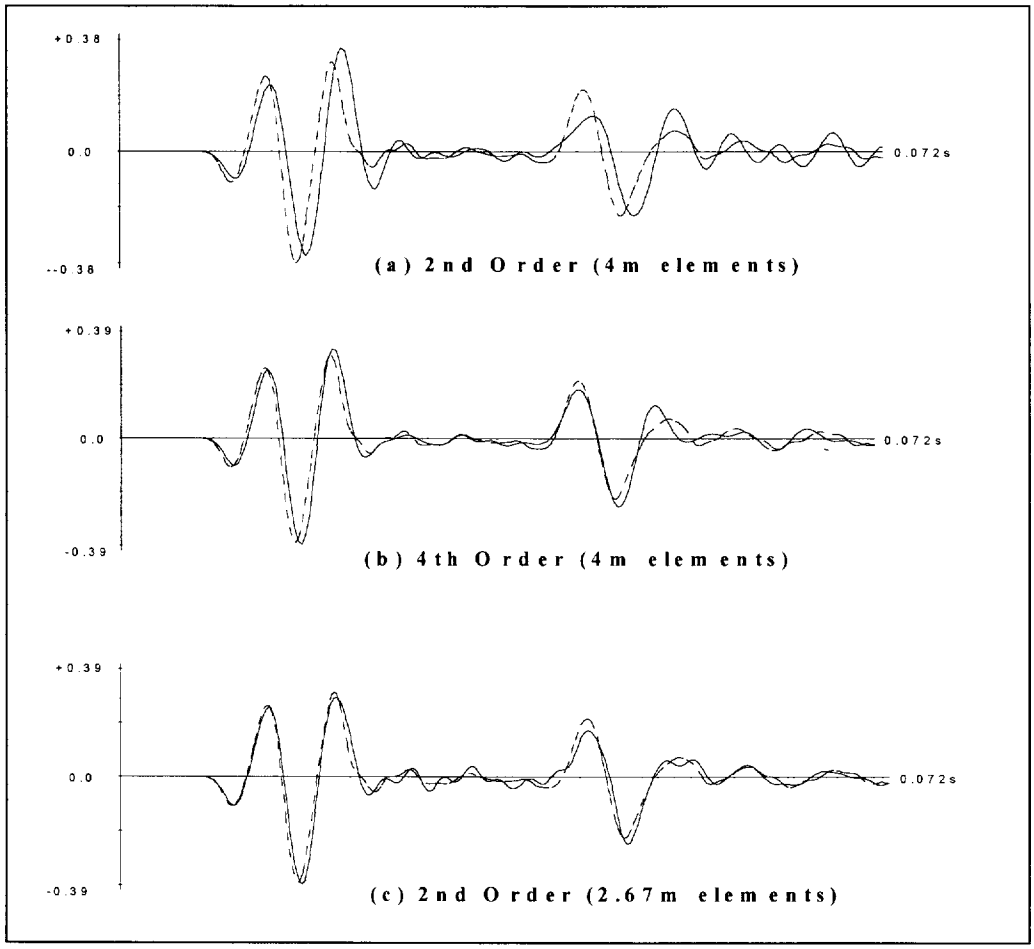

Figure 2.2.4.4: Comparison of different order solutions for a 3D stope model

It has been shown that the use of higher order differencing, has the potential to reduce memory and run-time requirements significantly. These benefits are particularly important in 3D modelling where the size and scope of problems will continue to be limited by computer hardware in the foreseeable future. To obtain full benefit would require all features such as stopes and boundaries to be higher order. The results do show however that there is an advantage in higher order differencing even without all features being higher order. It is recommended that future grid-based dynamic codes make use of high-order differencing where possible.

Stopes

An accurate static stress state due to the influence of a stope is important as it often provides the initial state for a dynamic investigation. WAVE obtains a static stress state through applied stress boundaries and asymptotic solution of the dynamic equations, and hence

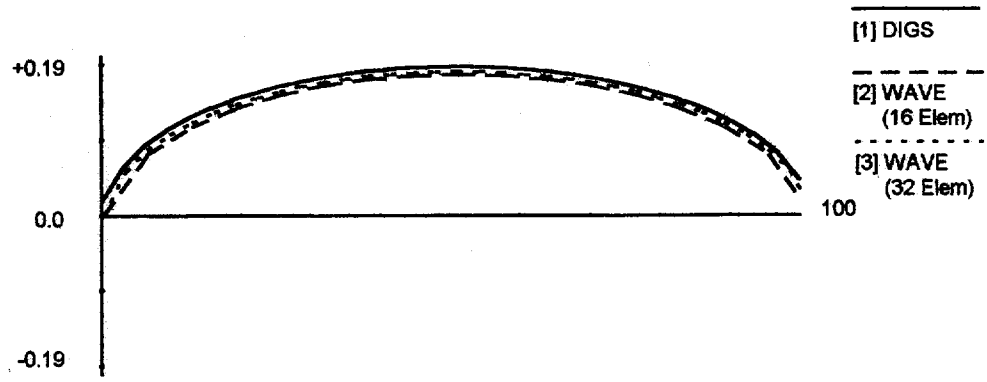

(a) Stope convergence

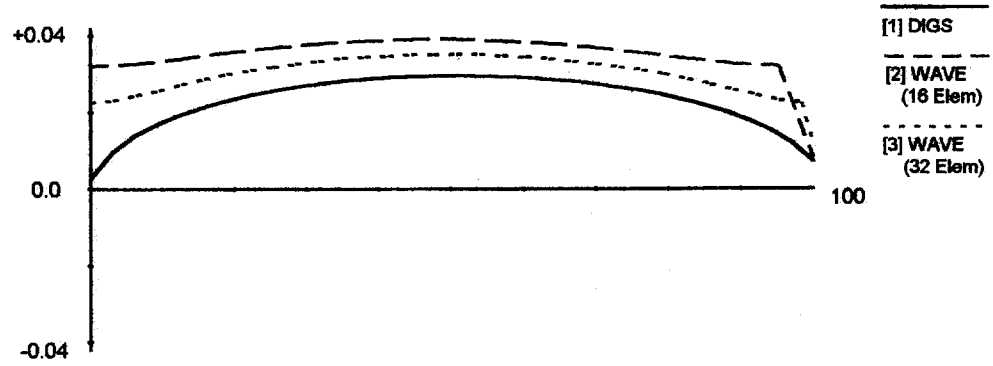

(b) Stope ride

Figure 2.2.4.5: Comparisons between DIGS and WAVE for a 100 m stope

inaccuracies in the static solution are an indication of inaccuracies in the overall dynamic implementation. DIGS was used to provide an accurate static solution for comparison with WAVE. Comparisons are shown in figure 2.2.4.5, for the case of a 100 metre stope in a rotated stress field (simulating a dip of 20°). It was found that normal stope components are accurate (e.g. convergence, figure 2.2.4.5a), while tangential stope components (e.g. ride, figure 2.2.4.5b) are less accurate. The cause of this inaccuracy is unclear, but it appears to be localized directly at the surface, and tangential stresses one element from the stope are more accurate. Figure 2.2.4.6 is for a similar case of a 400 metre stope where total closure occurs, and shows that the overall stress field is accurate. The convergence profile when total closure occurs was also shown to be accurate (Hildyard et al, 1995). The static accuracy for three-dimensional models has not been verified.

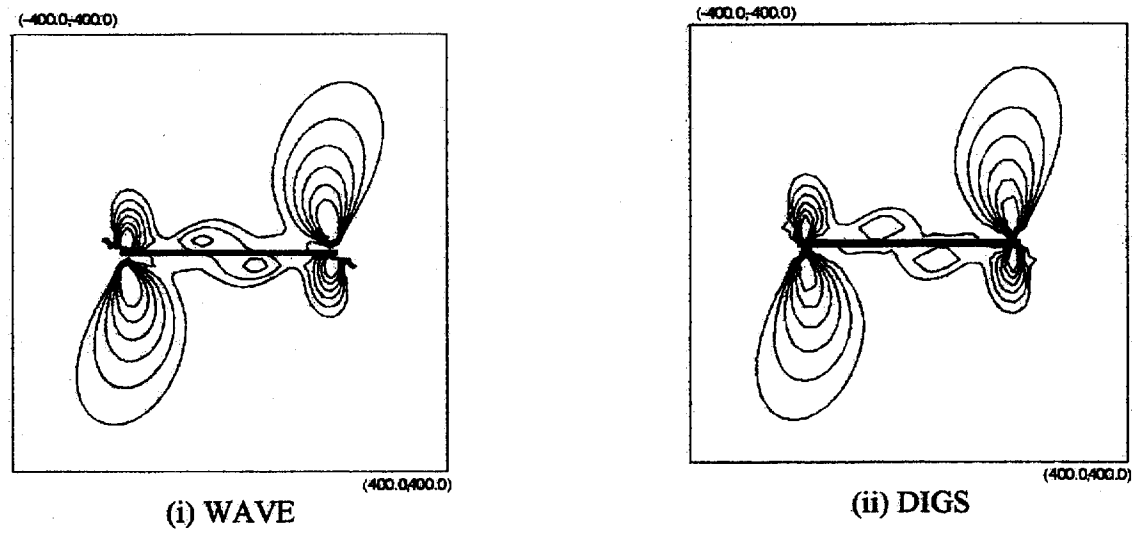

Figure 2.2.4.6: ESS contours (Min=0MPa, Max=20MPa) for DIGS and WAVE for a 400 metre stope

The accuracy of the dynamic behaviour of stopes and cracks in two-dimensions has been established through reproducing dynamic photoelastic experiments (*cf.* section 2.4). In particular the non-linear slip and contact laws were effective in reproducing behaviour from these experiments (*cf.* section 2.4.2), which gives some confidence in their usage. Similar experiments in three dimensions are recommended for testing the three-dimensional formulation.

Boundaries

In Siebrits and Hildyard (1993), boundary reflections were found to be minimal for high frequencies, but were present in problems with low frequency sources. It was later noted that the extremely low frequency in this example violates the absorbing boundary assumption of the waves being planar at the boundaries.

Reflections are generally small and are not normally visible in snapshots of wave patterns. The best way to highlight boundary reflections is to compare seismograms for the same model, but with boundaries at different distances. A simple model was used with a compressional point source and a shear source and a corresponding velocity recording. The 'far' case has the boundaries at least thirty elements from the source and from the recording point, while the 'near' case has the boundaries at least ten elements from the source and from the recording point. The results for different source pulse widths are compared in figure 2.2.4.7. Seismograms (a) to (c) are for a compressional source, and (d) to (f) for a shear source. The presence of boundary reflections can be noted, and reflections are greater for larger pulse-widths, i.e. lower frequencies. One reason for this is that the boundaries are most accurate for plane waves, and the distance of propagation required before a plane wave assumption is valid, is proportional to the wave-length. The reflections ae greater for the shear source than the compressional source. This is primarily due to the loading. A smoothed step load was used for the shear source, for which there is a nett stress change and hence a zero frequency (infinite wavelength component). A smoothed pulse was used for the compressional source, which has no nett stress change.

In all the above cases, the pulse-width is greater than ten elements, so we would expect reflections with the close boundaries. By moving the boundaries to at least 20 elements from the region of interest, reflections for the shortest pulse become negligible figure 2.2.4.7(g). In general, the boundaries should be at least one pulse-width from the region of interest. In two-dimensional models this requirement is acceptable, although in three dimensions it is generally necessary to accept some level of reflections.

Often of more significance than the distance of the boundaries required to minimize reflections, is the distance of the applied stress boundaries required to achieve an acceptable static stress distribution. Figure 2.2.4.8 compares the static results for a sixteen element, 100 metre stope, for different boundary positions. These are compared for convergence and

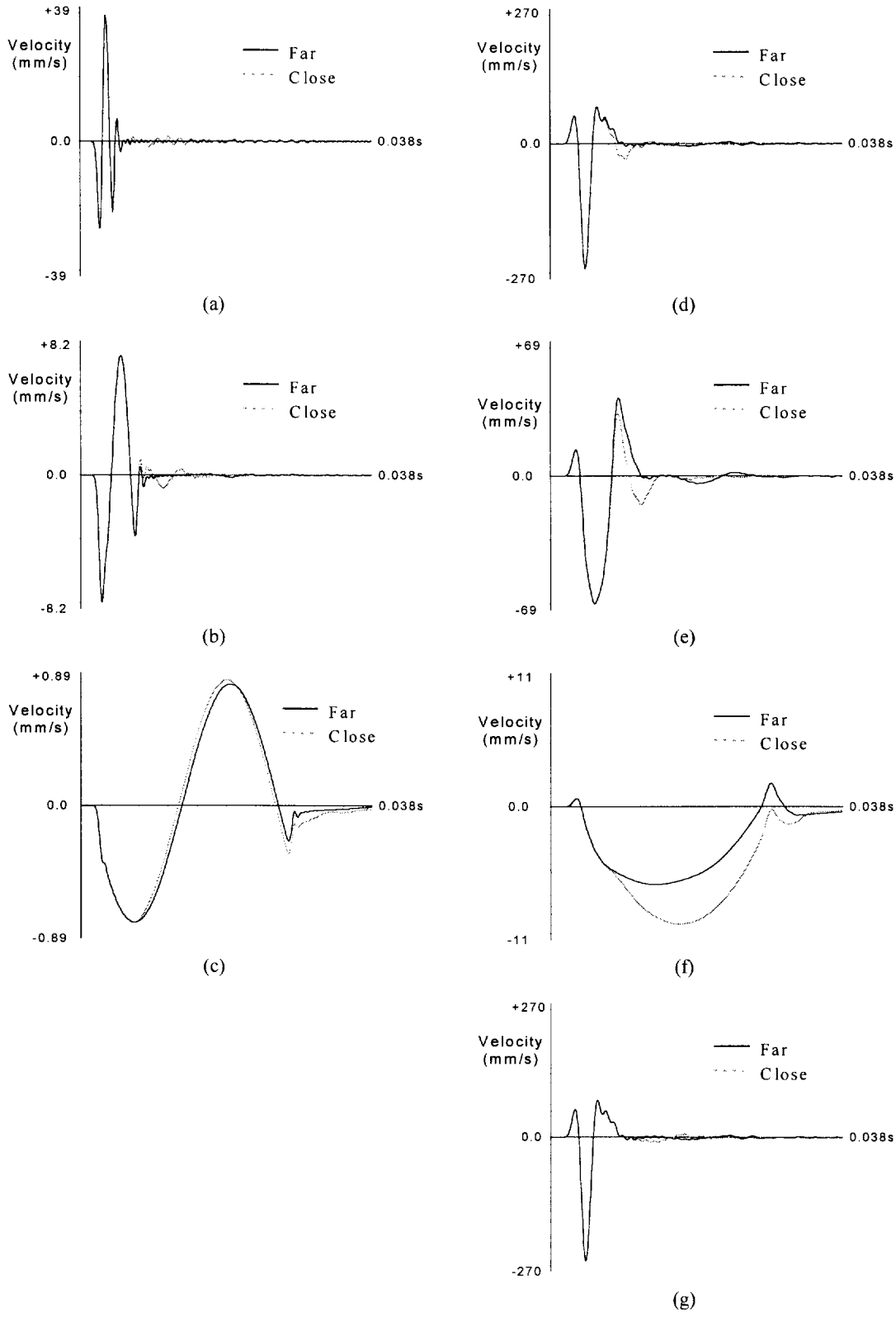

Figure 2.2.4.7: Comparison between far and very close boundaries for compressional and shear sources of varying pulse-widths

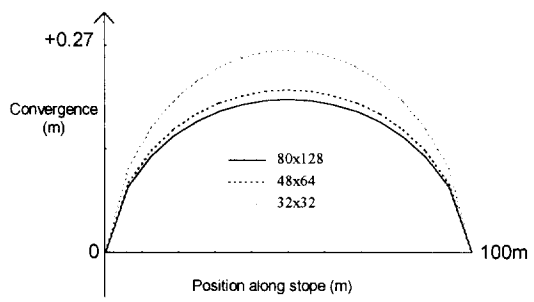

(a) Stope Convergence (m) for a 100 metre stope

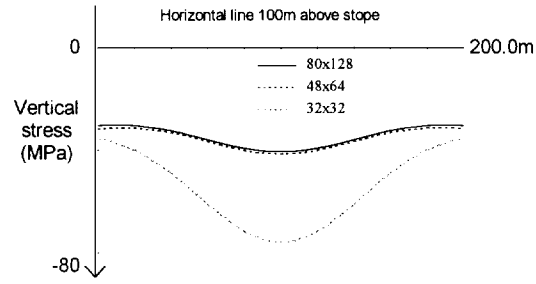

(b) Vertical stress (MPa) along a line 100 metres above a 100 metre stope

Figure 2.2.4.8: Comparisons of aspects of the static solution for different boundary positions

vertical stress distribution along a horizontal line 100 metres above the stope, as an arbitrary choice of the region of interest. The cases shown are for 80x128 elements, 48x64 elements and 32x32 elements, where the vertical boundaries are at a distance of four, two and one stope span from the stope, with the horizontal boundaries at two, one and half a stope span from the stope. The case with the vertical boundaries at a distance of two stope spans gives acceptable accuracy, but the grid size is four times that of the assumed region of interest. This is very limiting in three-dimensional problems. As discussed in section 2.2.3, it is undesirable to grade the mesh for dynamic models, although alternative approaches seem possible.

REFERENCES

Aki K. and Richards P.G. (1980) *Quantitative Seismology: Theory and Methods*. Freeman, Cooper, San Francisco, Vol 2, section 13.6, pp780.

Dablain M.A. (1986) 'The application of high-order differencing to the scalar wave equation'. *Geophysics*, Vol 51, pp 54-66.

Hildyard M.W., Daehnke A. and Cundall P.A. (1995) 'WAVE: A computer program for investigating elastodynamic issues in mining'. *Proc. 35th U.S. Symp. on Rock Mech.*, June 1995, pp. 519-524.

Pierce A.P. (1995) 'Properties of finite difference apporximations to the wave equation'. *Unpublished report, CSIR Mining Technology*, pp 1-16.

Siebrits E. and Hildyard M.W. (1993) 'Comparison between Dynamic Codes: FLAC, TWO4D and WAVE'. *Internal Note RE 1/93. CSIR Mining Technology*, pp 1-57.

2.2.5 Stability

Understanding the stability of a numerical scheme is important both for accuracy, and for efficiency, so that an efficient time-step can be chosen rather than a conservative estimate to ensure stability. The stability criteria for one-dimensional time-marching schemes is considered in Appendix II or Aki and Richards, 1980. For the leap-frog scheme as used in WAVE, this is shown to place a restriction on the maximum time-step of

$$\Delta t_{\max} \leq \frac{h}{c} \tag{2.2.5.1}$$

where h is the length of the spatial discretization, and c is the wave speed. Effectively this ensures that the speed of propagation of numerical information is faster than the physical wave speed. In WAVE itself, three separate stability conditions are required: for the grid, the stope and the boundary equations.

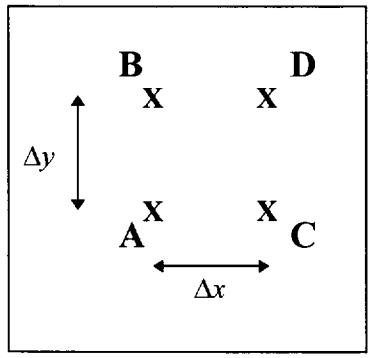

Figure 2.2.5.1: Schematic of four grid points of normal stress (only) in the WAVE mesh

We apply the above principle to the mesh equations in the two-dimensional WAVE grid. Figure 2.2.5.1 is a schematic of four cells in the WAVE mesh, where only the positions of normal stress are shown, represented by the 'X's. We note that numerical propagation from point A to point B requires a single time step, and hence

$$\Delta t_{\max} \leq \frac{\Delta y}{C_{P-\max}} \tag{2.2.5.2}$$

is a necessary condition, where $C_{P\text{-max}}$ is the maximum P-wave velocity throughout the grid (noting that the P-wave velocity is always higher than the S-wave velocity). However propagation from A to D requires 2 time-steps, so that

$$2\Delta t_{\max} \leq \frac{\sqrt{\Delta x^2 + \Delta y^2}}{C_{P-\max}} \tag{2.2.5.3}$$

is another necessary condition. If $\Delta x = \Delta y$ this gives a sufficient condition of

$$\Delta t_{\max} \leq \frac{\Delta y}{\sqrt{2}\, C_{P-\max}} \tag{2.2.5.4}$$

In general however $\Delta x \neq \Delta y$. For this we need to obtain the shortest physical distance requiring the largest number of time steps. This condition is reached when the number of x and y grids being traversed are in the proportions Δy^2 and Δx^2 respectively, giving a distance $\sqrt{\Delta y^4 \Delta x^2 + \Delta y^2 \Delta x^4}$, while the relative number of time steps required to propagate this distance is $\Delta x^2 + \Delta y^2$. This gives a more general condition of

$$\Delta t_{\max} \leq \frac{\Delta x \Delta y}{\sqrt{\Delta x^2 + \Delta y^2}\, C_{P-\max}} \tag{2.2.5.5}$$

In WAVE, the actual time-step used for the second order scheme in two dimensions is

$$\Delta t = \frac{1}{\sqrt{2}} \Delta t_{\max} \tag{2.2.5.6}$$

In three-dimensions, the same analysis yields

$$\Delta t_{\max} \leq \frac{\Delta x \Delta y \Delta z}{\sqrt{\Delta x^2 + \Delta y^2 + \Delta z^2}\, C_{P-\max}} \tag{2.2.5.7}$$

and the actual time-step used for the second order scheme in three dimensions is

$$\Delta t = \frac{\sqrt{3}}{2} \Delta t_{\max} \tag{2.2.5.8}$$

For both two-dimensional and three-dimensional higher order schemes, the time-step is reduced to 90% of the values given by equations 2.2.5.6 and 2.2.5.8 respectively.

Stopes, seams and faults may be given stiffness. The choice of normal stiffness is arbitrary, but the shear stiffness has as effect on the stability. The following empirical condition is used in WAVE

$$\Delta t_{\max} \leq \sqrt{\frac{\rho}{\frac{K_s}{\Delta y} + \frac{K + 4/3\, G}{\Delta x^2}}} \tag{2.2.5.9}$$

where K_s is the shear stiffness, and ρ, K and G are the material parameters of the surrounding material (density, bulk modulus and shear modulus). Alternatively, the maximum stable shear stiffness in stopes for a given time-step size, is limited by

$$K_{s(\max)} \leq \Delta y \left[\frac{\rho}{\Delta t^2} - \frac{K + 4/3\, G}{\Delta x^2} \right] \tag{2.2.5.10}$$

Finally, the present three-dimensional boundary conditions (specifically the edge conditions) also affect stability. An approximate and conservative empirical relationship is used with

$$\Delta t_{\max} \leq \frac{\min(\Delta x, \Delta y, \Delta z)}{2\sqrt{2}\, C_S} \tag{2.2.5.11}$$

where C_s is the shear velocity at the boundary.

REFERENCES

Aki K. and Richards P.G. (1980) *Quantitative Seismology: Theory and Methods*. Freeman, Cooper, San Francisco, Vol 2, section 13.6.

Conclusions

WAVE is extremely well-adapted for analysing dynamic mining problems, with fairly low geometrical complexity. WAVE has associated graphical facilities which provide a means of visualizing the development of wave patterns, and capturing and analysing synthetic seismograms. The command structure has been made more accessible by means of an extensive on-line help facility containing command syntax and example models. It is potentially a useful tool in obtaining an understanding of wave behaviour in a mining context.

Important developments have been made in the representations of stopes and cracks. While limited in orientation, the important characteristics of wave-stope and wave-fracture interactions are captured. Much effort has also been made to achieve optimum performance. This includes the overall efficiency of the difference scheme, and efficiency due to the assumption of an orthogonal mesh. Absorbing boundaries, static boundaries, high order schemes and stope/crack accuracy have important implications on efficiency, and ultimately determine the practical problem sizes which can be studied. Efficiency will remain a necessity in three-dimensional analyses in the foreseeable future, due to finite computer capabilities.

The efficiency leads to potentially fast model turn-around times, and this and the fact that models are easily designed and altered (due to the simple grid scheme), encourage greater experimentation with models, rather than setting up a single complex model.

WAVE's usefulness could be improved by direct extension of a few areas such as:

- applied boundaries which efficiently approximate far-field stress are very important to three-dimensional modelling.
- boundary and stope reflections due to switching from fourth order to second order difference schemes, would be improved if fully fourth order stope and boundary logic was implemented.
- Intersecting stopes in three-dimensions would allow three-dimensional cavity problems and stope fracture intersections to be investigated.

The biggest limitation in WAVE is the lack of general orientations for stopes and fractures. In this work area there are three needs - efficient analysis, particularly of three-dimensional problems, representation of stopes, faults and fractures with arbitrary orientation, and very

general and accurate crack orientations for studying crack growth. There are ways in which the WAVE scheme can be generalized. However it is unclear how best this is achieved, and indeed if another approach could not better combine the needs of efficiency and generality.

Finally, most of the issues encountered in WAVE will be important in any similar mesh-based dynamic code. The performance of WAVE can be used as a benchmark in evaluating simple but fundamental aspects of behaviour in alternative or more complex codes - with particular emphasis on quantifying accuracy, and the memory and run-time requirements to achieve that accuracy. From experience with WAVE, the following should be quantified:

- absorbing boundary efficiency (can the boundaries be close, and is there frequency-dependence)
- static stress state (how far do boundaries need to be to achieve far-field conditions)
- dispersion accuracy
- mesh dependence
- stope and crack accuracy (with particular reference to reproducing simple photo-dynamic experiments)

APPENDIX I: Summary of fundamental technical aspects of WAVE

WAVE solves the wave equation for an elastic solid, by numerically solving a system of first order equations given by the constitutive equations and equations of motion. This appendix gives a brief overview of fundamental theoretical aspects of WAVE - a full analysis can be found in Cundall (1992).

The time derivatives of the constitutive equations for a linear elastic isotropic material are:

$$\dot{\sigma}_{ij} = \delta_{ij}\left(K - \tfrac{2}{3}G\right)\dot{e}_{kk} + 2G\dot{e}_{ij} \tag{1}$$

where

$$\dot{e}_{ij} = \frac{1}{2}\left[\frac{\partial \dot{u}_i}{\partial x_j} + \frac{\partial \dot{u}_j}{\partial x_i}\right] \tag{2}$$

The equations of motion (ignoring body force) are:

$$\rho \frac{\partial \dot{u}_i}{\partial t} = \frac{\partial \sigma_{ij}}{\partial x_j} \tag{3}$$

where ρ is density, and $\dot{u}$ is velocity.

The continuum is discretized into a grid or mesh - i.e. equations (1) and (3) are satisfied at discrete points in time and space. For good accuracy, WAVE uses a staggered mesh with

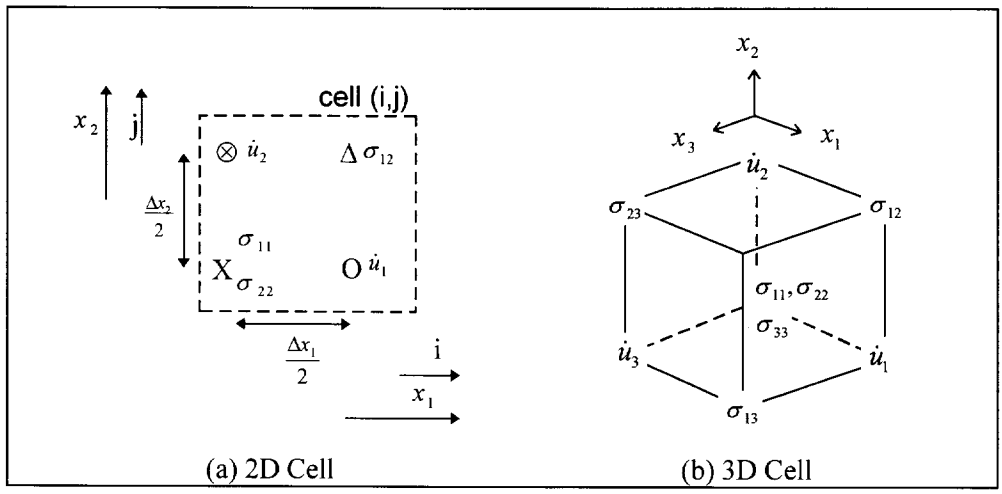

Figure 1: Unit Cell in the WAVE Mesh

central differences. In this formulation, each grid variable is computed at a different position in space. Figure 1 shows the positions of grid variables for a two and three dimensional unit cell in the WAVE mesh, while figure 2 shows a portion of a two-dimensional mesh, with a number of cells. Stresses are calculated from velocities using (1), and velocities from stresses using (3). Hence velocities are also staggered in time by $\Delta t/2$ with respect to stresses.

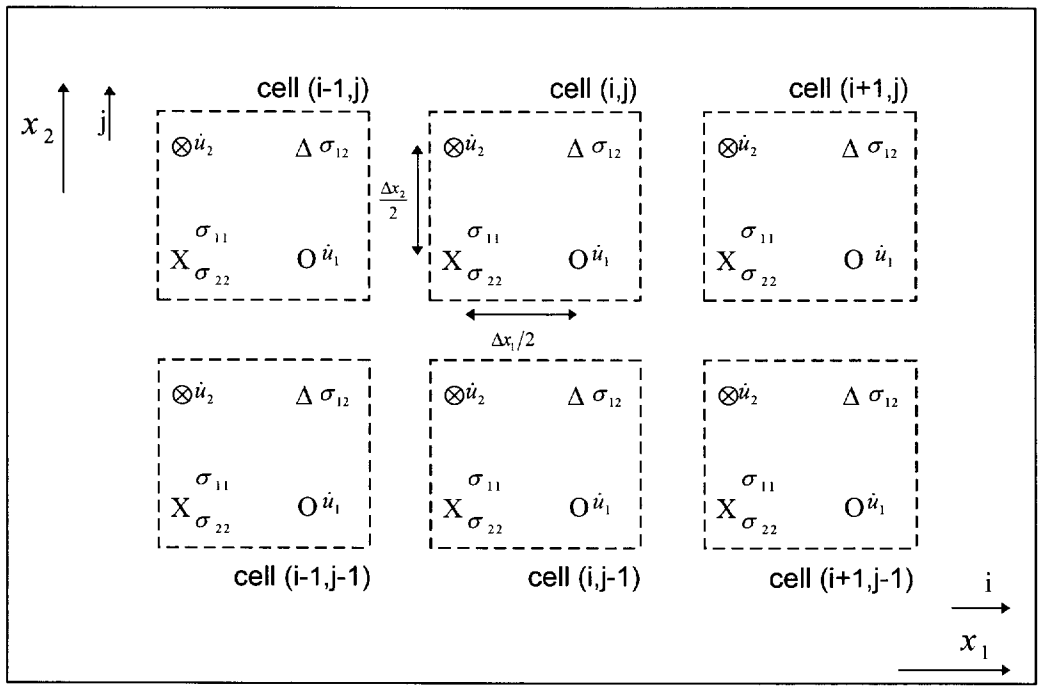

Figure 2 : Portion of a 2D WAVE mesh

Mesh Equations

Using equation (1) for σ_{22} in two dimensions, and substituting $E_1 = K + 4G/3$ and $E_2 = K - 2G/3$, gives:

$$\frac{\partial \sigma_{22}}{\partial t} = E_1 \frac{\partial \dot{u}_2}{\partial x_2} + E_2 \frac{\partial \dot{u}_1}{\partial x_1} \tag{4}$$

Applying this equation at time $t - \frac{1}{2}$ and at cell (i, j) in the grid, and discretizing with second order accuracy on the staggered grid gives:

$$\sigma_{22}^{t} = \sigma_{22}^{t-1} + E_1 \frac{\Delta t}{\Delta x_2}\left(\dot{u}_2^{j} - \dot{u}_2^{j-1}\right) + E_2 \frac{\Delta t}{\Delta x_1}\left(\dot{u}_1^{i} - \dot{u}_1^{i-1}\right) \tag{5}$$

where indices i and j refer to directions 1 and 2 and the velocities are known at time $t - \frac{1}{2}$. Similarly, for σ_{11} and σ_{12} we get

$$\sigma_{11}^{t} = \sigma_{11}^{t-1} + E_1 \frac{\Delta t}{\Delta x_1}\left(\dot{u}_1^{i} - \dot{u}_1^{i-1}\right) + E_2 \frac{\Delta t}{\Delta x_2}\left(\dot{u}_2^{j} - \dot{u}_2^{j-1}\right) \tag{6}$$

$$\sigma_{12}^{t} = \sigma_{12}^{t-1} + G \frac{\Delta t}{\Delta x_1}\left(\dot{u}_2^{i+1} - \dot{u}_2^{i}\right) + G \frac{\Delta t}{\Delta x_2}\left(\dot{u}_1^{j+1} - \dot{u}_1^{j}\right) \tag{7}$$

For velocities, applying equation (3) at time t gives:

$$\dot{u}_1^{t+\frac{1}{2}} = \dot{u}_1^{t-\frac{1}{2}} + \frac{1}{\rho}\frac{\Delta t}{\Delta x_1}\left(\sigma_{11}^{i+1} - \sigma_{11}^{i}\right) + \frac{1}{\rho}\frac{\Delta t}{\Delta x_2}\left(\sigma_{12}^{j} - \sigma_{12}^{j-1}\right) \tag{8}$$

$$\dot{u}_2^{t+\frac{1}{2}} = \dot{u}_2^{t-\frac{1}{2}} + \frac{1}{\rho}\frac{\Delta t}{\Delta x_2}\left(\sigma_{22}^{j+1} - \sigma_{22}^{j}\right) + \frac{1}{\rho}\frac{\Delta t}{\Delta x_1}\left(\sigma_{12}^{i} - \sigma_{12}^{i-1}\right) \tag{9}$$

These are the basic second order equations applied throughout a 2D WAVE mesh.

Absorbing Boundaries

For plane P-waves propagating in an infinite elastic medium,

$$\sigma = C_p \rho \, \dot{u}_n \tag{10}$$

where σ and $\dot{u}_n$ are the direct stress and particle velocity in the direction of propagation, and C_p is the P-wave speed. For plane S-waves,

$$\tau = C_s \rho \, \dot{u}_s \tag{11}$$

where τ and $\dot{u}_s$ are the shear stress and particle velocity perpendicular to the direction of propagation, and C_s is the S-wave speed.

If these conditions are enforced at the boundaries of the numerical grid, then for plane waves the boundary acts in the same manner as an infinite medium. Boundary reflection increases as the angle of incidence departs from 90°. Lysmer and Kuhlemeyer (1967) provide graphs showing how this absorbing boundary performs over a range of angles.

In WAVE the boundaries were chosen to fall on planes containing the direct stress grid-points (figure 3). Due to the staggered mesh, some boundary points correspond to stress, and others to velocity components. The equations at the boundary are developed by writing the standard mesh equations, using fictitious grid-points (which fall outside of the mesh). The fictitious values are then eliminated by combining with equations (10) and (11). The approach is illustrated for the lower boundary.

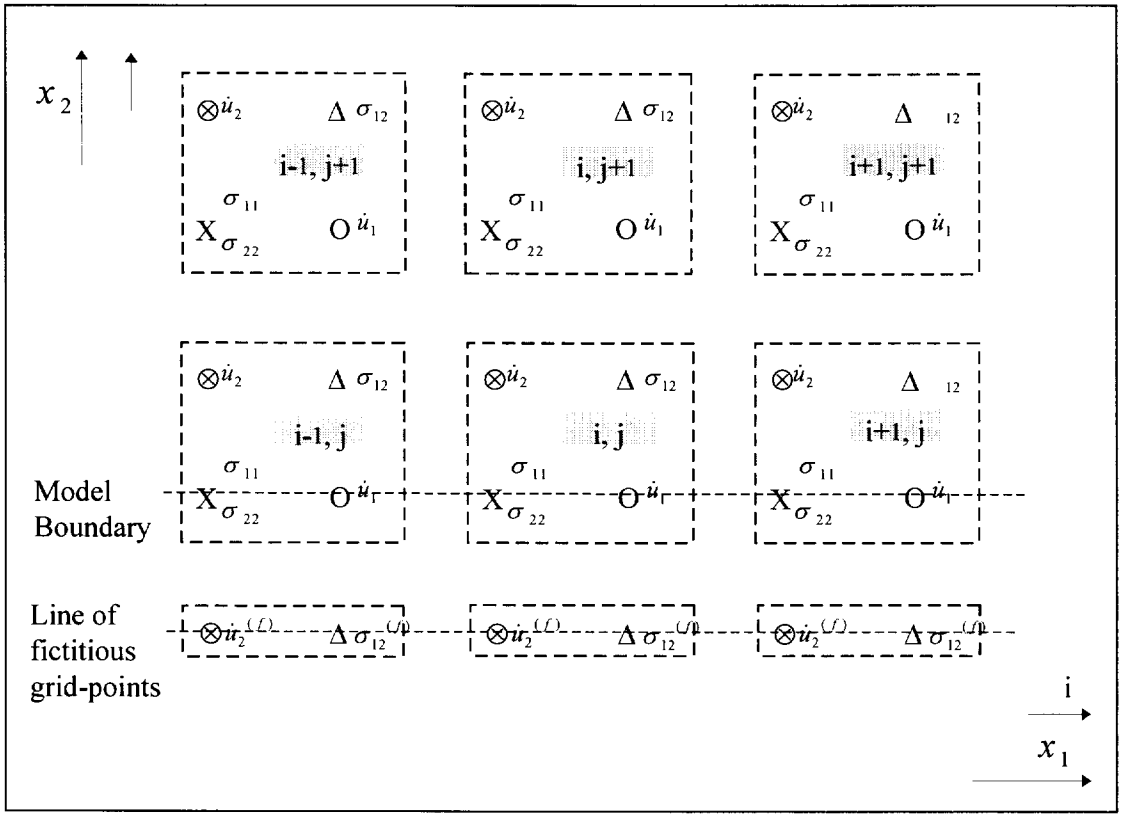

Figure 3: Lower grid boundary in 2D Mesh, showing line of fictitious grid-points

Writing the mesh equation (5) for the boundary at time $t - \frac{1}{2}$, gives

$$\sigma_{22}^{t} = \sigma_{22}^{t-1} + E_1 \frac{\Delta t}{\Delta x_2}\left(\dot{u}_2^{j} - \dot{u}_2^{j-1(f)}\right) + E_2 \frac{\Delta t}{\Delta x_1}\left(\dot{u}_1^{i} - \dot{u}_1^{i-1}\right) \tag{12}$$

and applying (6) at time $t - \frac{1}{2}$, gives

$$\frac{1}{2}\left(\sigma_{22}^{t} + \sigma_{22}^{t-1}\right) = \frac{1}{2}\frac{C_P}{\rho}\left(\dot{u}_2^{j} + \dot{u}_2^{j-1(f)}\right) \tag{13}$$

Combining (12) and (13) to eliminate the fictitious grid-point $\dot{u}_2^{j-1(f)}$, gives

$$\sigma_{22}^{t} = \frac{1}{\left(\frac{\Delta x_2}{E_1 \Delta t} + \frac{1}{C_P \rho}\right)}\left[\left(\frac{\Delta x_2}{E_1 \Delta t} - \frac{1}{C_P \rho}\right)\sigma_{22}^{t-1} + 2\dot{u}_2^{j} + \frac{E_2}{E_1}\frac{\Delta x_2}{\Delta x_1}\left(\dot{u}_1^{i} - \dot{u}_1^{i-1}\right)\right] \tag{14}$$

From (5) and (6), the mesh equation for σ_{11} can be written in terms of σ_{22} giving,

$$\Delta\sigma_{11} = \frac{2G(6K + 2G)\Delta t}{(3K + 4G)\Delta x_1}\left(\dot{u}_1^{i} - \dot{u}_1^{i-1}\right) + \frac{E_2}{E_1}\Delta\sigma_{22} \tag{15}$$

An equation for the velocity $\dot{u}_1$ on this lower boundary can be derived by writing the mesh equation (7), and then using equation (10) to eliminate the fictitious grid-points $\sigma_{12}^{(f)}$. A similar analysis is used to derive the equations on the remaining three boundaries.

Discontinuities

A discontinuity is implemented in the mesh as two infinitesimally thin planes on which certain grid variables are controlled and others allowed to be dual-valued. The approach taken in deriving the equations is to write the standard mesh equation for each of the surfaces using fictitious grid-points which are not in the mesh. Stress conditions on the surface, provide the third equation allowing these fictitious values to be eliminated.

The approach is illustrated for a 2D horizontal crack where the normal stress is assumed to be governed by a linear stiffness k_n. Grid variables falling on the crack have an upper and lower

value. Figure 4 shows that variables $\sigma_{11}^{u}, \sigma_{11}^{l}, \dot{u}_1^{u}$ and $\dot{u}_1^{l}$ must be calculated separately, where *u* and *l* denote the upper and lower surfaces.

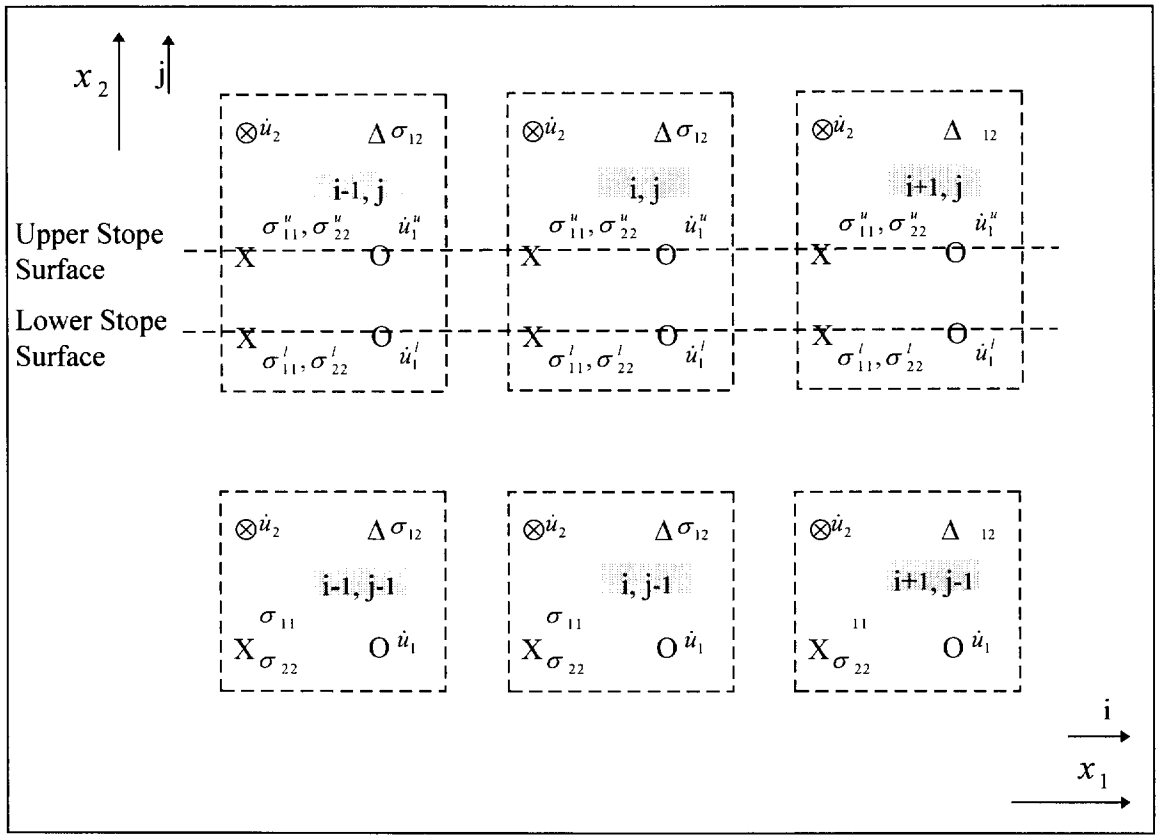

Figure 4: Position of 2D crack in the WAVE mesh

From continuity $\sigma_{22}^{u} = \sigma_{22}^{l}$, but we can write two separate equations:

$$\Delta\sigma_{22}^{u} = E_1 \frac{\Delta t}{\Delta x_2}\left(\dot{u}_2^{j} - \dot{u}_2^{(uf)}\right) + E_2 \frac{\Delta t}{\Delta x_1}\left(\dot{u}_1^{i(u)} - \dot{u}_1^{i-1(u)}\right) \tag{16}$$

$$\Delta\sigma_{22}^{l} = E_1 \frac{\Delta t}{\Delta x_2}\left(\dot{u}_2^{(lf)} - \dot{u}_2^{j-1}\right) + E_2 \frac{\Delta t}{\Delta x_1}\left(\dot{u}_1^{i(l)} - \dot{u}_1^{i-1(l)}\right) \tag{17}$$

where $\dot{u}_2^{(uf)}$ and $\dot{u}_2^{(lf)}$ are "fictitious" gridpoints, since $\dot{u}_2^{(uf)}$ is below the upper surface and $\dot{u}_2^{(lf)}$ above the lower surface of the crack.

σ_{22} is also related to the relative normal velocity of the two surfaces, by the stiffness k_n:

$$\Delta\sigma_{22} = \dot{u}^{rel} k_n \Delta t = k_n \Delta t \left[\frac{\dot{u}_2^j + \dot{u}_2^{(uf)}}{2} - \frac{\dot{u}_2^{j-1} + \dot{u}_2^{(lf)}}{2} \right] \tag{18}$$

The fictitious stresses $\dot{u}_2^{(uf)}$ and $\dot{u}_2^{(lf)}$ can be eliminated, giving:

$$\Delta\sigma_{22} = E_1 \frac{E_1 k_n \Delta t}{E_1 + k_n \Delta x_2} \left[\left(\dot{u}_2^j - \dot{u}_2^{j-1} \right) + \frac{1}{2} \frac{E_2}{E_1} \frac{\Delta x_2}{\Delta x_1} \dot{u}_1^{diff} \right] \tag{19}$$

$$\text{where } \dot{u}_1^{diff} = \dot{u}_1^{i(u)} - \dot{u}_1^{i-1(u)} + \dot{u}_1^{i(l)} - \dot{u}_1^{i-1(l)})$$

from which σ_{11}^u and σ_{11}^l can be calculated

$$\Delta\sigma_{11}^u = \frac{2G(6K+2G)\Delta t}{(3K+4G)\Delta x_1} \left(\dot{u}_1^{i(u)} - \dot{u}_1^{i-1(u)} \right) + \frac{E_2}{E_1} \Delta\sigma_{22} \tag{20}$$

$$\Delta\sigma_{11}^l = \frac{2G(6K+2G)\Delta t}{(3K+4G)\Delta x_1} \left(\dot{u}_1^{i(l)} - \dot{u}_1^{i-1(l)} \right) + \frac{E_2}{E_1} \Delta\sigma_{22} \tag{21}$$

By assuming that the surface shear stress is governed by a linear stiffness k_s, velocities $\dot{u}_1^u$ and $\dot{u}_1^l$ can be calculated in a similar manner.

REFERENCES

Cundall P.A. (1992) 'Theoretical basis of the program WAVE'. *Unpublished internal report, COMRO-CSIR Mining Technology*, pp 1-12.

Lysmer J. and Kuhlemeyer R. (1969). 'Finite dynamic model for infinite media'. *J. Eng. Mech., ASCE,* vol 95, No. EM4, pp 859-877.

APPENDIX II

PROPERTIES OF FINITE DIFFERENCE APPROXIMATIONS TO THE WAVE EQUATION

Model wave equations and properties

In these notes we analyze in some detail the accuracy, stability, and dispersive properties of finite difference models of the wave equation. In order to simplify the analysis we consider the simplest possible form of wave equation. In order to motivate this simplification we observe that the equations of elastodynamics reduce, via a Helmholtz decomposition (see for example Eringen and Suhubi 1975), to two coupled wave equations - one scalar and one vector. We therefore consider the right-moving component of the one dimensional wave equation:

$$0 = \frac{\partial^2}{\partial t^2} - c^2 \frac{\partial^2}{\partial x^2} U(x,t) = (\frac{\partial}{\partial t} - c\frac{\partial}{\partial x})(\frac{\partial}{\partial t} + c\frac{\partial}{\partial x})U(x,t) \tag{1}$$

namely,

$$\frac{\partial U}{\partial t} + c\frac{\partial U}{\partial x} = 0, \qquad U(x,0) = U_0(x), \tag{2}$$

This partial differential equation can be solved using the following Fourier Transform pair:

$$\hat{f}(\omega) = \int_{-\infty}^{\infty} e^{-i\omega x} f(x) dx, \quad f(x) = \frac{1}{2\pi} \int_{-\infty}^{\infty} e^{i\omega x} f(\omega) d\omega \tag{3}$$

Using (3) the Fourier transform of the spatial derivative of U becomes:

$$\begin{aligned} \frac{\hat{\partial U}}{\partial x} &= U(x,t)e^{i\omega x}\Big|_{-\infty}^{\infty} + i\omega \int_{-\infty}^{\infty} U(x,t)e^{i\omega x} dx \\ &= i\omega \hat{U}(\omega, t). \end{aligned} \tag{4}$$

Thus taking the Fourier transform of (2) reduces it to the following ordinary differential equation:

$$\dot{\hat{U}} + ci\omega \hat{U} = 0.$$

with the following solution

$$\hat{U} = e^{-ic\omega t} \hat{U}_0.$$

Using the inversion formula (3) we obtain the solution to (2)

$$U(x,t) = \frac{1}{2\pi} \int_{-\infty}^{\infty} e^{i\omega x} \hat{U}(\omega, t) d\omega$$

$$= \frac{1}{2\pi}\int_{-\infty}^{\infty} e^{i\omega(x-ct)}\hat{U}_0(\omega)d\omega$$
$$= U_0(x-ct) \tag{5}$$

We observe that the solution (5) represents the translation of the initial condition $U_0(x)$ by a Galilean reference frame moving at a constant speed c.

Spatial semi-discretization

The finite difference method replaces the continuum model in the form of the partial differential equation (2) by a discrete model in the form of a difference equation involving discrete approximates at desired meshpoints. A finite difference approximation to the differential equation is obtained by replacing the derivatives in (2) by various difference approximations. Depending on the form of these difference approximations a variety of finite difference models can be obtained each having different accuracies, stability properties and even spurious physical effects such as dispersion that are not present in the original problem (2).

In order to analyze the effects of the spatial and time discretization processes separately we first consider a discretization of the spatial derivative in (2). We assume that the domain $(-\infty, \infty)$ is divided into mesh points $\{x_n = nh,\ n = \ldots -2, -1, 0, 1, 2, \ldots\}$ and that at each of these meshpoints the approximate solution $u_n(t) \approx U(x_n, t)$ is sought. For example approximating $\partial U/\partial x$ by a central difference formula we obtain the following spatial semidiscretization of (2):

$$\dot{u}_n(t) + c\left(\frac{u_{n+1}(t) - u_{n-1}(t)}{2h}\right) = 0 \tag{6}$$

To illustrate that this semidiscretization is not unique we can write down other difference equations by using forward and backward difference approximations to the spatial derivative to obtain:

$$\dot{u}_n(t) + c\left(\frac{u_{n+1}(t) - u_n(t)}{h}\right) = 0 \tag{7}$$

and

$$\dot{u}_n(t) + c\left(\frac{u_n(t) - u_{n-1}(t)}{h}\right) = 0 \tag{8}$$

Truncation errors of spatial semidiscretizations

In order to determine the truncation error involved with each of the the above approximations we assume that the mesh values $\{u_n(t)\}$ are discrete samples of an analytic

function $u(x,t)$ at each time level. Performing a Taylor expansion about the meshpoint x_n we obtain:

$$\begin{aligned} 0 &= \dot{u}_n(t) + c\left(\frac{u_{n+1}(t) - u_{n-1}(t)}{2h}\right) \\ &= \dot{u}_n + \frac{c}{2h}\left(u_n + hu'_n + \frac{h^2}{2}u''_n + \frac{h^3}{3!}u'''_n + \frac{h^4}{4!}u^{(4)}_n + \dot{s}\right. \\ &\quad \left. - u_n + hu'_n - \frac{h^2}{2}u''_n + \frac{h^3}{3!}u'''_n - \frac{h^4}{4!}u^{(4)}_n + \dot{s}\right) \\ &= \frac{\partial u_n}{\partial t} + c\frac{\partial u_n}{\partial x} + \frac{ch^2}{6}\frac{\partial^3 u_n}{\partial x^3} + O(h^4) \end{aligned} \tag{9}$$

where $\dot{u} := \frac{\partial u}{\partial t}$ and $u' := \frac{\partial u}{\partial x}$.

If in equation (9) we replace $u_n(t)$ by $U(x_n,t)$, the solution to (2), we obtain the following expression for the truncation error associated with the finite difference approximation (6):

$$\frac{ch^2}{6}\frac{\partial^3 U(x_n,t)}{\partial x^3} \tag{10}$$

Which implies that the central difference approximation is accurate up to $O(h^2)$. Apart from yielding the truncation error (10), equation (9) has another interesting interpretation concerning the physical properties of the difference approximation (6) as opposed to those of the original continuum equation (2). If we retain the $O(h^2)$ error term in (9) we see that rather than approximating the wave equation (2), the difference equation (6) is an approximation to the following partial differential equation

$$\left(\frac{\partial}{\partial t} + c\frac{\partial}{\partial x} + \frac{ch^2}{6}\frac{\partial^3}{\partial x^3}\right)u(x,t) = 0 \tag{11}$$

The third derivative term in (11) which is multiplied by the small mesh parameter h^2 represents a singular perturbation to the right-moving wave operator (2). This equation is the linearized Korteweg-de Vries equation which involves dispersive wave motion. Thus the effect of this additional term is to introduce spurious numerical dispersion. In the following subsection we perform a Fourier analysis of the difference equations (6) directly to obtain a more complete understanding of the effect of this numerical dispersion.

Performing a similar Taylor expansion for the forward difference approximation we obtain:

$$\begin{aligned} 0 &= \dot{u}_n(t) + c\left(\frac{u_{n+1}(t) - u_n(t)}{h}\right) \\ &= \dot{u}_n + \frac{c}{h}\left(u_n + hu'_n + \frac{h^2}{2}u''_n + \frac{h^3}{3!}u'''_n + \ldots - u_n\right) \\ &= \frac{\partial u_n}{\partial t} + c\frac{\partial u_n}{\partial x} + \frac{ch}{2}\frac{\partial^2 u_n}{\partial x^2} + O(h^2) \end{aligned} \tag{12}$$

If in equation (12) we replace $u_n(t)$ by $U(x_n, t)$, the solution to (2), we obtain the following expression for the truncation error associated with the finite difference approximation (7):

$$\frac{ch}{2}\frac{\partial^2 U(x_n,t)}{\partial x^2} \tag{13}$$

Which implies that the forward difference approximation is only accurate up to $O(h)$. The physical properties of the difference approximation (7) as opposed to those of the original continuum equation (2) can be obtained by retaining the $O(h)$ error term in (12). We see that, rather than approximating the wave equation (2), the difference equation (7) is an approximation to the following partial differential equation

$$\left(\frac{\partial}{\partial t} + c\frac{\partial}{\partial x} + \frac{ch}{2}\frac{\partial^2}{\partial x^2}\right) u(x,t) = 0 \tag{14}$$

We observe that (14) is a backward heat equation - which is notoriously unstable for initial value problems. Thus we expect the forward difference approximation to yield an unstable numerical scheme. The fundamental flaw in the forward difference approximation stems from the fact that the information in the difference equations (7) is flowing from right to left, while for the original continuum equation the information is flowing from left to right.

Performing a Taylor expansion for the backward difference approximation we obtain:

$$\begin{aligned} 0 &= \dot{u}_n(t) + c\left(\frac{u_n(t) - u_{n-1}(t)}{h}\right) \\ &= \dot{u}_n + \frac{c}{h}\left(u_n - u_n + hu'_n - \frac{h^2}{2}u''_n + \frac{h^3}{3!}u'''_n + \ldots\right) \\ &= \frac{\partial u_n}{\partial t} + c\frac{\partial u_n}{\partial x} - \frac{ch}{2}\frac{\partial^2 u_n}{\partial x^2} + O(h^2) \end{aligned} \tag{15}$$

If in equation (15) we replace $u_n(t)$ by $U(x_n, t)$, the solution to (2), we obtain the following expression for the truncation error associated with the finite difference approximation (8):

$$-\frac{ch}{2}\frac{\partial^2 U(x_n,t)}{\partial x^2} \tag{16}$$

Which implies that the backward difference approximation is accurate up to $O(h)$. The physical properties of the difference approximation (8) as opposed to those of the original continuum equation (2) can be obtained by retaining the $O(h)$ error term in (15). We see that, rather than approximating the wave equation (2), the difference equation (8) is an approximation to the following partial differential equation

$$\left(\frac{\partial}{\partial t} + c\frac{\partial}{\partial x} - \frac{ch}{2}\frac{\partial^2}{\partial x^2}\right) u(x,t) = 0 \tag{17}$$

We observe that (17) is the convective heat equation - which is stable for initial value problems. Thus we expect the backward difference approximation to yield a stable numerical scheme provided the appropriate time stepping scheme is used. In this case stability is provided by the dissipative effect of the small diffusion term. As a result of this dissipation, we expect that energy will not be conserved by this difference approximation. In contrast to the situation for the forward difference approximation, the information in the case of the backward difference equations (8) flows from from left to right - the same direction as that for the original continuum equation (2). We will see that the classic Courant-Friedrichs-Lewy (CFL) stability condition for explicit time-marching of a given spatial semidiscretization boils down to requiring that the rate at which information can flow on the numerical mesh is faster that the rate at which information can flow physically.

Dispersive and dissipative properties of spatial semidiscretizations

In order to analyze the dispersive effects that are associated with the difference approximation (6) we use the following discrete Fourier transform pair (Vichnevetsky and Bowles 1982):

$$\begin{aligned} \mathcal{D}_f(u_n) = \bar{u}(\omega) &= h \sum_{n=-\infty}^{\infty} u_n e^{-inh\omega}, \\ u_n &= \frac{1}{2\pi} \int_{-\pi/h}^{\pi/h} e^{i\omega nh} \bar{u}(\omega). \end{aligned} \tag{18}$$

The discrete Fourier transform of a forward shift on the mesh is given by

$$\begin{aligned} \mathcal{D}_f(u_{n+1}) &= h \sum_{n=-\infty}^{\infty} u_{n+1} e^{-inh\omega} \\ &= h \sum_{m=-\infty}^{\infty} u_m e^{-i(m-1)h\omega} \\ &= e^{ih\omega} \bar{u}(\omega) \end{aligned} \tag{19}$$

Thus taking the discrete Fourier transform of (6) and using the shift property (19) we obtain the following ordinary differential equation for $\bar{u}(\omega, t)$:

$$\begin{aligned} \dot{\bar{u}} &= -\frac{ci}{h} \sin(\omega h) \bar{u} \\ &= -i \hat{A}(\omega) \bar{u} \end{aligned} \tag{20}$$

where $\hat{A}(\omega) = \frac{c}{h} \sin(\omega h)$.

The solution to (20) is given by:

$$\bar{u}(\omega, t) = \bar{u}(\omega, 0) e^{-i\hat{A}(\omega)t}. \tag{21}$$

Therefore using the expression for the inverse transform given in (18) we obtain

$$u_n(t) = \frac{1}{2\pi}\int_{-\pi/h}^{\pi/h} e^{i\omega\left(x_n - \frac{\hat{A}(\omega)}{\omega}t\right)}\bar{u}(\omega,0)d\omega. \tag{22}$$

Comparing (22) with (5) we can identify the phase velocity

$$C(\omega) = \frac{\hat{A}(\omega)}{\omega} = c\frac{\sin(\omega h)}{\omega h}$$

In contrast to (2) the speed of a signal moving through the discrete medium depends on the frequency ω of the signal. This phenomenon is known as dispersion. If the initial condition comprised a mixture of frequencies, then each of these frequencies move off with a different speed which depends on the frequency. After a long time we would expect to observe that an initial signal is split up into smaller groups of waves occupying distinct regions in space. The waves that belong to a particular group share frequencies that are close together. In order to locate these wave-packets we consider the limit as $t \to \infty$ in (22), which can be written in the form:

$$u_n(t) = \frac{1}{2\pi}\int_{-\pi/h}^{\pi/h} e^{i\left(\frac{\omega x}{t} - \hat{A}(\omega)\right)t}\bar{u}(\omega,0)d\omega, \qquad t \to \infty \tag{23}$$

In order to obtain an approximation to the above integral in this limit we define the phase function:

$$\phi(\omega) = \frac{\omega x}{t} - \hat{A}(\omega) \tag{24}$$

and observe that the complex exponential factor $e^{i\phi(\omega)t}$ acts as a carrier wave which is modulated by the function $\bar{u}(\omega,0)$. Consider an arbitrary point ω_0 within $[-\pi/h, \pi/h]$ and expand the phase function $\phi(\omega)$ in a Taylor series about this point. In this case

$$\begin{aligned} e^{i\phi(\omega)t} &= e^{i\phi(\omega_0)t}e^{i\{(\omega-\omega_0)\phi'(\omega_0)+\frac{1}{2}(\omega-\omega_0)^2\phi''(\omega_0)+\ldots\}t} \\ &\approx e^{i\phi(\omega_0)t}e^{i\{(\omega-\omega_0)\phi'(\omega_0)\}t} \text{ provided } (\omega-\omega_0)^2 t \ll 1 \end{aligned} \tag{25}$$

Now consider the contribution $I_t(\omega_0)$ to the integral (23) that comes from the small neighbourhood $|\omega - \omega_0| \sim 1/t \ll 1/t^{\frac{1}{2}}$:

$$\begin{aligned} I_t(\omega_0) &\approx \frac{e^{i\phi(\omega_0)t}}{2\pi}\int_{\omega_0-1/t}^{\omega_0+1/t} e^{i(\omega-\omega_0)\phi'(\omega_0)t}\bar{u}(\omega,0)d\omega \\ &\approx \frac{\bar{u}(\omega_0,0)e^{i\phi(\omega_0)t}}{2\pi}\int_{\omega_0-1/t}^{\omega_0+1/t} e^{i\{(\omega-\omega_0)\phi'(\omega_0)\}t}d\omega \text{ provided } \bar{u}(\omega,0) \text{ does not vary rapidly} \\ &\approx 0 \text{ due to the canceling effect of oscillations with the high frequency } \phi'(\omega_0)t \end{aligned} \tag{26}$$

Such an analysis can be carried out for each such point ω_0 in the interval $[-\pi/h, \pi/h]$ and we conclude that, due to such high frequency cancellations, the contribution to the integral

$u_n(t)$ is zero **except** for points ω_0 for which $\phi'(\omega_0) = 0$. Thus the major contribution to the integral comes form the immediate neighbourhood of the stationary points of the phase function $\phi(\omega)$ defined in (24). Differentiating (24) with respect to ω and equating the result to zero we obtain:

$$\begin{aligned} \phi'(\omega) &= \frac{x}{t} - \frac{d\hat{A}(\omega)}{d\omega} \\ &= \frac{x}{t} - c\cos(\omega h) = 0 \end{aligned} \tag{27}$$

Thus

$$x = c\cos(\omega h)t = G(\omega)t,$$

where

$$G(\omega) = \frac{d\hat{A}(\omega)}{d\omega}$$

is the *group velocity.*

In figure 1 the phase velocity ratio $C(\omega)/c$ and the group velocity ratio $G(\omega)/c$ are plotted for the central difference approximation (6). We observe that for the lower frequencies $\omega \approx 0$ the phase velocity of the central difference model (6) agrees well with the wave speed c of the partial differential equation (2). However, the phase velocities of the higher frequencies differ substantially from wave speed c. Since the wave speed for (2) does not depend on the frequency, there is no dispersion in the case of the partial differential equation. In contrast, it can be seen from figure 1 that the group velocity of the discrete equation (6) varies considerably over the range of frequencies $|\omega| \leq \pi/h$ that can be represented on a discrete mesh with spacing h. Indeed the group velocity for the frequencies in the neighbourhood of $|\omega| = \pi/2h$ (half the Nyquist frequency) is reduced to zero - so after some time we can expect to see a medium frequency wave group that remains fixed in space. The group velocity of frequencies close to the Nyquist frequency is $-c$ so we can expect to see a high frequency wave group moving with the opposite velocity to that of the solution for the partial differential equation (2). In figure 2 we plot the numerical solution of a square-wave pulse that is centered about the point $x = 13$ and follow its progress over a sequence elapsed time snapshots. The analytic solution (5) to the wave equation (2) will be a translation of the initial condition to the right at the wave-speed c. We observe that after some time the numerical solution that started out as the initial step-function has split up into groups or wave-packets. The stationary medium-frequency group at half the Nyquist frequency can be seen to remain at $x = 13$ throughout. The smaller amplitude Nyquist

frequency wave-packets can also be seen moving to the left - in the opposite direction to the exact solution. For all time-steps, the majority of the energy is still in the form of a low frequency wave-packet that moves to the right at the correct speed c. The amplitude of the various wave-packets depends directly on the frequency components that combine to make up the initial condition $U(x,0)$. To illustrate this point in figure 3 we plot time evolution of a Gaussian $U(x,0) = e^{-(x-12)^2/4}$ which is an analytic function and therefore has very small high frequency components. The numerical solution in this case is a very good model of the analytic solution and no noticeable numerical dispersion can be seen.

Unfortunately, in practical elastodynamic models high frequency signals will be common because of discontinuities in the form of fault planes or joints as well as impulsive loading conditions. The various spurious wave groups identified above are artifacts of the finite difference approximation. Naturally the amount of the energy that is trapped in the dispersive regime can be reduced by using a finer mesh - which unfortunately carries with it a concomitant computing cost. The effect of this numerical dispersion can also be alleviated to some extent by using higher order difference schemes or totally by using spectral methods to approximate the spatial derivatives. However spectral methods are more costly computationally and are not suitable for nonlinear problems and problems in which there are discontinuities such as faults or joints.

It is also interesting to note that (11) can be interpreted as a continuum model of the difference equation (6). Thus we would expect that the dispersive properties of (6) should be found in the continuum model too. To establish its dispersive properties we take the Fourier transform of (11) to obtain:

$$\dot{\hat{u}} = -ci(\omega - \frac{h^2}{6}\omega^3)\hat{u} \tag{28}$$

Solving for $\hat{u}(\omega,t)$ and using the inversion formula (3) we obtain the following expression for $u(x,t)$:

$$u(x,t) = \frac{1}{2\pi}\int_{-\infty}^{\infty} e^{i\omega[x-c(1-\frac{h^2}{6}\omega^2)t]}\hat{u_0}(\omega)d\omega \tag{29}$$

in which the phase velocity $C(\omega) = c(1-\frac{h^2}{6}\omega^2)$ is clearly a function of ω so that dispersive wave motion can be expected. In fact the phase velocity in (29) is just the first two terms in the Taylor expansion of the phase velocity of the difference equations given in (22).

If we consider a similar analysis of the continuum models of the forward and backward difference approximations (14) and (17) respectively, we obtain the following integral

representation of the solution:

$$u(x,t) = \frac{1}{2\pi}\int_{-\infty}^{\infty} e^{i\omega(x-ct)\pm\frac{ch\omega^2}{2}t}\hat{u_0}(\omega)d\omega \tag{30}$$

The plus sign in (30) holds in the case of the forward difference scheme and we see that the problem is ill-posed because the solution will blow up. The negative sign in (30) applies to the backward difference scheme so that the solution will decay with time due to the dissipative effect of the small diffusion term.

In order to see how the energy in the system evolves with time we apply Parseval's Theorem to the solution of the original wave equation

$$\begin{aligned}\int_{-\infty}^{\infty}|U(x,t)|^2dx &= \frac{1}{2\pi}\int_{-\infty}^{\infty}|\hat{U}(\omega,t)|^2d\omega \\ &= \frac{1}{2\pi}\int_{-\infty}^{\infty}|\hat{U}_0(\omega)e^{-ic\omega t}|^2d\omega \\ &= \frac{1}{2\pi}\int_{-\infty}^{\infty}|\hat{U}(\omega,0)|^2d\omega\end{aligned} \tag{31}$$

and we see that the energy in the system is conserved for all time. Applying Parseval's Theorem to the dispersive wave model (11) we see that the central difference scheme will also conserve energy for all time. While in the case of the forward and backward difference models we obtain

$$\begin{aligned}\int_{-\infty}^{\infty}|u(x,t)|^2dx &= \frac{1}{2\pi}\int_{-\infty}^{\infty}|\hat{u}(\omega,t)|^2d\omega \\ &= \frac{1}{2\pi}\int_{-\infty}^{\infty}|e^{i\omega(x-ct)\pm\frac{ch\omega^2}{2}t}\hat{u_0}(\omega)|^2d\omega \\ &= \frac{1}{2\pi}\int_{-\infty}^{\infty}|\hat{u_0}(\omega)|^2e^{\pm ch\omega^2t}d\omega\end{aligned} \tag{32}$$

Thus rather than conserving energy, the forward and backward difference models will exhibit exponential energy growth or decay respectively.

Stability properties of time-marching schemes

Once the spatial semidiscretizations have been established the numerical solution is typically determined by solving the system of ordinary differential equations governing the solution at each of the spatial meshpoints. The numerical schemes that have been developed to solve systems of ordinary differential can be used to solve these mesh based

ordinary differential equations. However, not all ODE solvers are appropriate for solving the semidiscrete systems. This is because a particular ODE solver may not be stable when the solution is marched forward in time. To illustrate this point we consider the following model problem:

$$\dot{\bar{u}} = \lambda \bar{u} \tag{33}$$

Equation (20) with $\lambda = -i\hat{A}(\omega)$ is a special case of this equation.

Let us assume that we were to use Euler's method

$$\bar{u}^{k+1} = (1 + \lambda \Delta t)\bar{u}^k \tag{34}$$

to solve (33). In order that the solution should not grow from one time step to the next (and so that round-off errors do not swamp the solution) we require that $\rho = (1 + \lambda \Delta t)$ should satisfy the condition:

$$|\rho| \leq 1 \tag{35}$$

In general λ can be a complex number, so the condition (35) implies that ρ should fall within the unit disk. The number λ can be considered known and fixed here (as it is determined by the ODE being solved or the spatial meshing of the semidiscretization if we are solving a partial differential equation). Thus the only parameter available to the user of an ODE solver to try to ensure that the stability condition (35) is satisfied is the parameter Δt. Indeed it is more useful to map the stability condition (35) into the $\lambda \Delta t$ plane. This is achieved by solving for $\lambda \Delta t$ in terms of ρ: $\lambda \Delta t = \rho - 1$. Under this mapping the unit disk centered at the origin is mapped onto the unit circle $|\lambda \Delta t + 1| \leq 1$ shown in figure 4. We observe that for the central difference semidiscretization (6) for which $\lambda = -i\frac{c}{h}sin(\omega h)$ is purely imaginary, there is no positive value of Δt for which $\lambda \Delta t$ will fall within the stability region. Thus Euler's method will be unstable no matter what stepsize we choose.

A method commonly used to time-march wave problems uses a central difference approximation in time. The so-called Leapfrog method applied to (33) assumes the form:

$$\bar{u}^{k+1} = \bar{u}^{k-1} + 2\Delta t \lambda \bar{u}^k \tag{36}$$

To investigate the stability properties of this difference equation we assume an exponential solution of the form:

$$\bar{u}^k = e^{i\theta k} \tag{37}$$

Substituting this solution into (36) we obtain the characteristic equation:

$$e^{i\theta} - 2\Delta t \lambda + e^{-i\theta} = 0 \tag{38}$$

or

$$\Delta t\lambda = isin(\theta) \tag{39}$$

This implies that the stability region for the Leapfrog method is given by the line segment between $-i$ and $+i$ on the imaginary axis as shown if figure 4. Thus if the Leapfrog method were used to time-march the central difference semidiscretization (6) then Δt will have to be chosen so that:

$$\lambda\Delta t = -i\frac{c}{h}sin(\omega h)\Delta t \in \text{the line from } i \text{ to } -i \tag{40}$$

which is satisfied provided:

$$\Delta t \leq \frac{h}{c} \tag{41}$$

This is the typical time-step stability criterion found in finite difference schemes that use central differences in space and time (e.g. WAVE). This is the classic CFL condition that states that the speed with which the information travels in the numerical approximation $\frac{h}{\Delta t}$ must be faster than the physical wave speed c.

References

Eringen A.C. and Suhubi E.S. (1975) *Elastodynamics: Volume II Linear Theory*, Academic Press, New York.

Vichnevetsky R. and Bowles J.B. (1982) *Fourier Analysis of Numerical Approximations of Hyperbolic Equations*, SIAM, Philadelphia.

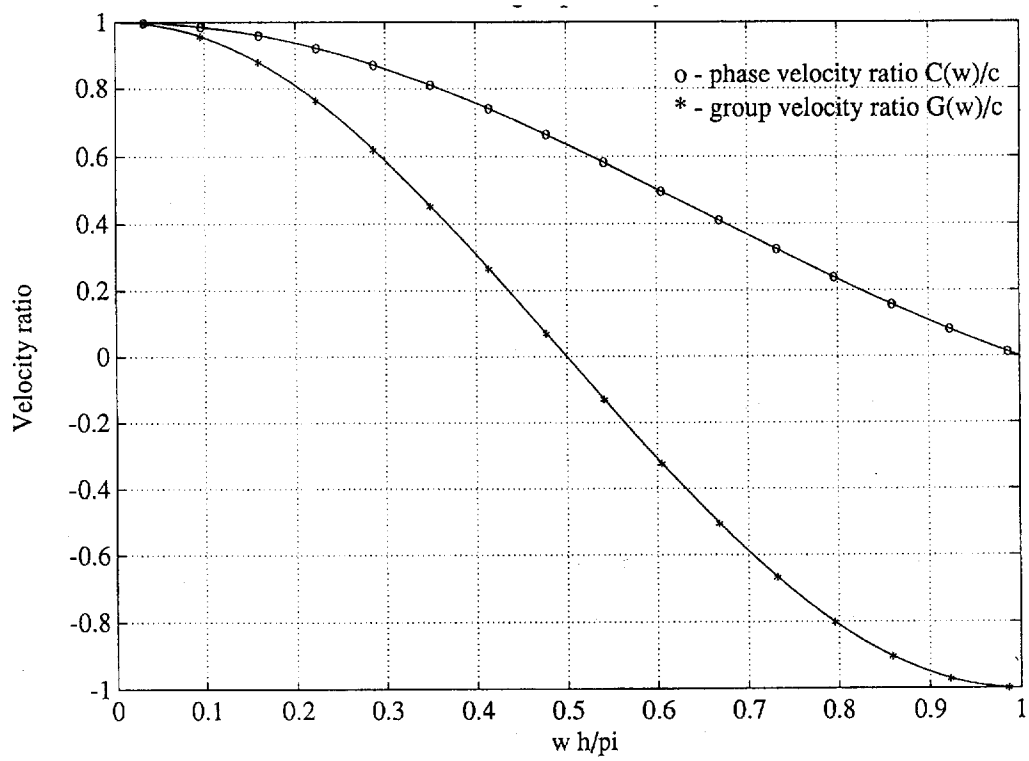

Figure 1: Phase and group velocity ratios

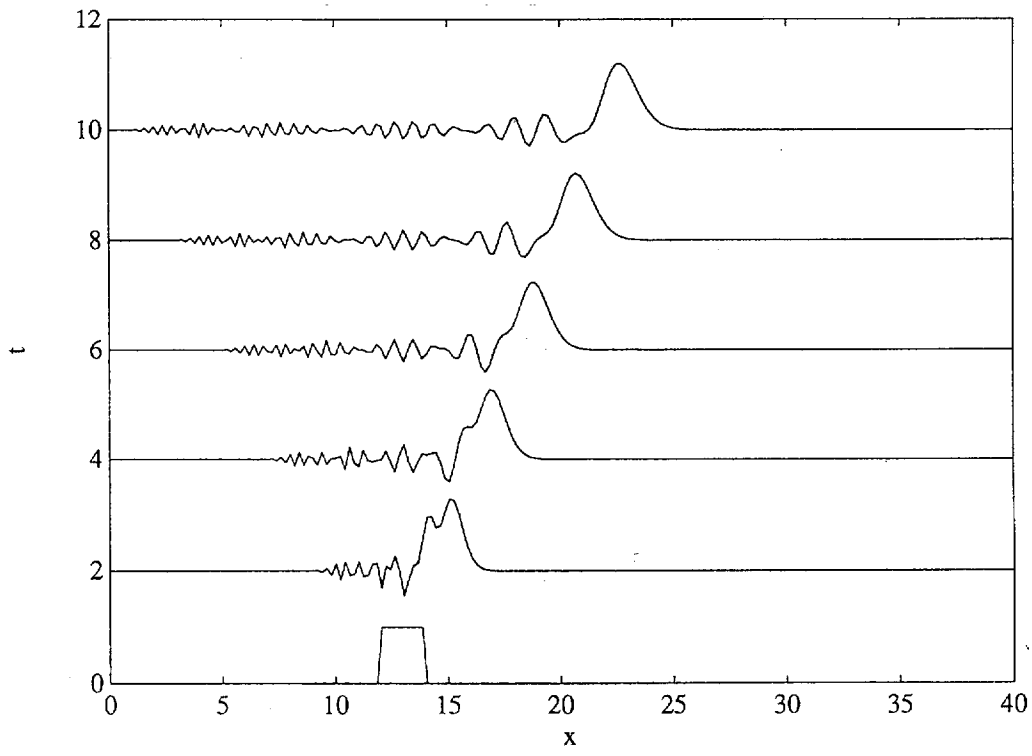

Figure 2: Emergence of wave groups due to numerical dispersion

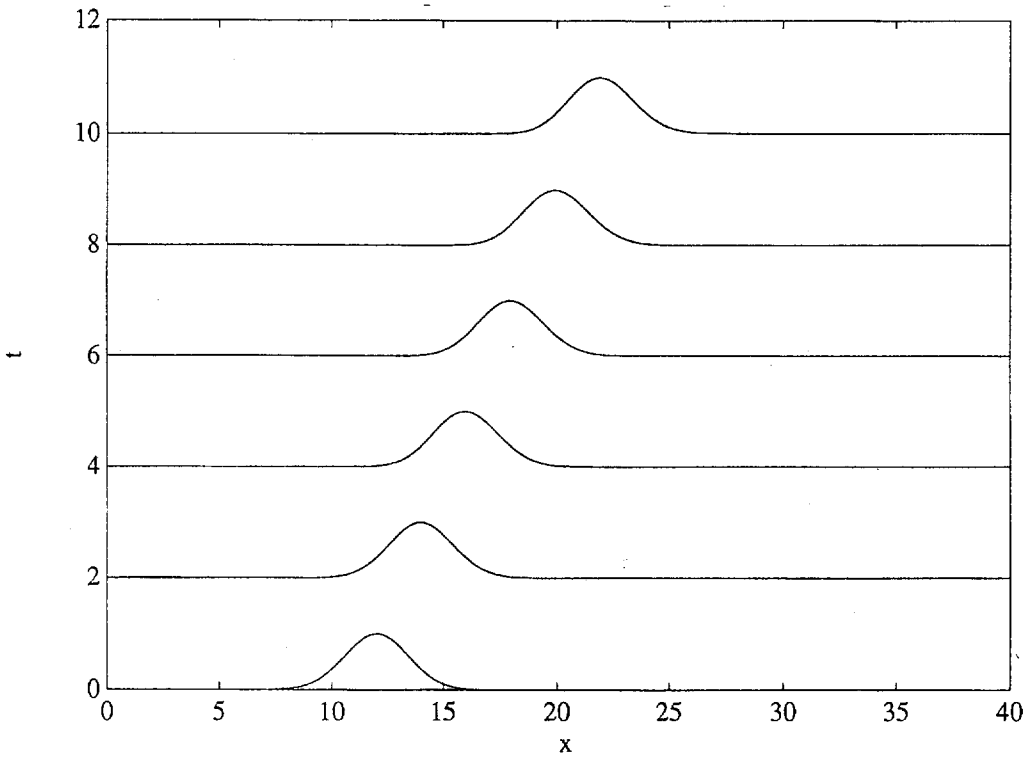

Figure 3: Limited numerical dispersion due to low frequency content of U(x,0)

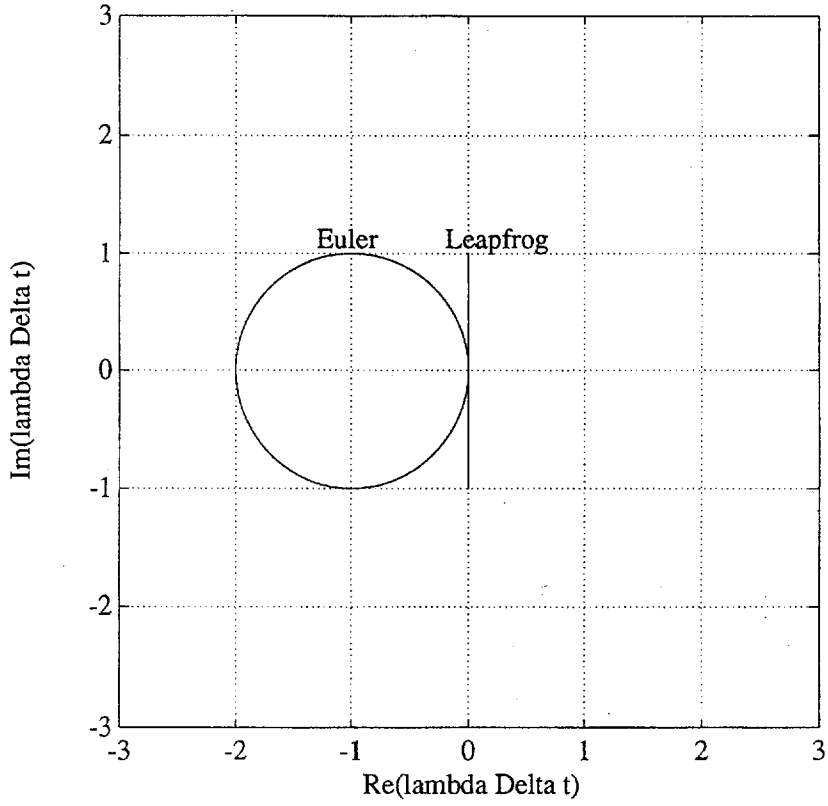

Figure 4: Stability regions

2.3 APPLICATIONS AND CASE STUDIES

This section covers case studies of how elastodynamic models have been applied to mining problems. The work ranges from investigating the effects of backfill in stopes, comparisons of fault slip models in two and three dimensions with empirical and theoretical results, the possibility of triggering a large event due to seismic wave propagation from an initial slip event and initial attempts at a full three-dimensional back-analysis of an actual rockburst. These contribute primarily to objectives 1.2, 1.3 and 1.4. This section also includes two reviews: a review of rockburst literature (objective 1.1) which aims to add insight in the investigation and representation of rockbursts and rockburst mechanisms, and a review of possible approaches in representing seismic wave propagation in the fracture zone of stopes (objective 1.5).

2.3.1 Literature Review on Rockburst Mechanisms

The purpose of this work was to summarize papers dealing with rockburst mechanisms (Objective 1.1). Some of the proposed mechanisms can then be tested by means of numerical modelling. The chronological summary is brief and incomplete, but it does provide insights into the way in which research into rockburst mechanisms has grown over the years. Some ideas for modelling work are suggested.

Chronological list of rockburst papers

Wood (1914): One of the first papers to recognize mining-induced seismicity on the Witwatersrand. Concludes that "... the tremors are semi-artificial in origin, and that the ultimate cause of them is to be found in the extraction of large amounts of rock....", and a suggested mechanism is "...slip by small amounts into positions of greater stability." During discussion on the paper, the President of the Chemical, Metallurgical and Mining Society notes that the tremors cannot always be correlated with (pre-existing) planes of discontinuity, and cites an example of a mining-induced fracture (with rockburst damage) of 100 m extent through a series of levels.

Allen (1931): Notes on observations of the effects of rockbursts and hangingwall behaviour at Robinson Deep. Induced fracture planes in the hangingwall and/or footwall are thought to be spaced more/less frequently as the face is more/less strong. Near remnant corners, the fractures are spaced more widely, because the face is not sufficiently strong to induce them, whereas near remnant centres, spacing is more dense. Concludes that, in order to have a burst, the surrounding rock mass must be sufficiently strong so that stress can be stored up until sudden failure occurs. A weaker rock mass would allow more frequent and safer fracturing. The suggestion is made that triangular remnants be mined so that their sides are concave to weaken the core more rapidly.

Altson (1933): Summarizes the different types of hangingwall control at that time. It is interesting to note that in the 1930s, backfill was thought to have a positive effect in terms of damping the vibrations caused by a burst.

Weiss (1938): Discusses elasticity, plastic flow or creep, elastic hysteresis, temperature and humidity effects, rock strength, rupture conditions, rockbursts, measurement techniques in prediction of rockbursts. One of the early papers to realize plastic effects in gold mines. Notes that creep implies differential pressures (up to that time, hydrostatic conditions had been assumed even though evidence showed otherwise). Elastic hysteresis is suggested to be a secondary cause of many bursts, because bursts only release a portion of the stress, and as mining proceeds, complete dissipation of stresses is not possible (hysteresis). Stresses accumulate with time, causing subsequent bursts. Moisture and temperature gradient is thought to act on fissures in rock, reducing elasticity of rock, resulting in flaking and spitting of exposed faces. It is suggested that use of an air- and water-tight paint could reduce spitting and flaking. Seismic wave velocity is said to be a function of applied stress. Areas of rock mass with lower wave velocity are therefore more highly stressed, and are areas of potential failure.

Anon (1943): Summarizes the presidential address of Jeppe to the Chemical, Metallurgical and Mining Society. Two generally postulated pressure burst theories were considered at that time: namely "dome" and "beam" theories. Beam theory used to explain remnant bursts as a fulcrum action at the face with tensile stresses ahead of the face. Any sudden failure in the hanging causes a reversal of stress ahead of the face, and pressure bursts can result. Advises using flexible support systems to cope with pressure bursts in tunnels.

Morrison (1948): A two part paper on a general theory of rock bursts. All aspects are explained in terms of a "dome" of fractured rock around an excavation. Suggests that this dome (elliptical shape around a stope) controls rock bursts. Sagging hangingwalls are only outward indications of the development of a fractured zone and its related dome. Notes that the size of opening versus depth of mining are inter-related - i.e. a shallow large excavation can experience more rock bursts than a deeper but smaller excavation. Notes that a grid system of pillar support, so as to shorten spans, is ineffective and worsens the situation. The stresses set up by such a system must ultimately overcome the resistance of individual domes in the process of building a single dome.

Spalding (1948): General observations about rock bursts. Suggests that rocks which consist of a single ingredient (e.g. quartz) are more likely to burst than agglomerates. Inhomogeneities and varying grain sizes cause plastic flow and result in progressive failure. More homogeneous rocks will tend to fail over a larger area and more violently when the elastic limit is reached.

Hill (1954): Notes a number of factors in relation to bursts that need to be investigated in order to determine their importance, viz. stoping method, face shapes, leads, percentage mining, spans, support types, closure amounts, closure rates, face advance rates, depth of workings, and geological features. Concludes that face lead/lags should be avoided, longwalling is better than scattered mining, acute angles of incidence should be avoided, dykes and faults have a pronounced effect on burst incidence, and blasting can act as a trigger. Other questions remained unanswered.

Roux and Denkhaus (1954): Divide bursts into extra- and intra-dosal types. Intradosal if source is within the fractured zone around the mining excavation, and extradosal otherwise. Extradosal bursts occur in abutments usually, but can trigger failure remote from the source as a result of accompanied movement in intradosal ground. Mentions destressing (natural or imposed) as a way to alleviate face bursting. Also suggests that creep or plastic deformations are partly responsible for causing rockbursts several hours after blasting.

Cook et al, (1966): 100 pages on all aspects of rockbursts. Summarizes research approach to rockburst problem as a four stage effort: 1) observations, 2) attach rational significance to documented experience and thereby develop hypotheses concerning certain aspects of rockburst problem, 3) combine hypotheses to postulate a rockburst mechanism consistent with observations, 4) design controlled experiments underground to test proposed

mechanisms, and eventually aim to minimize rockburst effects. The paper summarizes key observations, rock properties, elastic theory, and energy effects and concludes that the "existence or otherwise of the rockburst hazard depends on whether the geometrical rate at which energy must be released, is greater or smaller than the rate at which energy can be dissipated non-violently as the excavation is enlarged." Rockbursts are thus postulated to be manifested as a release of that part of the energy generated by the elastic closure which is not absorbed in strain energy and is in excess of that which can be absorbed in fracturing of rock and in friction along fractures. With respect to de-stressing of the face to alleviate rockburst conditions, the authors claim that it has almost no effect, and base their argument on the type of seismic wave radiated during preconditioning (compressional) versus during an event (shear). The argument is flawed, and one needs to look at the evidence for destressing, not at the type of wave radiated. In the discussion on the paper, Plewman suggests that two further breakthroughs are needed in order to understand more fully the rockburst problem: 1) a full understanding of in-situ fracturing processes and the behaviour of fractured materials, 2) an understanding of the dynamic loading processes and the behaviour of rock around stopes under dynamic loading.

Gay (1976): an excellent paper on experimental tests on blocks of quartzite and sandstone, containing circular or rectangular holes, and subjected to uniaxial and biaxial tests over long time periods. Experiments include the mining of slots while under load. Analysis of strain data showed that stresses built up in rock as the mining advance towards the measuring point, with sudden jumps in strain at each mining stage, followed by periods of creep. Fracture patterns that developed resembled those seen underground. As holes were enlarged (or confinement was increased) the following stages were noted: spalling, extension cracks, larger cracks outside spalling zone, steeply dipping cracks with shearing and accompanied collapse into holes.

Gay and Ortlepp (1979): microscopic observations suggest a sequence of development of fault surfaces:- development of extension cracks in the region of planes of maximum shear stress, coalescence of extension cracks to form conjugate shear planes, rapid movement along the more favourably oriented shear planes to form major gouge zones and feather fractures.

McGarr et al. (1979): a study of the seismicity and source parameters of tremors at E.R.P.M. Important facts noted were:

- stress drops of mine tremors and natural earthquakes invariably are low at 1 to 100 bars, regardless of source magnitudes; nearly all tremors at E.R.P.M, locate within 100 m of active faces (mining depth of 3 km);
- typical shear stresses in seismogenic area are 700 bars, which is an order of magnitude greater than the stress drops; - observed fault displacements are much larger than those predicted from Brune model;
- shear displacements are quite variable along faults suggesting an inhomogeneous slip mechanism involving high but localized stress drops;
- approximate time taken to create a shear fracture dynamically is limited by the dynamic deformations of the mine stope, because the interaction between the ambient stress field and the stope provides the strain energy to allow fracture to occur. It is thus suggested that the formation of a fracture is slowed down considerably compared to the rate for a fracture which occurred independently. Therefore, only a small fraction of the released energy is radiated seismically, and this explains the discrepancy between low stress drops and high shear stresses.

Rice (1980): all encompassing course on mechanics of earthquake rupture, covering topics such as elasticity, Green's functions, double couples, propagating shear sources, stress drops, fracture mechanics, elastodynamics, slip-weakeneing models, frictional slip, nonelastic materials, shear zones, pore fluid infiltration in cracks, dilatancy, etc. Notes that stress drops on enchelon crack systems of say 10 to 20 staggered cracks can be at least 5 to 10 times higher than on an equivalent single planar system. In terms of stickslip mechanisms, notes that the presence or absence of stick-slip can be explained by comparing the stress drops to the stiffness of the system.

Brink and O'Conner (1983): research into the prediction of rockbursts at Western Deep Levels gold mine. For cases investigated, results show that seismic events within the local area monitored were preceded by an increased level of microseismicity, which concentrated in the zone of eventual failure. There was usually a short-lived marked drop in activity immediately prior to the event.

Salamon (1983): Summary of progress made until 1983 in developing effective face support, good layout design, and control of convergence volume as ways of alleviating the rockburst hazard. Mechanism: Seismic energy released in a region is much less than energy released by

mining (0.1% efficiency), which raises the question of what causes a rockburst (clearly not correlated with ERR). Salamon notes that a small mining step can cause a large rockburst, which implies that either the rock mass must be discontinuous, or the rock must become an unstable material under certain loads. Suggests that alleviation of rockbursts can be accomplished through better layout design, reduction in stoping width, use of backfilling, partial extraction, and improved support systems.

Cook (1983): "Origin of Rockbursts" paper: Conceptual model of fracture zone (needed in order to understand origin of rockbursts) around a stope is presented, based on practical, theoretical and experimental work. Three types of fractures are postulated: cleavage (tensile failure), inclined shear, and vertical shear fractures. Vertical fractures are suggested to be more likely candidates for the origin of rockbursts. Cook suggests a cycle of cleavage, accompanied by dilatancy, which increases confining stresses and stops cleavage, followed by inclined shear (after sufficient build up of confinement), which reduces confining stresses, followed by cleavage again. This process continues with advance of the stope face. The inclined shear direction coincides with Mohr-Coulomb planes of failure. The vertical shear fractures develop along the line of maximum stress difference, on a plane through the stope face. Cleavage is not possible here because of high confinement.

Gay et al. (1984): correlate seismicity with geology and mining in order to better understand origin of large mining-induced seismic events. Gay stresses the importance of faults and dykes - stiffer properties of dykes allows more energy to be stored up, and more chance of brittle failure. He mentions that the in situ stress field in the Klerksdorp area is such that large deviatoric stresses are present, capable of causing movement along faults and dykes. Mining activity disturbs this potentially unstable stress field, with the result that the generation of large events is quite possible in large volumes of rock.

Piper (1984): Experimental investigation into propagation velocities of rock fragments into mining excavations during a rockburst situation. Initial propagation velocities of 50-55 m/s were required to cause penetration of pipe coatings.

Gay and Jager (1986): The section of the paper dealing with rockbursts notes that the violent energy released during a rockburst is due to falling rock fragments, enhanced stresses induced in rock by mining, and residual stresses stored up by tectonics. Most events are near mining activity, but some are remote, and these are due to geology.

Brehaut and Hedley (1987): Annual report of Canada-Ontario-Industry Rockburst project. Strain bursts, pillar bursts and fault-slip are identified as the three main mechanisms. The authors suggest that the explosive energy liberated during a rockburst comes from the surrounding rock mass and not from the failing structure. The violence of the failure is controlled by the stiffness of the loading system. During rock failure, the released energy which is liberated seismically varies with different mechanisms (low for fault slip, high for pillar bursts). Destressing of pillars by blasting is found to alleviate the rockburst problem in Ontario,

Lenhardt (1988): investigations into influence of geology on seismicity. In one case study on Peggy dyke, two events within five hours of each other occurred on the same dyke. The two events located about 300 m away from each other along the dyke and the sense of shear was opposite. This indicates that slip along fault-like structures is an inhomogeneous process, and that the sense of slip is not always governed purely by what would be expected from excess shear stress lobes.

Petit and Barquins (1988): Carried out experiments to investigate whether a planar defect can propagate in its own plane under mode II conditions, as supposed by classical rupture mechanics models, and in particular, whether mode II can be an elementary fracture mechanism. Results suggest that mode II cannot exist as an elementary fracture mechanism, but can only be a macroscopic feature which must necessarily involve mode I failure. A shear zone involving mode I fractures, can propagate in the direction of the defect if a positive but low confining stress exists to inhibit branch fractures, and if a very dense population of defects is present. At depth, with increasing pressure and temperature, mode II shear can develop from preexisting joints as long as these joints are oriented in the direction of maximum shear stress.

Singh (1989): outlines an approach for defining rockburst prone regions in mines. A knowledge of various bursting indices, rock properties, in-situ approaches, geological features, mining conditions, and observations can be used to facilitate classifying mine workings according to their proneness to bursting. A "decrease modulus index" shows correlation with a "burst proneness index", strength, brittleness, and strain energy stored in the rock. Burst proneness is shown to depend on the Schmidt rebound hardness test and the shear wave velocity of the rock.

Tanimoto and Ikeda (1983): Studied relationships between wave velocities, fracture frequency, aperture size, moisture content, contact pressure on joints. Results indicate that an aperture wider than 1 mm and a decrease of contact pressure to less than 3 MPa markedly influence the seismic behaviour of the rock mass.

Lenhardt (1989): Seismic event mechanisms at Western Deep Levels gold mine. Geological features (dykes, faults), abutments, pillars are high risk areas for large events. Smaller events tend to be more blasting related. Suggested cures are to alter mining layouts (e.g. oblique mining towards a dyke), preconditioning or triggering of an impending event, and backfill (to effectively decrease stope width).

Ortlepp (1990): overviews the rockburst problem in RSA, and compares with El Teniente mine in Chile. Suggests that the best way to understand rockbursts is via seismic research. Such research and studies of rockburst damage should be used to develop guidelines (in Chile) for improved layouts and sequences to minimize the frequency of rockbursts, and for improved criteria for design of support to reduce damage to workings.

Huang and Turcotte (1990): Investigation into whether earthquakes are deterministically chaotic. A simple stick-slip friction law on a two block mass-spring system is used under static and dynamic conditions. Results show that with a simple static/dynamic friction law, spatially inhomogeneous frictional strength is a necessary condition for the occurrence of deterministic chaos. Chaotic behaviour was (apparently) also observed with a velocity weakening friction law. The applicability of a spring-block model is questioned, but it is considered possible that more realistic earthquake models can also exhibit chaotic behaviour under a static/dynamic friction law.

Adams, Hemp and Spottiswoode (1990): studied the influence of backfill on ground motion. Found, amongst other things, that dominant frequencies are higher in backfilled stopes than in unfilled stopes, vibration times are reduced with increased backfilling, backfilling layout can cause amplifications of waves in some areas, but these amplifications are apparently not likely to be greater than the waveforms resulting due to unfilled stopes.

Knoll and Kuhnt (1990): From investigations in GDR, claim that rockbursts can be divided into two types - mining rockbursts, associated with immediate mining activities, and tectonic rockbursts, associated with tectonic conditions around the mine and large scale stress redistributions around the mine. Analysis of seismic records by spectral analysis shows that

there are different scaling laws for the seismic moment and source radius for the two types of rockbursts. It is proposed that, according to the seismologically indicated type of rockburst, appropriate measures can be taken to limit the effects of rockbursts in a mine.

Johnston and Einstein (1990): A survey of mining associated seismicity in a number of countries. An attempt is made to sort events into two types. Type I: seismicity linked directly to mining and geometry. Type II: seismicity occurring on faults, more similar to earthquakes. Six mechanisms of failure are identified: (a) ore extruded because of high vertical stress from overburden, (b) roof collapse, (c) slip along faults, (d) fracture of intact rock ahead of advancing face, (e) fracture at the face from stress concentrations, (f) pillar bursting. Claim that (d). (e) and (f) produce rockbursts.

Gibowicz (1990): Reviews types of mine tremors, double couple vs non double couple mechanisms, moment tensors, seismic source modelling, source parameters, scaling, attenuation and scattering. Notes that rockburst behaviour is erratic, in that large tremors do not necessarily generate rockbursts, whereas small events can cause considerable damage. Quotes Salamon (1983): "Virtually no systematic research has been done to elucidate the basis of setting apart those seismic events which become rockbursts and those which do not". However, seismic parameters can give clues as to mechanisms. For instance, high stress drops often have simple pulses with well defined corner frequencies, steep fall offs, whereas low stress drop events often are more complex. Large tremors with low stress drop events are often associated with faults (double couples), and have large source sizes. Large events with high stress drops are often due to failure of relatively intact rock (single couples), and have smaller source sizes. Suggests that source modelling in time domain could provide insight into double couple vs single couple mechanisms.

Muller (1991): Used FLAC to model rockbursts in a coal seam. In order to generate a violent failure, an asperity was needed (e.g. zone of higher friction). Sliding bursts required sliding along zone of previously enhanced friction, and pillar bursts required zone of previously enhanced strength.

King (1991): Conducted a laboratory scale fault experiment, where 8 blocks connected by springs are driven to slide on a frictional surface. Suggests that frictional sliding may be chaotic. Also, rupture initiation points are not generally near maximum slip points.

Ortlepp (1992): Elaboration on "rock-flour" of rhombic dodecahedral shape that forms part of the comminuted filling in shear fractures (visible under scanning electron microscope in some samples. Suggests that this is evidence of shock rebound phenomena during a rockburst, because such shapes can only form by rapid unloading. Implication for rupture mechanism is that this evidence implies that the formation of a pristine fault by a shearing action is a more violent and less homogeneous process than was previously thought possible.

Mendecki (1993) describes a concept of "quantitative real-time seismology in mines". Defines quantitative as a reliable knowledge of source parameters beyond timing and location, such as seismic moment, radiated seismic energy and stress drop. Real-time implies immediate seismic processing and response to certain conditions. Proposes guidelines for 'qualitative' assessment of the stress and strain regime, from a 'quantified' description of microseismicity. Suggests a number of relationships between apparent stress and level of stress or rock strength, and between the rate of coseismic inelastic deformation and expected seismic events.

Van Aswegen and Butler (1993) apply the above relationships to detect variation in rock mass behaviour in the Welkom gold-mining area. Relationships highlighted are:

- energy index (E_i), defined as the ratio of energy to the average energy for events of the same moment, indicates the state of stress
- ratio of the energy index for S-waves and for P-waves, indicates the source mecanism, whether fault slip events or dyke/pillar events.
- positions of asperities (potential large events), are identified by small events with relatively high apparent stress
- cumulative apparent volume scales the volume of non-elastic strain of the source - deviation in this slope reflects anomolous rockmass behaviour prior to major events.

Conclusions

A number of ideas on rockburst mechanisms, raised in the aforegoing summary, can be tested out or confirmed using numerical modelling. What does slip really look like in time and space on a fault surface (Wood 1914)? Can blasting act as a trigger for rockbursts (Hill 1954)? How significant an effect do plasticity and creep have on triggering events hours or days after blasting (Roux and Denkhaus 1954)? Is it possible to trigger large events with low stress drops (McGarr 1979 and Salamon 1983)? Under what conditions is the slip mechanism

non-homogeneous (McGarr 1979)? How different are echelon to planar fault systems in statics and dynamics (Rice 1980)? Are vertical fractures more likely candidates for slip than other orientations (Cook 1983)? What effect does fault or dyke stiffness have on the amount of slip (Gay et al. 1984)? Under what conditions does the sense of slip become non-homogeneous on a particular fault (Lenhardt 1988)? Are faults always chaotic in behaviour (Huang and Turcotte 1990, and King 1991)?

Future investigations of elastodynamic modelling will attempt to explain these phenomena in terms of explicit failure and slip mechanisms.

REFERENCES

Anon, (1943) 'Problems of pressure bursts'. *S.A. Mining Review*, Vol 74, pp 65-68.

Adams D.J., Hemp D.A. and Spottiswoode S.M. (1990) 'Ground motion in a backfilled stope during seismic events', in: *Static and Dynamic Considerations in Rock Engineering* (ed: R. Brummer), Balkema, Rotterdam, pp 13-22.

Allen W. (1931) 'Notes on recent observations of remnants'. *J. Chem. Metall. and Mining Soc. of S.A.* XXXII, pp 1-5.

Altson B.T. (1933) 'Hangingwall control in deep level mines on the Witwatersrand - its ultimate effect on maximum ore extraction'. *Assoc. of Mine Managers of the Transvaal (Inc),* June, pp 61-114.

Brink A.v.Z. and O'Conner D.M. (1983) 'Research on the prediction of rockbursts at Western Deep Levels', *J. S.A. Min. Metall*, vol 83, pp 1-10.

Brehaut C.H. and Hedley D.G.F. (1987) '1986-1987: Annual report of the Canada-Ontario-Industry Rockburst project'. *CANNET special report SP 87-7E.*

Cook N.G.W. (1983) 'Origin of rockbursts', in: *Rockbursts: Prediction and Control,* Inst. Min. and Metall, London, pp 1-9.

Cook N.G.W., Hoek E., Pretorius J.P.G., Ortlepp W.D. and M.D.G. Salamon M.D.G. (1966) 'Rock mechanics applied to the study of rockbursts'. *J. S.A. Inst. Min. and Metall.*, pp 435-528, discussion pp 695-714.

Gay N.C. (1976) 'Fracture growth around openings in large blocks of rock subjected to uniaxial and biaxial compression', *Int. J. Rock Mech., Min. Sci. and Geomech. Abstr.*, Vol 13. pp 231-243.

Gay N.C. and Jager A.J. (1986) 'The influence of geological features on problems of rock mechanics in Witwatersrand mines', in: *Mineral deposits of Southern Africa,* (eds: C.R. Anheuser and S. Masks), Geol. Soc. S.A.

Gay N.C. and Ortlepp W.D. (1979) 'Anatomy of a mining-induced fault', *Geological Society of America,* Part I. 90, pp 47-58.

Gay N.C., Spencer D., van Wyk J.J. and van der Heever P.K. (1984) 'The control of geological and mining parameters in the Klerksdorp gold mining district', proc: *1st Int. Congress on Rockbursts and Seismicity in Mines,* (eds: N.C. Gay and E.H. Wainwright), Johannesburg, 1982, SAIMM, pp 107-120.

Gibowicz S.J. (1990) 'Keynote Lecture: The mechanism of seismic events induced by mining', *Rockbursts and Seismicity in Mines* (ed: C. Fairhurst), Balkema, Rotterdam, 1990, pp 3-27.

Huang J. and Turcotte D.L. (1990) 'Are earthquakes an example of deterministic chaos?', *Geophys. Res. Letters,* vol 17, pp 223-226.

Hill F.G. (1954) 'An investigation into the problem of rockbursts. An operational research project', *J. Chem., Metall. and Mining Soc. of S.A.*, Oct and Nov 1954, pp 63-83.

Johnston J.C. and Einstein M.H. (1990) 'A survey of mining associated seismicity', in: *Rockbursts and seismicity in Mines* (ed: C. Fairhurst), Balkema, Rotterdam, pp 121-125.

King C-Y. (1991) 'Multicycle slip distribution along a laboratory fault', *J. Geophys. Res,* vol 96, pp 14,377-14,381.

Knoll P. and Kuhnt W. (1990) 'Seismological and technical investigations of the mechanics of rock bursts', in: *Rockbursts and Seismicity in Mines,* (ed: C. Fairhurst), Balkema, Rotterdam, pp 129-138.

Lenhardt W.A. (1988) 'Some observations regarding the influence of geology on mining induced seismicity at Western Deep Levels', proc: *SANGORM Symp. on Rock Mechanics in Africa, 1988,* pp 45-48.

Lenhardt W.A. (1989) 'Seismic event characteristics in a deep level mining environment', in: *Rock at Great Depth* (ed: Maury and Fourmaintraux), Balkema, Rotterdam, pp 727-732.

McGarr A., Spottiswoode S.M., Gay N.C. and Ortlepp W.D. (1979) 'Observations relevant to seismic driving stress, stress drop, and efficiency', *J. of Geophysical Research,* vol 84, pp 2251-2261.

Mendecki, A.J. (1993). Keynote address: Real time quantitative seismology in mines, in: *Rockbursts and Seismicity in Mines* (ed. Young), Balkema, Rotterdam, 287-295.

Morrison R.G.K. (1948) 'A general theory of rock bursts', *Eng. and Mining J.*.Part I, vol 148, pp 70-73.

Morrison R.G.K. (1948) 'A general theory of rock bursts', *Eng. and Mining J.* Part II, vol 149, pp 68-70.

Muller W. (1991) 'Numerical simulation of rock bursts', *Mining science and Tech,* vol 12, pp 27-42.

Ortlepp W.D. (1990) 'Rockbursts: An overview of the problem in South Africa and a comparison with some rockbursts at El Teniente mine', *A.A.C. Gold and Uranium Div. report 014/23 April 1990.*

Ortlepp W.D. (1992) 'Note on fault-slip motion inferred from a study of micro-cataclastic particles from an underground shear rupture', *unpublished material.*

Petit J-P. and Barquins M. 'Can natural faults propagate under mode II conditions?', *Tectonics,* vol 7, pp 1243-1256.

Piper P.S. (1984) 'Analysis of rockburst damage at Durban Roodepoort Deep Limited', *COMRO report.*

Rice J.R. (1980) 'The mechanics of earthquake rupture', in: *Physics of the Barthos interior,* proc: Int. School of Physics "Enrico Fermi", course 78, 1979, (eds: Dziewonski and Boschi), Italian Physical Soc., North Holland pp 555-649.

Roux A.J.A. and Denkhaus H.G. (1954) 'An investigation into the problem of rock bursts, An operational research project', *J. Chem, Metall. and Mining Soc. of S.A.*, pp 103-124.

Salamon M.D.G. (1983) 'Rockburst hazard and the fight for its alleviation in South African gold mines', in: *Rockbursts: Prediction and Control,* Inst. of Min. and Metall, London, pp 11-36.

Singh S.P. (1989) 'Classification of mine workings according to their rockburst proneness', *Mining Science and Tech.*, vol 8, pp 253-262.

Spalding J. (1948) 'Observations on rock bursts'. *Engng. and Mining J.,* vol 149, pp 91-93.

Tanimoto C. and Ikeda K. (1983) 'Acoustic and mechanical properties of jointed rock', *5th Int. Congr. on Rock Mechanics*, Melbourne, 1983, A.A. Bell, Rotterdam, vol 1, pp A15-A18.

Van Aswegen G. and Butler A.G. (1993). Applications of quantitative seismology in South African gold mines, *Rockbursts and Seismicity in Mines,* (ed. Young), Balkema, Rotterdam, pp 261-266.

Weiss 0. 'The theory of rockbursts and the possibilities of geophysical methods in predicting rockbursts on the producing mines of the Witwatersrand', *J. Chem., Metall. and Mining Soc. of S.A,* vol 38, pp 273-329.

Wood H.E. (1914) 'The Witwatersrand earth tremors', *J. Chem. Metall. and Mining Soc. of S.A.,* vol 14, pp 423-427.

BIBLIOGRAPHY

Bibliography of Rock Bursts (1991), Part 1 (1900-1979), (eds: I.M. Petukhov and I.M. Batugina). Balkema, Rotterdam, 308 pages.

2.3.2 Backfill Analysis

TWO4D and WAVE were applied to consider the importance of backfill in the dynamic behaviour of stopes. The evaluation involved comparing the overall dynamic motions in a stope as well as the convergence and ride responses near the face, for filled and unfilled stopes. The differences due to backfill were small if a homogenous elastic rock mass was assumed. However, if the presence of the fracture zone was represented in some manner, significant effects due to backfill were observed. These effects included a reduction in both the duration of the dynamic activity and in the peak particle velocities in the vicinity of the stope. This compared qualitatively with conclusions reached from underground seismic measurements. No attempt was made to carry out a quantitative comparison with actual seismic data. This work is presented in a paper by Siebrits, Hildyard and Hemp (1993). The study contributes to objectives 1.3 and 1.4. of the project plan.

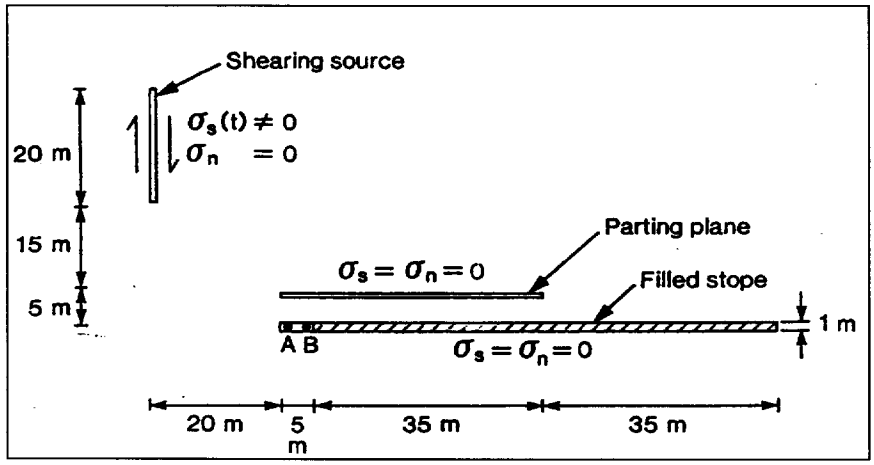

Fig 2.3.2.1: Model geometry showing positions of the stope, source and parting plane

The model considered was a simple two-dimensional stope with a twenty metre slip event, twenty metres ahead of the face and twenty metres into the hangingwall. The fracture zone was represented in three different ways:

- an (open) parting plane five metres in the hangingwall
- a ten metre elastic softened zone with a reduced bulk modulus of 60% and a reduced shear modulus of 20%, relative to the rock-mass. There was no attenuation or scattering in this softened zone.

- a parting plane five metres in the hangingwall in a static stress field, which could open/ close under the combined static and dynamic loading.

In all cases the elastic constants in the rock mass were E = 85GPa, ν = 0.19 and ρ = 2700kg/m^3. Backfill was represented by linear normal and shear stiffnesses of 400 MPa/m and 200 MPa/m, with the stope filled to within five metres of the face.

Figure 2.3.2.1 shows the model geometry for the case where the fracture zone is represented by a single open parting plane. The convergence velocity envelopes for this geometry without the parting plane (i.e. a purely elastic rock-mass) are compared for a filled and an unfilled

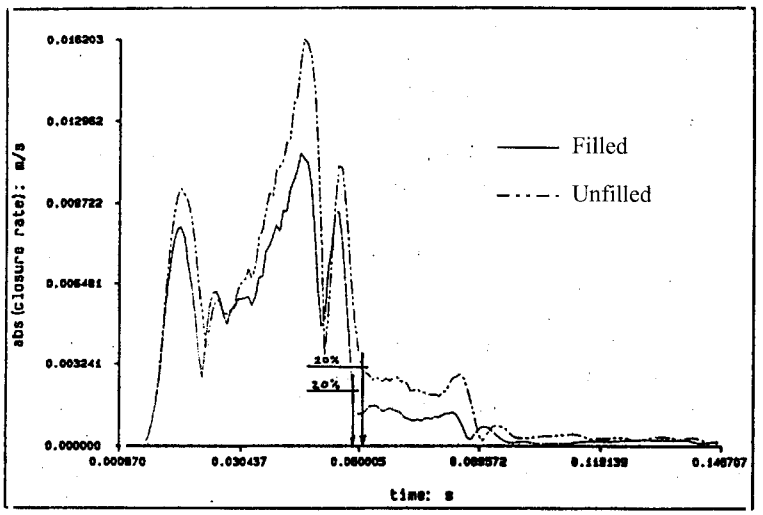

Fig 2.3.2.2:Convergence velocity envelopes for unfilled and filled stopes with no parting plane

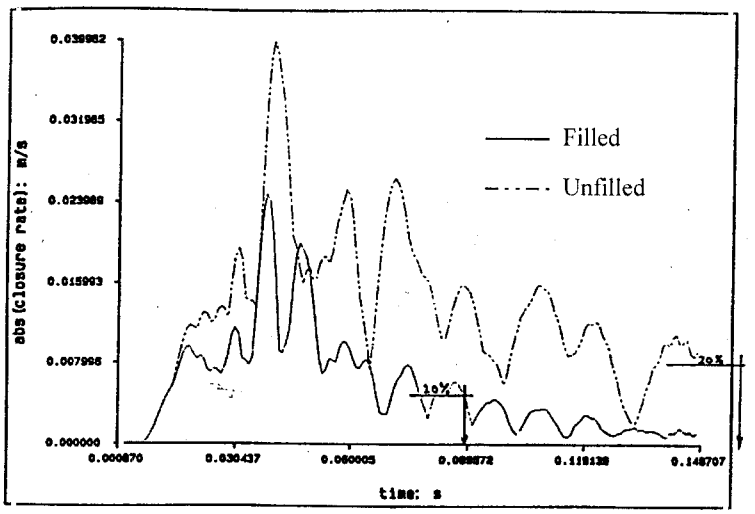

Fig 2.3.2.3: Convergence velocity envelopes for unfilled and filled stopes with a parting plane

stope in figure 2.3.2.2. In this case the fill causes only a small reduction in the convergence velocities. Figure 2.3.2.3 shows the same envelope comparison when the parting plane is introduced, showing that the overall dynamic motions are significantly reduced when the stope is filled.

Figure 2.3.2.4 shows the model geometry when the fracture zone is represented by a 10 metre zone of softened elastic material. In this case a greater effect is noticed on the ride velocities than on the convergence velocities, and figure 2.3.2.5 compares envelopes of ride velocities for unfilled and filled cases. The third (dotted) graph represents a bounding case with extreme values for the backfill, with a normal stiffness of 2GPa/m and a shear stiffness of 1 Gpa/m.

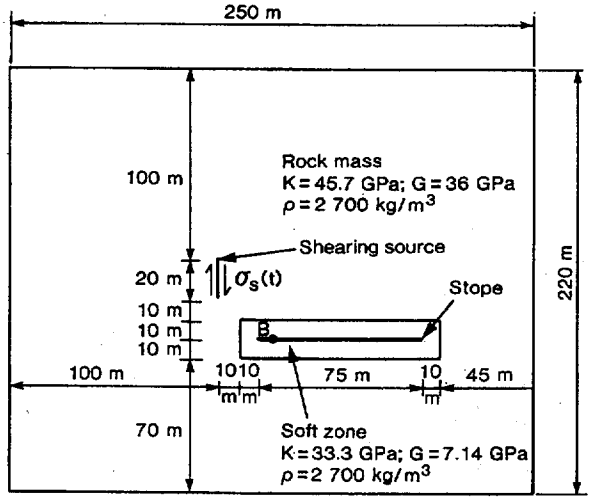

Fig 2.3.2.4: Model geometry introducing an elastic softened zone

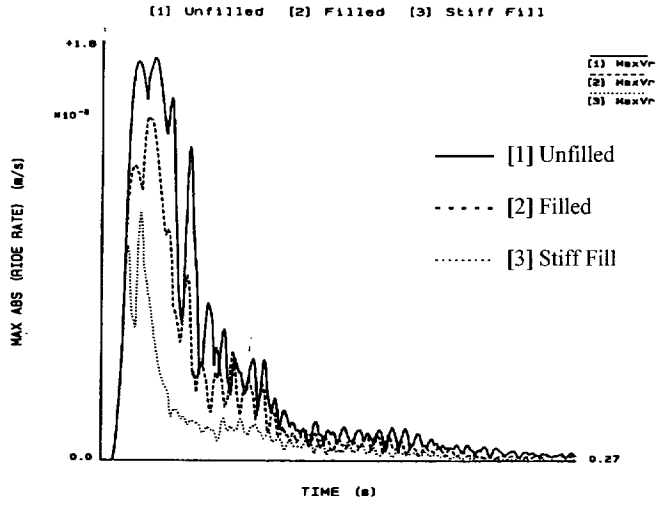

Fig 2.3.2.5: Ride velocity envelopes for unfilled, filled and stiffly-filled stopes with softened zone

The third representation of the fracture zone allows for the effects of differences in the initial static condition. The opening-closure logic in WAVE has since been improved, but no further experiments have been done. However this is an important facet of the work, since for example, the clamping stress on a crack has a significant influence on the transmission of waves, and hence on the transmission and trapping of waves in the stope area (cf section 2.4, photo-elastic experiments).

It was evident in this work that backfill can have a significant influence on the dynamic motions in stopes in spite of its relatively low stiffness, due to the effects of the fracture zone. The representation of the fracture zone was however crude, and further work should be done to implement more realistic representations of the fracture zone, either volumentrically or through explicit fractures. Differences in the initial state prior to the event can be an important consideration. It was also noted that more information is needed on the dynamic behaviour of backfill and other support.

REFERENCES

1. Siebrits E., Hildyard M.W. and Hemp D.A. (1993). 'Stability of backfilled stopes under dynamic excitation'. *Proc: 3rd Int. Symp. on Rockbursts and Seismicity in Mines,* Aug 1993, pp 117-121.

2.3.3 Comparisons between *WAVE* and seismological data

This work contributes towards SIMRAC objectives 1.2 and 1.3.

The correlation of numerically predicted elastodynamic ground movements and seismological field data was investigated in order to assess the suitability of the *WAVE* program for the modelling of mining related problems. An elastodynamic finite difference program, *WAVE* has been used to compare fault slip and the resulting wave propagation with seismological data. Peak particle velocities calculated by *WAVE* are correlated with analytical models and seismic field studies.

The objectives of this investigation are:

1. To model fault slip and wave propagation in two- and three-dimensions.

2. To determine the effect of reducing fault cohesion according to a slip-weakening law.

3. To compare the far-field peak particle velocity attenuation calculated by *WAVE* with that of the analytical model of Brune (1970/1971) and the empirical relationship of McGarr (1984).

The *WAVE* model

A 60 m span horizontal stope is assumed to be subjected to a stress field at a depth of 2600 m below surface of 70 MPa in the vertical and 35 MPa in the horizontal directions. The stress field interacts with the stope and generates the zero excess shear stress (ESS) contour (Napier 1987, Ryder 1988) is depicted in figure 2.3.3.1. The ESS can be defined as the difference between the prevailing shear stress prior to slip and the dynamic strength of the fault plane. Thus,

$$ESS = |\tau| - \mu\sigma_n ,$$

where $\mu = \tan\phi$ and ϕ is the friction angle, τ is the shear stress and σ_n is the normal stress acting across planes of weakness in an assumed orientation. In this study the friction angle on the fault interface is assumed to be 10 degrees. A vertical fault is situated ahead of the stope and, with no cohesion on the fault interface, the section of the fault contained within the zero ESS contour will rupture.

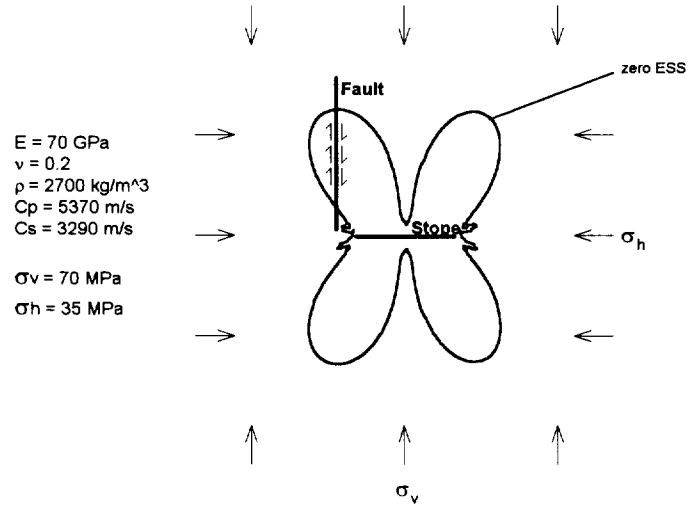

Figure 2.3.3.1 The two-dimensional *WAVE* model, where E is Young's modulus, υ is Poisson's ratio, ρ is rock density, and C_p and C_s are respectively the P- and S-wave velocity.

WAVE is a finite-difference code which is able to simulate wave propagation in a two- or three-dimensional elastic medium. To do this second-order interlaced finite-difference equations are used on an orthogonal grid of uniform spacing. *WAVE* has the ability to model dislocations which can represent faults or tabular stopes.

The *WAVE* analyses are completed in two steps:

- In Step 1, the fault is locked by the application of a high cohesion to the interface, the external stress field is applied, and *WAVE* is cycled until the stope reaches an equilibrium closure when the maximum velocities in the finite difference mesh are negligible.

- In Step 2, the fault cohesion is reduced and the fault ruptures. Fault cohesion is either set to zero instantaneously, resulting in sudden fault rupture along the length of the fault situated within the zero ESS lobe, or a slip-weakening law is applied to the fault interface. In the latter case, the cohesion along the whole fault is reduced such that slip just commences at a point on the fault. As slip occurs at this point, the cohesion is reduced linearly as a function of the slip (figure 2.3.3.2), and shear stress is increasingly transferred to adjacent grid points until they slip. Thus, by the application of a slip-weakening law to the fault interface, fault slip occurs progressively away from the initial point of rupture. A progressive fault-rupture model is considered to be more realistic than an instantaneous fault-rupture model.

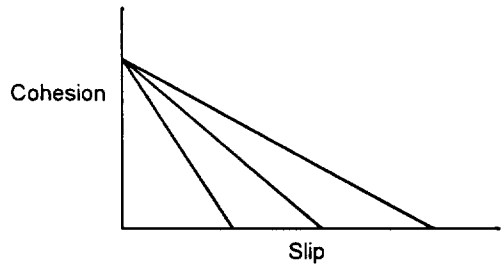

Figure 2.3.3.2 The *WAVE* slip-weakening relationship for three different slip-weakening rates.

The sequence of snapshots in figures 2.3.3.3, 2.3.3.4 and 2.3.3.5 illustrate the absolute velocity in the region surrounding the two-dimensional geometry outlined in figure 2.3.3.1, at 11, 24 and 30 ms after sudden fault rupture, i.e. the fault cohesion drops to zero instantaneously. The fault and stope are oriented parallel to the y- and x-axes respectively.

The waves displayed in the carpet plots of figures 2.3.3.3 to 5 can be categorised according to the following types:

(i) A strong shear wave demarcated by 'S' propagates away from the fault.

(ii) A Rayleigh wave ('R') propagates along the stope hanging-wall.

(iii) The faster P-wave ('P') has propagated further than the shear or Rayleigh waves, but absolute velocities within the P-wave are small compared with peak velocities associated with the shear or Rayleigh waves.

In figure 2.3.3.4, the Rayleigh wave has propagated along the length of the stope hanging-wall and, since the Rayleigh wave propagation speed is 2980 m/s versus 3290 m/s for the shear wave speed, it lags behind the shear wave front. The P-wave is about to propagate beyond the window for which the carpet plot was created. After 30 ms (figure 2.3.3.5), the Rayleigh wave is reflected at the end of the stope and then propagates along the foot wall back towards the fault.

The P- and S-waves emitted by a progressively rupturing fault are not as clearly defined as the waves radiating from a suddenly rupturing fault. During progressive rupture multiple P- and S-waves are initiated and the overall wave pattern is noisy and complicated. However, the Rayleigh waves propagating along the stope surfaces are equally prominent in the sudden and progressive fault rupture analyses.

The three-dimensional *WAVE* model comprises a vertical fault situated ahead of a horizontal 60 × 60 m stope. The fault-slip model is identical to the two-dimensional case: both the sudden fault rupture and the progressive slip-weakening case are investigated. The three-dimensional model is discretised into a grid of 82 × 64 x 64 elements consisting of 3 x 3 x 3 m elements.

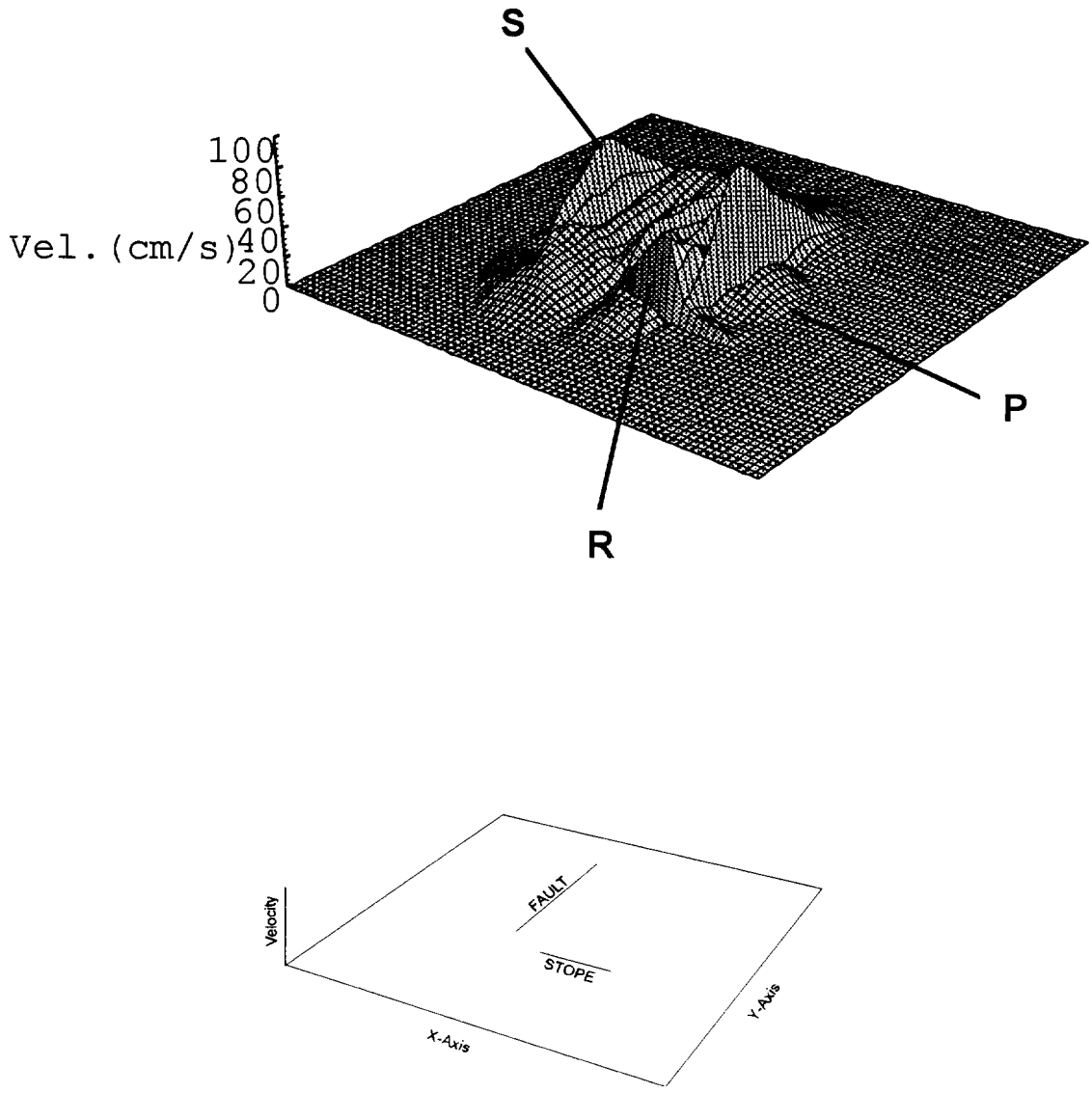

Figure 2.3.3.3 Carpet plot of the absolute velocity at t = 11 ms. Also shown is a schematic diagram indicating the fault and stope positions.

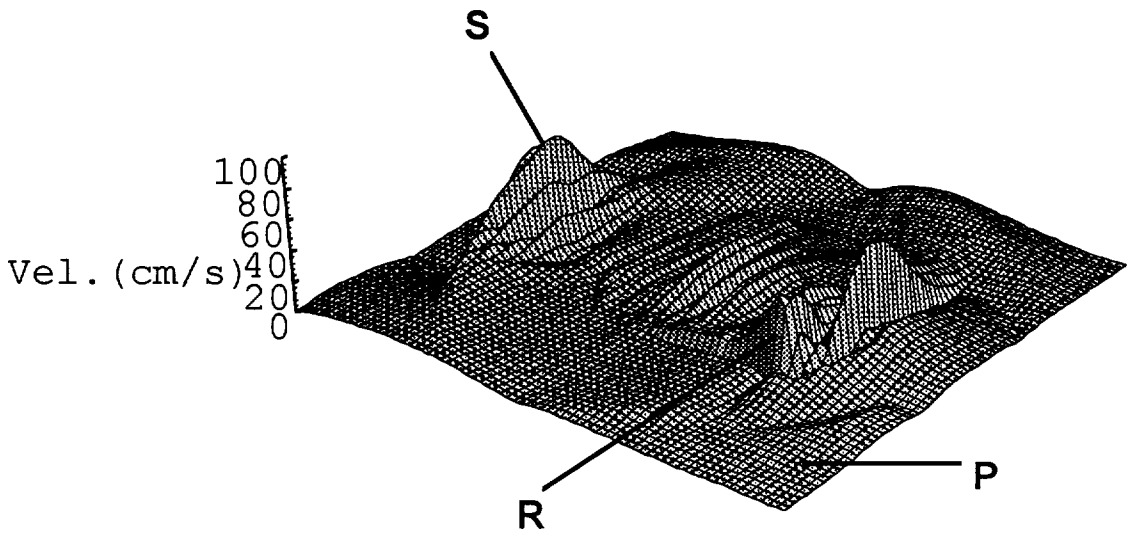

Figure 2.3.3.4 Absolute velocity at t = 24 ms.

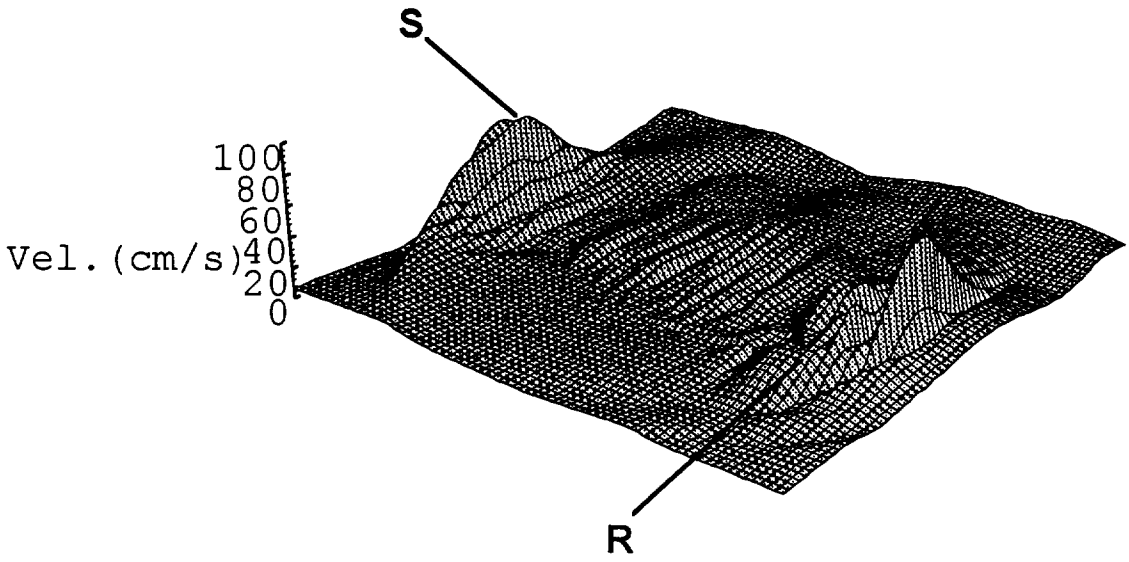

Figure 2.3.3.5: Absolute velocity at t = 30 ms.

Correlation of far-field peak particle velocities

In this section, the attenuation of far-field peak particle velocity calculated by *WAVE* is compared with the analytical model of Brune (1970/1971) and an empirical relationship determined by McGarr (1984).

The Brune Model

Brune (1970/1971) presented a model of the seismic source in which the fault is represented as a circular area. A shear stress loading is applied to a circular area on the fault surfaces at time zero resulting in the propagation of a pure shear stress wave perpendicular to the dislocation surface. The effects of fault propagation and friction are neglected in the Brune (1970/1971)

model. Thus the model of Brune (1970/1971) can be closely compared with the *WAVE* analyses where fault cohesion is eliminated instantaneously. He determined the initial near-field peak particle velocity to be:

$$\dot{u} = \frac{\Delta\tau}{G}\beta$$

where $\Delta\tau$ is the shear stress pulse, G is the bulk modulus and β is the shear wave velocity. The far-field peak particle displacement is given by

$$u(t) = R_{\theta\phi}\frac{\Delta\tau\beta r_o}{GR}te^{-\omega_b t}, \qquad (2.3.3.1)$$

where $R_{\theta\phi}$ = 0,57 is the median value of the radiation factor for a double-couple source calculated at 1000 points randomly distributed over the focal sphere (Spottiswoode and McGarr 1975), $\omega_b = 2\pi f_o$ and f_o is the corner frequency, where the low- and high- frequency spectral asymptotes meet, R is the hypocentral distance, r_o is the source radius and t is the retarded time related to the time after the event t' by $t = t' - R/\beta$; for $t < 0, u(t) = 0$. Differentiating equation 2.3.3.1 with respect to time yields

$$\dot{u}(t) = R_{\theta\phi}\frac{\Delta\tau\beta r_o}{GR}e^{-\omega_b t}(1 - \omega_b t),$$

and, noting that the peak velocity occurs at the retarded time $t = 0$,

$$RV_{\max} = 0{,}57\frac{\Delta\tau\beta r_o}{G}.$$

From Brune (1970/1971), $\Delta\tau = \frac{7}{16}\frac{M_o}{r_o^3}$, thus

$$RV_{\max} = 0{,}57\frac{\Delta\tau\beta}{G}\sqrt[3]{\frac{7M_0}{16\Delta\tau}}. \qquad (2.3.3.2)$$

Equation 2.3.3.2 is used to calculate the analytical velocity attenuation as predicted by the model of Brune (1970/1971). The shear stress difference, $\Delta\tau$, before and after fault rupture is determined for each stope-fault geometry by calculating the average ESS on the fault plane which intersects the positive ESS lobe. The fault position is varied in 3 m increments (the element size) from 6 to 27 m ahead of the stope. For the two-dimensional geometries, the shear stress drop was found to vary from 5,3 MPa for a fault situated 9 m ahead of the stope to 0,4 MPa for a fault 27 m from the stope. In three dimensions, the stress drop ranged from 4 MPa for a fault 6 m ahead of the stope to 0,2 MPa for a fault 15 m ahead. The stress drops were found to be compatible with mine seismic data (McGarr 1984, Spottiswoode 1993).

Empirical relationships relating RV_{max} to seismic moment

The model of Brune (1970/1971) and peak particle velocities calculated by *WAVE* are compared with an empirical relationship that relates the product of hypocentral distance and peak particle velocity to seismic moment. The majority of published papers relating such relationships have concentrated on large magnitude seismic events, with measurements made at large distances from the seismic source. McGarr *et al.* (1981) provided the first relationship for mine tremors based on 12 events. Other studies relating the peak particle velocity attenuation of mine tremors to the event size have been conducted by, amongst others, Spottiswoode (1984), McGarr (1984), Hedley (1990) and Butler and van Aswegen (1993). In this investigation the following relationship by McGarr (1984) based on 24 mine induced events and 28 non-mining related events is used:

$$\log(RV_{\max}) = -4,78 + 0,44\log(M_o),$$

where R is the hypocentral distance in m, V_{max} is the peak particle velocity in m/s and M_o is the seismic moment in Nm.

Comparing Peak Particle Velocities

To relate the far-field peak particle velocities of the numerical analysis to analytical and seismological data, the peak velocities are calculated by *WAVE* along a line extending perpendicular to the fault away from the stope. The line, which is drawn from the point of maximum fault slip, represents the location at which, for any given time instant, the peak particle velocities occur in the numerical model. Figure 2.3.3.6 depicts the variation of hypocentral distance versus peak velocity for the three-dimensional model with a fault situated 9 m ahead of the stope. Using $M_o = GDA$ (Aki and Richards 1980), where M_o is the seismic moment, G is the bulk modulus, D is the average absolute slip over the rupture area, and A represents the rupture area, the seismic moment for this stope-fault geometry is calculated to be 98 GNm. The local magnitude on the Richter scale can be related to the seismic moment on an empirical basis. A number of such empirical relations have been derived from actual data. They are all expressed in the same form, but with slightly different parameter values. Thus the average of $\log M_o = 8,7 + 1,2M_L$ (Spottiswoode and McGarr 1975), $\log M_o = 10,2 + 1,2M_L$ (Gibowicz 1975), $\log M_o = 9,2 + 1,3M_L$ (Brummer and Rorke 1990) and $\log M_o = 7,05 + 1,5M_L$ (Hanks and Kanamori 1979) is used to estimate the event magnitude as $M_L \approx 1,6$. The average source radius for this event is 25 m. In this study the far-field is assumed to be greater than twice the source radius (Spottiswoode - personal communication). Also shown in figure 2.3.3.6 are the far and near-field peak particle velocities predicted by the analytical model of Brune (1970/1971) and the far-field peak velocity attenuation predicted by the empirical relationship of McGarr (1984).

The *WAVE* velocity attenuation depicted in figure 2.3.3.6 radiates from a progressively rupturing fault, i.e. a slip-weakening law is applied to the fault interface, where fault cohesion is linearly reduced to zero after 0,1 mm relative slip. Thus it is expected that the sudden fault rupture model of Brune (1970/1971) will predict higher velocities than *WAVE*. The empirical relationship of McGarr (1984) predicts lower peak velocities than the *WAVE* and Brune (1970/1971) models.

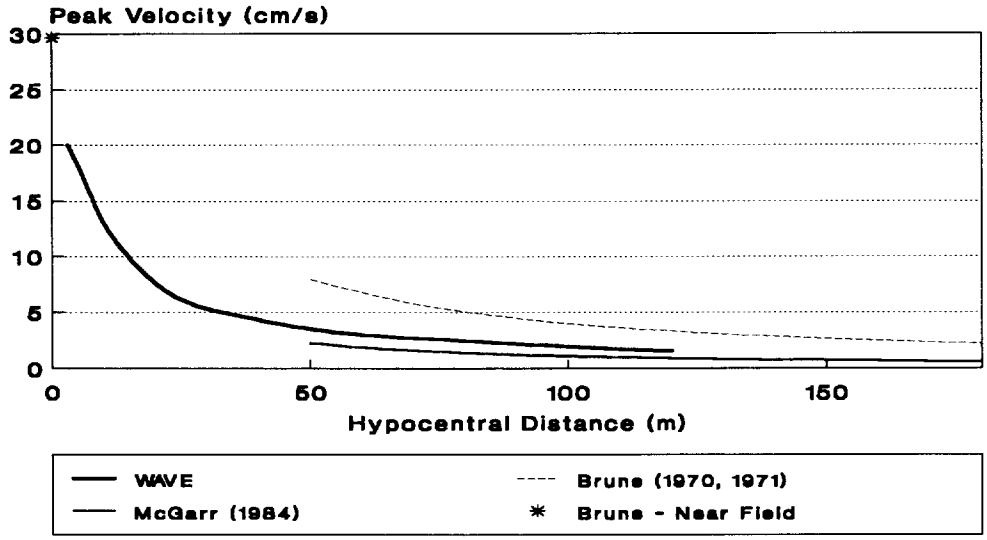

Figure 2.3.3.6 Three-dimensional velocity attenuation as predicted by *WAVE*, the analytical model of Brune and the empirical relationship of McGarr (fault 9 m ahead of the stope, M_0 = 98 GNm, M_L = 1,6 and r_0 = 25 m).

The velocity attenuation shown in figure 2.3.3.6 is also plotted for the two-dimensional case (figure 2.3.3.7). The fault is again 9 m ahead of the stope, and, assuming a circular rupture plane as suggested by Sjöberg (1993) in his two-dimensional analyses, the seismic moment is 2500 GNm and the source radius is 48 m. Compared with the three-dimensional case, the plane strain assumption in the two-dimensional *WAVE* model generates a more extensive zero ESS zone, rupture occurs along a greater fault length, and a larger event is generated.

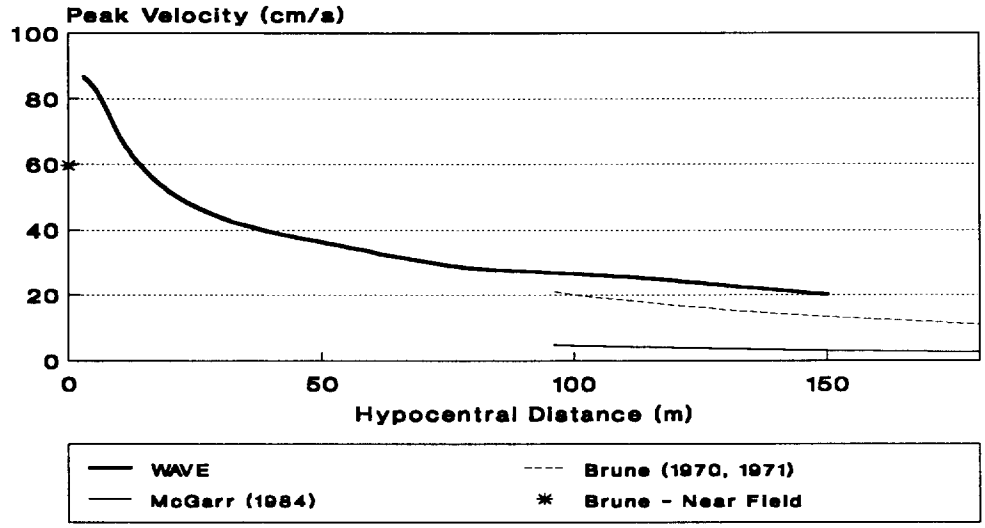

Figure 2.3.3.7 Two-dimensional velocity attenuation (fault 9 m ahead of stope, M_0 = 2500 GNm, M_L = 2,7 and r_0 = 48m).

In an evaluation of the effect of slip weakening and an increasing distance from the fault to the stope, the peak particle velocity attenuation of numerous two- and three-dimensional *WAVE* models was calculated.

The far-field peak particle velocity calculated by *WAVE* is found to be approximately inversely proportional to the hypocentral distance, i.e. $RV_{max} \approx$ constant. The average standard deviation of the hyperbola fit (RV_{max} = constant) for the 13 three-dimensional models is 4,9 per cent, whilst for the 20 two-dimensional models the average standard deviation is 7,2 per cent. When the attenuation of far-field peak particle velocity is represented by an RV_{max} product, a single log-log chart, the abscissa representing seismic moment and the ordinate depicting the RV_{max} product, can be plotted for the comparison of numerical analyses with various degrees of slip-weakening and a range of stope-to-fault distances.

Figure 2.3.3.8 displays such a graph for the two-dimensional model for stope-to-fault distances ranging in 3 m increments (the element size) from 9 m to 27 m with an instantaneously rupturing fault, and 0,01 mm and 1 mm slip-weakening. Also shown is the analytical model of Brune (1970/1971) and the McGarr (1984) empirical relationship. Some of the 52 actual McGarr (1984) events are also plotted.

Figure 2.3.3.8 indicates that the event magnitude decreases with increasing stope-to-fault distance. The event magnitude decreases slightly with an increasing degree of slip weakening, but more slip weakening strongly reduces the RV_{max} product. The two-dimensional plane-strain approximation over-estimates the far-field peak particle velocities, and the two-

dimensional *WAVE* analyses predict higher peak particle velocities than the models of Brune (1970/1971) and McGarr (1984).

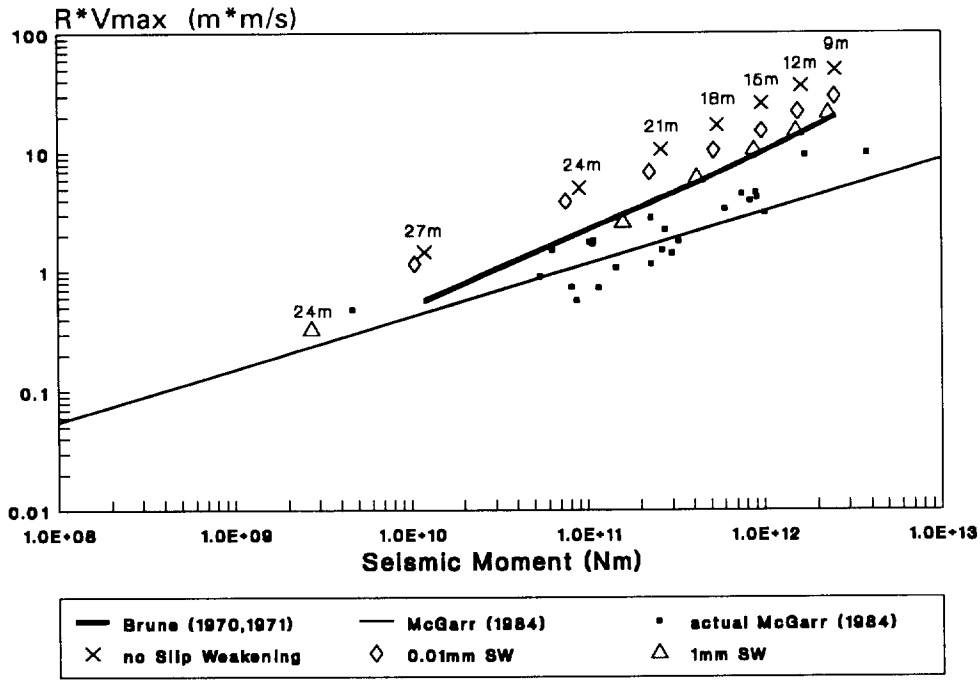

Figure 2.3.3.8 Velocity attenuation as calculated by the two-dimensional *WAVE* model (slip-weakening is abbreviated by SW). The markers (crosses, diamonds, triangles) are labelled with the stope-to-fault distance for each model geometry analysed. In the case of the markers representing one model geometry (but various degrees of slip-weakening) lying directly below each other, only one label is used to specify the stope-to-fault distance. Also shown are the results of the analytical Brune model and the empirical relationship of McGarr.

The velocity attenuation for the three-dimensional *WAVE* model, the Brune (1970/1971) model and McGarr's (1984) empirical relation is shown in figure 2.3.3.9. The *WAVE* models were analysed for stope-to-fault distance of 6 m to 15 m, and for an instantaneously rupturing fault and slip weakening of 0,01 mm, 0,1 mm and 1 mm. Whereas, in the two-dimensional analysis, rupture occurs along a fault situated up to 27 m ahead of the stope, the three-dimensional zero ESS lobe extends only 15 m ahead of the stope; thus, no rupture occurs if the fault is situated further than 15 m ahead of the stope.

The three-dimensional instantaneous fault rupture *WAVE* model correlates well with the model of Brune (1970/1971), which also analyses an instantaneously rupturing fault, and it is encouraging to note that the numerical analyses compare well with the analytical solution. As in the two-dimensional case, by increasing the degree of slip-weakening the RV_{max} product is strongly reduced.

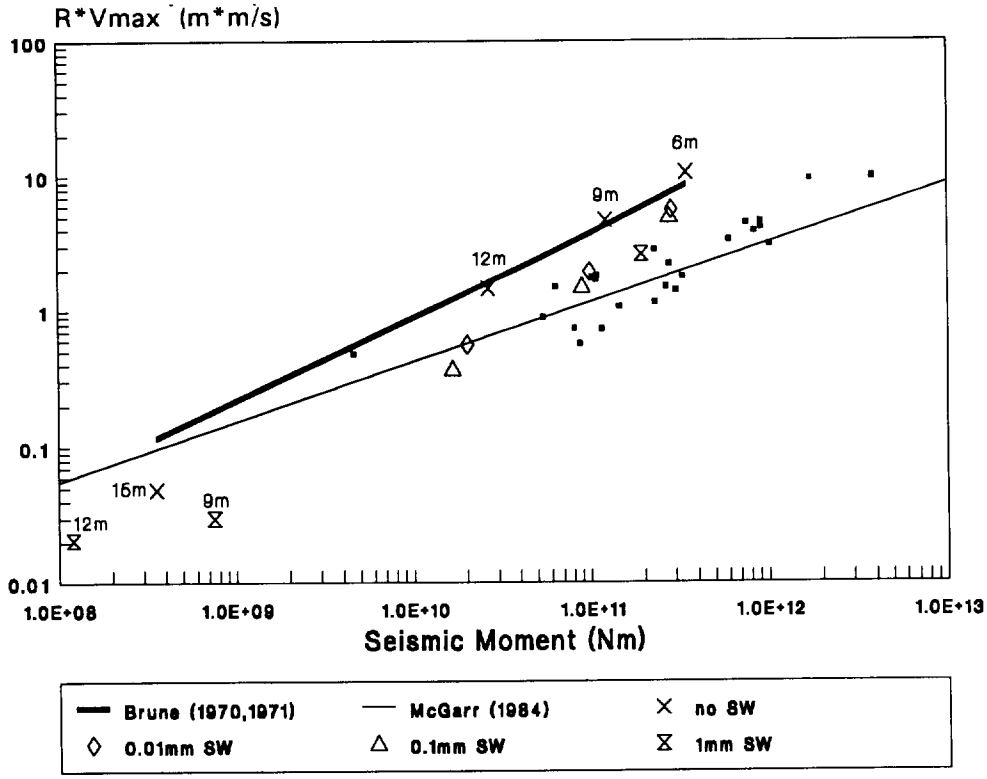

Figure 2.3.3.9 Velocity attenuation as calculated by the three-dimensional *WAVE* model. Also shown are the results by the analytical model of Brune and the empirical relationship of McGarr.

The numerical values follow a steeper trend line compared with the McGarr (1984) relationship and the model of Brune (1970/1971). This might be due to the slip weakening logic applied to the fault interface, and it is recommended that alternative cohesion-weakening logic, such as velocity weakening, should be investigated. By the incorporation of alternative cohesion-weakening logic, numerical models might yield superior approximations of the far-field peak particle velocities, at increasing fault-to-stope distances, than the slip weakening model used in this study. In the interim, to approximate seismological far-field velocities closely, the appropriate degree of slip-weakening needs to be chosen. Faults close to the stope need to be modelled with a high degree of slip weakening ($\approx$ 1 mm), whereas faults further from the stope should be modelled with less slip weakening.

Conclusions

The finite difference elastodynamic code *WAVE* has been used to model fault slip and the resulting wave propagation in two and three dimensions. The far-field peak particle velocities have been compared to the analytical fault rupture model of Brune (1970/1971) and the empirical relationship established by McGarr (1984).

1. *WAVE* is an efficient numerical tool for the modelling of fault slip and wave propagation.

2. The far-field peak velocity comparisons showed that:

    - The two-dimensional plane-strain assumption over-estimates the peak velocities compared with the analytical solution of Brune (1970/1971) and McGarr's (1984) empirical relationship.

    - Velocities calculated by the three-dimensional *WAVE* model with instantaneous fault rupture compare well with the analytical solution of Brune (1970/1971).

    - By choosing an appropriate slip-weakening rate, peak particle velocities of the three-dimensional *WAVE* analyses correlate closely with seismological field data.

References

Aki K. and Richards P. G. (1980) *Quantitative Seismology: Theory and Methods*. Freeman, Cooper, San Francisco. Vol. 1, chap. 3, pp. 49.

Brummer R. K. and Rorke A. J. (1990) Case studies on large rockbursts in South African gold mines. *Rockbursts and Seismicity in Mines*. Fairhurst (ed.). Balkema, Rotterdam. pp. 323-329.

Brune J. N. (1970) Tectonic stress and the spectra of seismic shear waves from earthquakes. *J. Geophys. Res.*, Vol. 75. pp. 4997-5009.

Brune J. N. (1971) Tectonic stress and the spectra of seismic shear waves from earthquakes (correction). *J. Geophys. Res.*, Vol. 76. pp. 5002.

Butler A. G. and van Aswegen G. (1993) Ground velocity relationships based on a large sample of underground measurements in two South African mining regions. *Rockbursts and Seismicity in Mines*. Young (ed.). Balkema, Rotterdam. pp. 41-48.

Gibowicz S. J. (1975) Variation of source properties: the Inangahua, New Zealand Aftershocks of 1968. *Bull. Seism. Soc. Am.*, Vol. 65. pp. 261-276.

Hanks T. C. and Kanamori H. (1979) A moment amplitude scale. *J. Geophys. Res.*, Vol. 84. pp. 2348-2350.

Hedley D. G. F. (1990) Peak particle velocity for rockbursts in some Ontario mines. *Rockbursts and Seismicity in Mines*. Fairhurst (ed.). Balkema, Rotterdam. pp. 345-348.

McGarr A., Green R. W. E. and Spottiswoode S. M. (1981) Strong ground motion of mine tremors: some implications for near-source ground motion parameters. *Bull. Seism. Soc. Am.*, Vol. 71. pp. 295-319.

McGarr A. (1984) Scaling of ground motion parameters, state of stress and focal depth. *J. Geophys. Res.*, Vol. 89. pp. 6969-6979.

Napier J. A. L. (1987) The application of excess shear stress to the design of mine layouts. *J. S. Afr. Inst. Min. Metall.*, Vol. 87. pp. 397-405.

Ryder J. A. (1988) Excess shear stress in the assessment of geologically hazardous situations. *J. S. Afr. Inst. Min. Metall.*, Vol. 88. pp. 27-39.

Sjöberg J. (1993) Numerical analysis of a fractured rock mass response to the dynamic loading by fault slip. *COMRO Rock Eng. consultancy report*, Johannesburg.

Spottiswoode S. M. and McGarr A. (1975) Source parameters of tremors in a deep-level gold mine. *Bull. Seism. Soc. Am.*, Vol. 65. pp. 93-112.

Spottiswoode S. M. (1993) Seismic attenuation in deep-level mines. *Rockbursts and Seismicity in Mines*. Young (ed.). Balkema, Rotterdam. pp. 409-414.

Spottiswoode S. M. (1984) Underground seismic networks and safety. *Monitoring for Safety in Geotechnical Engineering*. SANGORM, Johannesburg.

2.3.4 Fault-triggering

A stope-fault model was investigated wherein under certain conditions the waves generated by an initial slip event trigger a much larger event. Importantly, a static analysis would not directly predict such behaviour.

The two-dimensional model considered, is shown in figure 2.3.4.1. The dip is 20° and the fault is at 90° to the reef plane, with a 40m throw. The left hand stope of 96m span was mined to 4m of the fault. The effects of a number of different positions of the right hand stope were considered (no stope, or the distance from the fault ranging from 40m down to 12m). The dip is represented by a rotatation in the applied stress field, so that the stope and fault are aligned with WAVE's orthogonal mesh. The model could represent mining parallel to the fault, rather than mining toward the fault.

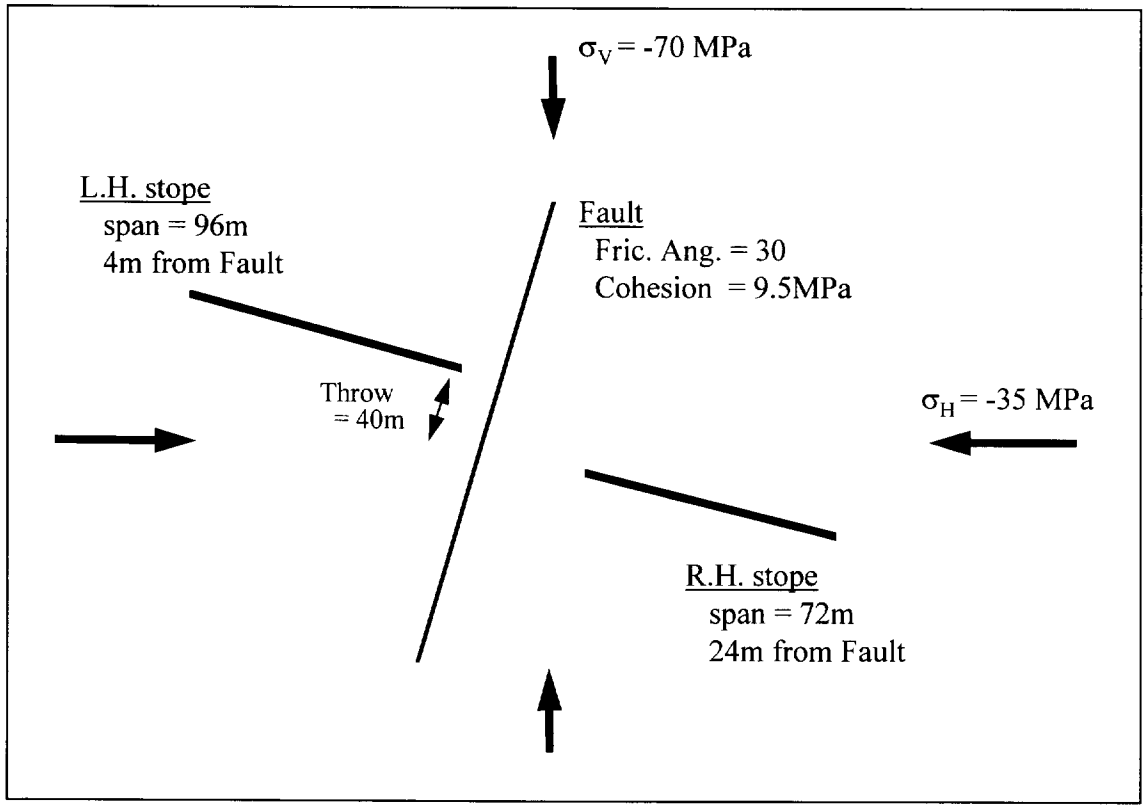

Figure 2.3.4.1: Model geometry for triggered fault slip

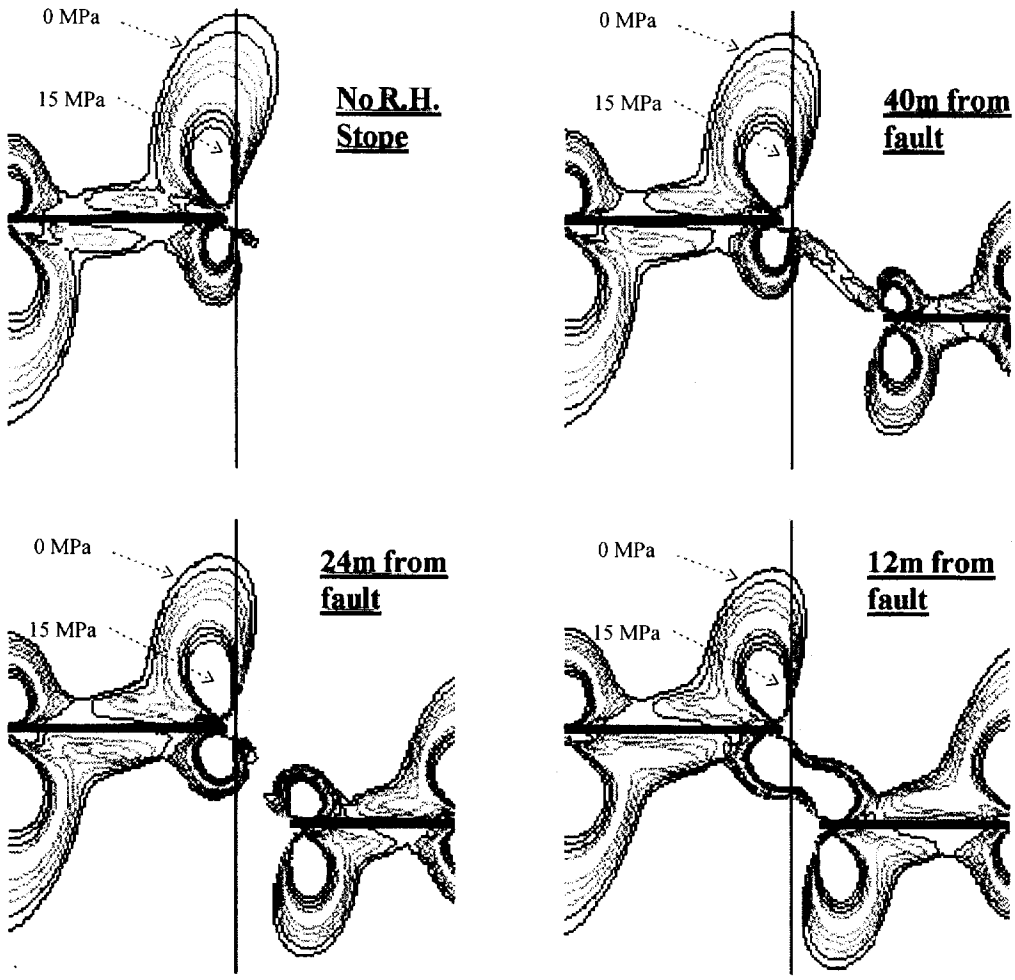

Figure 2.3.4.2: ESS contours for various positions of the right hand stope

Figure 2.3.4.2 shows contours of ESS (excess shear stress) from 0 to 15MPa for this fault orientation based on a 30° friction angle and a zero cohesion - firstly for no right hand stope, and then with the right hand stope face at 40m, 24m and 12m from the fault. What should be noted are the two lobes of ESS which intersect the fault - a larger upper lobe and smaller lower lobe. For closer positions of the right hand stope, the upper lobe becomes smaller and less intense, while the lower lobe becomes more intense. At some position, conditions in the lower area become more conducive to slip than those in the upper area. Figure 2.3.4.3(a) shows this same trend for the ESS along the fault itself. Figure 2.3.4.3(b) shows a similar trend where the normal stress on the fault is increasingly less compressive for the closer right hand stope faces.

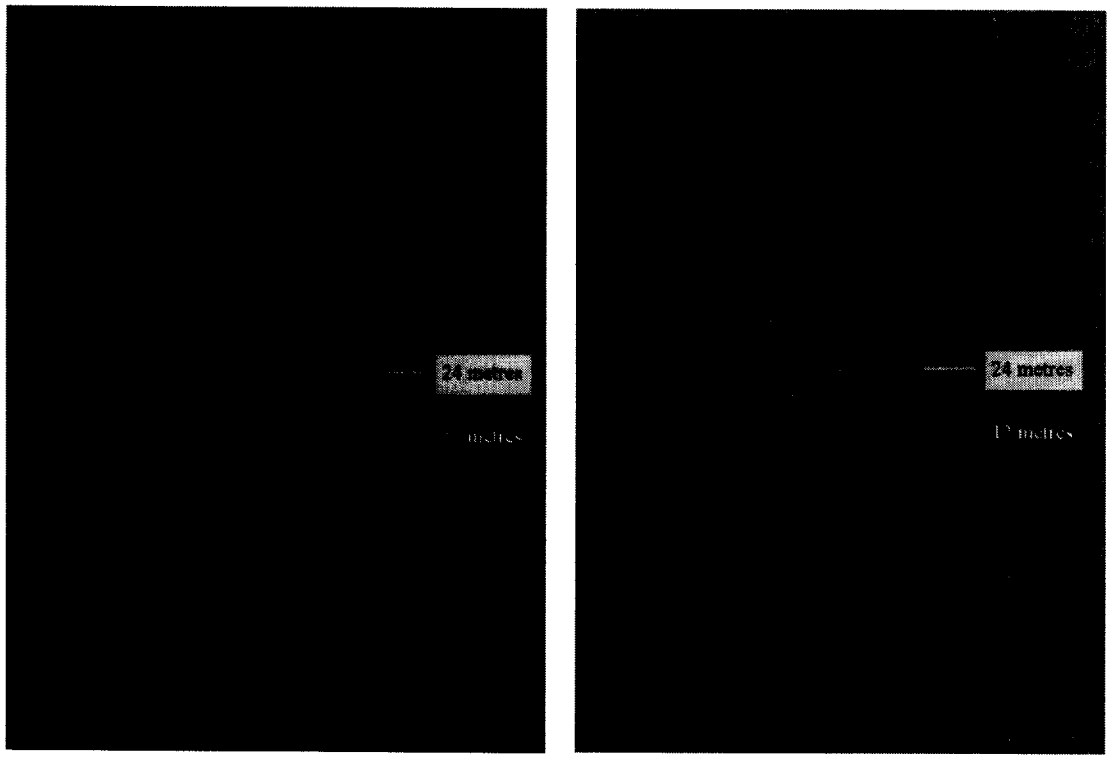

(a) ESS (b) Normal Stress

Figure 2.3.4.3: Stress on the fault for different positions of the right hand stope

In the first case considered, the right hand stope is at 24m, and the conditions on the fault are a 30° friction angle and 9.5MPa cohesion (a cohesion of up to 9.9MPa was found to produce the same effect). The maximum ESS in the upper lobe is less than 9.3MPa, while that in the lower lobe is 10.1MPa. These static conditions will cause slip to initiate in the lower lobe, but not in the upper.

The model was then allowed to slip dynamically. The slip-weakening law described in section 2.2.2 was used, whereby the cohesion is reduced linearly to zero as slip takes place. Figure 2.3.4.4 contains snapshots of particle velocity contours at 4 different times, showing how the energy propagates from the initial slip event in the lower ESS lobe. In the second and third snapshots one can distinguish the separate P and S wavefronts. Once the shear wavefront reaches the upper ESS lobe, slip is triggered in the upper section of the fault.

A static analysis was performed by damping out the wave motion from the initial slip event, and considering the final equilibrium state after stress redistribution. In this case, the second event is not triggered - in fact the effect of this stress redistribution is to slightly decrease the upper ESS lobe, making the second event less likely. Figure 2.3.4.5 shows how the slip on

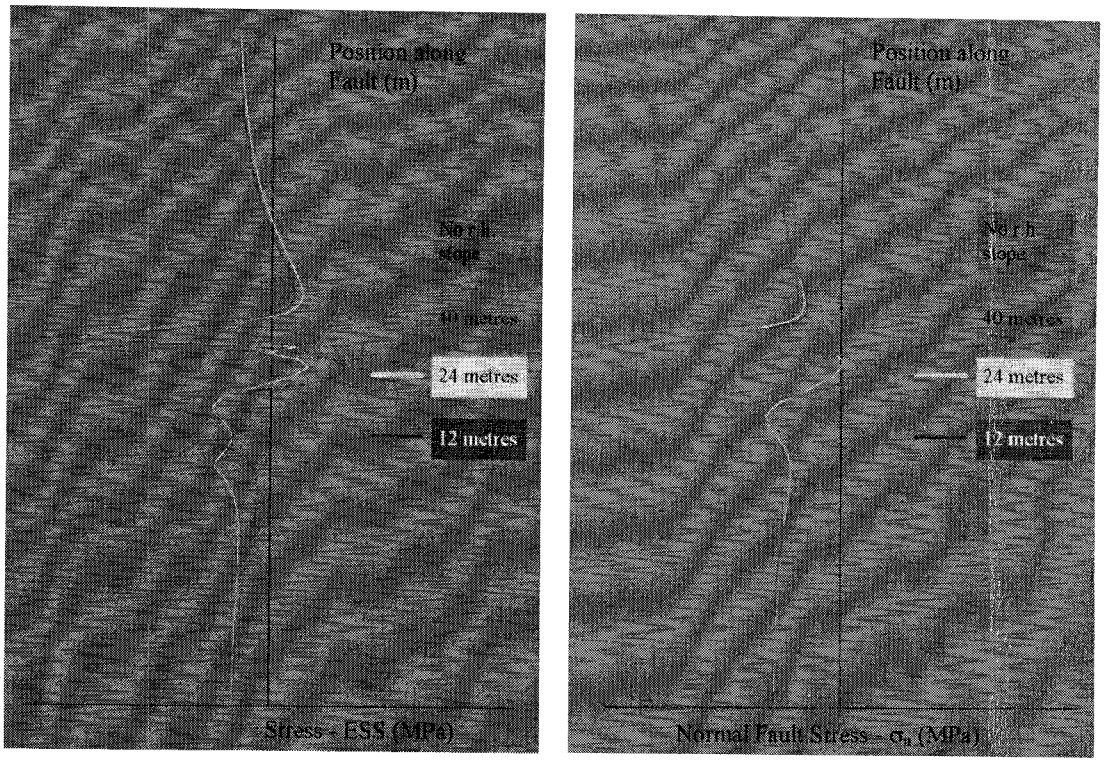

(a) ESS (b) Normal Stress

Figure 2.3.4.3: Stress on the fault for different positions of the right hand stope

In the first case considered, the right hand stope is at 24m, and the conditions on the fault are a 30° friction angle and 9.5MPa cohesion (a cohesion of up to 9.9MPa was found to produce the same effect). The maximum ESS in the upper lobe is less than 9.3MPa, while that in the lower lobe is 10.1MPa. These static conditions will cause slip to initiate in the lower lobe, but not in the upper.

The model was then allowed to slip dynamically. The slip-weakening law described in section 2.2.2 was used, whereby the cohesion is reduced linearly to zero as slip takes place. Figure 2.3.4.4 contains snapshots of particle velocity contours at 4 different times, showing how the energy propagates from the initial slip event in the lower ESS lobe. In the second and third snapshots one can distinguish the separate P and S wavefronts. Once the shear wavefront reaches the upper ESS lobe, slip is triggered in the upper section of the fault.

A static analysis was performed by damping out the wave motion from the initial slip event, and considering the final equilibrium state after stress redistribution. In this case, the second event is not triggered - in fact the effect of this stress redistribution is to slightly decrease the upper ESS lobe, making the second event less likely. Figure 2.3.4.5 shows how the slip on

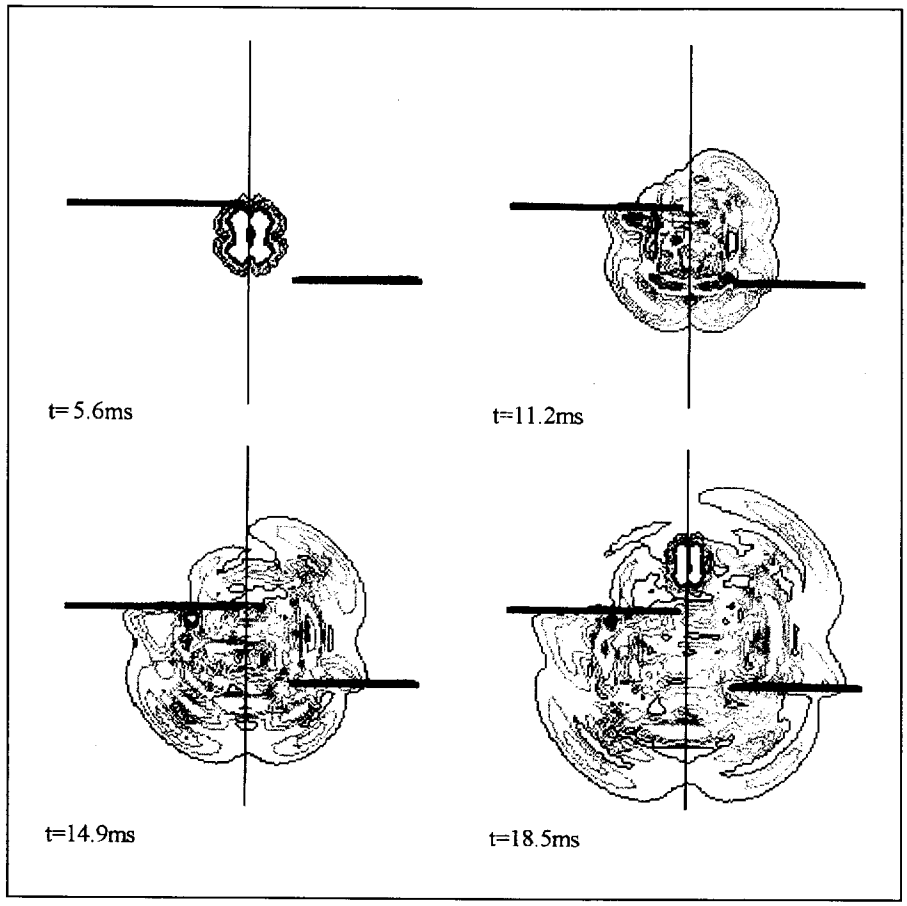

Figure 2.3.4.4: Snapshots of particle velocity contours showing the wave propagation from the initial event triggering a second event

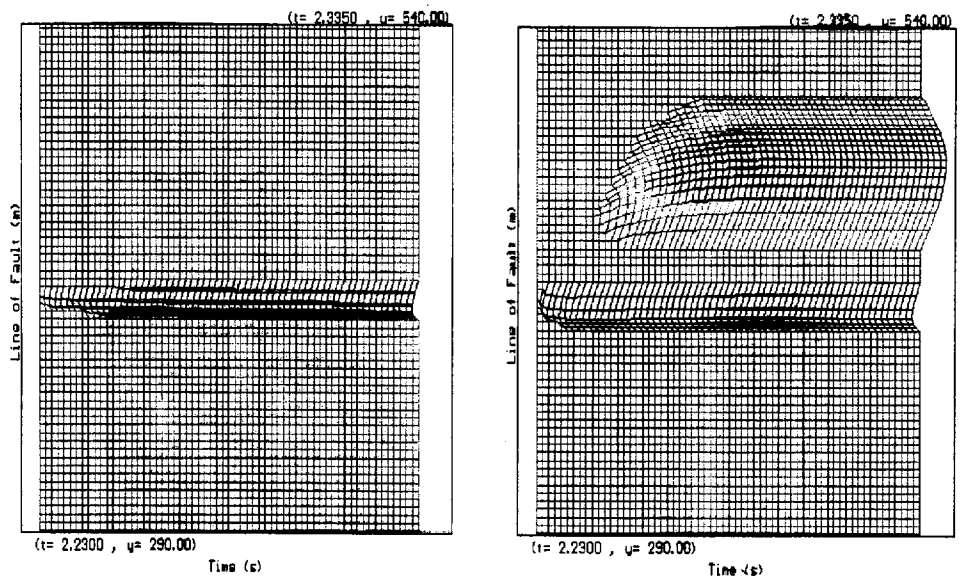

(a) Static **(b) Dynamic**

Figure 2.3.4.5: Development of fault slip with time for (a) static and (b) dynamic cases

the fault develops with time for the static and dynamic cases. In this figure, the horizontal axis is time and the vertical axis is a position on the fault. Essentially, a vertical line shows the slip profile of the fault at a point in time, while a horizontal line shows the slip development with time for a particular position on the fault. This diagram shows a single slip event in the static case, while in the dynamic case at some time after the initial event, there is a significantly larger second event.

The ESS analysis gives insight into the conditions required for this triggered event (assuming a homogenous fault requires two lobes of ESS similar in intensity but not size). For the assumption of 30° friction and a homogenous fault, the optimal position of the right hand stope was 24m. Two other cases were considered which deviate from this criterion and allow such a mechanism to occur for other positions of the right hand stope. Taking the position at 28m from the fault, ESS in the upper lobe was less than 9.9MPa and in the lower lobe less than 7.5MPa. Assuming a 'point of weakness' in the lower lobe (represented by a cohesion of 7MPa), allows slip to initiate once again triggering the large upper lobe. Finally a third case considered a position at 32m, but with a higher friction angle of 40°, and cohesion of 4.3MPa. Whereas the previous cases represent mining parallel to the fault, this case could also represent mining toward the fault, since no slip would occur in previous mining steps. The size of the triggered event in this case is much smaller than the others due to the smaller ESS lobes.

Conclusions

The importance of this work is to show that there may be underlying dynamic mechanisms which are not directly predicted by static analysis. In this particular model, the static condition itself was close to failure, and there is a fairly narrow band of conditions under which the triggering occurs. The ESS analysis gives insight into the conditions required for such a triggered event (the case of an homogenous fault required two lobes of ESS, similar in intensity but not size). Assuming a distribution in the strength of the fault however, increases the range of conditions under which such a mechanism could occur. There is scope for further work, such as to examine P-wave initiation (the above work concentrated upon S-wave initiation), to include and examine the influence of the fracture zone and to examine simple 3D models to see under what conditions the same effect can occur.

2.3.5 Numerical models for the propagation of seismic waves in the fractured rockmass around a stope

Numerical modelling of the dynamic behavior of the rockmass around stopes is currently undertaken by assuming that the rock is isotropic and elastic. In finite difference programs, such as FLAC, WAVE or UDEC, and finite element programs such as ABAQUS and ELFEN, large joints can be included explicitly using Coulomb friction laws for the constitutive response. However, the rockmass surrounding stopes at great depth is highly fractured and may consist of a number of layers of different rock types. A report has been prepared for output 1.5, based on a literature review undertaken to identify methods for modelling the effect of seismic wave on stopes in a highly fractured rockmass (Sellers 1995).

Techniques have been developed for altering the elastic constants of cracked materials with weak concentrations of parallel cracks (Crampin 1981, Hudson 1986). The elastic behavior of composite materials is represented by means of a set of effective elastic constants, expressed in terms of the crack density and direction. More complex formulations represent the cracking by a second order crack density tensor (Sayers 1994). The equivalent elastic stiffness displays anisotropic symmetries if the material has an overall crack alignment. Once effective elastic constants are determined, the calculation of the effect of the cracks on the propagation of seismic waves with wavelengths much greater than the dimensions of the inhomogeneities is possible. Considerable controversy surrounds the assumptions made in obtaining the elastic constants, and the maximum allowable crack density (Sayers 1994).

It is found that in the case of aligned cracks, polarization of the wave forms occurs. Shear waves, in particular, are found to be sensitive to even a small anisotropy, and a characteristic feature of all but the weakest crack anisotropies is the splitting of shear waves into two orthogonally polarized waves (not necessarily SH and SV). Polarization diagrams are found to be a reliable way of identifying shear wave splitting, and can thus be used to quantify dilatancy in a material. The quality factor representing attenuation (Q^{-1}) is shown to depend on the third power of frequency which contradicts observations of constant Q^{-1} (Aki and Richards 1980). This discrepancy suggests that a comparative study of in-situ measurements and numerical

modelling is required to assess whether the equivalent elastic models are relevent for representing the rockmass around a stope.

The equivalent elastic medium has been implemented into the ABAQUS explicit finite element program (Mitchell and Dalrymple 1995). Dynamic photoelastic experiments of idealised stope models in layered materials, shown in Figures 2.4.1.2 to 2.4.1.7, were analysed and produced stress wave patterns as expected. An equivalent elastic material was included around the stope, beween two horizontal bedding planes, to simulate a fractured zone around the stope. The model was loaded by a blast source initiated in the hangingwall. Peak velocities were found to decrease as the crack density increases. The decrease was most significant in the footwall, and much less in the hangingwall. The stress patterns are altered considerably and the overall stress magnitudes appear to decrease in the cracked material.

The equivalent elastic medium formulations do not hold when the wavelength is of the same order as the crack dimensions. The damaged solid can then be approximated by an equivalent effective medium which is statistically homogeneous and linearly viscoelastic (Zhang and Gross ,1992). For shear waves, the attenuation is approximately constant. Constructive interference may arise for non-random sets of cracks (Gross and Zhang 1991). The effective phase velocity can also be greater than the wave velocity in the undamaged material. Thus, for aligned cracks the dispersed wave may ultimately dominate the solution in contrast to the isotropic solution for random cracks in which the interference is destructive. The analysis neglects the multiple scattering effects between cracks, and is thus only valid for low crack densities. The selection of combinations of viscoelastic rheological models implies that the material behaves as a viscoelastic medium and permits the formulation of models with constant, or near constant, attenuation (Kjartansson 1979)

The fractures or joints in an elastic material can be represented by displacement discontinuity elements having a specific joint stiffness (Pyrak-Nolte 1990, Cook 1992). Analytical solutions of a plane wave propagating across a single joint shows that the fracture causes reflections and a delay in the wave front. Multiple, parallel joints are analyzed as a sum of single joints, thus neglecting multiple reflections from the joints. Significant differences are observed between the equivalent elastic medium and the displacement discontinuity approaches which can influence the interpretation of observed data. Specifically, in the displacement discontinuity method, the reflection and attenuation occurs directly at the fracture, whereas in the equivalent elastic medium the changes are smeared throughout the material. The displacement discontinuity

approach predicts a much greater variation of group velocities with angle of incidence than the equivalent elastic medium. A series of welded elastic layers will lead to the attenuation of high frequency components of incident waves by "stratigraphic filtering" and "tunnelling of low frequency components along high velocity layers (Deng 1994)

The models described above have assumed that the seismic wave does not affect the integrity of the rockmass. Graham et al. (1991) investigated the shear wave anisotropy observed in rockburst induced shear waves in South African mines. The shear wave splitting results from microcracks which are aligned parallel to the regional stress field. Cracking due to stress concentrations from mining excavations appeared to have a negligible effect on the shear wave splitting as measured at the earth's surface

However, when a seismic wave interacts with a stope at great depth, observations suggest that failure of the rockmass occurs as intensely fractured material is expelled into the stope by slip on the pre-existing fractures or, if the intact rock fails due to the application of a stress state outside the failure envelope. This latter response appear to have been investigated for stopes and so models developed for other applications must be considered.

A number of dynamic damage models have been developed for modelling fragmentation due to blast loading and could be applied to study failure of the rockmass under dynamic loading. Grady and Kipp (1986) consider that the elastic modulus is reduced when the material experiences tensile stress and an isotropic damage model with a constitutive model of the form

$$\sigma = E(1-D)\varepsilon$$

is developed. The reduction in Young's modulus E is described by defining the evolution of the damage parameter, D, in terms of the initial distribution of flaws. The dynamic fracture strength depends on the distribution of flaws in the material, the time τ, the magnitude of the tensile strain, and the strain rate. Once failure has occurred, the kinetic energy of expelled particles is included in the overall energy balance. This damage model can be extended to model a larger range of material responses by including a plasticity model to represent the behaviour in compression (Taylor et al. 1986).

Other procedures such as the discrete element method, which explicitly models the rock as a series of blocks formed by pre-existing joints and fractures, have been applied to simulate fragmentation due to blasting (e.g. Preece 1994). Progressive fragmentation of an intially solid rockmass can be modelled using a combination of the finite element method and the distinct element method (Munjiza et al. 1994). The application of these techniques to represent the expulsion of fractured rock around stopes as a result of seismic waves must still be evaluated.

REFERENCES

Aki K., Richards, P.G., Freeman, W.H. or Company New York (1980). *Quantitative Seismology*:- Theory Methods.

Cook, N.G.W, (1992) Natural Joints in Rock: Mechanical, Hydraulic, and Seismic Behaviour and Properties under Normal Stress. *Int. J. of Rock Mech and Mining Sci.* vol 29, 198-223.

Crampin, Stuart. (1984) Effective anisotropic elastic constants for wave propagation through cracked solids. *Geophys. J. R. astr. Soc.* 76, 135 14.

Deng, Lydia H. (1994); Acoustic-wave propagation in thin-layered media with steep reflectors. *Geophysics*, Vol. 59, No. 10 p. 1593-1604, 14 figs., 1 table.

Grady D. and Kipp, M. (1986) Dynamic rock fragmentation, *In Fracture Mechanics of Rock*, Atkinson (ed), Academic Press, 429 - 472.

Graham, G, Crampin, S and Fernandez, L. (1991) Observations of shear-wave polarizations from rockbursts in a South African gold field: an analysis of acceleration and velocity recordings. *Geophys. J. Int.* 107, 661-672

Gross, D. and Zhang, C.H. (1992) Wave Propagation in Damaged Solids. *Int. J. Solids Structures* Vol. 29, No. 14; 15, pp. 1763-1779,.

Hudson, J.A. (1986) A higher order approximation to the wave propagation constants for a cracked solid. *Geophys. J. R. astr. Soc.* 87, 265-274.

Kjartansson Einar. (1979) Constant Q-Wave Propagation and Attenuation. Reprinted from the *Journal of Geophysical Research*, v. 84, p. 4737-4748.

Mitchell, G. Dalyrmple, M., (1995) Modelling the propagation of stress waves in the presence of parting planes and stopes, *CERECAM report No 271*, University of Cape Town.

Munjiza, A., Owen, D.R.J., Bicanic, N., Williams, J., (1994) *Computer Methods and Advances in Geomechanics*, Siriwardane & Zaman (eds) , Balkema, 857-862.

Preece, D. (1994) A numerical study of bench blast row delay timing and its influence on percent cast, *Computer Methods and Advances in Geomechanics*, Siriwardane & Zaman (eds) , Balkema, 863-868.

Pyrak - Nolte, L.J. (1988) Seismic Visibility of fractures, *PhD thesis*, University of California, Berkeley.

Sayers, C.M. Reply. (1994) *Journal of Geophysical Research*, Vol. 99, No. B6, pages 11,753-11,754.

Sellers, E.J. (1995) A review of models for the propagation of seismic waves in the fractured rockmass around a stope, *CSIR Mining technology report.*

Taylor, L.M., Chen, E-P., Kuszmaul, J.S. (1986) Microcrack-induced damage accumulation in brittle rock under dynamic loading, Comp. Meth. Appl. Mech. Eng. Vol 55, No 3, 301-320.

2.3.6. Rockburst back-analysis

A three-dimensional back-analysis using elastodynamic numerical models was attempted for a rockburst event that occurred at a deep-level gold mine. Results from the numerical model were compared with observed seismic data and a damage map. It was found that the model can be calibrated to match observed peak particle velocities, and that there is also good correspondence between the regions of highest particle velocities in the numerical model and the damage map.

The event was modelled with a three-dimensional elastodynamic computer code (ABAQUS), using parameters calculated from the seismic data. The modelling was forward-based, i.e. the source dimensions and parameters were specified *a priori*, and comparisons made with the seismic data and damage records. No attempt was made to compute the slip and opening movements at the source from the above observed seismic waveforms, i.e. no inversion was attempted.

Results show that three-dimensional elastodynamic models can be used to simulate observed ground motion in a deep gold mine to a limited extent. Peak particle velocities can be calibrated, but it was not possible to match the complete waveform because of the complicated non-linear structure of the rock mass around a deep tabular excavation, and because of the lack of detailed knowledge of the source mechanism.

Past work

Only a few three-dimensional elastodynamic investigations into rockburst or earthquake phenomena have been carried out because computer hardware and software limitations have prevented these types of investigations until recently. Yomogida and Etgen (1993) and Frankel (1993) are two examples of such studies on basins in Southern California which have experienced earthquakes. Both of these studies were based on finite difference methods, and entailed runs where up to 2.4 million and 4.1 million grids, respectively, were used. Yomogida and Etgen's model covered a volume of 98 by 96 by 32 km, and Frankel's model covered a volume of 37 by 16 by 7 km. These analyses are on a much larger scale than the scale in a rockburst study, which usually involves a volume with dimensions of less than 1 km in each direction. In both analyses, the authors concluded that the application of three-

dimensional models was limited by insufficient knowledge of the basins under investigation, but that numerous aspects of the observed wave motion recorded by geophones were reproduced. Other notable three-dimensional studies include those of Hart *et al.* (1988) and Bigarre *et al.* (1993), but these studies were based upon pseudo-static analyses.

Event statistics

The rockburst event that was back-analyzed occurred in a deep gold mine during 1994. The seismic event located on a fault and dyke structure (figure 2.3.6.1), and had a magnitude of 3.9 (Richter) on the mine's seismic system. Other relevant information is listed below.

location:	$(x,y,z) = (29\,000, -41\,963, 2\,530) \pm 25$ m location error
moment M_0:	286×10^{12} Nm
apparent stress σ_A:	15 MPa
source type:	"pop"
apparent volume V_A:	9.7×10^6 m^3

In the above list, the apparent stress (σ_A) is defined as the stress available to induce seismic ground motion, and is derived from the total work expended during slip and the dissipated energy, or the difference between the average loading stress and the average resisting stress (e.g. McGarr 1993, p. 4). If no dynamic overshoot occurs during slip, then the apparent stress

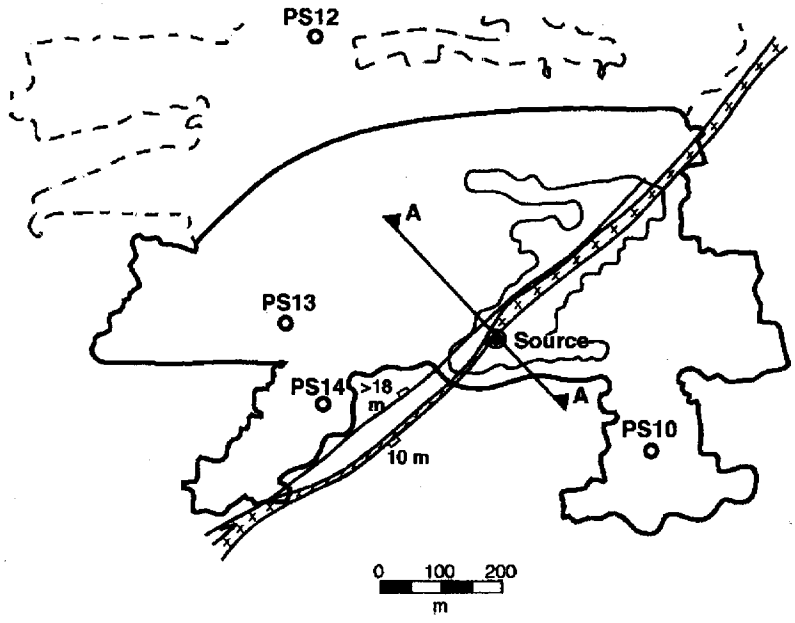

Figure 2.3.6.1: Mine plan showing event location and extent, geological features, and geophone sites

is exactly half the stress drop, so we expect a stress drop of about 30 MPa. Apparent volume (V_A) is defined as a volume of rock which experiences large inelastic strains, and is calculated by dividing the seismic moment by twice the apparent stress (Mendecki 1993). A "pop" source type implies that there was significant compressional wave content in the observed seismic waveforms, as opposed to a "slip" source type, which contains significant shear wave content.

The seismic location had an error of 25 m, and the fault and dyke (18 m throw) are within this range. The location and source parameters listed above were based on records from 13 triaxial geophones. In figure 2.3.6.1, the geophones shown are the four nearest to the event location for which there are records of the event. The traces from these four geophones were digitized from seismic records for direct comparison with the results of the numerical model.

The event was modelled as slip on the fault. Although the source registered as a "pop"-type event, the geology and location are such that the source is probably a shear event, in the sense that it is located along the fault/dyke structure. Slip-based mechanisms can have both normal and shear components. Alternatively, dyke-bursting could generate a "pop"-type event.

With the assumption of a planar slip source, it is unclear how the source radius and stress drop should be inferred from the apparent volume and apparent stress data. A planar slip structure with a finite thickness, has a much smaller "volume" than a spherical source of the same radius. In the numerical models, extensive tests were done to determine suitable source dimensions for given choices of fault friction. The results which best matched the seismic data in terms of peak particle velocities, damage maps, and geophone velocity histories, were found to be those that corresponded to a much smaller apparent volume (i.e. dyke thickness times source area) and apparent stress, but a larger source radius than those from the seismic data calculations.

Using MINSIM-D (1987) and assuming a single material model, reveals that the peak excess shear stress (ESS) on the plane of the fault was 12 MPa, based on a friction angle of 15° and no cohesion. Figure 2.3.6.2 shows the MINSIM-D ESS contours on a window in the plane of the fault looking SE, and covering an area approximately equal to the source area. There is a large area with ESS between 10MPa and 12MPa in the hangingwall with a radius of approximately 70 m. Assuming ESS drops to 0 MPa during the event, gives a peak stress drop of 12 MPa, which is less than half the expected 30 MPa based on the apparent stress of

15MPa calculated from the seismic data. however this must be viewed in conjunction with the source size.

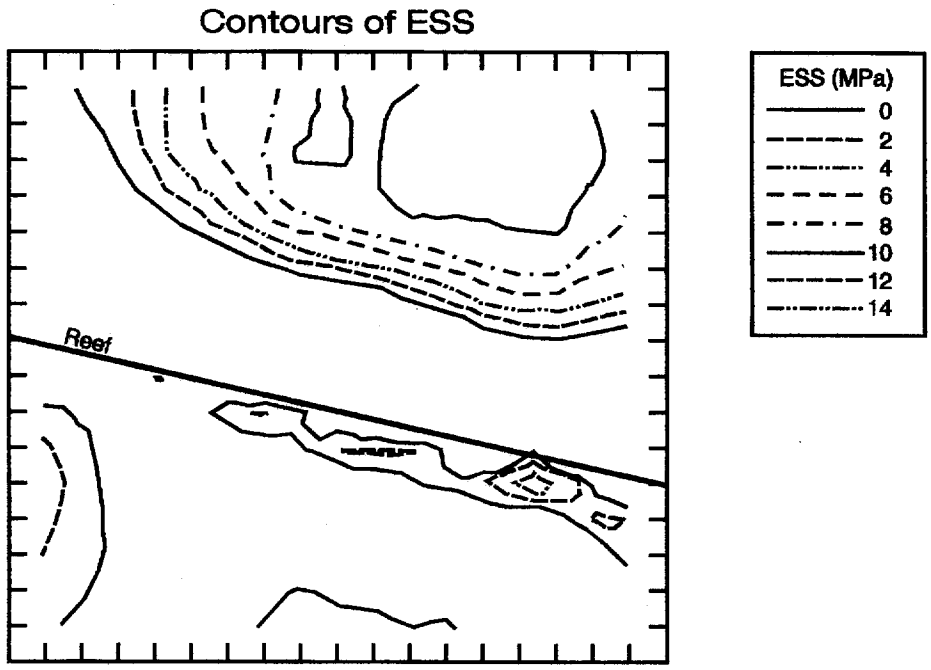

Figure 2.3.6.2: ESS pattern within source dimension on fault plane, looking SE

Numerical tools

The back-analysis was performed in two and three dimensions. WAVE was used in the two-dimensional investigations and the finite element code ABAQUS/EXPLICIT (1994) was used in the three-dimensional ones. The choice of computer codes was governed entirely by the availability of relevant software capable of performing the analyses required. In the case of the three-dimensional models, ABAQUS/EXPLICIT has multiple material capabilities, infinite element logic, slip logic, and its accuracy is established. In the case of the two-dimensional models, WAVE has multiple material capabilities, absorbing boundaries, slip logic, and is very efficient to run. WAVE runs are generally more accurate if a sufficient number of elements are used in the mesh. WAVE's three-dimensional capability was not fully developed at the time of this study, and could not be used for the three-dimensional analyses.

Material type	E (GPa)	ν	ρ (kg/m^3)	c_1 (km/s)	c_2 (km/s)	$c_1/c_1(q)$	$c_2/c_2(q)$
lava	95	0.25	2 900	6.3	3.6	1.13	1.06
quartzite (q)	75	0.2	2 700	5.6	3.4	1.00	1.00
shale	60	0.3	2 900	5.3	2.8	0.95	0.82
dyke	90	0.3	2 900	6.5	3.5	1.16	1.03

Table 2.3.6.1: Elastic material properties

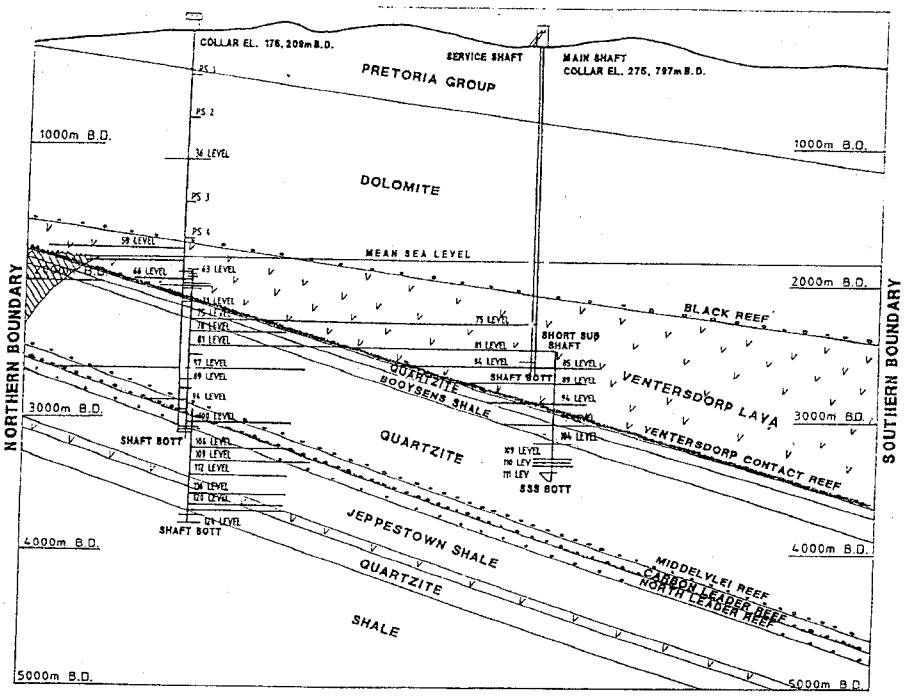

Figure 2.3.6.3: Transverse section through the mine looking East.

Geology

The stratigraphy is indicated in figure 2.3.6.3. The stope hangingwall consists of Ventersdorp lava and the footwall is predominantly quartzite, but contains a shale layer. The elastic material parameters given in Table 2.3.6.1 were supplied by the mine's Rock Mechanics Department. In Table 2.3.6.1, E is Young's modulus, ν is Poisson's ratio, ρ is density, c_1 is the compressional (P) wave velocity, and c_2 is the shear (S) wave velocity.

In the numerical model, all four materials were included, viz. the lava hangingwall, the shale and quartzite footwall, and the dyke. Plane strain modelling (using Section A-A in figure 2.3.6.1) with WAVE revealed that the material effects are important. If the hangingwall is

assumed to consist of lava and the footwall of quartzite, then the ESS in the hangingwall is reduced and the ESS in the footwall is increased, as opposed to the case when the entire rock mass is assumed to be either lava or quartzite. The inclusion of the dyke also causes an increase in the footwall ESS.

Figure 2.3.6.4 demonstrates the different material cases for identical mining geometries. A stope dimension of 75 m was selected for this comparison, and was chosen to coincide with the stope span over which closure was assumed to have not yet occurred. The effect of different stope dimensions was not found to contribute significantly to the relative material effects described above. Figure 2.3.6.4(a) is the case where a quartzite rock mass is used and no dyke is present, and figure 2.3.6.4(b) is the case where the dyke is added. figure 2.3.6.4(c) is the case where the hangingwall is lava and the footwall is quartzite and no dyke is present, and figure 2.3.6.4(d) is the case where the dyke is included. Notice that the shale layer has been excluded from these static analyses because it is outside the field of interest. It is expected to only have an effect in the dynamic analyses.

Table 2.3.6.1 indicates, under dynamic conditions, the ratio between the wave velocities of each rock type with respect to the quartzite (q). Notice that compressional and shear wave velocities can vary by as much as 20 per cent from that of quartzite. It was felt that this variation was sufficiently large to justify the use of multiple materials in the numerical models, especially because three of the four selected geophones were located in the footwall in or near the shale layer.

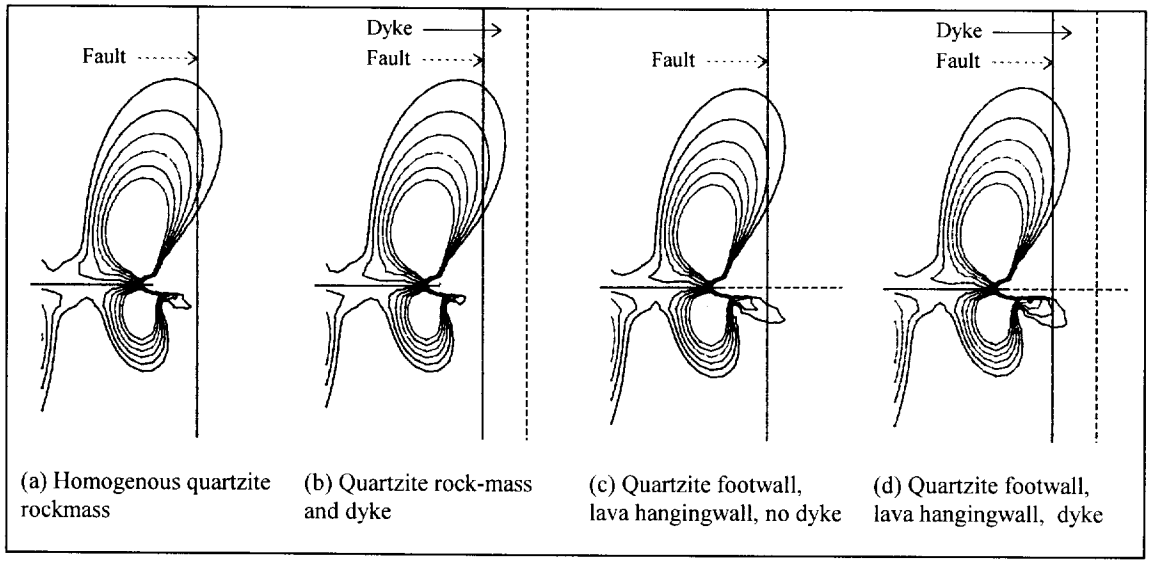

Figure 2.3.6.4: Effects of different materials on the ESS contours (portion of geometry shown)

Numerical models

In order to develop a numerical model of the rockburst event, it is necessary to decide which geological features are of importance, how much of the mining layout is of importance, and most importantly, what the source parameters are. Thereafter, the numerical model must be built up in stages, starting with a simple model, and adding complications only as needed. The modeller must also work within any limitations imposed by the numerical tool being used. In order to model the rockburst event, each run was split into a two-stage process. Firstly, the virgin stress field was imposed on the mesh, and the model (with the final mine layout, i.e. one mining step) was allowed to reach static equilibrium. Secondly, the entire fault was unlocked and allowed to slip according to a prescribed Coulomb friction weakening law, where friction was reduced linearly with time.

The three-dimensional model was set up in a multistage process. Firstly, MINSIM-D was used to digitize the mine layout of interest in the dynamic model. From figure 2.3.6.1, it is clear that the region of interest is fairly large. This large area of mining was chosen to ensure that the ESS lobes fell within the model. The second stage was to transform the digitized information into a data file suitable for the ABAQUS pre-processor, ARIES (1992), to read. The third stage was to erect a three-dimensional numerical mesh around the mine layout large enough so that ESS was zero at the mesh boundaries. This mesh contained some 36,000 elements, and covered a volume of 1.8 by 1.2 by 0.8 km. The fourth stage was to add infinite elements to the free surfaces of the mesh so that an infinite rock mass could be simulated. The purpose of the infinite elements is to transmit stress waves at all frequencies without generating numerical reflections which would distort the geophone histories, and to approximate the far-field stress conditions. The fifth stage was to decide on the seismic source representation. This can be achieved by prescribing a source based on relevant seismic data, or by allowing the fault/dyke structure to slip according to a frictional slip law. Both alternatives were attempted. Assumptions were also made as to how the friction became mobilized on the fault surface. Thereafter, numerous numerical experiments were performed to test the sensitivity of different parameters, and to "calibrate" the model against the available seismic and damage data.

Various friction-weakening laws were used, with friction being specified as a function of time, as shown in figure 5 (no cohesion weakening law was available). The relationship that produced results that matched seismic data most closely was a simple linear degradation in

friction from a high static value (of 60°) at time $t = 0$ to a lower value (of 15°) at time $t =$ 50 ms (see figure 5). Fault cohesion was assumed to be zero. A linear degradation of friction with time is a numerical technique to tune the model results. In other words, a sudden release of friction will cause slip to occur more violently than a slower release of friction would. This implies that the particle velocities at the geophone positions will be higher, and the stress waves will have higher frequencies if slip is allowed to occur more suddenly. Moreover, a weakening law enables slip to start at a point, and spread out dynamically depending on the rate of reduction of friction angle. This is more natural than allowing slip to initiate over a large area simultaneously.

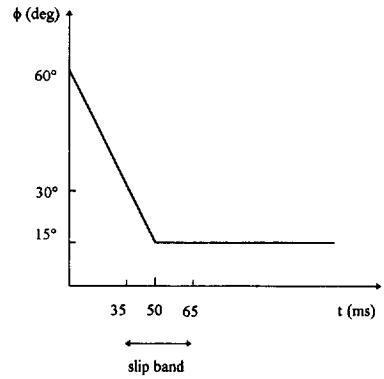

Figure 2.3.6.5: Friction-weakening slip law used in numerical model

Results

The friction-weakening law was applied after obtaining static equilibrium due to the applied stress field. Slip initiates in the hangingwall, at a friction angle of approximately 30°, and progresses until the fault section in the footwall is also activated. The fault in the model was active from time $t = 35$ ms (at 30° friction angle) to 65 ms (at 15° friction angle), as is depicted in figure 2.3.6.5.

Figure 2.3.6.6 compares the measured seismic data with the velocities generated by the model for geophone stations 10, 12, 13, and 14. The poor match in first motions suggests that the source was not a simple slip mechanism, such as was obtained from ESS calculations. Seismic data suggests a significant "pop" component, perhaps associated with crushing or bursting of the dyke into the face area. There is however good agreement between the real and numerical data for peak particle velocities and arrival times. Table 2.3.6.2 quantifies the differences between the observed (OBS) and numerical (NUM) peak particle velocities for each geophone (GEO). The mean ratio, between the two sets of data is approximately 1.0 ± 0.27 (value $\pm$ one standard deviation). Improved knowledge and better representation of the source mechanism would enable the modeller to obtain a better match between observed and numerical waveforms in terms of first motions.

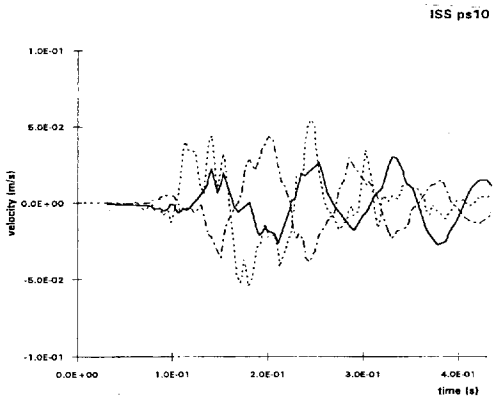

(a) Geophone velocity traces for station 10

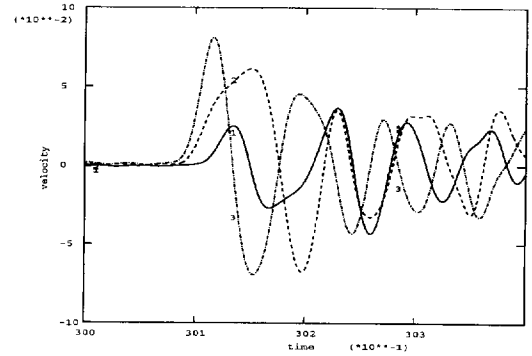

(b) ABAQUS velocities for station 10

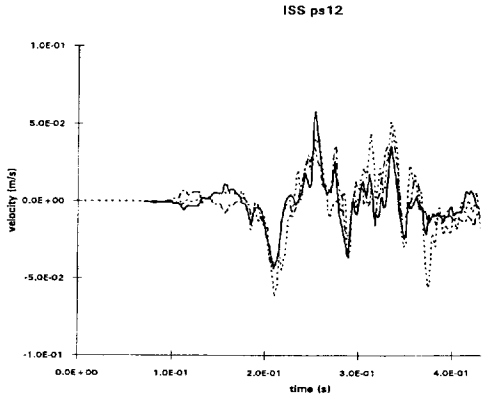

(c) Geophone velocity traces for station 12

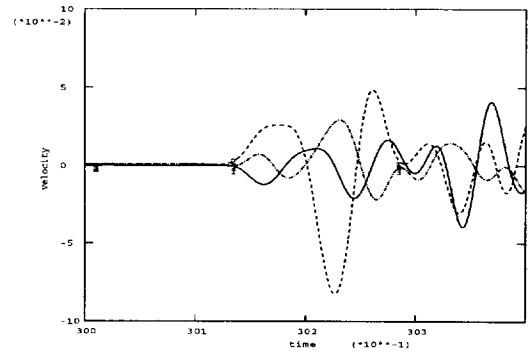

(d) ABAQUS velocities for station 12

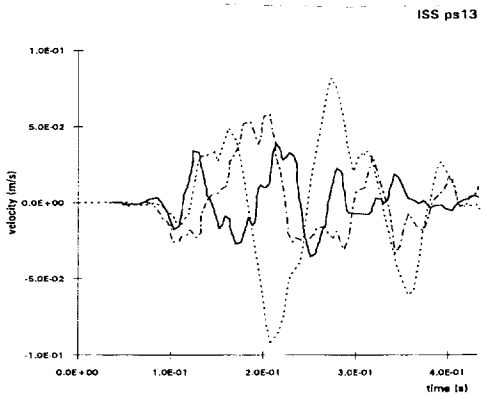

(e) Geophone velocity traces for station 13

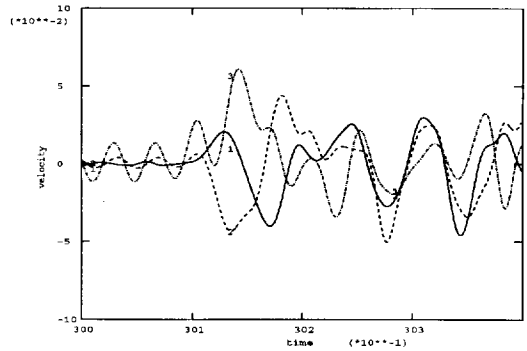

(f) ABAQUS velocities for station 13

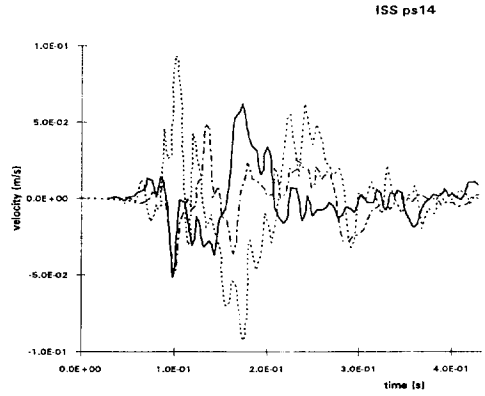

(g) Geophone velocity traces for station 14

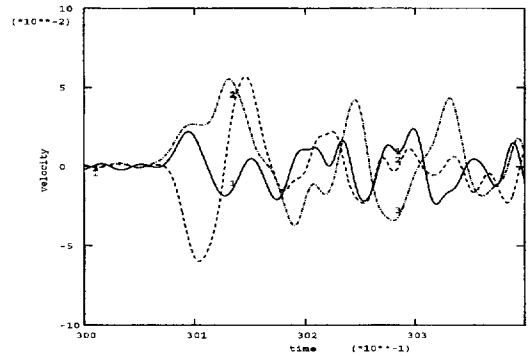

(h) ABAQUS velocities for station 14

Figure 2.3.6.6: Comparison between the geophone and model velocity traces

GEO	OBS	OBS	OBS	NUM	NUM	NUM	NUM /OBS	NUM /OBS	NUM /OBS	Average of NUM/OBS
	V1	V2	V3	V1	V2	V3	V1	V2	V3	ALL V
PS10	0.03	0.05	0.05	0.04	0.07	0.07	1.3	1.4	1.4	1.4
PS12	0.06	0.06	0.04	0.04	0.08	0.03	0.7	1.3	0.8	0.9
PS13	0.04	0.09	0.06	0.05	0.04	0.06	1.3	0.4	1.0	0.9
PS14	0.06	0.09	0.05	0.03	0.06	0.06	0.5	0.7	1.2	0.8

Table 2.3.6.2: Peak particle velocities (m/s) and ratios between observed (OBS) and numerical (NUM) data

In figure 2.3.6.7, comparisons are made between actual damage and particle velocity predicted by the model. Figure 2.3.6.7(a) shows a damage map, compiled by the Rock Mechanics department of the mine, indicating where the most damage to mine workings occurred as a result of the rockburst. The degree of damage is indicated by three different cases: severe, moderate, and minor. Severe damage implies that there were major rock falls, support was destroyed, and the area was considered dangerous to enter. Major clean-up and re-supporting was necessary. Moderate damage implies that there were widespread rock falls, some support was damaged and minor clean-up and repairs to support were required. Minor damage implies that there were scattered falls of ground but the support was still functional, and a minor clean-up was required.

Figures 2.3.6.7 (b) to (e) show contour plots of components of particle velocities at time t = 190 ms. Velocities in (b) to (d) are for a reef-parallel plane just inside the footwall, while (e) is for a reef-parallel plane just inside the hangingwall. The figures were chosen specifically because they represented a snapshot at which particle velocities were largest, and all indicate good agreement with the damage map. Whether or not particle velocities should be used to indicate the potential for rockburst damage, is debatable. In fact, Hsiung *et al.* (1992) have shown that peak particle velocities are not necessarily a sufficient measure of the potential for rockfalls or rockbursts. The accumulation of a large number of small events can have a greater damaging effect than a single event with high peak particle velocities. However,

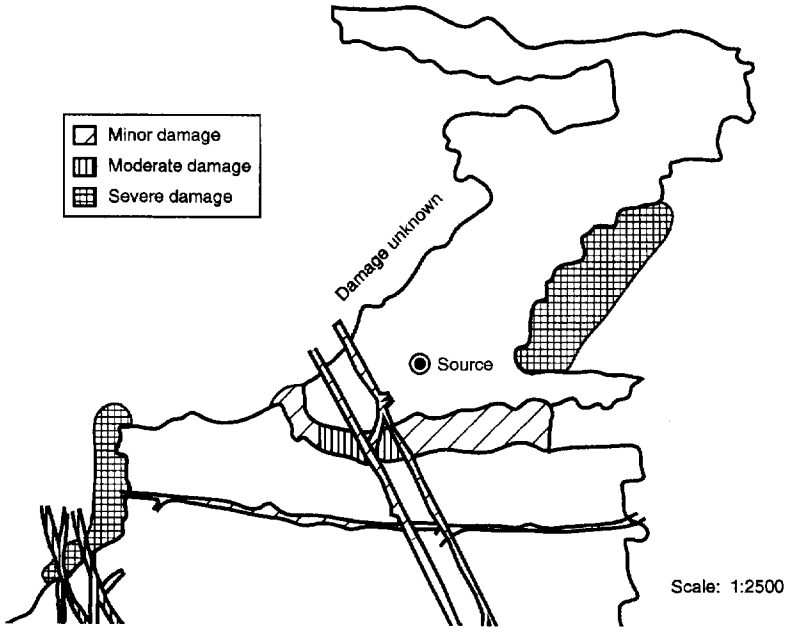

(a) Damage map from the mine's Rock Mechanics department

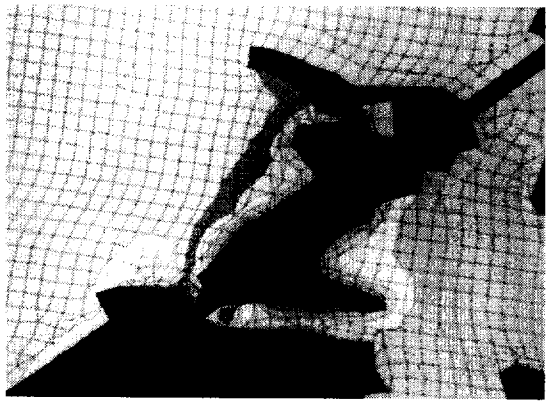

(b) x_1 component of footwall velocity

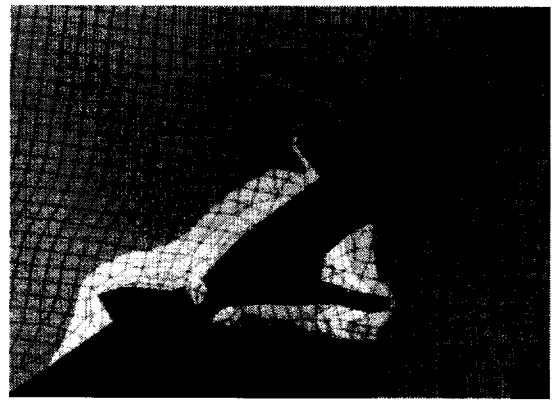

(c) x_2 component of footwall velocity

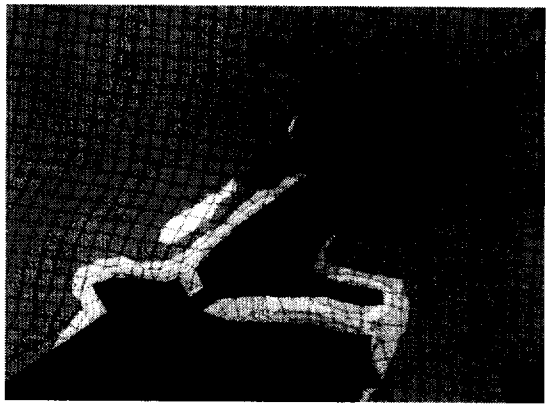

(d) x_3 component of footwall velocity

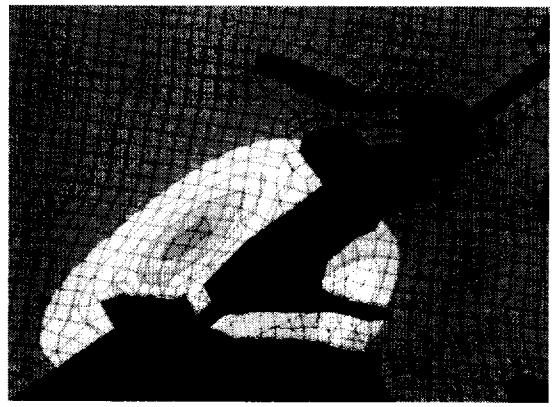

(e) x_2 component of hangingwall velocity

Figure 2.3.6.7: Comparison between the mine's recorded damage map and contours of particle velocity in the model at time t=190ms

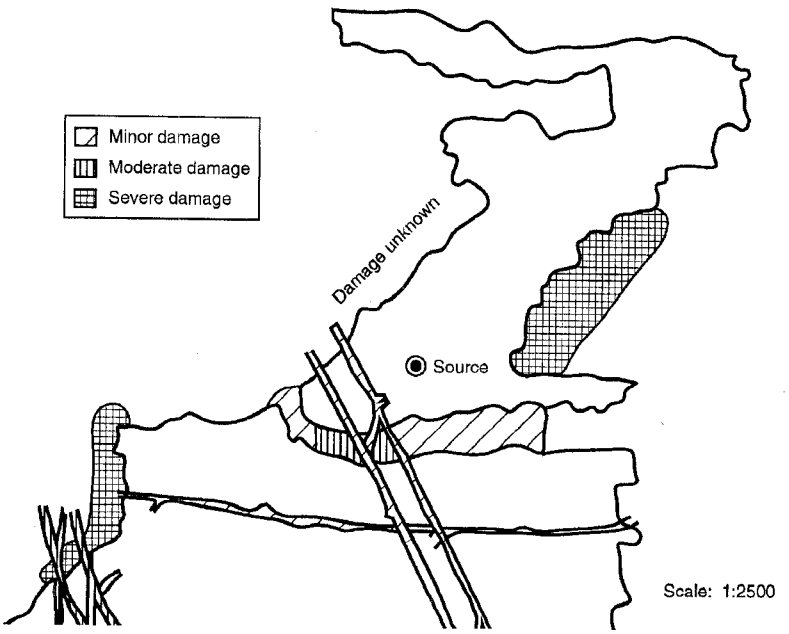

(a) Damage map from the mine's Rock Mechanics department

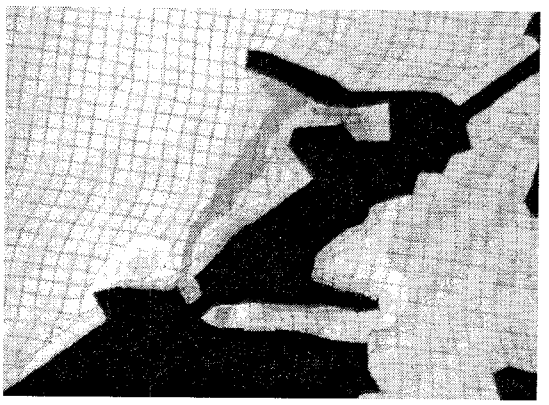

(b) x_1 component of footwall velocity

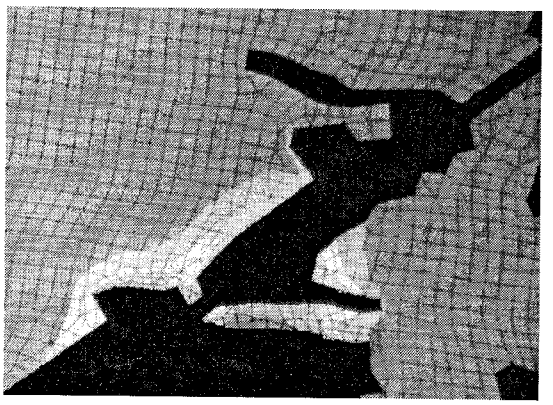

(c) x_2 component of footwall velocity

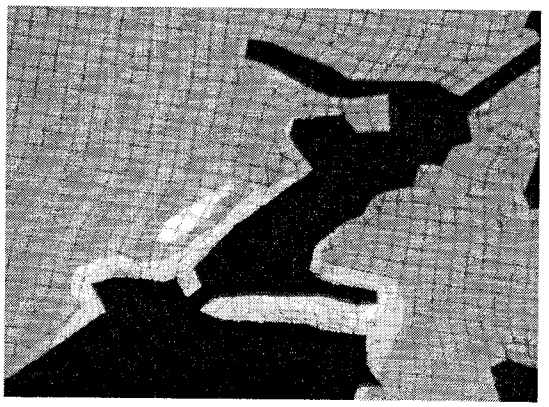

(d) x_3 component of footwall velocity

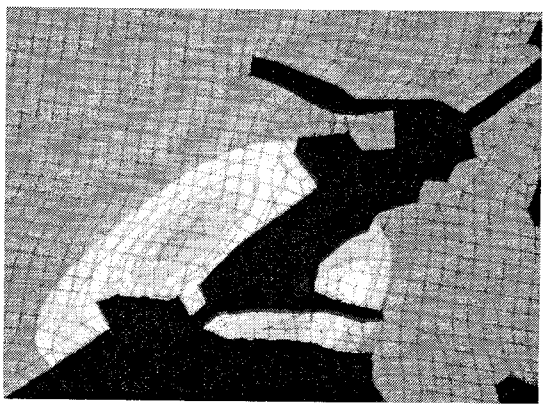

(e) x_2 component of hangingwall velocity

Figure 2.3.6.7: Comparison between the mine's recorded damage map and contours of particle velocity in the model at time t=190ms

given a particular hangingwall, a *single* event that generates higher peak particle velocities can be expected to generate more damage. This rockburst back-analysis should be repeated for a non-damaging event in the same mining area in order to make a more definite statement about the effect of particle velocity on possible damage to mine excavations.

The peak particle velocity obtained from the numerical analysis is approximately 1.4 m/s, which compares well with the (near field) analytical value of $\sigma_s/(\rho c_2)$ = 15 x 10^6 / (2700*3500) = 1.6 m/s for a shear driven source (Freund 1990, p98), where σ_s is the dynamically applied shear traction loading. This value compares very favourably with other mine seismic data, and the numerical result is plotted in figure 2.3.6.8. Notice that particle velocities above 1.5 m/s are sufficient to cause stope convergence rates of over 3 m/s (McGarr 1993) - sufficient to cause failure of rapid-yielding hydraulic props. Numerically determined stope convergence rates were lower than this threshold and, from figure 2.3.6.7 (b) and (d), a typical value of approximately 1.0 m/s was achieved. It is unlikely that particle velocities of this magnitude are sufficient to cause the extent of damage that was associated with this rockburst. This may indicate an insufficiency in the continuum-based modelling approach, viz. particle velocities are not amplified in the highly fractured rock mass close to the mining excavations because the rock mass is assumed to be unfractured.

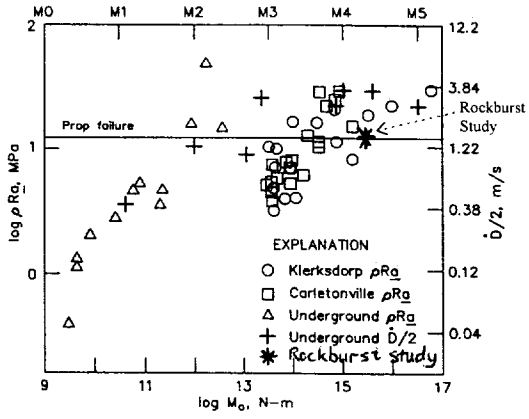

Figure 2.3.6.8: Peak particle velocity versus *log* (M_0) [after McGarr 1993]

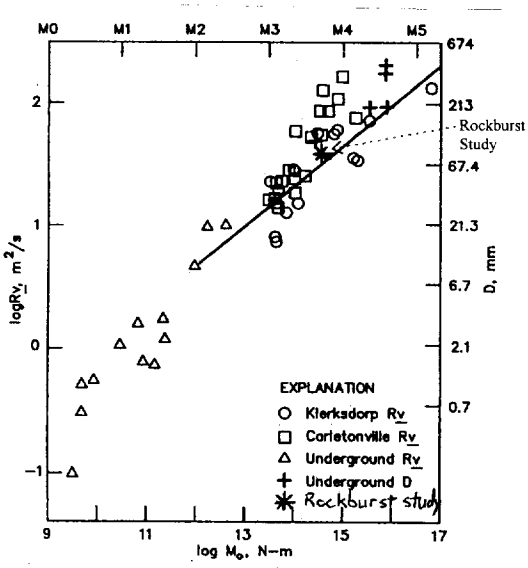

Figure 2.3.6.9: *Log* (R^*v_{max}) versus *log* (M_0) [after McGarr 1993]

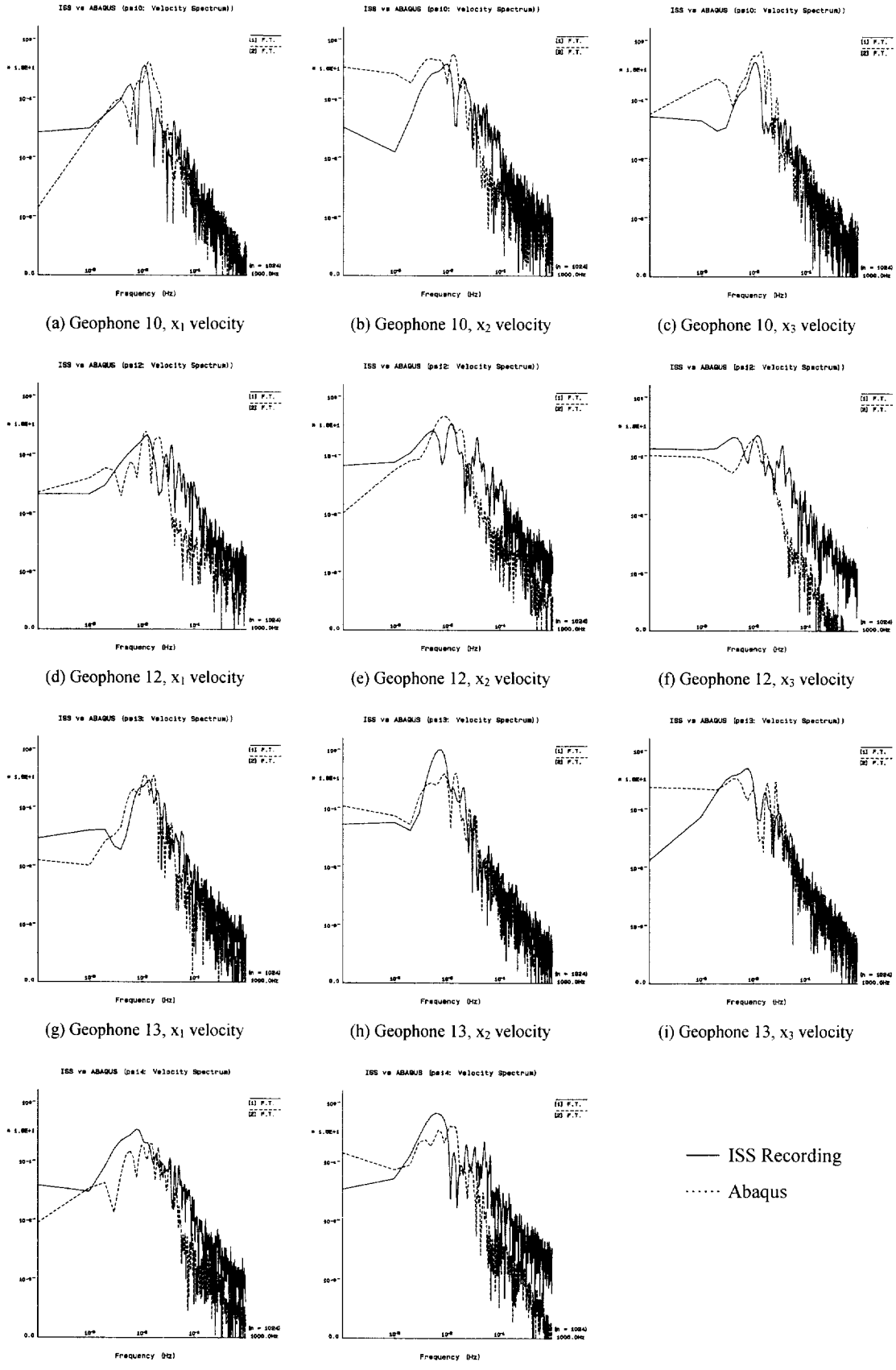

(a) Geophone 10, x_1 velocity (b) Geophone 10, x_2 velocity (c) Geophone 10, x_3 velocity

(d) Geophone 12, x_1 velocity (e) Geophone 12, x_2 velocity (f) Geophone 12, x_3 velocity

(g) Geophone 13, x_1 velocity (h) Geophone 13, x_2 velocity (i) Geophone 13, x_3 velocity

(j) Geophone 14, x_1 velocity (k) Geophone 14, x_2 velocity

Figure 2.3.6.10: Comparison between the observed and numerical velocity spectra

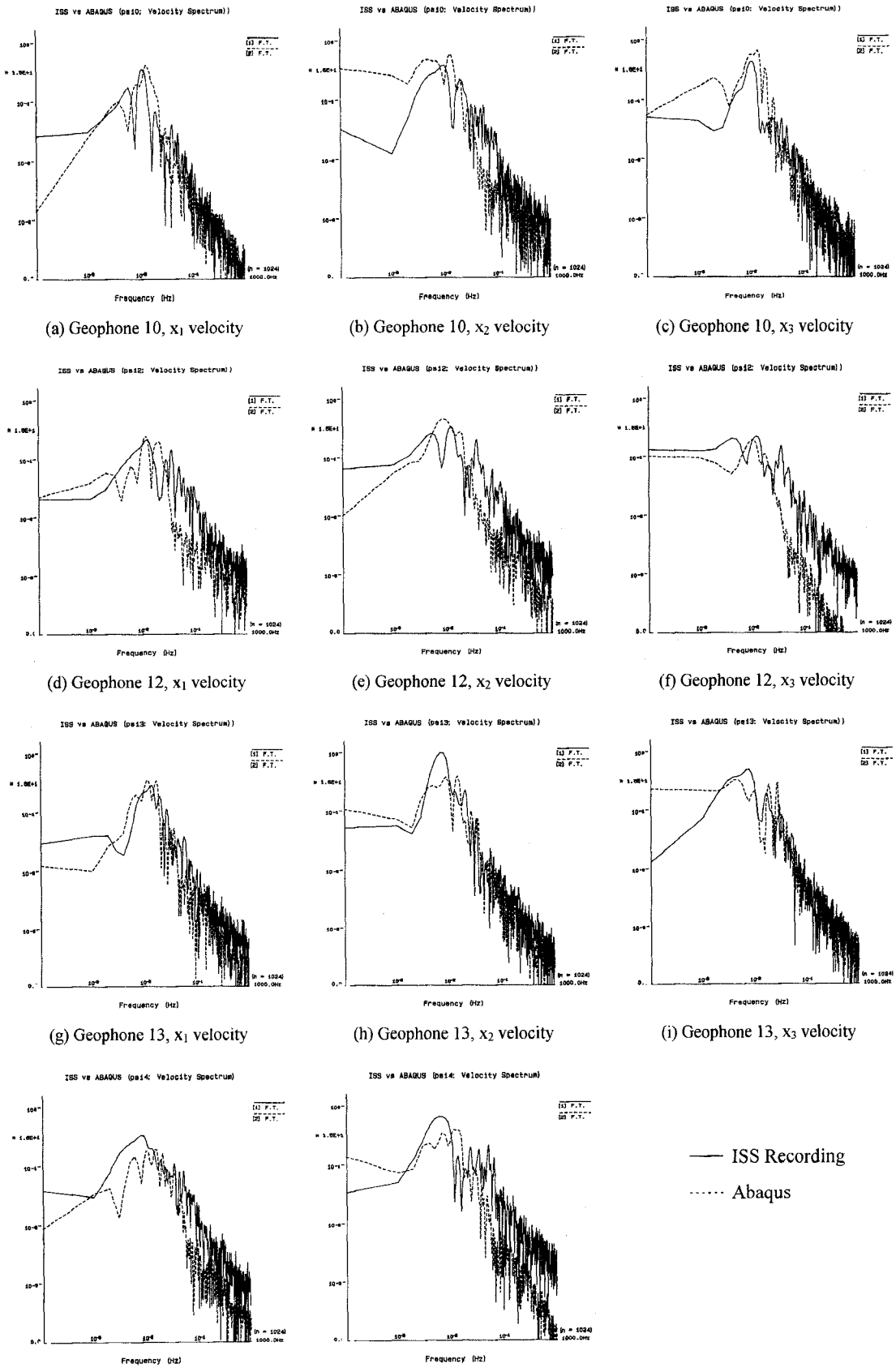

(a) Geophone 10, x_1 velocity (b) Geophone 10, x_2 velocity (c) Geophone 10, x_3 velocity

(d) Geophone 12, x_1 velocity (e) Geophone 12, x_2 velocity (f) Geophone 12, x_3 velocity

(g) Geophone 13, x_1 velocity (h) Geophone 13, x_2 velocity (i) Geophone 13, x_3 velocity

(j) Geophone 14, x_1 velocity (k) Geophone 14, x_2 velocity

Figure 2.3.6.10: Comparison between the observed and numerical velocity spectra

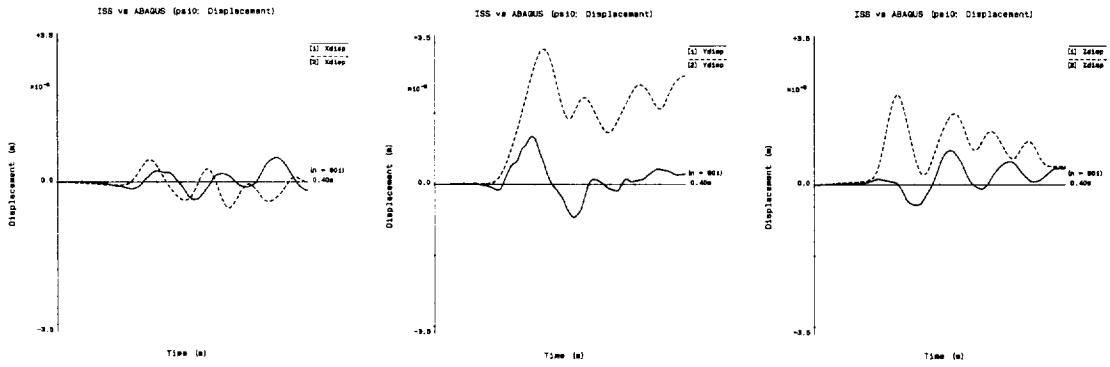

(a) Geophone 10, x_1 displacement (b) Geophone 10, x_2 displacement (c) Geophone 10, x_3 displacement

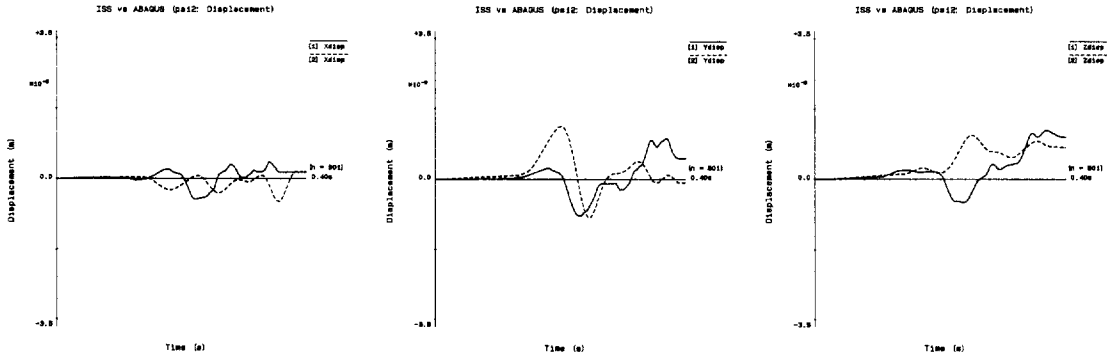

(d) Geophone 12, x_1 displacement (e) Geophone 12, x_2 displacement (f) Geophone 12, x_3 displacement

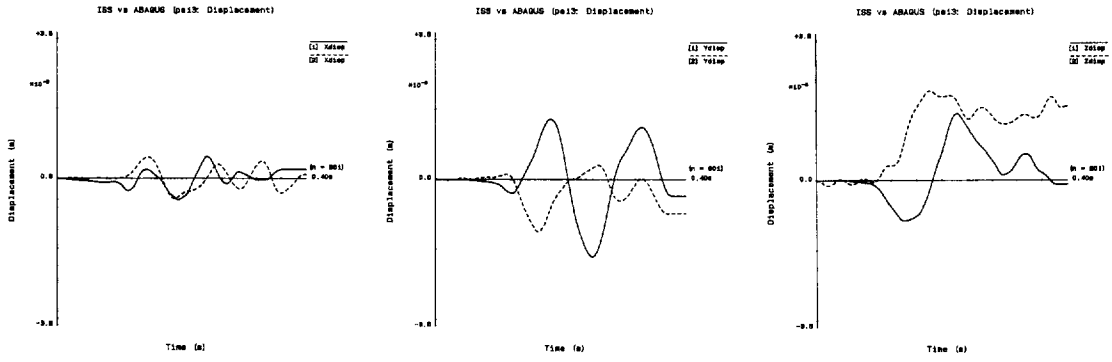

(g) Geophone 13, x_1 displacement (h) Geophone 13, x_2 displacement (i) Geophone 13, x_3 displacement

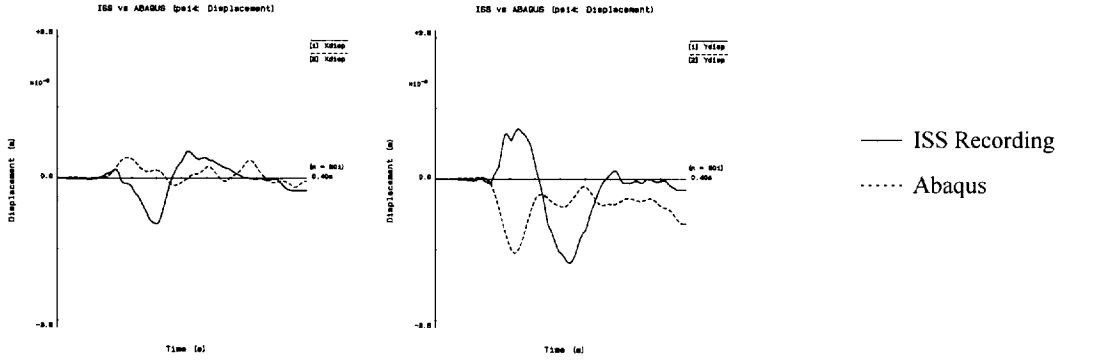

(j) Geophone 14, x_1 displacement (k) Geophone 14, x_2 displacement

Figure 2.3.6.11: Comparison between the observed and numerical displacement histories

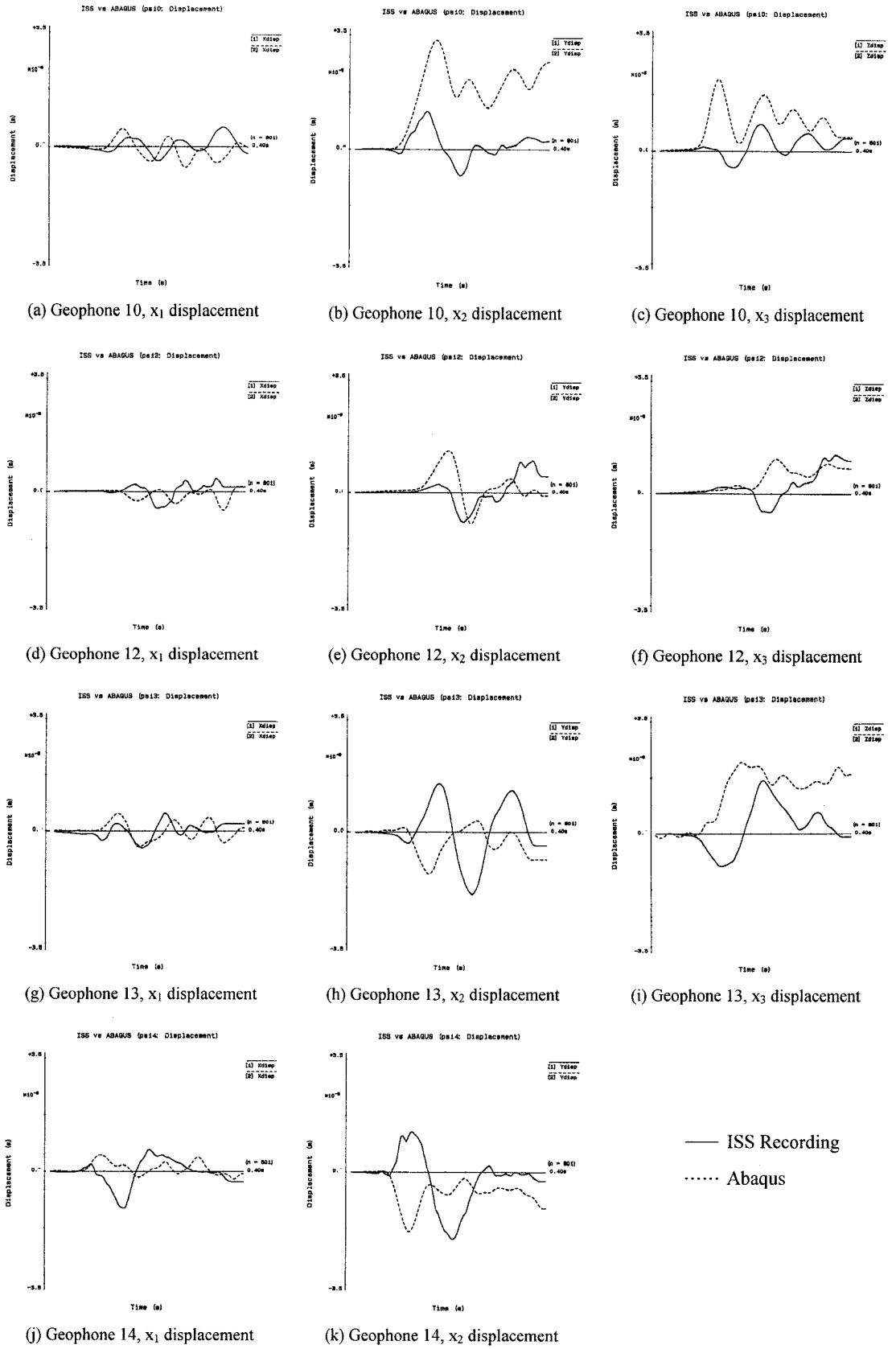

(a) Geophone 10, x_1 displacement (b) Geophone 10, x_2 displacement (c) Geophone 10, x_3 displacement

(d) Geophone 12, x_1 displacement (e) Geophone 12, x_2 displacement (f) Geophone 12, x_3 displacement

(g) Geophone 13, x_1 displacement (h) Geophone 13, x_2 displacement (i) Geophone 13, x_3 displacement

(j) Geophone 14, x_1 displacement (k) Geophone 14, x_2 displacement

Figure 2.3.6.11: Comparison between the observed and numerical displacement histories

Observed and numerical values of $log\ (R^*v_{max})$ for the four geophones are tabulated in Table 2.3.6.3. The mean value of 1.4 ± 0.2 m^2/s (same for observed and numerical) is shown in figure 2.3.6.9.

GEO	R	OBS v_{max}	OBS $log(R^*v_{max})$	NUM v_{max}	NUM $log(R^*v_{max})$
PS10	345	0.05	1.2	0.07	1.4
PS12	594	0.06	1.6	0.08	1.7
PS13	312	0.09	1.4	0.06	1.3
PS14	298	0.09	1.4	0.06	1.3

Table 2.3.6.3: Observed (OBS) and numerical (NUM) values of $log\ (R^*v_{max})$ for the geophones

Analysis of the frequency content of the observed and simulated wave forms reveals that the corner frequencies are well matched in all cases (figure 2.3.6.10). Stations 12 and 14 are not well matched for higher frequencies, as opposed to stations 10 and 13, which match well. This could indicate a cut-off in the frequencies that the numerical model is able to cope with. Mesh resolution studies would determine whether the higher frequencies could be better matched by reducing the element size. It is not meaningful to compare the low frequencies as this part of the frequency spectrum is based on very limited data.

The displacement waveforms obtained by numerical integration of the velocities are compared in figure 2.3.6.11, and show that the source mechanism used in the numerical model was poorly matched to the real one. Once again, more detailed knowledge of the observed source mechanism would aid the modeller in obtaining a much better match between real and synthetic waveforms.

Conclusions

This work implements a three-dimensional elastodynamic numerical model of a rockburst event, and demonstrates that by using a dynamic fault slip model with time dependent friction weakening the results of numerical models can be adjusted to resemble in certain respects real seismic data. However, there are numerous factors related to source specifications, rock material parameters, and damage properties that need to be taken into account, all of which could have an influence.

The above analysis represents the first rudimentary attempts to reproduce real mine data. It should be emphasized that much useful information can still be obtained by investigating idealized geometries as well as real data - for example examining dynamic stope deformations and support requirements for different mining layouts. The results are nevertheless sufficiently encouraging to suggest that back analysis is possible, and further attempts are recommended.

It would be interesting to see the effect on the model of taking into account the non-linear nature of the rock mass. The same runs could be repeated with a dynamic damage material model in order to examine the effects of a damaged rock mass on the numerical geophone data.

This type of modelling can benefit from sensitivity analyses, and it would have been desirable to experiment with a number of aspects of this model - such as different source mechanisms, representation of the fracture zone, cumulative damage - to determine their effects, and in an attempt to match the seismic records more closely.

In theory the huge efficiency advantages and model turn-around times using WAVE would make it a most useful tool in this respect. WAVE however has limitations in modelling general geometries, more complex material for the fracture zone, static boundaries and cumulative damage. Combining the efficiency of WAVE with these features would have great potential for back-analysis. Initial attempts at back-analysis using WAVE are currently in progress on mine geometries which are approximately orthogonal.

It should also be emphasized that any prediction of rockbursts is impossible with these numerical models. In order to attempt to predict rockbursts, an absolute minimum requirement would be a history of past seismicity with ongoing seismic monitoring of the mine, both of which are completely excluded from this numerical study. It may however be possible, that modelling related to seismic records could ultimately be used to understand aspects of a mine geometry such as the condition of material in various parts of the mine.

Acknowledgments

Thanks are expressed to the Rock Mechanics Department of the mine involved, for their help in providing the seismic data, damage map, and mine plans, and permission to perform the study.

REFERENCES

ABAQUS/EXPLICIT (1994). version 5.3-1, Hibbit, Karlsson, and Sorensen, Inc., Rhode Island.

Aki, K. and Richards, P.G. (1980). *Quantitative Seismology Theory and Methods*: volume I, W.H. Freeman and Co., New York, p. 61.

ARIES (1992). version 5.3, The MacNeal-Schwendler Corp, Los Angeles.

Bigarre, P., Slimane, K.B. and Tinucci, J. (1993). 3-dimensional modelling of fault-slip rockbursting, in: *Rockbursts and Seismicity in Mines* (ed: Young), Balkema, Rotterdam, pp 315-319.

Brune, J.N. (1970). Tectonic stress and spectra of seismic shear waves from earthquakes, *J. Geophys. Res.*, 75, 4997-5009. (correction: *J. Geophys. Res.*, 76, 5002, 1971).

Frankel, A. (1993). Three-dimensional simulations if ground motions in the San Bernardino Valley, California, for hypothetical earthquakes on the San Andreas fault, *Bull. Seism. Soc. Am..*, 83, 1020-1041.

Freund, L.B. (1990). *Dynamic Fracture Mechanics*, Cambridge University Press, Cambridge.

Hart, R.D., Board, M., Brady, B., O'Hearn, B. and Allan, G. (1988). Examination of fault-slip induced rockbursting at the Strathcona mine, in: *Key Questions in Rock Mechanics* (eds: Cundall *et al.*), Balkema, Rotterdam, 369-379.

Hsiung, S-M, Chowdury, A.H. Blake, W., Ahola, M.P. and Ghosh, A. (1992). Field site investigation: Effect of mine seismicity on a jointed rock mass, NRC-02-88-005, Center for Nuclear Waste Regulatory Analyses, San Antonio.

Keilis-Borok, V.I. (1959). On estimation of the displacement in an earthquake source and of source dimensions, *Annali di Geofisica.*, 12, 205-214.

McGarr, A.M. (1984). Some applications of seismic source mechanism studies to assessing underground structures, Proc: *1st int. Conf. on Rockbursts and Seismicity in Mines* (eds. Gay and Wainwright), Johannesburg, 1982, SAIMM, 199-208.

McGarr, A. (1993). Keynote address: Factors influencing the strong ground motion from mining-induced tremors, in: *Rockbursts and Seismicity in Mines* (ed. Young), Balkema, Rotterdam, 3-12.

Mendecki, A.J. (1993). Keynote address: Real time quantitative seismology in mines, in: *Rockbursts and Seismicity in Mines* (ed. Young), Balkema, Rotterdam, 287-295.

MINSIM-D. (1987). version PC1, COMRO, Johannesburg.

Yomogida, K. and Etgen, J.T. (1993). 3-D wave propagation in the Los Angeles Basin for the Whittier-Narrows Earthquake, *Bull. Seism. Soc. Am.*, 83, 1325-1344.

2.4 PHYSICAL MODELLING OF ELASTODYNAMIC PROBLEMS

The work reported here addresses SIMRAC objective 1.3.

In South African deep level gold mining, rockburst and rockfall related accidents account for approximately 40% (Heunis 1980) of the fatalities. Due to high geological and mining-induced stresses, sudden shear can occur on planes of weakness, and the resulting seismic waves which interact with mining excavations can, in many cases, trigger rockbursts and rockfalls. To reduce the fatality rate and continue mining at ever increasing depths, it is necessary to spend considerable effort on investigations dealing with mining related seismicity.

Theoretical aspects of wave propagation and the interaction of stress waves with discontinuities such as cracks and the interface between two dissimilar media have been investigated in numerous studies. Amongst them Achenbach (1973), Brekhovskikh (1960), Rinehart (1975), Borejko *et al.* (1992) and Fokkema (1981) have concentrated on the geophysical aspects of wave interaction with geometrical discontinuities.

In spite of the large number of available theoretical analyses, it is difficult to obtain quantitative information of wave interaction in terms of stress magnitudes of real wave pulses. Of the few experimental analyses that have been conducted, dynamic photoelasticity has been used successfully in two-dimensional models. The photoelastic technique offers full-field visualisation and allows qualitative and quantitative interpretation of the complicated behaviour associated with actual stress waves interacting with discontinuities.

This study concentrates on the application of the photoelastic method to investigate stress wave interactions with a stope and the effects of propagating waves on cohesive and non-cohesive parting planes separating the rock massif from the stope hangingwall beam. The dynamic finite difference program WAVE (Hildyard *et al.* 1995) is used to back-analyse the photoelastic experiments. The purpose of the numerical investigation was to assess the accuracy of the WAVE analyses when modelling stress waves propagating through layered media.

2.4.1 Using dynamic photoelasticity to investigate stress waves interacting with stopes

The gold mined in South Africa occurs typically in tabular ore deposits. Narrow stopes give access to the reef, and the interaction between the mining excavations and the geological and dead-weight stresses leads to stress concentrations in the stope vicinity. Geological planes of weakness such as faults and the interface between dykes and the rock massif are loaded by the stress concentrations, and sudden rupture can occur. The resulting seismic waves interact with mining excavations, in some cases triggering rockbursts and rockfalls.

Figure 2.4.1.1 shows an idealised stope and some geological and mining induced features, namely (1) parting planes (stope parallel geological features offering little or no cohesion), (2) shear fractures and (3) extension fractures (Adams *et al.* 1981). Also shown is the idealised stope model used in this study. A horizontal slot, representing the stope, is cut into a strip of bi-refringent material (Makrolon) with a lower impedance than the Araldite B bi-refringent material. The Makrolon represents the heavily fractured, and thus softer, hangingwall and footwall beam, whilst the stiffer Araldite B models the surrounding rock massif. The interface between Makrolon and Araldite B is either glued or left unglued, thereby representing either a cohesive or non-cohesive parting plane.

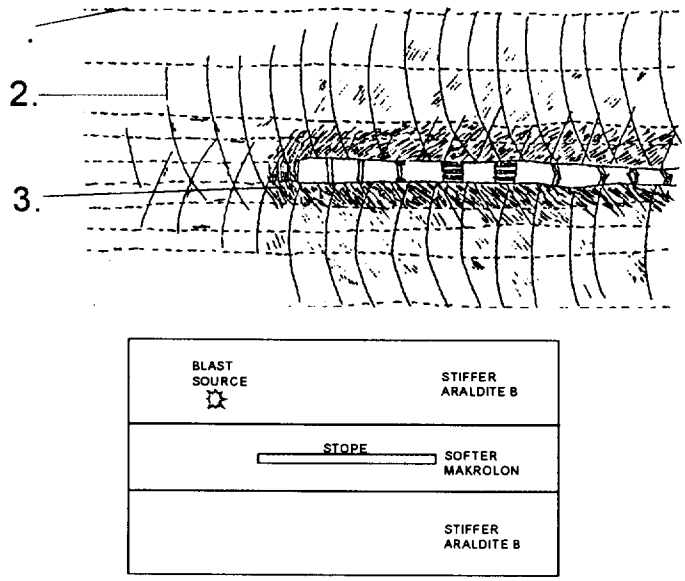

Figure 2.4.1.1 Typical mining geometry in a South African gold mine (Adams *et al.*, 1981). Also shown is the simplified model used for the photoelastic experiments.

Mining induced seismicity is usually associated with shear type events. However, no experimental technique exists currently to generate shear type events in photoelastic models. In this study stress waves are initiated by a point blast source, located in the hangingwall so that the blast induced waves travel through the fractured hangingwall rock and interact with the stope. Dynamic photoelasticity, in conjunction with high speed photography, has been used to analyse the interaction between stress waves and an open slot. The modelling techniques of dynamic photoelasticity are well documented and detailed descriptions can be found in Dally and Riley (1978), and Rossmanith and Fourney (1983).

The plane models are cut from 6 mm thick Makrolon and Araldite B plate. Using circularly polarised monochromatic light, optical interference of the bi-refringent material produces isochromatic fringe patterns, where an isochromatic contour is a line of equal maximum shear stress. The order of interference N is related to the state of stress in the model by the stress-optic law, $\sigma_1 - \sigma_2 = N f_\sigma / h$ (Dally and Riley 1978), where σ_1 and σ_2 are the principal stresses, f_σ is the material fringe value and h is the model thickness.

Wave propagation through three model geometries (Models A, B and C) was investigated. Model A was constructed from Araldite B and was used to investigate the stress wave interaction with the stope in a homogeneous medium. Model B included a Makrolon layer in the model centre, the interface between the Makrolon and the Araldite B being bonded; the glued interface represents a cohesive parting plane, while the Makrolon layer above and below the stope represents the fracture softened hangingwall and footwall beam. Model C consists of the same elements as Model B, however the interface between the Araldite B and Makrolon was not bonded to allow the wave interaction with a non-cohesive parting plane to be investigated.

To represent the geological stresses at depth, the models were placed in a rigid frame and the boundaries loaded by hydraulic jacks to 5,8 kN in the vertical direction and 3,0 kN in the horizontal direction, giving a k ratio of approximately 0,5. These were the maximum loads the models could sustain without becoming unstable and buckling.

A Cranz-Schardin (1929) type multiple spark gap camera was used to record the dynamic fringe patterns. The camera is triggered by detonation of the explosive and the exposure of the first negative occurs after a selected delay period. Twenty four frames were recorded at discrete times during the dynamic event at a framing rate of 220 000 frames per second. A short exposure time of 200 ns is necessary to record sharp photographic images of moving fringe patterns.

Numerical analysis procedure

The analysis of actual stress pulses was used to evaluate the dynamic finite difference program WAVE in terms of its accuracy and modelling capabilities. WAVE is a program that models wave propagation in a two- or three-dimensional elastic medium. Second order interlaced finite difference equations are used on an orthogonal grid with uniform grid spacing. WAVE has the ability to model grid-aligned dislocations which can represent faults and tabular stopes, as well as incorporating various material properties.

WAVE analyses were completed in two steps: During Step 1 the stress field was applied to the model, and the program cycled until the velocities in the finite difference mesh were low enough (< 1 % of velocities generated by blast waves) to approximate the equilibrium state. In Step 2 a point blast source generated stress waves which interacted with the stope and parting planes. Steps 1 and 2 were superimposed in order to obtain the total elastodynamic behaviour.

The WAVE blast source was tailored such that the resulting far field stress pulse approximated the stress amplitude, pulse period and pulse shape of the stress wave propagating through the photoelastic models.

The non-cohesive interfaces were modelled with zero cohesion and with an interface friction angle of 10 degrees.

Photoelastic and numerical results

The interaction of waves with geometric discontinuities results in complicated wave patterns due to the superposition of incident, diffracted, reflected and refracted waves. In many cases most of the waves predicted by theory cannot be identified directly in photoelastic patterns, however the presence of the waves can be deduced from disturbances caused in the fringe patterns of other waves. To help identify some of the weaker waves, each of the photographs describing photoelastic fringes is accompanied by a diagram showing the theoretical wave pattern at that time instant.

The following notation is adopted to identify wave types: longitudinal, transverse, von Schmidt and Rayleigh waves are referred to as P, S, V and R waves respectively. Reflected waves are labelled with subscript r, refracted (transmitted) waves are given the subscript t and diffracted waves are described by subscript d. Waves reflected from the stope are given the additional subscript s. Diffracted waves are labelled with a superscript indicating the slot tip (a or b) at which they are diffracted.

Model A: Stope in a homogeneous medium

After applying the preload, Model A was loaded explosively and the resulting dynamic fringe pattern was recorded by the exposure of 24 photographs. One photograph exposed 92 μs after detonation is chosen to highlight prominent features of the wave interactions. Figure 2.4.1.2 displays the photoelastic fringe patterns and the corresponding theoretical wave pattern.

The incident P-wave has propagated 60 % along the stope hangingwall. The comparatively weak incident shear wave, generated by cracking at the blast hole, is just interacting with stope tip *a*, creating a stress concentration which can be identified by the pseudo caustic at the bottom left hand corner of the slot. The pseudo caustic is formed by nesting of fringes beyond the resolution power of the high speed photographic system. The incident P-wave has attenuated to a maximum fringe value of 7, however at the point of reflection at the slot, the fringe number increases to 11. During reflection at the slot, most of the incident P-wave energy is converted to a prominent shear wave (S_{sr} P). Effects such as fringe islands and the bending of fringes indicate the presence of diffracted P- ($P_d{}^a$ P) and S- ($S_d{}^a$ P) waves. The characteristic wave shape of the Rayleigh wave is apparent in the footwall and 5 fringe lines can be discerned in the subsurface peak. Fringes indicating a von Schmidt wave at $\text{asin}(c_s/c_p) = 35^o$ to the stope between $P_d{}^a$ P and $S_d{}^a$ P can be identified.

Figure 2.4.1.3 shows the isochromatic pattern generated by WAVE at a time of 92 μs after source activation. The WAVE analysis compares very well with the photoelastic results and isochromatic lines indicating the S_{sr} P, diffracted P- ($P_d{}^a$ P) and S- ($S_d{}^a$ P) waves, Rayleigh (R) and von Schmidt (V) waves can be identified.

Model B: Stope in a softened layer bounded by cohesive parting planes

Figure 2.4.1.4 depicts the photoelastic fringes and theoretical wave positions 95 μs after detonation. Most of the incident P-wave energy is refracted in the form of a P-wave (P_t P) across the Araldite B - Makrolon interface, and the energy of the refracted P-wave is converted to a shear wave (S_{sr} P_t P) as reflection occurs at the hangingwall surface. Due to the slight acoustical impedance mismatch between Araldite B and Makrolon (14 % mismatch), only slight bending of the P- and S-waves occurs as the waves propagate from one medium to the next. The epoxy bond between the two bi-refringent material types is not separated by the tensile components of the stress waves, and fringe lines progress smoothly from one material

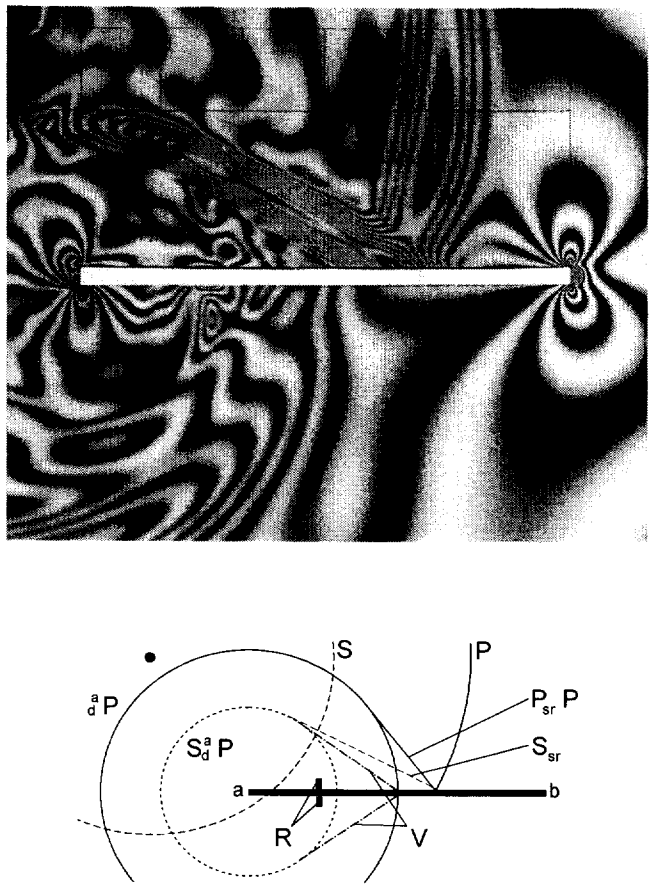

Figure 2.4.1.2 Model A: Photoelastic fringe pattern and theoretical stress wave maxima 92 μs after detonation.

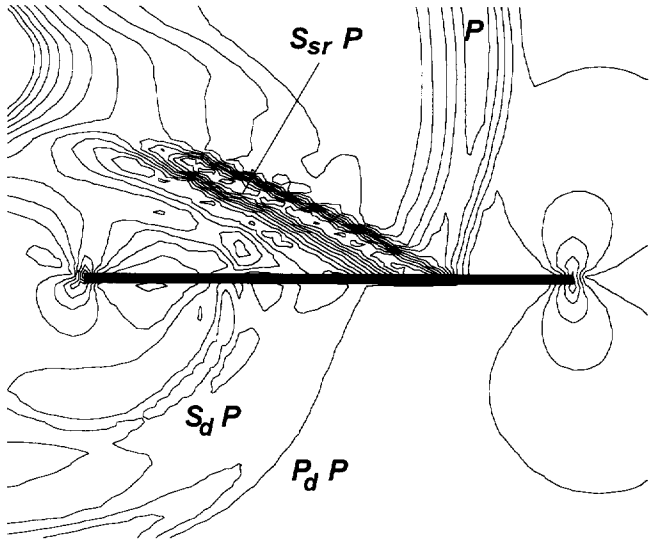

Figure 2.4.1.3 A snapshot in time of isochromatic contours generated by a WAVE analysis 92 μs after blast source activation.

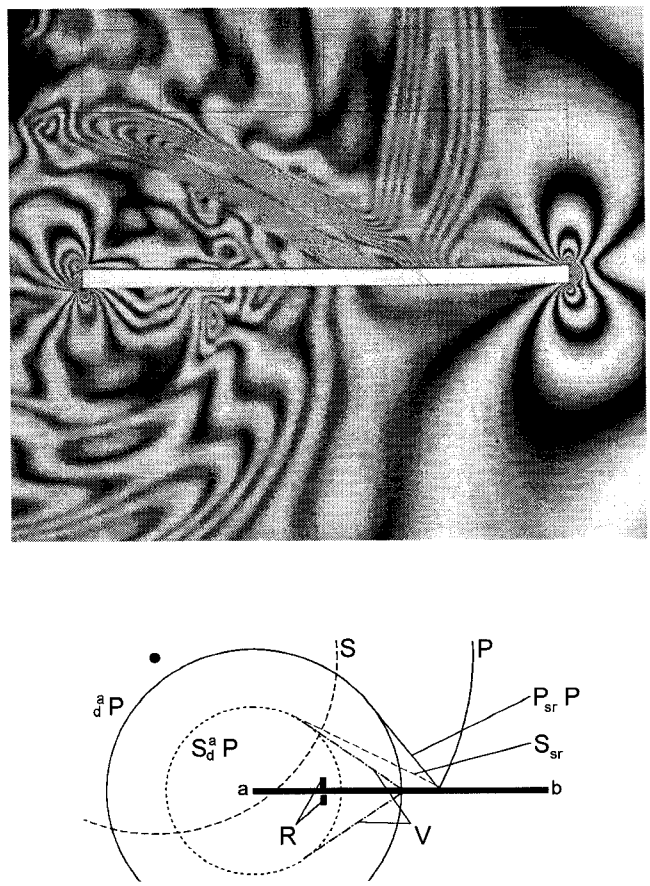

Figure 2.4.1.2 Model A: Photoelastic fringe pattern and theoretical stress wave maxima 92 μs after detonation.

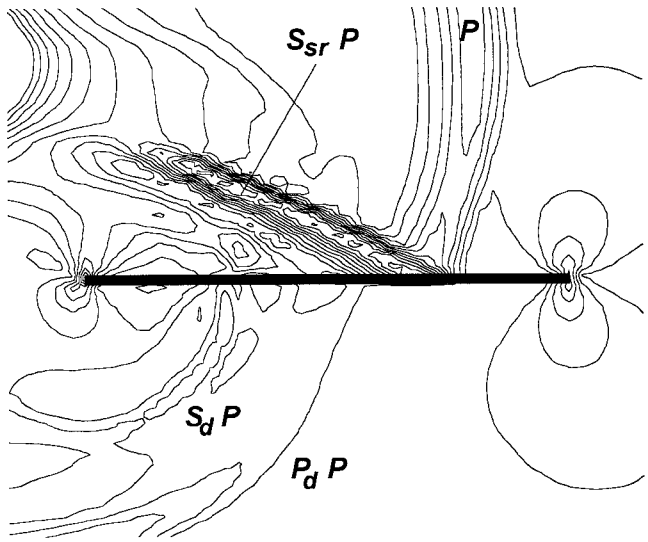

Figure 2.4.1.3 A snapshot in time of isochromatic contours generated by a WAVE analysis 92 μs after blast source activation.

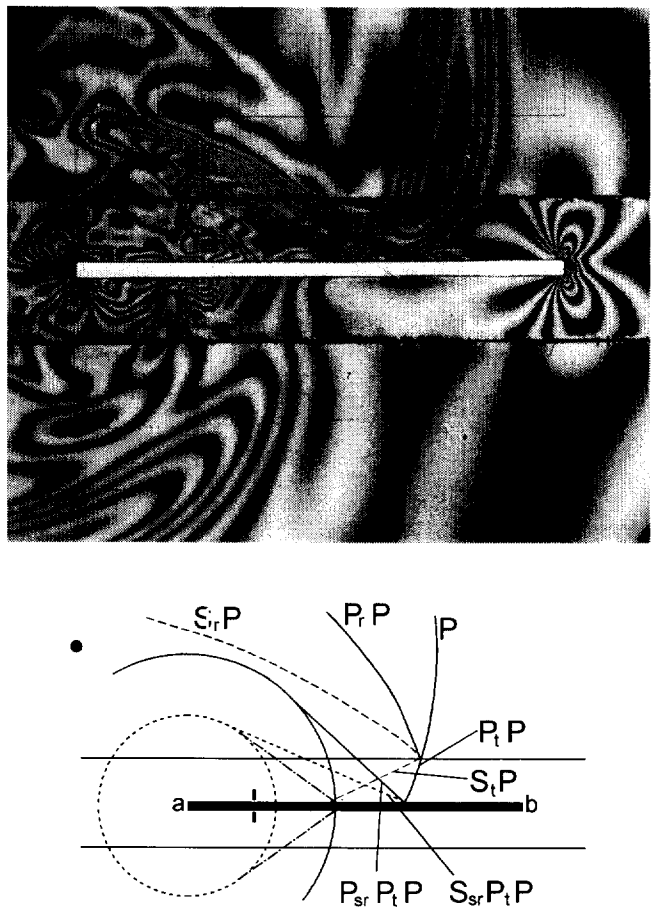

Figure 2.4.1.4 Model B: Photoelastic fringe pattern and theoretical stress wave maxima 95 μs after detonation.

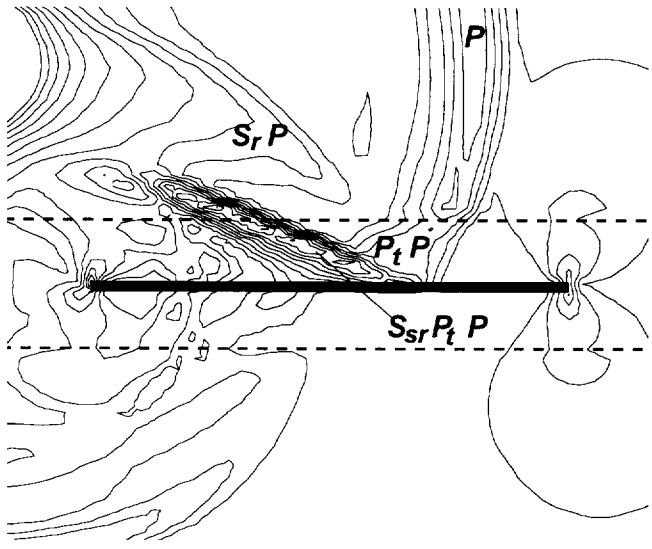

Figure 2.4.1.5 A snapshot in time of isochromatic fringes generated by a WAVE analysis 95 μs after blast source activation.

into the next. Fringe patterns indicating Rayleigh and von Schmidt waves can be identified by comparing the photoelastic fringes with the theoretical wave positions.

Figure 2.4.1.5 shows the isochromatic pattern generated by WAVE 95 μs after source activation. The overall isochromatic WAVE contours compare well with the photoelastic results, and isochromatics indicating the S_r P, P_t P, S_{sr} P_t P as well as von Schmidt waves can be identified.

Model C: Stope in a softened layer bounded by non-cohesive parting planes

The frame chosen to describe wave interaction in Model C was exposed 93 μs after detonation (figure 2.4.1.6 describes the photoelastic fringes and the theoretical wave positions). The energy of the incident P-wave has been partitioned into reflected P- and S-waves, and refracted P- and S-waves. Traces of all four of these wave types are apparent in the photograph, however the most prominent are the S_r P and P_t P wave. As in the photographs describing the fringes of Models A and B, the formation of a strong shear wave due to the reflection of the transmitted P-wave (S_{sr} P_t P) is visible. The S_{sr} P_t P wave is reflected at the Araldite B/Makrolon interface and the energy is redirected back towards the stope in the form of a S_r S_{sr} P_t P and P_r S_{sr} P_t P wave.

The wave pattern of Model C is quite different to that of Model B. The non-cohesive boundary traps energy in the form of reflected waves, whereas the cohesive boundary transmitted most of the shear wave energy. This is an important effect which will influence the dynamic hangingwall behaviour.

The isochromatic contours calculated by WAVE 93 μs after source activation for Model C are displayed in figure 2.4.1.7. Prominent wave types consistent with the photoelastic results are a strong shear wave reflected by the material interface (S_r P), the reflection of the transmitted P-wave at the stope (S_{sr} P_t P), and the high density of reflected waves within the hangingwall beam. The isochromatic contours calculated by the numerical analysis correlate closely to the actual contours observed in the photoelastic experiments.

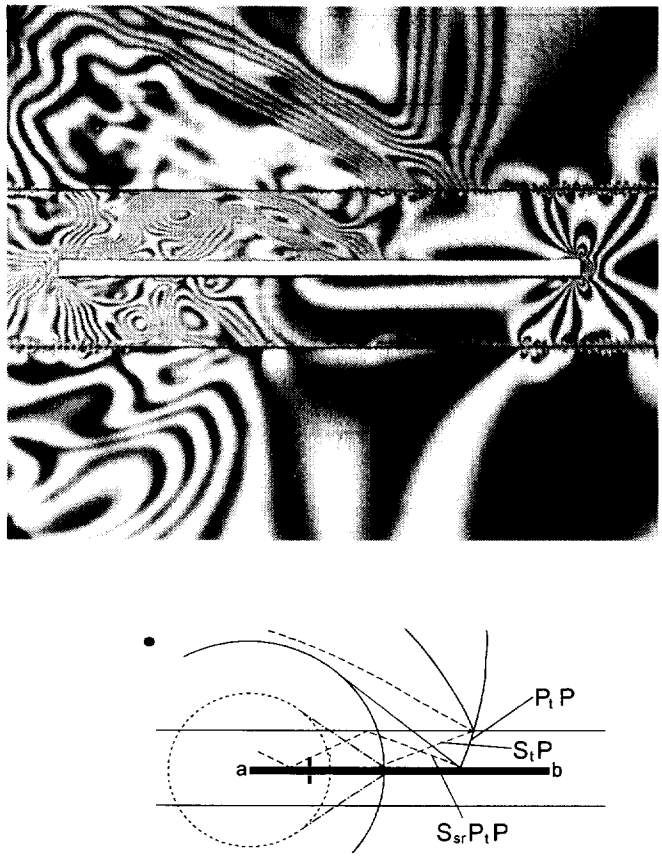

Figure 2.4.1.6 Model C: Photoelastic fringe pattern and theoretical stress wave maxima 93 μs after detonation.

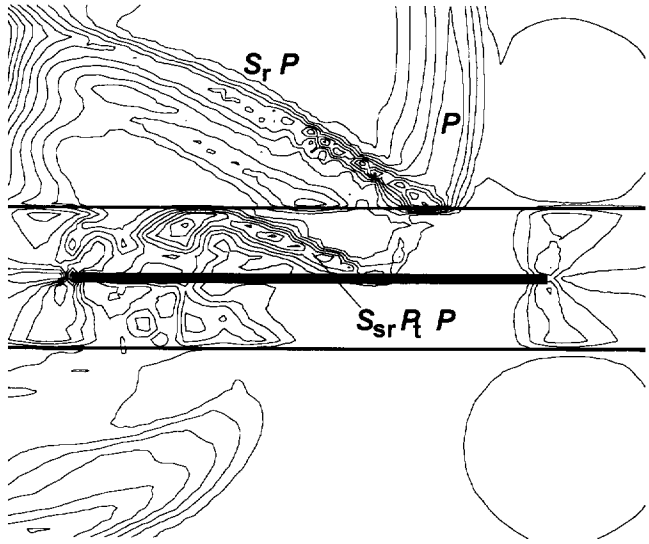

Figure 2.4.1.7 A snapshot in time of isochromatic fringes generated by a WAVE analysis 93 μs after blast source activation.

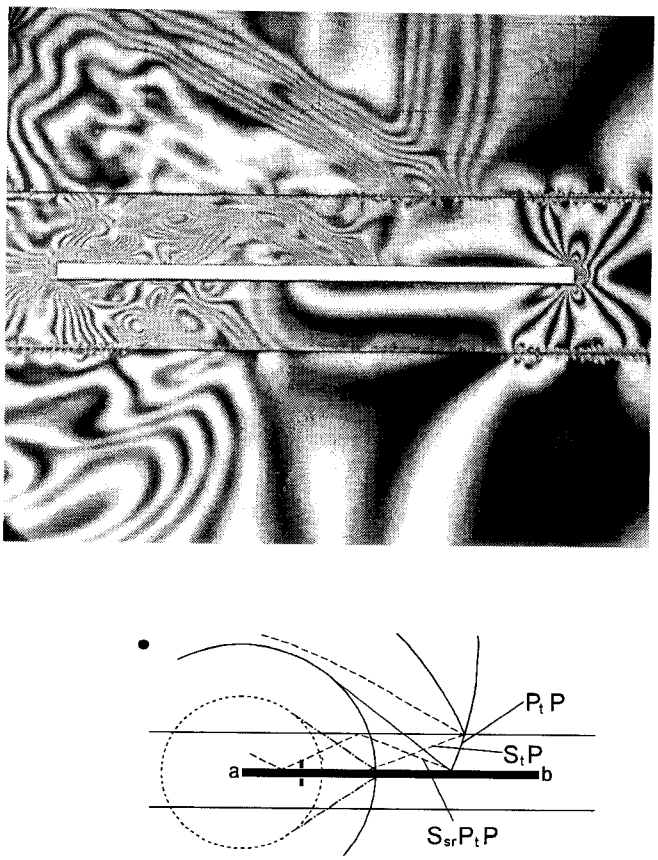

Figure 2.4.1.6 Model C: Photoelastic fringe pattern and theoretical stress wave maxima 93 μs after detonation.

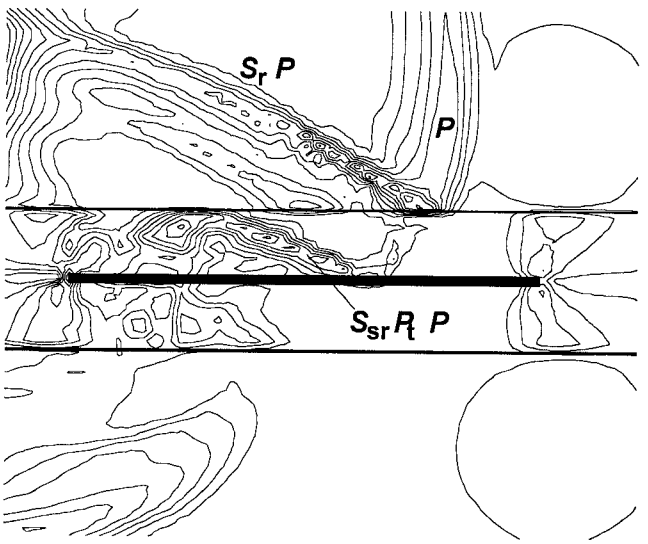

Figure 2.4.1.7 A snapshot in time of isochromatic fringes generated by a WAVE analysis 93 μs after blast source activation.

Analysis of Results

High dynamic stresses in the rock immediately adjacent to the stope are critical as they can initiate rockbursts and rockfalls which endanger human life and disrupt mining operations. By plotting the isochromatic fringe order distribution along the hangingwall skin, the dynamic stresses can be determined, and the effect of cohesive and non-cohesive parting planes can be evaluated. To allow a direct comparison of the stress magnitudes, the fringe orders are normalised relative to the peak stress propagated within the incident P-wave.

It is instructive to plot the stress in three-dimensional form, the two horizontal co-ordinate axes representing hangingwall position (X-axis) and time (Y-axis), and the vertical axis representing normalised dynamic stress ($(\sigma_1 + \sigma_2)/2$). Figures 2.4.1.8, 2.4.1.9 and 2.4.1.10 give the three dimensional plots for the normalised hangingwall skin stress of Models A, B and C, respectively.

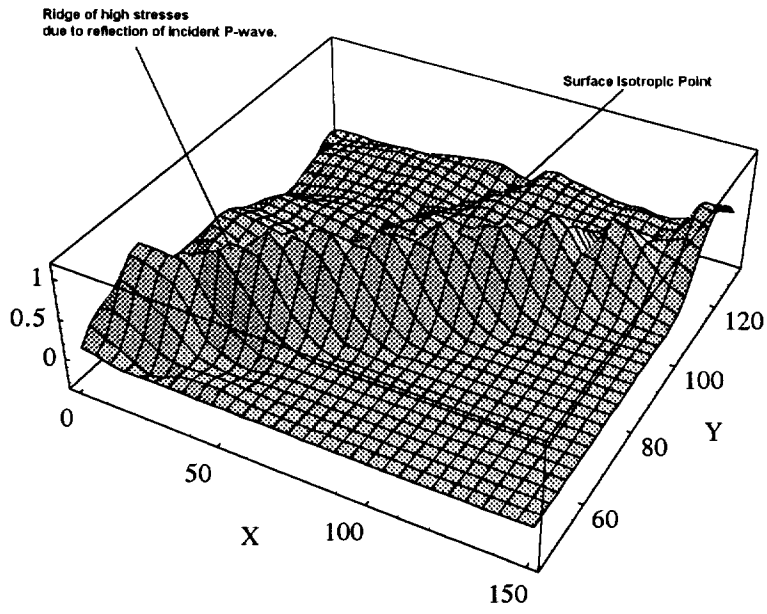

Figure 2.4.1.8 Normalised dynamic stress along the hangingwall skin for Model A as determined from photoelastic experiment.

Model A: The most prominent feature of figure 2.4.1.8 is a ridge of high stresses propagating along the hangingwall at the point where the incident P-wave is reflected. Also apparent is the surface isotropic point (zero stress) bounded by the leading and trailing surface peak of the Rayleigh wave propagating at just under half the P-wave speed.

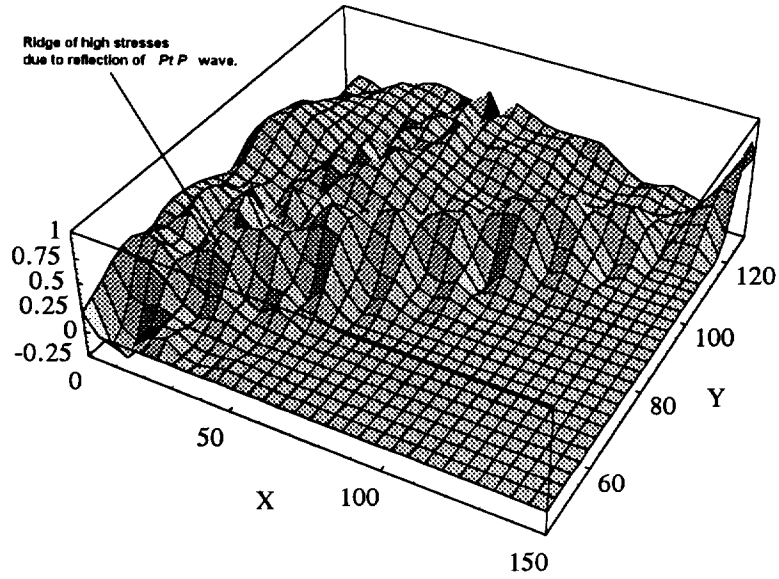

Figure 2.4.1.9 Normalised dynamic stress along the hangingwall skin for Model B as determined from photoelastic experiment.

Model B: In this model a portion of the incident energy is reflected by the Araldite B-Makrolon interface, less energy is propagated by the P_t P wave compared with the incident P-wave, and the hangingwall skin stresses are lower in Figure 2.4.1.9 compared with figure 2.4.1.8.

Stresses propagating behind the reflection point of the P_t P wave are due to Rayleigh, von Schmidt and comparatively low magnitude S_r S_{sr} P_t P and P_r S_{sr} P_t P waves which are reflected by the material interface back towards the stope.

Model C: The incident P-wave energy refracted across the non-cohesive interface decreases as the angle of incidence increases (measured from vertical), and thus the stress at the P_t P wave reflection point decreases with increasing distance along the hangingwall. Most of the refracted incident energy is reflected by the stope in the form of a shear wave (S_{sr} P_t P), which is reflected at the Araldite B-Makrolon material interface and redirected back towards the stope, thus accounting for the high stresses propagating behind the P_t P wave ridge shown in figure 2.4.1.10.

Equivalent carpet plots generated by the numerical back-analyses showed that the wave interactions calculated by the numerical analyses correlated closely with the experimental data (Daehnke *et al.* 1995).

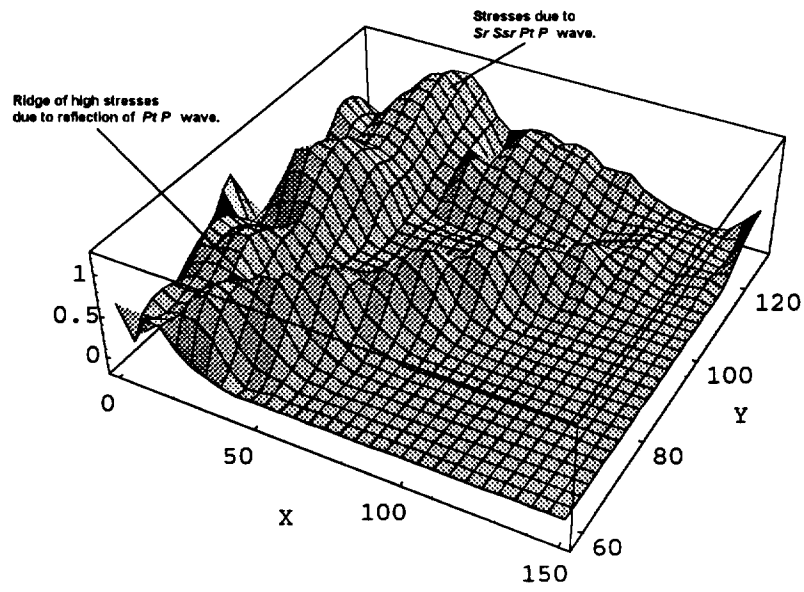

Figure 2.4.1.10: Normalised dynamic stress along the hangingwall skin for Model C as determined from photoelastic experiment.

A third order interpolation function in space and time was applied to the data generating the carpet plots of the experimental and numerical models. The interpolation function was integrated along the stope from 0 to 150 mm and in time from 60 to 129 μs, thus giving an energy measure describing the influence of cohesive and non-cohesive parting planes.

In the photoelastic case the total energy relative to Model A of Models B and C is 76% and 96% respectively. In the numerical analyses the relative energies of Models B and C are 70% and 92% respectively.

The cohesive parting plane reflects a portion of the incident energy, the waves reflected by the stope are transmitted back into the bulk material, and thus it is expected that the total hangingwall energy is less in Model B than in Model A.

In Model C the non-cohesive parting plane traps reflected waves in the hangingwall beam, and the total hangingwall skin energy of Model C is similar to the energy of Model A.

Conclusions

Dynamic photoelasticity is a useful experimental technique for visualising complex stope-wave interactions and obtaining quantitative information in terms of stress magnitudes of real wave pulses. The experimental technique is one of the few means available for judging the quality of

numerical simulations of dynamic behaviour. The dynamic finite difference program WAVE has been proven to model accurately the diffraction, refraction and reflection of stress waves in a homogeneous medium and the interaction of waves propagating across cohesive and non-cohesive interfaces separating two material types.

The experimental and numerical work described here has demonstrated that parting planes reflect a portion of the incident energy and thus shield the stope. However, a non-cohesive parting plane traps energy within the hangingwall beam, thereby negating any shielding benefits associated with parting planes.

This work is limited by the simplified and idealised nature of the model geometries analysed. It is recommended that further investigations are conducted, using dynamic photoelasticity, on the wave interactions in more complicated model geometries incorporating discontinuities representing shear fractures and additional parting planes.

References

Achenbach J.D. (1973) *Wave propagation in elastic solids.* North-Holland Publishing Company, Amsterdam.

Adams G.R., Jager A.J. and Roering C. (1981) Investigation of rock fractures around deep-level gold mine stopes. *Proc. 22nd U.S. Sym. Rock Mech.*, pp. 213-218.

Borejko P., Rossmanith H.P. and Wei Y.Z. (1992) Stress waves in layered rocks. *Acta Mechanica,* Vol. 92. pp. 175-181.

Brekhovskikh L.M. (1960) *Waves in layered media.* Academic Press, New York.

Cranz C. and Schardin H. (1929) Kinematographie auf ruhendem Film und mit extrem hoher Bildfrequenz. *Zeits. f. Physik,* Vol. 56. pp. 147.

Daehnke A., Rossmanith H.P. and Knasmillner R.E. (1995) Using dynamic photoelasticity to evaluate the influence of parting planes on stress waves interacting with stopes. *Int. J. for Num. and Analyt. Methods in Geomech.*, Vol. 19.

Dally J.W. and Riley W.F. (1978) Experimental stress analysis. McGraw-Hill, New York.

Fokkema J.T. (1981) Reflection and transmission of elastic waves by spatially periodic interface between two solids (Numerical results for the sinusoidal interface). *Wave Motion,* Vol. 3. pp. 33-48.

Heunis R. (1980) The development of rock-burst control strategies for South African gold mines. *J. S. Afr. Inst. Min. Metall.*, Vol. 80. pp. 139-149.

Hildyard M.W., Daehnke A. and Cundall P.A. (1995) WAVE: A computer program for investigating elastodynamic issues in mining. *Proc. 35th U.S. Symp. of Rock Mech.*, pp. 519-524.

Rinehart J.S. (1975) *Stress transients in solids*. HyperDynamics, Santa Fe, New Mexico.

Rossmanith H.P. and Fourney W.L. (1983) Rock fracture mechanics. H.P. Rossmanith (ed.) Springer-Verlag, Wien-New York.

2.4.2 Modelling of photoelastic experiments with high angle fractures

Further dynamic photo-elastic experiments were performed to study the effects of high angle fractures in the vicinity of the stope. The emphasis in these studies is on the wave interaction with fractures, and the growth of pre-existing fractures under dynamic stress loading. The experimental work was not carried out under this project. However attempts were made to model the wave interaction using TWO4D and WAVE. There was no attempt to model fracture extension, although this is an important future topic.

A series of photo-elastic experiments were made for cases analogous to those in section 2.4.1 (i.e. a homogenous material, softened material with bonded interface and softened material with unbonded interface), but with the addition of high angle fractures intersecting the stope. The experiment which was modelled is that of the homogenous material, shown in figure 2.4.2.1. Both compressional and shear waves were generated by an explosive source at the surface of the model. A compressive load of 1MPa in the vertical direction and 0.75MPa in the horizontal direction, was applied to the sample. To capture wave patterns in the experiments, a series of photographs of isochromatic fringe patterns indicating lines of equal maximum shear stress, were recorded.

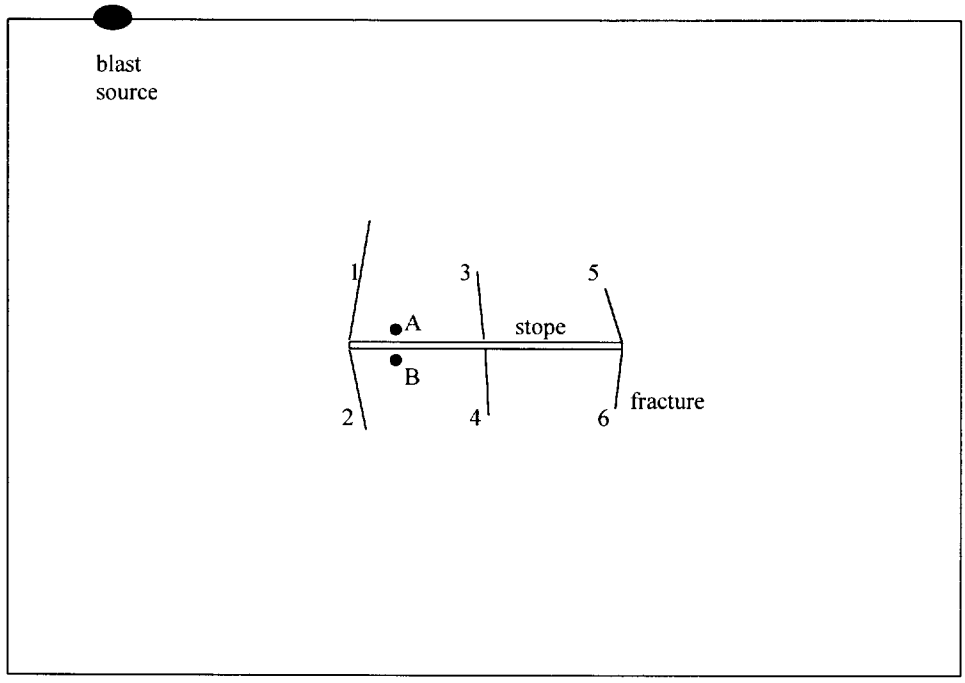

Figure 2.4.2.1: Geometry for the single material model, showing the approximate positions of the stope, fractures and source. The fractures are numbered 1 to 6, while points A and B are positions for which synthetic seismograms are shown.

A first comparison was made using TWO4D which has the advantage of being able to accurately represent the positions and orientations of the cracks. As the simplest first approach, all cracks were modelled as open (no contact possible), and the static loading of the experiment was neglected. (The static load is a small percentage of the stress due to the dynamic waves). Figure 2.4.2.2 reproduced from Siebrits et al (1995), compares the experimental isochromatic fringe patterns with the TWO4D maximum shear stress contours at a time of 206 μsec. This is just after the arrival of the shear wave and some time after the arrival of the P-wave. It can be seen that the transmission and reflection of the shear wave at crack 1 is represented accurately. This indicates that crack 1 (*cf:* figure 2.4.2.1 for crack numbering) behaves as an open crack - at least for shear waves. The shear wave reflected by the stope from the incident P-wave (S_r^sP) is however poorly developed, indicating that there is insufficient P-wave transmission at crack 1 and insufficient S-wave transmission at crack 3.

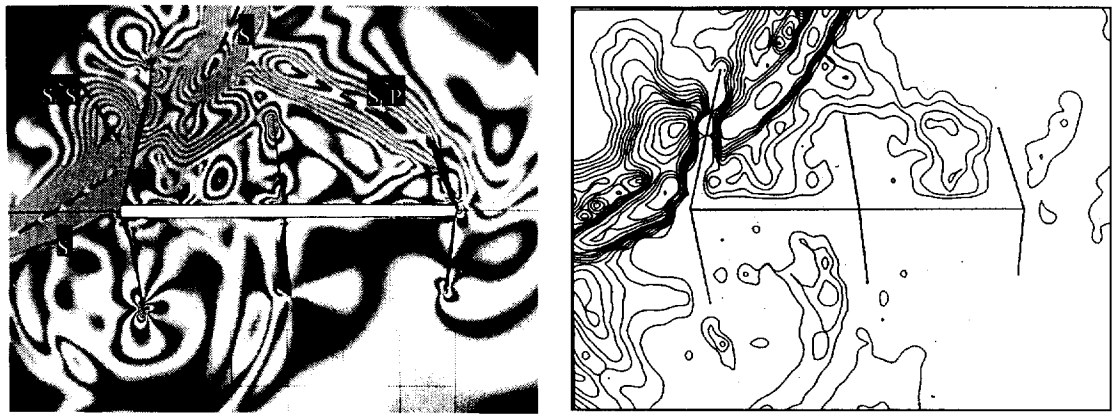

(a) Experiment, t=206μsec

(b) TWO4D, t=206μsec

Figure 2.4.2.2 Comparison between the experiment and the TWO4D result after 206 μsec, just of the arrival of the shear wave

In the experimental results at earlier times (figure 2.4.2.3, 1a and 2a), it is evident that there is both P-wave transmission and reflection at crack 1, very little transmission at crack 2, and significant S-wave transmission at crack 3. This reveals that the cracks behave differently from one another, in terms of their response to P- and S- waves. A large number of numerical experiments were made using WAVE and implementing different crack conditions, in an attempt to understand the important characteristics and also to more accurately reproduce the experiment. In WAVE the correct orientations of the cracks were replaced by vertical cracks as can be seen in the WAVE models in figure 2.4.2.3.

Figure 2.4.2.3 compares five different WAVE models (b to f) with the experiment (a) at four different time steps. The following discussion refers to this figure. In the first case (b), all cracks are once again open (with no closure allowed) and there is insufficient P-wave transmission at cracks 1 and 3, resulting most noticably in the shear wave reflection by the stope from the incident P-wave (S_r^sP) being very weak (2b and 3b). The second case (c) has closed cracks, where the surfaces of each of the cracks are always in contact and there is a high normal and shear stiffness (Kn = 1e5 GPa/m, Ks=1e3 GPa/m), so that both compressional and shear waves are transmitted, and it behaves virtually as intact rock. It can be seen that the reflection from the transmitted P-wave (S_r^sP), prominent in the experiment, is more evident in the closed case than it is in the open case. The reflected waves (S_r^cP) from cracks 1 and 2, also visible in the experiment, are not captured. The third case (d) also has closed cracks but with slip allowed and assuming 0° friction. This captures the correct P-wave transmission and reflection at cracks 1 and 2 (1d and 2d), and shear wave transmission at crack 3 (2d). However the shear wave behaviour at cracks 1 and 2 is poorly modelled. In the fourth case (e) the cracks have a non-linear contact law, such that they behave as either open or closed cracks depending on the normal loading. In this case the P-wave is fully transmitted (1e) which is incorrect. However the interaction of the shear wave with each crack is well represented. Finally, in (f) both contact and slip laws are combined, and there is a close correspondence between the model and the experiment for all time-steps.

Figure 2.4.2.4 records the seismograms for the x and y velocities at position A in the hangingwall (*cf:* figure 2.4.2.1) for each of the above models. Similarly figure 2.4.2.5 records the seismograms for the x and y velocities at position B in the footwall (*cf:* figure 2.4.2.1) for each of the models. No seismograms were recorded in the experiment, although to some extent these could be approximated by analysing the photoelastic fringes over all time-steps. It is assumed that the experimental seismograms would correspond most closely to the last case (cracks with both contact and friction laws), since this model produces closely matching wave patterns. There are significant variations in the behaviour captured by the seismograms for the different crack types. This is encouraging for back-analyses performed from seismic data alone, without the detailed visual wave patterns. As a step toward the back-analysis of more complex experiments, it would be useful to perform similar photo-elastic experiments which also record selected seismograms, and to perform equivalent simple experiments in rock where only the seismic data can be recorded.

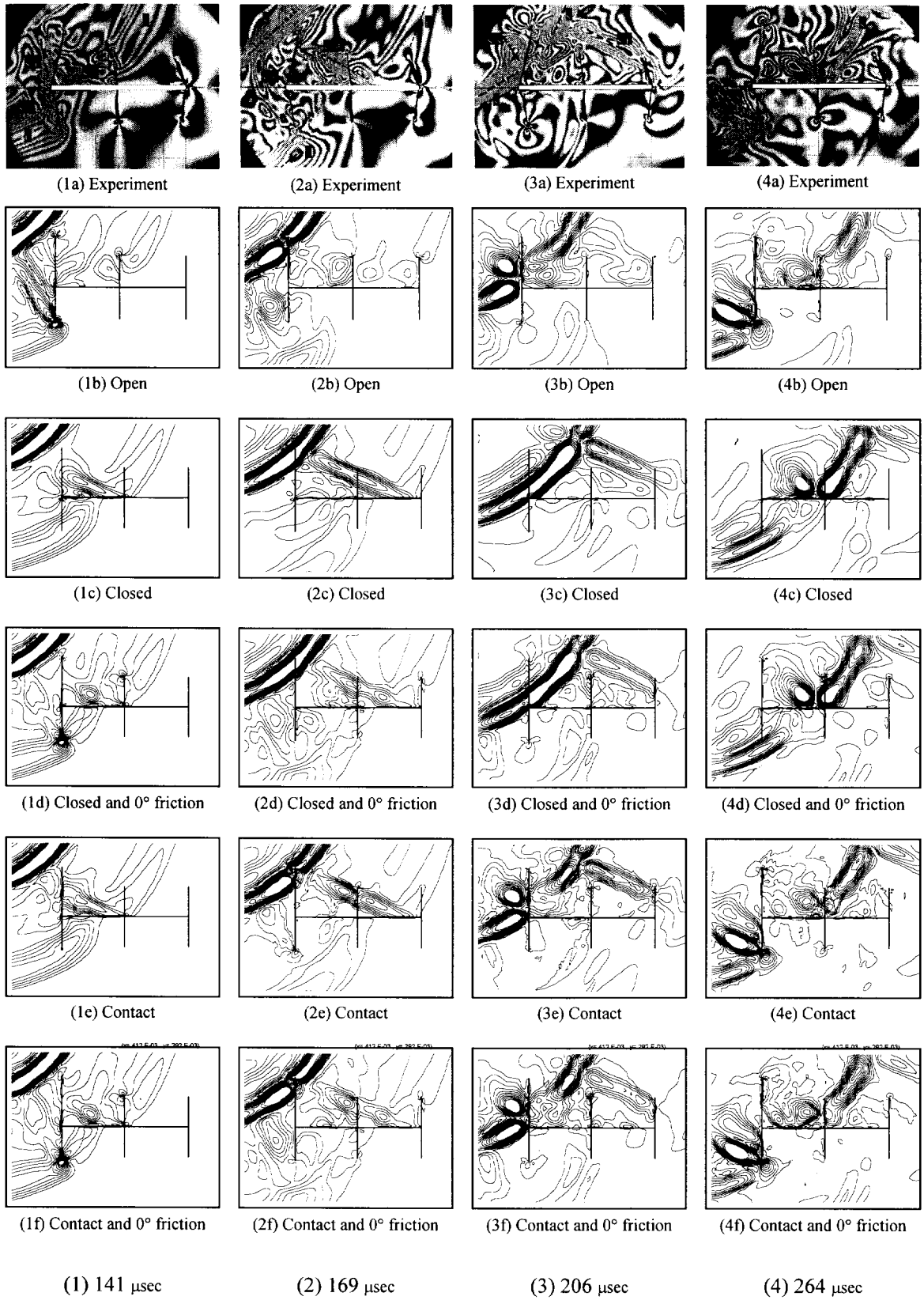

Figure 2.4.2.3: Comparisons between the experiment at four different time-steps and five WAVE models with different crack conditions (a) experiment, (b) open cracks, (c) closed cracks, (d) closed cracks with a 0° friction, (e) contact law on cracks, (f) contact law and 0° friction.

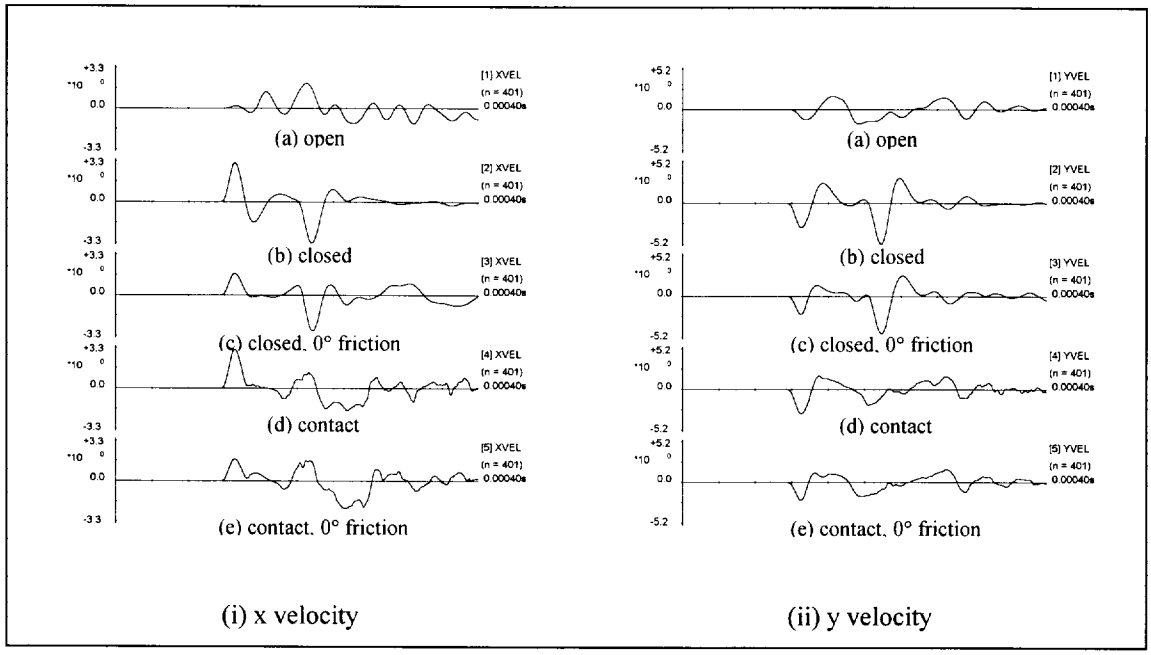

Figure 2.4.2.4: Seismograms at point A in the stope hangingwall for the various crack conditions

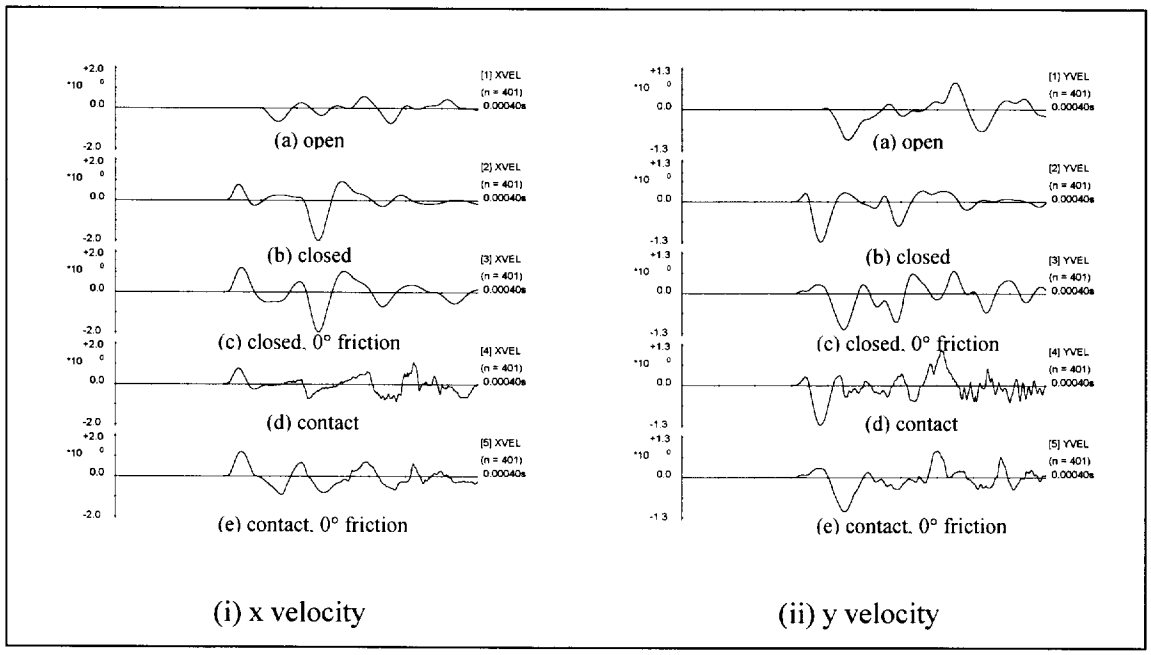

Figure 2.4.2.5: Seismograms at point B in the stope footwall for the various crack conditions

The analysis obtained when the applied load is also included, is compared with the experiment in figure 2.4.2.6 for the four time-steps. Although the error in crack orientations causes differences in the orientations and positions of some of the wave-fronts, it is clear that the actual wave interaction with the fractures is represented very accurately. Therefore, provided that crack slip and contact laws are included, these models can accurately represent wave interaction with discrete fractures.

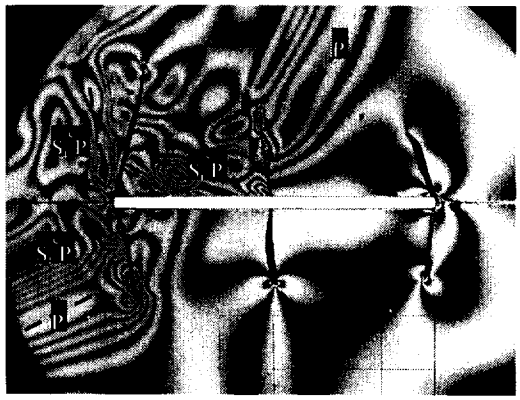

(a) Experiment, t=141μsec

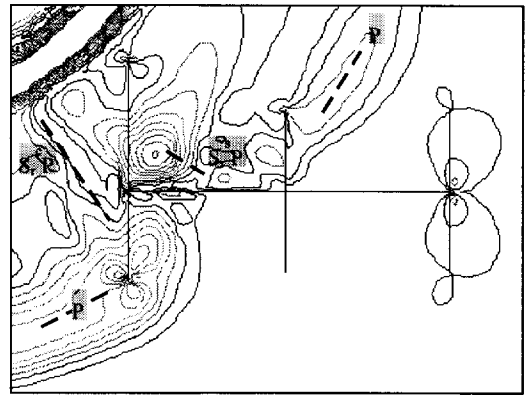

(b) WAVE, t=141μsec

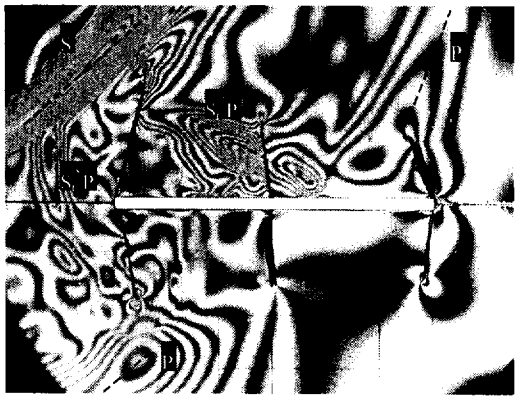

(c) Experiment, t=169μsec

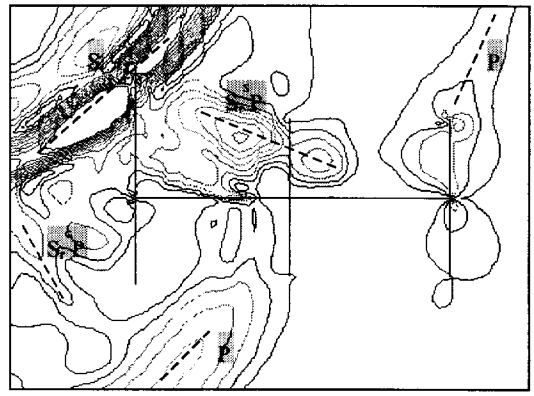

(d) WAVE, t=169μsec

(e) Experiment, t=206μsec

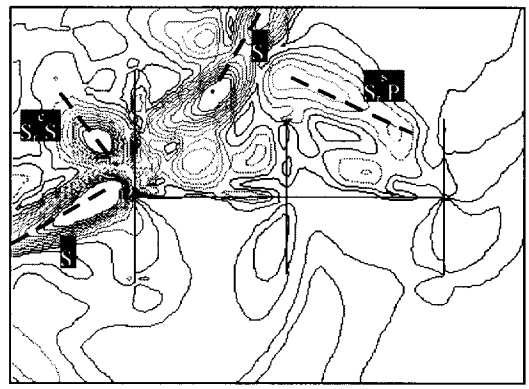

(f) WAVE, t=206μsec

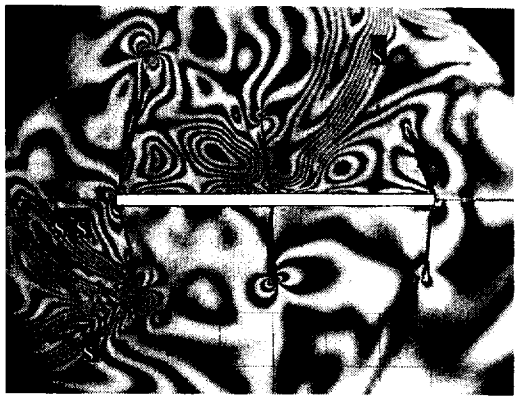

(g) Experiment, t=264μsec

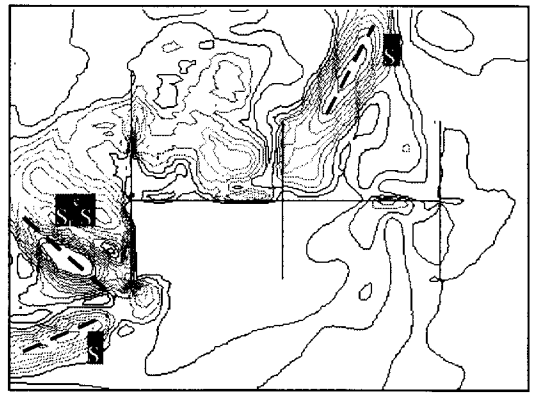

(h) WAVE, t=264μsec

Figure 2.4.2.6: Comparisons between the experimental and WAVE models showing snapshots of maximum shear stress at four different points in time

The experiments contain further detail, specifically the extension of fractures due to the dynamic loading. Figure 2.4.2.7 compares the experiment just after the shear wave has passed crack 1, with the final state after all dynamic motions have died down. The area 'A' highlights where fracture extension has occurred. In the numerical models, there was no attempt to model fracture extension. This is an important future topic, for which representation of accurate crack orientations is likely to be important.

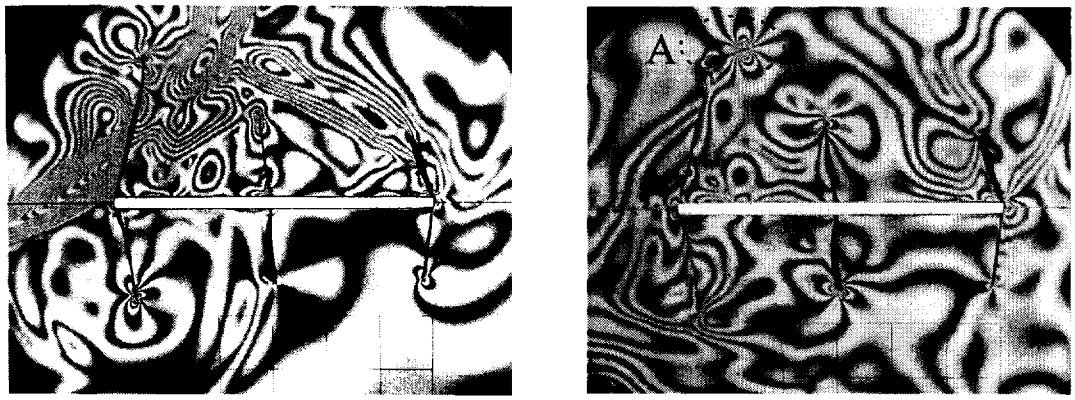

(a) t=204 μsec (b) Final state

Figure 2.4.2.7: Fracture growth in the photoelastic model occurred in the area marked 'A'

Conclusions

The above comparisons with experiments show that these numerical tools can accurately represent wave interaction with fractures, excluding actual fracture growth. It has been highlighted that non-linear slip and contact laws are essential for the representation of dynamic crack behaviour. For WAVE, the above suggests that the representation of numerous cracks would be accurate, provided these are orthogonal. Given the orthogonal limitation, a number of useful experiments can be performed to look at the effects of large scale fracturing. For more general fractures and in particular fracture growth, arbitrarily oriented fractures are necessary. In this regard, boundary element methods such as TWO4D would be useful, if stability and efficiency limitations can be solved. TWO4D could then be re-applied with slip and contact behaviour on the cracks. The above experiment would also be a useful test case in simulating fracture growth.

It is suggested that further photo-elastic experiments should provide a bridge for the modelling of dynamic experiments with fractures in rock, both in two and three dimensions, since the existence of full wave patterns greatly simplifies the back-analysis.

REFERENCES

Siebrits E., Daehnke A. and Hildyard M.W. (1995) 'Experimental and numerical modelling of dynamic stope-wave interactions', *SAIMM SIMRAC Symposium*, September 1995.